UNIVERSITÀ DEGLI STUDI DI CATANIA

Dipartimento di Scienze Biologiche, Geologiche e Ambientali,
Sezione Scienze della Terra

DOTTORATO DI RICERCA IN
GEODINAMICA E SISMOTETTONICA

XXV CICLO

INSIGHTS INTO ERUPTION DYNAMICS AND SHALLOW PLUMBING SYSTEM OF MT. ETNA BY INFRASOUND AND SEISMIC SIGNALS

Dott.ssa Mariangela Sciotto

Coordinatore

Prof. Carmelo Monaco

Tutor

Prof. Stefano Gresta

Co-tutor

Dott. Andrea Cannata

Dott. Eugenio Privitera

DICEMBRE 2012

To my family

INDEX

PREFACE

The success in eruption forecasting needs the knowledge of the eruptive processes and the plumbing system of the volcano. Indeed, the eruptive styles are controlled by the interplay between magma dynamics and the plumbing system. In multi-vent volcanoes, such as Mt. Etna, where volcanic activity can rapidly vary over time and be simultaneously at the different craters, the shallow plumbing system is quite complex.

For forecasting purposes, volcano monitoring measures many geophysical parameters and interprets sub-aerial volcanic phenomena. Lots of volcanic processes occur at or near the boundary between the earth and the atmosphere, thus, beside seismic signal, acoustic waves mainly in the range of infrasound are generated. In particular, infrasound activity is usually evidence of open conduit conditions and its quantification can provide information on explosive phenomena and source mechanism. A more comprehensive knowledge of the source mechanism, as well as of the source depth into the conduit, can be achieved by exploring seismo-acoustic sources, exciting mechanical waves both in the volcano edifice and in the atmosphere.

The aim of the thesis is to look closely at the eruption dynamics at Mt. Etna, with a focus on explosive activity, and at the shallow plumbing system by means of analysis of infrasound and seismo-acoustic signals.

1. INTRODUCTION

Volcanic activity comprises a wide range of phenomena. Processes that start in the volcanic plumbing system determine the nature of subsequent events and control eruption styles (Gilbert and Lane, 2008). Beside the analysis of erupted products, one of the approaches for assessing hazard is the monitoring of the volcano. In both cases the challenge is to relate measurements made outside the volcano to active processes in inaccessible regions far below the surface (Gonnermann and Manga, 2007). Monitoring can provide insights into patterns and consequences of activity that can help draw evacuation plans. The ascent of magma in volcanoes is typically accompanied by seismicity, release of magmatic gases, and surface deformations (Sparks, 2003). Several techniques have been developed in the last decade aiming to measure these parameters and obtain useful information about state of a volcano. Nevertheless, volcanoes remain some of the most complex systems on Earth.

1.1. Volcano monitoring

Traditional volcano monitoring techniques involve analysis of seismic signals, gas monitoring, ground deformation measurements, which in the last years are performed by means of GPS, SAR interferometry and satellite data, and magnetic and gravimetric studies. Volcanic eruptions are almost always preceded by increasing seismicity, and the most reliable indicators of impending eruption are shallow earthquakes and tremor (e.g., Chouet, 1996). Seismology gives useful information about the location of magma bodies/hydrothermal fluids in depth, their dynamics and composition and the plumbing system geometry (e.g. Kumagai and Chouet, 1999; Chouet et al., 2003; Patanè et al., 2006).

In the last decade, new insights into explosive volcanic processes have been made by studying infrasound signals (e.g., Johnson et al., 2003; Vergniolle et al., 2004; Matoza et al., 2009b). In particular, it has proved to be very useful in conjunction with seismic signal analysis (Arrowsmith et al., 2010). There is a natural synergy between seismology and infrasound not only because they share a link to some sources but also because Earth's free surface is not an opaque boundary to either seismic or infrasonic energy (e.g., Arrowsmith et al. 2010). Such studies have provided new insights into eruption source mechanisms, by constraining the source position and obtaining quantitative information on the plume features (velocity, height and eruptive flux) (e.g. Petersen and McNutt, 2007; Caplan-Auerbach et al., 2009). In

addition, by analysing infrasound signals, inferences on the geometry of the very shallow part of plumbing systems have been made (e.g. Fee et al., 2010a; Goto and Johnson, 2011).
Other novel monitoring techniques, such as portable ground radar, which is already being deployed to document explosive eruptions and ash clouds, Muon tomography which holds promise for imaging the interior of internal structure of volcanoes (e.g. Gibert et al., 2010), and Unmanned Aerial Vehicle (UAV; e.g. McGonigle et al., 2008), may provide new monitoring capability. However, these methods will need considerable development to become widely used.
Nevertheless, the most promising method for both monitoring volcanoes and investigating their dynamics is the multiparametric approach (e.g., McNutt et al., 2000; Tilling, 2008). Recently, joint analysis of seismic, infrasonic and thermal/video signals has proved very useful in investigating explosive processes and distinguishing the different eruptive styles and dynamics in various volcanoes, such as Stromboli (Ripepe et al., 2002), Tungurahua (Johnson et al., 2005), Karymsky, (Johnson, 2007), Santiaguito (Johnson et al., 2004; Sahetapy-Engel et al., 2008), Villarica and Fuego (Marchetti et al., 2009a). Moreover, recent multiparametric approaches, based on the investigation of infrasound, several different types of seismic signals, such as earthquakes and seismo-volcanic signals, ground deformation and so on, have allowed tracking the evolution of activity in both deep and shallow parts of volcanoes (e.g., Matoza et al., 2007; Moran et al., 2008a; Di Grazia et al., 2009; Peltier et al., 2009; Aiuppa et al., 2010).

1.2. Seismo-volcanic signals

Volcanoes are the source of a great variety of seismic signals that behave differently than those originating on tectonic earthquake faults (McNutt, 2005). Seismic signals originating from volcanoes and associated with volcanic activity are the subject of the Volcano Seismology. The variety of volcanic processes, related to magma movement at depth, and occurring during the emission at the surface of the solid, liquid, or gaseous products, may generate the seismic signals. Although earthquakes are fundamentals for tomographic studies in volcanoes, they cannot provide precise information about the location and geometry of the shallow magma conduits (Almendros et al., 2002). A more useful approach consists of investigating the seismo-volcanic signals, whose variations and features are often closely related to the eruptive activity. Indeed, they are generally considered as an indicator of the

internal state of activity of volcanoes (Neuberg, 2000). For this reason, their investigation can be very useful for both monitoring and research purposes (Patanè et al., 2011).

Therefore, the fundamentals of volcano seismology concern not only the mathematical approximation of the sources generating the seismic waves but also the description of involved magmatic processes and of the physical properties of medium where they occur (Zobin, 2012). Based on the seismo-volcanic signal nature, the main difference between earthquake and volcano seismology lies in the source mechanism and method of analyses.

Following the most widely used classification in volcano seismology, seismo-volcanic signals include high frequency earthquakes, long-period and very long period events, volcanic tremor, hybrid events and volcanic explosions (McNutt, 2005; Zobin, 2012):

- High frequency (HF) earthquakes are characterized by clear onsets of P and S waves and frequency content higher than 5 Hz (**Fig. 1.1a**). They are also called volcano-tectonic (VT) earthquakes since they are generated by shear fracture and are useful at volcanoes to determine stress orientation (e.g., Moran, 2003). The sources of stress causing HF events have been attributed to regional tectonic forces, gravitational loading, pore pressure effects and hydrofracturing, thermal and volumetric forces associated with magma intrusion, withdrawal, cooling, or some combinations of any or all of these (McNutt, 2005).
- Long period (LP) events are characterized by dominant frequencies in the band 0.5 - 5 Hz (Chouet, 1996) (**Fig. 1.1b**). Features of LP events, also called low frequency (LF) events, are the emergent P wave and the lack of S waves (Chouet, 1996). LP seismic signals originating from the vibration of the stable non-destructive fluid-filled sources (dykes, conduits, cracks) carry information about the geometry of these sources and have been recorded at volcanoes during both eruptive and non-eruptive periods (Zobin, 2012 and reference therein). Investigations on the relationship between LP events and eruptions include moment tensor inversion, source location, spectral content analysis, occurrence rate, and their changes in time (e.g. Patanè et al., 2008; Cannata et al., 2009a; De Barros et al., 2009). Among the models invoked to explain source mechanism of LP events, the most accepted are the fluid-filled resonators, as cracks, conduits or spherical cavities, flow induced oscillations and bubble dynamics (Kawakatsu and Yamamoto, 2007 and reference therein). A peculiar type of LP events are the tornillos (Zobin, 2012), characterized by slowly decaying coda waves. These

signals have been recorded at different volcanoes worldwide during various stages of volcanic activity (e.g., Gomez and Torres, 1997; Milluzzo et al., 2010).

- Very Long Period (VLP) events are characterized by dominant periods in the range 2-100 s (Neuberg et al., 1994; Ohminato et al., 1998) and are assumed to be linked to mass movements, and to represent inertial forces resulting from perturbations in the flow of magma and gases through conduits (Cannata et al. 2009a and reference therein). They have been recorded at many volcanoes, such as Stromboli (Neuberg et al., 1994; Chouet et al., 2003), Popocatépetl (Chouet et al., 2005), Kilauea (Ohminato et al., 1998) and Etna (Cannata et al., 2009a). Seismo-volcanic signals with period longer than 100s are named by some authors Ultra Long Period events (ULP; e.g. Ohminato et al., 1998; Houlie and Montagner, 2007).
- Volcanic tremor consists of a continuous record of monotonic (harmonic) or nonharmonic vibrations that may continue for minutes to months (Zobin, 2012) and is recorded at nearly every volcano during different activity stages. Volcanic tremor has onsets emergent or impulsive, and shares the same frequency band as the LP events but has a different duration in time (**Fig. 1.1c**). The main features of volcanic tremor are (Konstantinou and Schlindwein, 2002): spectra consisting of a series of sharp peaks, representing either a fundamental frequency and its harmonics, or a random distribution, which exhibits temporal variations; strongly variable depths of the source, depending on the volcano, in the range of a few hundred meteres to 40 km; it may occur prior to, during and/or after eruptions. Many authors have suggested that tremor is a series of LP events occurring at intervals of few seconds (Chouet, 1992). Indeed, the models developed to explain the tremor source, generally involve complex interactions of magmatic fluids with the surrounding rocks (e.g. Kubotera, 1974; Steinberg and Steinberg, 1975; Aki et al., 1977; Chouet, 1981), and are similar to the models of LP events. A peculiar feature of seismic volcanic tremor at Mt. Etna is its continuity in time, as also observed at other basaltic volcanoes with persistent activity like Stromboli, Italy (e.g., Martini et al., 2007). Most of the energy of seismic volcanic tremor at Mt. Etna is radiated below 5 Hz (e.g., Schick and Riuscetti, 1973; Gresta et al., 1991; Cannata et al., 2008). Another interesting aspect of the seismic volcanic tremor at Mt. Etna is its close relation with eruptive activity, highlighted by variations in amplitude, spectral content, wavefield features and source location of seismic volcanic tremor at the same time as changes in volcanic activity (e.g., Gresta et al.,

1991; Alparone et al., 2007a; Patanè et al., 2008; Cannata et al., 2008, 2009b). Peculiar types of volcanic tremor are banded tremor (also observed at Etna; Cannata et al., 2010a), and gliding (phenomenon in which harmonics shift as time elapses keeping the same horizontal distance from each other; Hagerty et al., 2000). Furthermore, even acoustic radiation can appear in the shape of volcanic tremor and is therefore called infrasonic volcanic tremor (for details see **section 2.1**) .

- Hybrid events are seismo-volcanic signals that share the waveform and the frequency content of both LP and HF events (**Fig. 1.1d**). These events begin with a high-frequency phase followed by a monochromatic signal similar to a LP event. Causes of hybrid events may be the mixture of source mechanisms from both HF and LP, such as brittle failure on a plain intersecting a fluid body (Lahr et al., 1994) or crack nucleation and deformation and the subsequently motion of fluid through the crack network (Benson et al., 2010).
- Volcanic explosions or explosion-quakes are signals easily identifiable since they are recorded during explosive eruptions (**Fig. 1.1e**) and are usually accompanied by the occurrence of an air wave (**Fig. 1.1f**) generated by the gas release at the vent. On the other hand, it is very difficult to describe them from a seismological point of view, since they may have different features depending on the volcano, particularly conduit geometry and magma composition. Explosion-quakes may occur as a single event or as an earthquake sequence. Studying explosion earthquake at Sakurajima volcano, Uhira and Takeo (1994) demonstrated that an explosive and implosive cylindrical moment tensor component at the source depth is the dominating source mechanism for the explosion-quakes. Acoustic sensors and studies of infrasound signals have greatly improved the knowledge of volcanic explosions as will be discussed further on. Explosion earthquakes are studied with reference to their source depth and the coupling of energy between the ground and the atmosphere, and therefore the seismic and acoustic efficiency (McNutt, 2005).

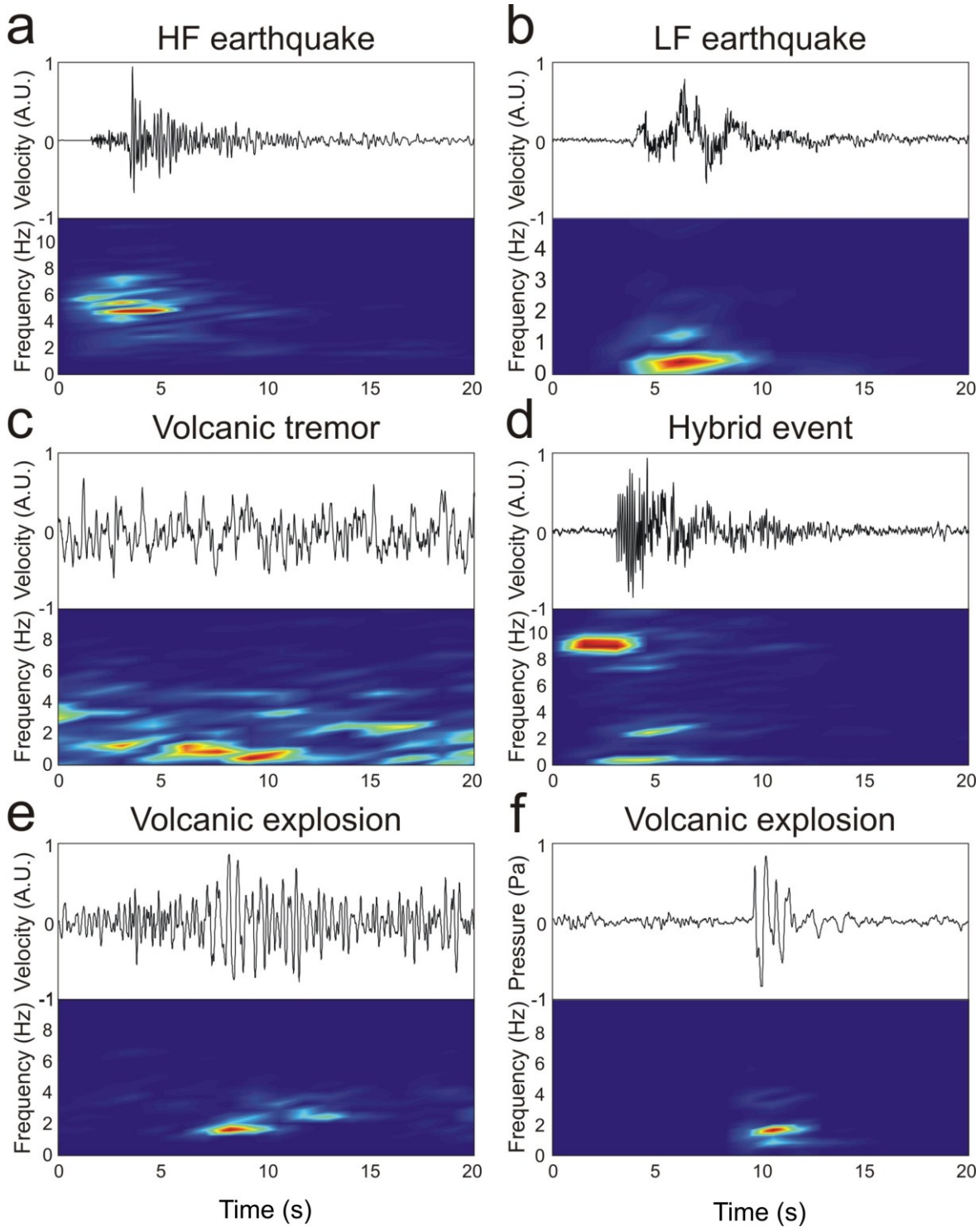

Fig. 1.1 *Examples of seismo-volcanic signals at Mt. Etna:* ***(a)*** *HF earthquake,* ***(b)*** *LF earthquake,* ***(c)*** *volcanic tremor,* ***(d)*** *hybrid event,* ***(e)*** *seismic and* ***(f)*** *infrasound trace of Volcanic Explosion. From Cannata (2009).*

1.3. Mt. Etna volcano

Mt. Etna is a 3330 m high composite Quaternary volcano and lies in a complex regional setting. The volcano is located at the intersection between the front of the Appenine-Maghrebian Chain and the NNW–SSE Malta escarpment fault belt (**Fig. 1.2*;*** Barreca et al., 2012 and reference therein), which is the south-western continental margin of a Mesozoic basin of oceanic nature and extends northward with the Messina-Giardini fault zone (Doglioni et al., 2001 and reference therein). Indeed, at N and W it lies on the sediments of the chain and the E and S sectors on the Quaternary foredeep deposit of the Iblean foreland, belonging to the Pelagian block, the northernmost part of the African plate. Apart from deformations associated with uprising magma (Cocina et al., 1998), structural and seismic data indicate that the regional deformation in the Etnean area is generally dominated by N-S compression and on the eastern side by E-W extension concentrated along the Malta fault system, both offshore and onshore (Doglioni et al., 2001).

The origin of Mt. Etna has been ascribed to the tectonic control, even if an interpretation invoking an hot spot exists (Tanguy et al., 1997). Monaco et al. (1997) related the magmatism of Mt. Etna to the dilation strain on the footwall of an east-facing normal fault in the Siculo-Calabrian rift zone.

According to other authors magma uprising will be favoured by the coexistence of three main fault zones, trending ENE, NNW and WNW (Ritmann, 1973; Cristofolini et al., 1979; Lo Giudice et al., 1982). Nevertheless, recent studies invoke the south-eastward subduction rollback of the Ionian lithosphere with respect to the Hyblean plateau, along the Malta escarpement, as the cause of the development of the volcano (Gvirtzman and Nur, 1999; Doglioni et al., 2001). In particular, according to Doglioni et al. (2001) this mechanism would have generated a sort of vertical “slab window” causing the decompression and melting of magma. Furthermore, several authors have acknowledged the role of the instability of eastern flanks of the volcano on the dynamic processes on Etna (e.g. Borgia et al., 2000; Rust et al., 2005). Geophysical studies, among which GPS and SAR, revealed a continuous eastward to south-eastward motion of part of the eastern sector of the volcano (Palano et al., 2008 and reference therein). This sliding motion may cause the decompression of the plumbing system, facilitating the ascent of magma to the surface (Branca et al, 2003; Neri et al., 2004). Nevertheless, this topic is still open to debate, and several measures about the depths and the geometry of the sliding sector and interpretations dealing with the cause-effect eruption dynamics exist (Lo Giudice and Rasà, 1992; Borgia et al., 1992; Rust and Neri, 1996;

Bousquet and Lanzafame, 2001; Palano et al., 2008; Bonforte et al., 2011; Apuani et al., 2012).

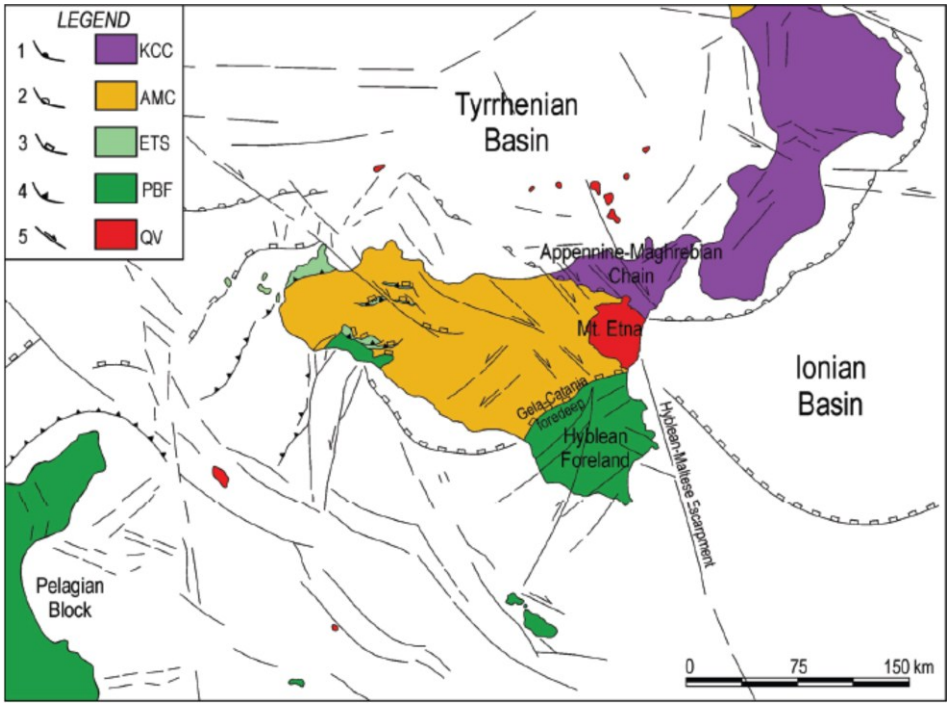

Fig. 1.2 *Structural setting of central Mediterranean Sea and location of Mt. Etna.* ***1)*** *Regional overthrust of the Sardinia-Corsica block upon Calabride units;* ***2)*** *Regional overthrust of the Kabilo-Calabride units upon the Apennine-Maghrebian Chain;* ***3)*** *External front of the Apennine-Maghrebian Chain upon the Foreland units and the External Thrust System;* ***4)*** *Thrust front of the External Thrust System;* ***5)*** *Main normal and strike-slip faults. KCC: Kabilo-Calabride Chain Units; AMC: Appennine-Maghrebian Chain Units; ETF: External Thrust System Units; PBF: Pelagian Block Foreland Units; QV: Quaternary Volcanoes. From Patanè et al. (2011) redrawn from Lentini et al. (2006).*

The volcanism of Etna evolved from submarine and subaerial activity along regional fissures (500–200 ka) to the successive development of numerous vents dispersed over a wide area (Falsaperla et al., 2010 and reference therein). The present volcanic center is the result of two westward shifts of the plumbing system, that occurred about 130 ka and 60 ka ago together to the change of volcanism type to a central one (Branca et al., 2007, De Beni et al, 2011). About 15 ka ago a large summit caldera formed (Coltelli et al., 2000) and during the Holocene, the resuming of the eruptive activity inside the caldera built the volcanic succession of the present active volcanic center (Branca et al., 2004).

Currently, there are five active craters at the summit area of Mt. Etna: Voragine, Bocca Nuova, North-East Crater, South-East Crater and the New South-East Crater, which is a pit-

crater built on the eastern flank of South-East Crater during 2011 (hereafter referred to as VOR, BN, NEC, SEC and NSEC, respectively; see **Fig. 1.3**).

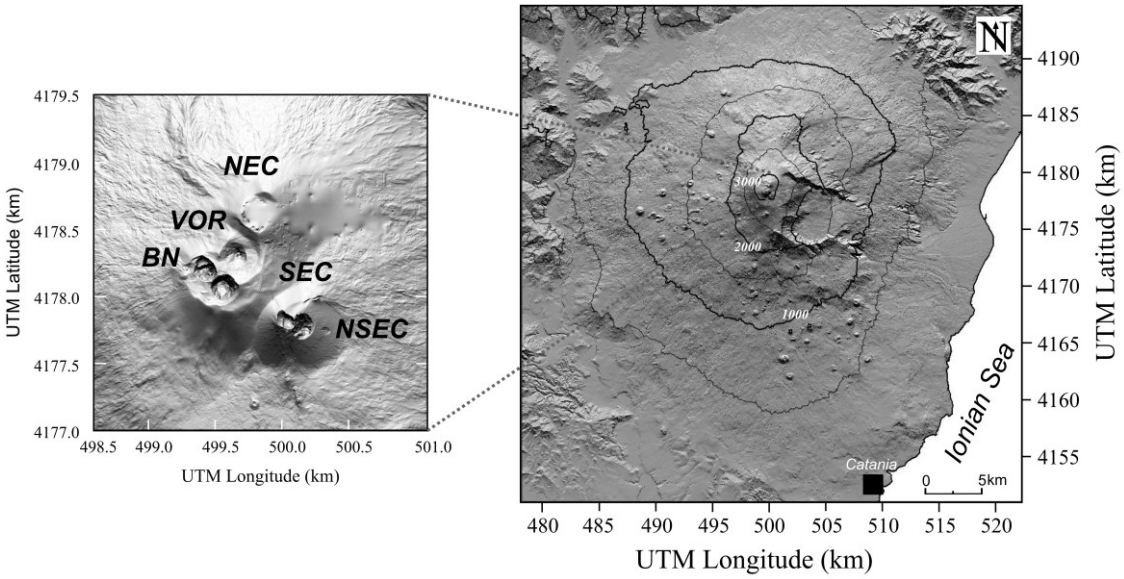

Fig. 1.3 *Digital elevation model of Mt. Etna. In the left inset, the digital elevation model of the summit area with the five summit craters (VOR= Voragine; BN= Bocca Nuova; NEC= North-East Crater; SEC= South-East Crater; NSEC= New South-East Crater).*

These craters are characterized by persistent activity which consists of continuous degassing from vents or fumaroles on the walls of the crater, sometimes producing juvenile or lithic ash emission, and from weak to violent Strombolian explosions and short-lived lava fountains. These last volcanic phenomena are usually accompanied by the emission of lava flows.

Alongside summit eruptive activity, which also includes lava flows originating from eruptive fissures opened on the flanks of the summit cones (Andronico et Lodato 2005), flank eruptions periodically occur (occurrence rate interval can vary from a few months to several decades; Allard et al., 2006). These types of eruptions take place on fissures on the slopes of the volcanic edifice and are related to the central conduit system (Andronico and Lodato, 2005). Rare eruptions, occurring on the flanks of the volcano in which magma rise throughout vertical dikes (Acocella and Neri, 2003), rather than following the central conduit path, are named peripheral eruptions.

As regarding the plumbing system of Etna, several studies of seismo-volcanic signals (for the shallowest portion) and tomographic analysis (for the intermediate portion) have been carried out in order to define its structure. Literature data agree that there is no evidence of a large magma reservoir in the crust below the volcano (Patanè et al., 2011 and reference therein). On the other hand, an high-velocity body (HVB), at a depth of 10 km beneath the Central Crater

area and the south-eastern flank of the volcano, has been recognized (Aloisi et al., 2002; Patanè et al., 2006). This has been interpreted as a large volume of non-erupted volcanic material and represents the deepest portion of the plumbing system. In the upper and lower crust seismic tomography revealed a complex high V_p body representing the old shallow plumbing system and solified magma chambers (Patanè et al., 2011).

During an eruption, activity can be of different and sometimes simultaneous types at the different vents on Etna suggesting a quite complex shallow plumbing system. This portion of the plumbing system is studied by means of the analysis and location of seismo-volcanic signals, rather than by seismic tomography. The reason lies in resolution of tomographic analysis which is too low to allow identifying structure with scale sizes of the conduits or small temporary magma chamber in the shallower portion of plumbing system.

Recent analyses of seismo-volcanic signals carried out at Etna have allowed to image the geometry of the shallow plumbing system and track temporal variations of source location during an eruption (Lokmer et al., 2007a, Patanè et al., 2008; De Barros et al., 2009). Source locations of volcanic tremor in the time period including two lava fountains (4-5 September and 23-24 November 2007 at SEC) have evidenced two connected dike-like bodies oriented NNW-SSE and NW-SE extending from sea level to the surface, the shallower of which crossing the central craters (Patanè et al., 2008). The results of these authors are in agreement with the crack-like structure individuated by Lokmer et al. (2007a) by performing the moment-tensor inversion of LP events collected on Etna during 2004. Indeed, the hypothesized crack is centered at about 500 m below the summit, strikes in NNW-SSE direction and has an inclination from the vertical of about 20° toward the WNW (Lokmer et al., 2007a). Furthermore, De Barros et al. (2009) locating two families of LP events recorded during 2008 eruption obtained the geometry of the structure in which they are generated and move. The geometry depicted consists of a deeper planar structure which at 300 m below the summit craters splits into two branches. The authors identified the deeper structure with the dike-like body found by Patanè et al. (2008) and Lokmer et al. (2007a). The LP events have been associated to magma or gas dynamics into conduit leading to the summit craters (De Barros et al., 2009).

Moreover, further indications about shallow plumbing system geometry and the relation among conduits of the summit craters come from investigation of volcanic gas emission and petrological studies of the erupted volcanics (Burton et al., 2003; Corsaro and Pompilio, 2004; Corsaro et al., 2007, 2012; La Spina et al., 2010).

1.4. Organization of the thesis

The present thesis is structured in six chapters and an appendix.

Chapter 1 consists of an introduction about volcano monitoring, focusing on volcano seismology, and the description of geodynamic setting and eruptive features of Mt. Etna.

Chapter 2 introduces acoustics in order to define infrasound waves and in particular the different types of infrasound signals recorded in volcanic areas. This chapter also includes infrasound activity at Mt. Etna, acoustic wave speed, and detailed description of resonance models generating this kind of signal.

Chapter 3 summarizes the methods of analysis of both infrasound and seismo-acoustic signals in frequency and time domain used in the thesis.

Before describing case studies, a description of eruptive activity of Mt. Etna during the last few years is given in **Chapter 4**.

Chapter 5 deals with data analysis of selected eruptive episodes with the aim of characterizing both explosive dynamics and shallow plumbing system. In particular, infrasound signal recorded during the 16 November 2006 paroxysmal activity has been analysed and compared with seismic signal. The second dataset consists of seismo-acoustic events collected during 12-13 May, before the 2008-2009 eruption: features of signal and their temporal variation are analysed in order to investigate the shallower portion of plumbing system and magma dynamics therein. Furthermore, relation between infrasound and seismic energy radiated during three minor ash emissions taking place during 2010 is explored, the last section of **Chapter 5** presents the application of subspace detector on infrasound data recorded during 3 lava fountains of 2011.

Chapter 6 summarizes the main results obtained.

Finally**,** the **Appendix** deals with a synthetic test aiming to the optimization of sensor deployment based on an infrasound monitoring experiment, carried out in a geothermal area of Yellowstone National Park.

2. ACOUSTIC WAVES

Acoustic waves are accountable not only for the sound that humans can hear, but also for the inaudible one. Indeed, acoustic waves can be divided into three types based on their frequency range: i) audible between ~20-20,000 Hz; ii) ultrasound above 20,000 Hz; and iii) infrasound below 20 Hz. At longer wavelengths (~ 300 s) acoustic-gravity waves are generated (Pierce, 1981).

Acoustic waves are produced as response to oscillatory processes. When the molecules of a fluid or solid are displaced from their normal configurations, the internal elastic restoring force, coupled with the inertia of the system, enables the medium to participate in oscillatory vibrations and generate acoustic waves (Kinsler, 1982). Once generated, acoustic energy propagates as a mechanical pressure wave through a medium. In the atmosphere, sound waves propagate within a gas, compressing and rarefying the medium and no shear waves are supported (Fee and Matoza, 2013).

A wide range of phenomena is able to generate infrasound waves, such as auroras, earthquakes, tsunamis, landslides, meteors, lightning and sprites, and oceanic-atmospheric dynamics (Hedlin et al., 2012 and reference therein). As mentioned in **section 1.1**, in the last decade infrasound has been widely employed next to volcano seismology signals, and a large literature about this topic exists (e.g., Johnson and Ripepe, 2011, Fee and Matoza, 2013 and reference therein).

2.1. Infrasound waves in volcanic area

Due to the large length scales involved in volcanic processes, the majority of volcano acoustic oscillations occur at infrasonic frequencies (Fee and Matoza, 2013). The study of infrasound signal has many advantages. Indeed, despite potential atmospheric variability, over intermediate distances (<5 km) infrasound propagation is relatively simple compared to seismic propagation (Johnson, 2003). Furthermore, the relatively low acoustic attenuation in the atmosphere at these frequencies allows infrasound from large eruptions to propagate long distances and to be recorded globally (Fee and Matoza, 2013).

Pressure sensors, as for example microphones, record infrasonic pressure traces, which represent the time history of atmospheric pressure perturbations relative to background atmospheric pressure. This excess pressure is usually very small compared to ambient

atmospheric pressure. Thus, most of volcanic infrasonic signals can be treated as linear elastic waves rather than nonlinear shock waves (Zobin, 2012).

Analysis of infrasound signal generated by volcanoes has mainly been used for three aims: i) to understand the eruption dynamics (which includes location of infrasound sources, quantification of the outflux of volcanic materials, imaging of the very shallow portion of the plumbing system); ii) monitoring of restless volcanoes in order to assess and mitigate hazards; iii) probing of the atmosphere (Johnson and Ripepe, 2011 and reference therein). One of the advantages of infrasound monitoring is that when the efficiency of video cameras and thermal sensors is reduced (or inhibited) in the case of poor visibility due to clouds or gas plumes, it may prove a very powerful tool for the detection and characterization of explosive activity (e.g., Cannata et al., 2009b).

Arrowsmith et al. (2010), in a review of seismo-acoustic wavefield, have highlighted how the joint study of seismic and infrasound radiation provides unique constraints for studying a broad range of topics. One of these topics regards volcanic phenomena. Indeed, lots of sources relative to volcanic activity radiate energy both down into the solid Earth and up into the atmosphere (Hedlin et al., 2012). Several studies have demonstrated the usefulness of coupled seismo-acoustic investigation to constrain the position of seismo-acoustic sources inside the conduit (e.g., Ripepe et al., 2001a; Gresta et al., 2004; Kobayashi et al., 2005; Ruiz et al., 2006; Petersen and McNutt, 2007), the acoustic properties of the fluid-filled conduit (e.g., Hagerty et al., 2000), as well as to obtain a more complete model of seismo-acoustic source (e.g., Matoza et al., 2007, 2009a). Recently, seismo-acoustic studies have also been performed at Mt. Etna (e.g., Di Grazia et al., 2009).

Fee and Matoza (2013), in their review on volcano infrasound, highlighted how individual volcanoes and eruptions can exhibit multiple types of activity. Nevertheless, according to these authors, associations between eruption style and features of infrasound signals can be made.

Infrasound signals recorded in volcanic areas can be classified in explosion, jetting and infrasound tremor (Fee and Matoza, 2013):

- Explosions or degassing bursts are transient events typically characterized by impulsive and compressional onset, followed by rarefaction. They can exhibit a coda lasting from few seconds to minutes. As addressed in **section 1.2**, volcanic explosions have a wide variety of characteristics and at times complicated source-time functions. They are commonly associated with Strombolian and Vulcanian eruptions but can occur during nearly every type of activity such as degassing activity (Fee and Matoza,

2013 and reference therein). Infrasound transients recorded in association with LP events have been ascribed to gas-release mechanism (Petersen and McNutt, 2007) or to the trigger mechanism initiating LP resonance (Matoza et al., 2009a).

- Jetting is a broadband infrasound signal accompanying sustained volcanic explosions. Jetting signal observed at Tungurahua volcano by Ruiz et al. (2006) was characterized by waveforms with emergent onset and long duration codas. Based on the similarity with man-made jet noise, this kind of infrasound signal has been attributed to turbulence processes (Matoza et al., 2009b). Fee et al. (2010b) observed a low-frequency jetting during Plinian activity and pyroclastic density flow at Tungurahua.
- Infrasonic tremor is defined as a low frequency (<10 Hz) continuous vibration of the atmosphere lasting from seconds to months. This kind of signal has been recorded at several volcanoes (e.g., Arenal, Garcés et al., 1998; Kilauea, Garcés et al., 2003, Fee et al., 2010a; Sakurajima, Morrissey et al. 2008; Mount St. Helens and Tungurahaua, Matoza et al., 2009a, b; Villarica, Ripepe et al., 2010). Similarly to volcanic tremor (see **section 1.2.**), several types of infrasonic tremor exist. Based on frequency and time domain features, harmonic, monochromatic, and broadband tremor can be distinguished. Harmonic tremor includes chugging, which is a tremor accompanied by audible pulses and is characterized by spectra with a fundamental peak at around 1 Hz and integer overtones. It has been interpreted as a succession of pressure pulses at the surface (Lees and Ruiz, 2008) and attributed to resonance of fluid-filled conduit (Garces, 2000). Furthermore, spasmodic tremor, characterized by amplitude variations, episodic tremor (bursts of tremor separated in time) and gliding (with time variations of spectral peaks) can be observed (Fee and Matoza, 2013 and reference therein). Infrasonic tremor is usually associated with lava fountain activity (e.g. Cannata et al., 2009b), and persistent effusive degassing (Matoza et al., 2010).

On the other hand, if we want to classify infrasound transients based on frequency content, and follow the nomenclature of seismo-volcanic signals, we have (Fee et al., 2010a): Infrasonic Short Period (ISP; 1-10 Hz), Infrasonic Long Period (ILP; 0.1-1 Hz), Infrasonic Very Long Period (IVLP; 0.03-0.1 Hz).

In a volcanic environment, several phenomena are able to generate infrasound signals such as rockfalls (Moran et al., 2008b) or pyroclastic flows (Oshima and Maekawa, 2001). Moreover, in a system consisting of a conduit filled with magma and gas many source mechanisms can be responsible of infrasound wave radiations, like the sudden uncorking of the volcano (Johnson and Lees, 2000), the oscillation of bubbles at the surface of a lava lake (e.g. Bouche

et al., 2010), the swelling–up of the lava plug (Yokoo et al., 2009), degassing phenomena (e.g. Fee et al., 2010a), lava fountaining and Strombolian activity (e.g. Cannata et al., 2009b), the opening of "valves" sealing fluid-filled cracks (Matoza et al., 2009a), gravity-driven bubble column dynamics responsible for conduit convection (Ripepe et al., 2010), bubble cloud oscillations in a roiling lava body and interaction of the escaping stream of gas with the vent and near-surface cavities (Matoza et al., 2010). Processes associated to magma-fluid dynamics, generating both infrasonic tremor and transients, have been modeled also invoking resonance phenomena of cavity-conduit (e.g., Garces and McNutt, 1997; Fee et al., 2010a; Goto and Johnson, 2011) and resonating gas bubbles (e.g., Vergniolle and Brandeis, 1996; Vergniolle and Caplan-Auerbach, 2004; Vergniolle et al., 2004; Kobayashi et al., 2010). Few examples of infrasound signals recorded at several volcanoes are reported in **Fig. 2.1.**

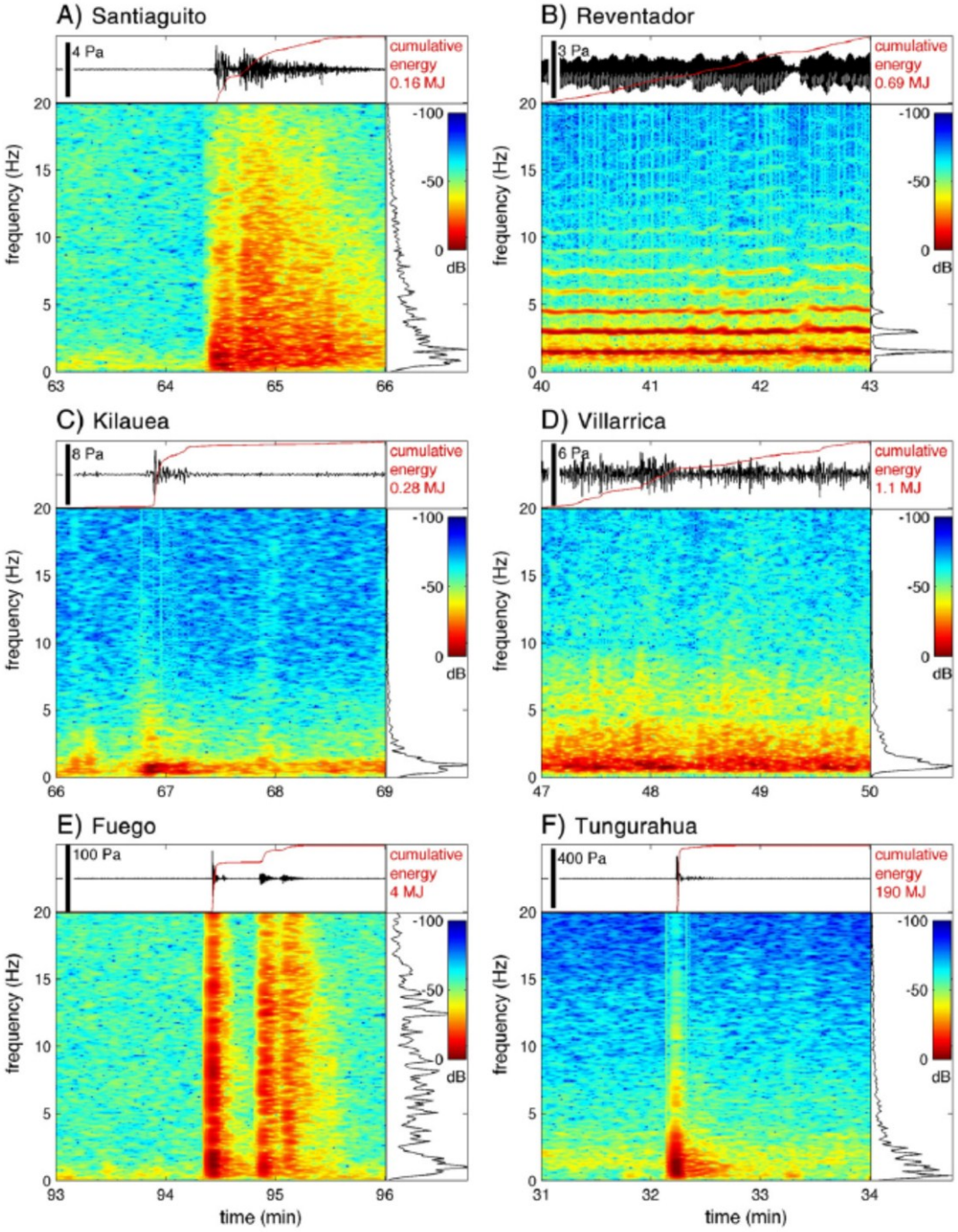

Fig. 2.1 *Examples of 3-minute long infrasound waveforms and the relative spectrograms at several volcanoes: pyroclastic-laden explosions from a dome at Santiaguito* ***(A)****, chugging at Reventador* ***(B)****, degassing from an open magma column at Kilauea* ***(C)****, infrasonic tremor due to degassing from a roiling lava lake at Villarrica* ***(D)****, infrasound explosions from Strombolian activity at Fuego* ***(E)*** *and Vulcanian ash-rich eruptions at Tungurahua* ***(F)****. Cumulative energies (red lines) and power spectra (on the right) for each signal are also shown. From Johnson and Ripepe (2011).*

2.1.1. Infrasound at Mt. Etna

Since 2006, the Istituto Nazionale di Geofisica e Vulcanologia (INGV), Osservatorio Etneo– Sezione di Catania, has been recording and studying the infrasound signal at Mt. Etna by a permanent network. Before the deploying of the permanent network infrasound investigations at Mt. Etna were carried out during temporary experiments (e.g. Ripepe et al., 2001b; Gresta et al., 2004).

Infrasound signals at Mt. Etna generally consist of amplitude transients, with variable duration (from 1 to a few tens of seconds), impulsive compression onsets and peaked spectra with most energy in the frequency range 1–5 Hz (Cannata et al., 2009b, c; Montalto et al., 2010). Such infrasonic signal features are similar to those observed at several volcanoes, though characterized by different volcanic activity, such as Santiaguito (Sahetapy-Engel et al., 2008), Stromboli (Ripepe et al., 1996; Marchetti et al., 2008), Tungurahua (Ruiz et al., 2006), Klyuchevskoj (Firstov and Kravchenko, 1996), Erebus (Rowe et al., 2000), Arenal (Hagerty et al., 2000), Sangay and Karymsky (Johnson and Lees, 2000). In addition, at Mt. Etna infrasonic volcanic tremor has been recorded in association with lava fountain episodes and seismic banded tremor activity (Cannata et al., 2009b, 2010a). Four summit craters have been recognized as active from the infrasonic point of view (Cannata et al., 2009b, c): NEC, BN, SEC and NSEC (the new pit-crater built on the eastern flank of the SEC cone). Infrasound radiation from these vents can be classified into continuous and sporadic activity. The former consists of short-duration releases of pressure bursts constantly generated by NEC and related to degassing activity (Cannata et al., 2009c), while the latter occurs solely during explosive activity (Strombolian explosions, lava fountains, ash emissions).

2.2. Acoustic wave speed in atmosphere and into the conduit

In facing the study of infrasound waves in volcanic area, the acoustic speed has to be taken into account. Indeed, infrasound waves, once generated, travel into the conduit, and in the atmosphere at high altitudes, and can propagate for several kilometers before reaching the microphone. Thus, they pass through different ambient conditions, which affect their propagation.

The acoustic speed of an ideal gas, characterised by a certain chemical composition, is given by:

$$c_{mixt} = \sqrt{\gamma_{mixt} R_{mixt} T} \tag{2.1}$$

where γ_{mixt} and R_{mixt} are the heat capacity ratio and the constant for the gas mixture, respectively. The heat capacity ratio for a gas mixture (γ_{mixt}) is given by:

$$\gamma_{mixt} = \frac{\frac{\sum X_i \gamma_i}{(\gamma_i - 1)}}{\frac{\sum X_i}{(\gamma_i - 1)}} \tag{2.2}$$

where X_i and γ_i are the mass fraction and the heat capacity ratio of the *i*-component, respectively (Rienstra and Hirschberg, 2012). At the same way, R_{mixt} is defined by the sum of the constant of the gas components (R_i). **Equation 2.1** shows how c_{mixt} for a given gas depends on the temperature (T) and the gases composing the mixture. For example, acoustic waves in the lower atmosphere propagate with speed of 306 m/s at -40° C, 355 m/s at 40° C (Johnson, 2003), and 344 m/s at 20° C in dry air.

The estimation of acoustic speed in conduit is more difficult, since in most cases the exact values of T and gas components are unknown. Nevertheless, measures of these parameters are present in literature. For instance, Sahetapy-Engel et al. (2008) and Weill et al. (1992) considered a fluid temperature in the conduit of 1173° K for both Stromboli and Santiaguito. Fee et al. (2010a) by means of FLIR imagery estimated an average temperature inside the cavity of Halema'uma'u of about 470° K. Other authors also performed some measurements of lava temperature by FLIR, obtaining for instance ~1100-1200° K at Stromboli (Harris et al., 2005) and ~1000-1300° K at Etna (Bailey et al., 2006).

With the aim of constraining the acoustic speed in the conduit at Mt. Etna, we used chemical compositions of gas emitted by NEC during 2008 and 2009 (La Spina et al., 2010), and applied the ideal mixing theory, as reported in Morrissey and Chouet (2001). Acoustic speeds were calculated by considering temperatures equal to 300°, 800° and 1200° K and the associated R_{mixt} and γ_{mixt} values. In particular, for each gas specie, the R_i and γ_i values at 300° K were found in Serway and Jewett (2006) and at 800° and 1200° K in Morrissey and Chouet (2001).

Therefore, applying **equations 2.1** and **2.2**, we obtained an acoustic speed ranging between 400 and 750 m/s.

2.3. Volcano acoustic source modelling

Since in this thesis the analyzed infrasonic signals are interpreted as resulting from resonance phenomena related to the conduit, in the following section such phenomena will be addressed. Resonance is a propagation path effect inside the conduit and is generated by multiple reflections of pressure disturbances in the fluid against boundaries (e.g. Garces and McNutt, 1997; De Angelis and McNutt, 2007). A conduit can act as an acoustic resonator to an excitation source.

2.3.1. Pipe resonance

If the cross-sectional dimensions of a resonator are much smaller than the acoustic wavelength, the excited sound field develops a spatial variation only along the length of the resonator, i.e., longitudinal modes of the pipe are dominant and the effects of small variations in the radius are negligible (Kinsler et al., 1982). Thus, a narrow conduit can be regarded as an one-dimensional acoustic resonator. In the standing wave modes the acoustic pressure waves in the cavity volume will create a steady pattern consisting of a fixed number of sinusoidal waves between opposite cavity boundaries (Jong and Bijl, 2010). The frequencies for a closed-closed or open-open pipe resonator are equal to:

$$f = \frac{mc_c}{2L} \tag{2.3}$$

where c_c is the acoustic speed of fluid into the conduit, m is the longitudinal mode number (m = 1, 2, 3,…) and L is the resonating conduit portion length. For an open-closed pipe the possible frequencies are:

$$f = \frac{(m - \frac{1}{2})c_c}{2L} \tag{2.4}$$

Open-open or closed-closed conduits are characterized by spectra with peaks consisting of the fundamental mode f_o ($f_o = c_c/2L$) and integer harmonics which are multiples of f_o ($f_n = m\, f_o$), while open-closed conduit conditions generate the fundamental frequency and odd harmonics ($f_n = (m - 1/2)\, f_o$) (De Angelis and McNutt, 2007). The relevant parameters in the pipe resonance are the conduit length and the impedance of the conduit terminations. The

impedance of the conduit terminations may indicate changes in the cross-sectional area of the conduit and/or changes in the density and sound speed of the fluid filling the conduit (Graces and McNutt, 1997). In order to state if a termination is closed or open the contrast of impedance should be taken into account. Further, the end correction has to be considered (Morse and Ingard, 1986). Physically the end correction can be understood as an effect of the mismatch between the one-dimensional acoustic field inside the pipe and the three-dimensional field outside that is radiated by the open end. The end correction for a closed end is naturally zero, while for an open end is 0.6**l* (where *l* is the pipe radius) (Miklos et al., 2001).

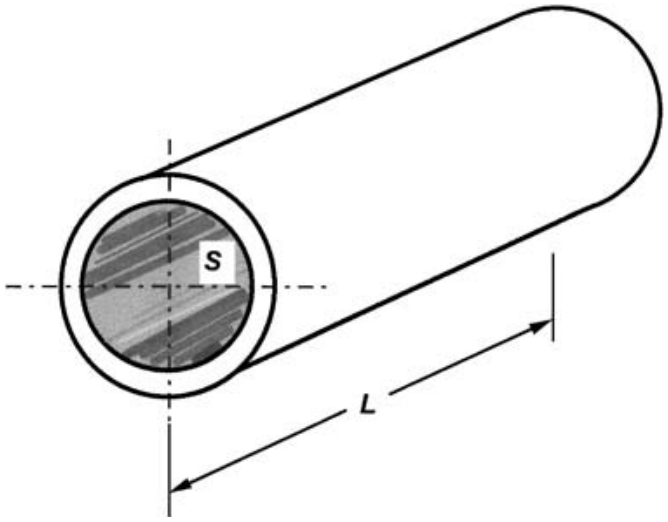

Fig. 2.2 *Sketch of a pipe resonator. From Raichel (2006).*

2.3.2. Helmholtz resonance

Another possible excitation mechanism of volumes with a small opening is Helmholtz resonance. Helmholtz resonator is a harmonic oscillator with only one degree of freedom (volume) and is termed a lumped acoustic element (Kinsler et al., 1982). It consists of a cavity connected with the outside space through a narrow neck or through an opening (**Fig. 2.3**; Alster, 1972).

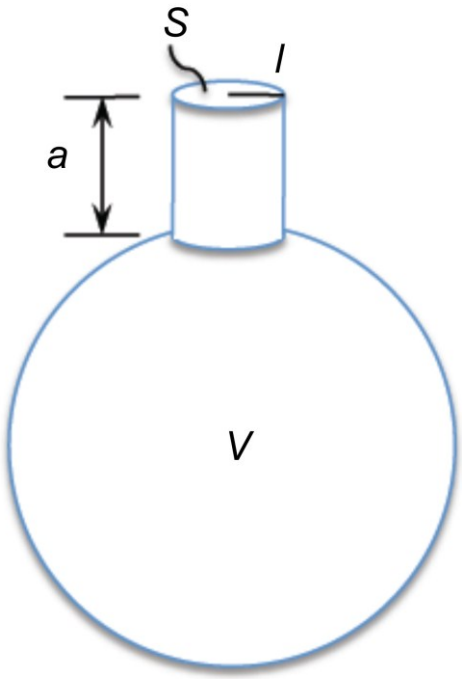

Fig. 2.3 *Sketch of a Helmholtz resonator. From Campbell and Peatross (2011).*

Helmholtz resonators do not work on the principle of formation of standing wave pattern. Instead, they can be modeled as a simple mass loaded on a spring system. The fluid in the neck acts as the mass, while the fluid pressure on both inside and out of the resonator acts as the spring. The effective mass of the fluid in the neck is given by (Kinsler et al., 1982):

$$m = \rho SL' \tag{2.5}$$

where ρ is the density of the fluid, S is the area of the neck (narrowing) and L' is the effective neck length. This effective neck length L' is longer than the physical length (a) because of its radiation mass loading. The air pressure acts as a spring in the system. The "spring constant" of the air pressure (stiffness) is given by (Raichel, 2006):

$$k = \rho c^2 \frac{S^2}{V} \tag{2.6}$$

V is the cavity volume (conduit). The driving force acting on the opening is given by:

$$F = PS \tag{2.7}$$

where P is the sound pressure. The equation for spring mass oscillation can be written as:

$$m\frac{d^2\delta}{dt^2} + k\delta = SP \tag{2.8}$$

where δ is the displacement of the slug of air contained in the neck. Solving **equation 2.8**, resonance frequency is obtained:

$$\omega_0 = \sqrt{\frac{k}{m}} \tag{2.9}$$

Substituting in **equation 2.9** m and k (**equations 2.5** and **2.6**, respectively) we obtain that the Helmholtz resonator frequency is equal to:

$$f = \frac{c_c}{2\pi}\sqrt{\frac{S}{VL'}} \tag{2.10}$$

As regarding the effective length, it takes into account the air/fluid above and below the neck region acting as inertial mass. The end correction is equal to 0.85**l* if the outer opening of the neck is flanged, and 0.6**l* if it is unflanged, as aforementioned. While the inner opening of the neck is assumed to be equivalent to a flanged termination (Kinsler et al., 1982). We considered the outer end of the narrowing unflanged, therefore the combination of the corrections gives:

$$L' = a + 1.45 * l \tag{2.11}$$

where l is the neck radius and *a,* as aforementioned, is the physical length of the neck. One assumption that has to be done in deriving the frequency of the Helmholtz resonator is that all dimensions of the system are much smaller than the acoustic wavelength. In the case of the lower infrasonic frequencies recorded at Etna (e.g. 0.4-0.7 Hz), wavelengths (~500-850 m), with an acoustic speed of 340 m/s, are much longer than the reasonable dimensions of the conduit.

3. METHODS OF ANALYSIS

3.1. Triggering algorithm

The analysis of seismo-volcanic events needs, as the first step, the extraction of the signal portion containing the transient from the continuous recording.

Several kinds of trigger algorithm have been developed based on the specific requirements of seismological applications. Withers et al. (1998) have categorized previous trigger algorithms for onset picking into time domain, frequency domain, particle motion processing, or matched filter.

The automatic detection of infrasound and seismic transients analyzed in this work has been performed by means of Short Time Average through Long Time Average (STA/LTA). STA/LTA is an energy detector in so far as it depends on the amplitude fluctuations of the signal. It is the most common technique in seismological study since it requires little information about the signal to be detected. Indeed, it depends on the amplitude fluctuations of seismic signal, rather than signal polarization and frequencies (Sharma et al., 2010). The algorithm first calculates the absolute amplitude of the signal, then averages the amplitudes in both the short and the long window. The short period average represents the average of the shortest period over which an event of interest could occur, while the long period average represents the average of the longest period to assess the background noise. In the next step a ratio of STA/LTA is calculated and is continuously compared to a preset threshold value. Once the ratio exceeds the threshold, the trigger is declared (Trnkcnozy, 2012).

3.2. Spectral analyses

The time and frequency domains are alternative ways of representing signals and analyses in time and frequency domain, and are complementary for the understanding of the behaviour of a dynamic system. Time domain analysis allows to study variations in time of parameters like for example the shape or the amplitude of the signal waveform. In the frequency domain the signal is represented as decomposed in sinusoidal components. Most signals and processes involve both fast and slow components happening at the same time. Frequency domain analysis separates these components and helps to keep track of them.

3.2.1. Fast Fourier Transform

The time and frequency domain representations are related to each other by the Fourier transform (Rauscher et al., 2001), so each signal in the time domain has a characteristic frequency spectrum:

$$F(f) = \int_{-\infty}^{\infty} x(t) e^{-j2\pi ft} dt \tag{3.1}$$

where *f* is the frequency, *x(t)* is the signal in time domain, *F(f)* is the Fourier transform of *x(t)*, and j is equal to $\sqrt{-1}$. The calculation of the signal spectrum from the samples of the signal in the time domain is referred to as a discrete Fourier transform (DFT). DFT is almost always computed in practice by Fast Fourier Transform (FFT; Cooley and Tukey, 1965), which is not a new transform, but is the most widely used algorithm for efficiently computing the DFT for applications such as spectrum analysis (**Fig. 3.1**).

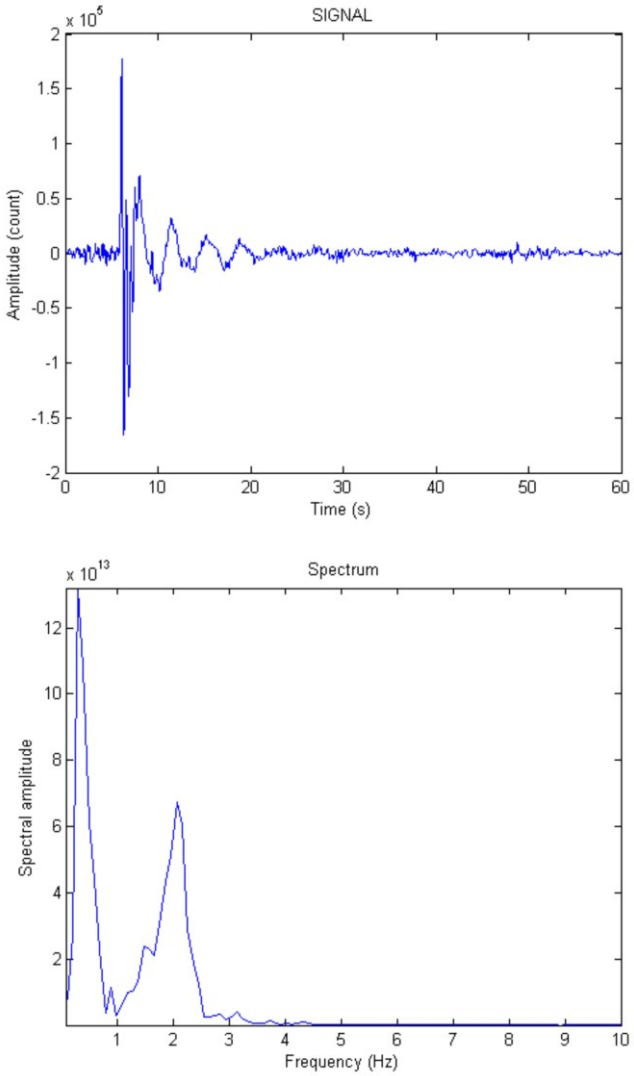

Fig. 3.1 *Infrasonic event recorded at Mt. Etna (top) and its spectrum calculated on 10.24 second-long time-window (bottom).*

3.2.2. Short Time Fourier Transform

Seismic and acoustic signals are of non-stationary nature, that is, their spectral content changes over time. In this case, FFT, since it is based on the assumption of stationary behaviour of the signal, is not able to show the temporal distribution of frequencies. To become accurate in time, a frequency versus time representation of the signal is needed. This kind of spectral decomposition is provided by the Short Time Fourier Transform (STFT). By assuming that signal *x(t)* is stationary when seen through a small time window, then the FFT can be computed on a windowed signal. The signal is segmented by means of sliding window functions *(g)* of a limited extent *(t)* and centered in τ. The Fourier transform of the windowed signal yields to the STFT, which mathematically is defined as (Rioul and Vetterli, 1991):

$$STFT(\tau, f) = \int x(t) g^*(t-\tau) e^{-j2\pi ft}\, dt \tag{3.2}$$

where g^* is the complex conjugate of the sliding window function. Therefore, the STFT method is able to analyze a non-stationary signal in the time domain through a segmented algorithm. A moving window process breaks up the signal into a set of segments (time windows), and each of them is processed by the FFT algorithm. The sliding window function plays an important role in the STFT, and once has been chosen, it fixes the time-frequency resolution of the analysis. If this function has a long duration in time, it implies a fine sampling of the frequency, but small changes in the time domain are obscured because of averaging. Instead, a window function of short time duration defines short-lived variations in time but has a poor frequency resolution. Due to the Heisenberg's uncertainty principle a small time window and a narrow bandwidth window cannot exist contemporaneously, thus a trade-off window size needs to be selected according to frequency and time resolution such that the interesting features of the signal one is looking for are solved (**Fig. 3.2**).

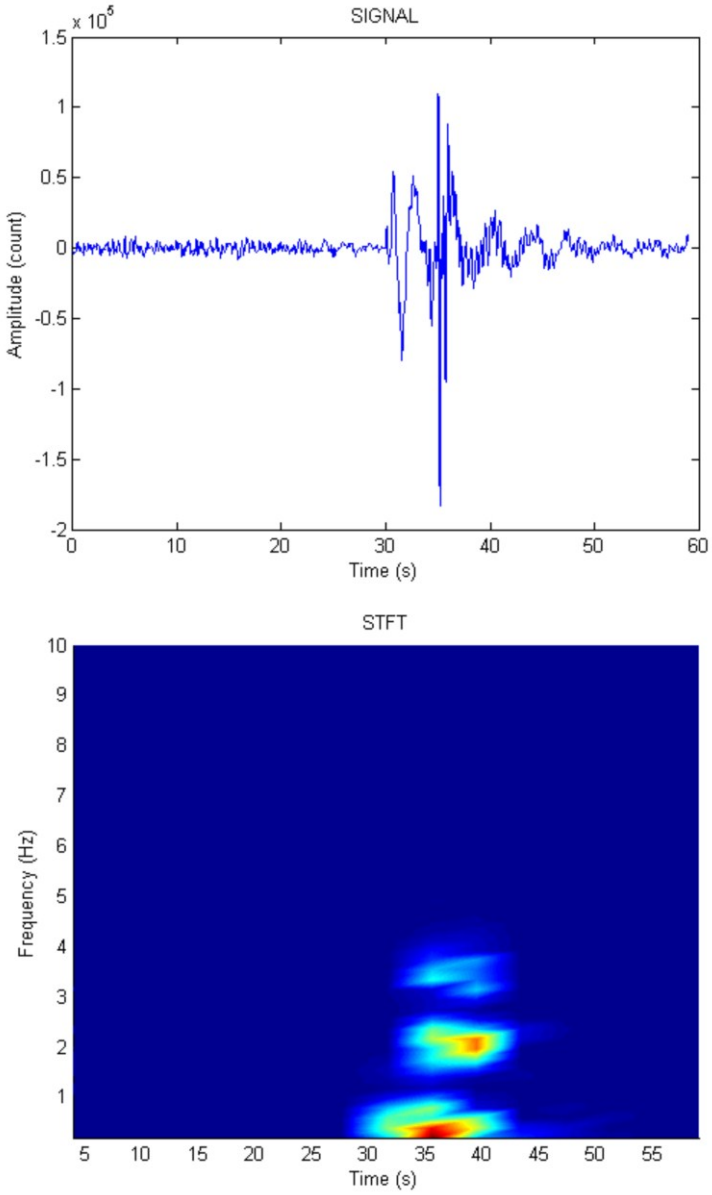

Fig. 3.2 *Infrasonic event recorded at Mt. Etna (top) and STFT calculated on 5.12 second-long time-window (bottom).*

3.2.3. Sompi analysis

Beside the Fourier transform, there is another type of approach for spectral analysis which implies a time series modelling based on the characteristic property of a linear dynamic system. Several seismo-volcanic signals show a clear trend of amplitude to decay with time, then the decomposition of time series into purely harmonic components (Fourier transform case) can cause a loss of information (Kumazawa et al., 1990). Various studies (Chouet, 2003 and references therein) demonstrated that in such cases spectral features will be reasonably represented in the complex frequency space, rather than in the real frequency space as in the

previous method. In particular, a method called "Sompi" has become commonly used in volcano-seismology for his high spectral resolution in determining the decay characteristics and the oscillation period of time series corrupted by noise (e.g. Kumagai and Chouet, 1999, 2000). Sompi method assumes that the observed signal is the realization of a hypothetical linear dynamic system and estimates the characteristic frequencies by determining the autoregressive model (AR) equations that best describe the system (Kumazawa et al., 1990). In practice, a given signal is decomposed into a linear combination of finite-number coherent sinusoids with amplitudes exponentially decaying (or growing) with time such as:

$$x(t) = \sum_{i=1}^{n_\omega} A_i e^{\gamma_i t} \cos(\omega_i t + \theta_i) + \varepsilon(t) \tag{3.3}$$

where n_ω is the number of sinusoids called wave elements, $\varepsilon(t)$ is incoherent noise and ω_i, γ_i, A_i, θ_i are the real parameters characterizing each wave element. In particular, ω and γ correspond respectively to the real and imaginary parts of the complex angular frequency ($z = exp(\gamma+i\omega)$), and A_i and θ_i are respectively the real amplitude and the phase angle of the complex amplitude α ($\alpha = Ae^{i\theta}$). From these parameters we can extract spectral features of the signal as the real frequency *(f)* and the growth rate *(g)* (Kumazawa et al., 1990):

$$f = \frac{\omega}{2\pi} \tag{3.4}$$

$$g = \frac{\gamma}{2\pi} \tag{3.5}$$

Further, the quality factor Q is related to f and g through:

$$Q = -\frac{f}{2g} \tag{3.6}$$

In order to apply the Sompi method a transient in a signal, composed of superposition of simple decaying sinusoids is taken into account, its onset is neglected, and the analysis is performed on the tail (grey are in **Fig. 3.3a**). The first step is the extraction of the wave elements from the signal, then each wave element is characterised by a set of *f* and *g* without information about excitation (amplitude and phase). Spectral analysis results of the Sompi method are usually plotted in 2D diagram with f-g axes (**Fig. 3.3b**). This kind of diagram

allows to identify the dominant modes (circled points in **Fig. 3.3b**), corresponding to the wave elements remaining mainly stable as the AR order changes, from the noise whose wave elements are scattered in the plot (Hori et al., 1989). Besides the frequency and the growth rate, another important parameter obtainable from the Sompi analysis is the quality factor *Q*. It can be considered a measure of the decay time of the sinusoids, thus can give information about the features of the resonator system in terms of attenuation (Chouet, 2003 and references therein).

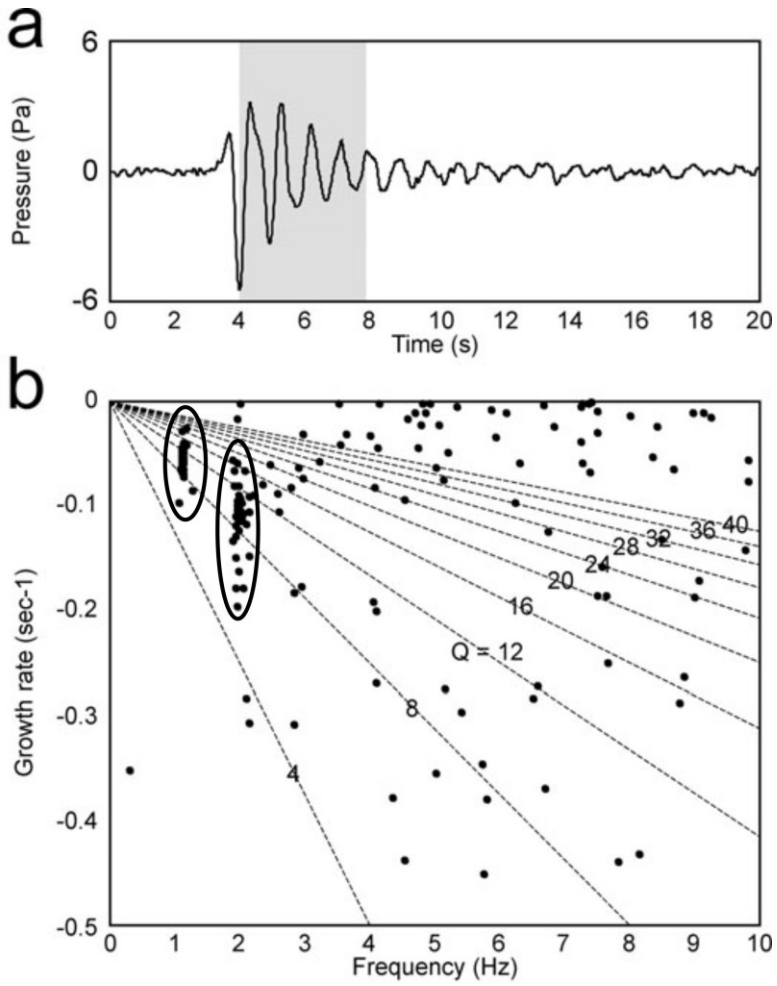

Fig. 3.3 ***(a)*** *Infrasound event recorded at Mt. Etna and corresponding* ***(b)*** *frequency-growth rate plot (AR order 2–60). The dashed lines in* ***(b)*** *represent lines along which the quality factor (Q) is constant. Circled points in* ***(b)*** *indicate dominant spectral components of the signal; scattered points represent noise. From Cannata et al. (2011b).*

3.2.4. Coherence analysis

In some volcanoes seismo-acoustic investigations have shown how seismic and infrasonic signals sometimes share almost the same spectral content, suggesting a common source for both the signals (e.g., Stromboli, Ripepe et al., 1996; and Kilauea, Matoza et al., 2010). The coherence function provides the correlation between two signals at a certain frequency λ. It is defined by (Saab et al., 2005):

$$\left|C_{XY}(\lambda)\right| = \frac{\left|P_{XY}(\lambda)\right|^2}{P_{XX}(\lambda)P_{YY}(\lambda)} \tag{3.7}$$

where P_{XX} and P_{YY} are the autospectra of signal X and Y, respectively, and P_{XY} is the cross spectrum. The result is a real number between 0 and 1. This function allows to investigate the coherence between two signals over time and can be represented in 2D diagram in which x axis is the time, y axis indicates the frequency and the colour scale shows the coherence values.

3.3. Time domain analyses

3.3.1. Cross-correlation analysis

Recent applications of correlation methods to seismological problems illustrate the power of coherent signal processing applied to seismic waveforms. Examples of these application include detection of low amplitude signals buried in ambient noise and cross-correlation of sets of waveforms to form event clusters. The waveforms of earthquakes and long period events are often similar enough that waveform cross correlation can be used to detect them and obtain much more precise differential times in order to perform high-precision relocation (e.g. Lin et al., 2007, De Barros et al., 2009). Beside the relocation, given a signal template from a preciously observed event, the cross-correlation can simply detect subsequent occurrences of that signal on the incoming data (Schweitzer et al., 2011).

During a given eruptive episode hundreds or thousands of low-frequency events can occur. Often variations in the characteristics of the low-frequency events are strictly related to changes in source mechanism. In order to identify patterns and systematic changes in the signal a classification of the events in groups is very useful. Besides the spectral content, the

classification can be based on waveforms. These cross-correlation based methods rely in the quantification of the similarity of waveforms which is defined as (Green and Neuberg, 2006):

$$cc_{xy}(i, i-l) = \frac{\sum_{i=1}^{n}(x_i - \bar{x})(y_{i-l} - \bar{y})}{\sqrt{\sum_{i=1}^{n}(y_{i-l} - \bar{y})^2}\sqrt{\sum_{i=1}^{n}(x_i - \bar{x})^2}} \tag{3.8}$$

where x_i is the *i-th* sample of the signal x, y_i-l is the *(i-l)-th* sample of the signal y and the overbar represents the mean value of the signal. The index l is the lag between the two signals; changing this parameter varies the relative position of signal x with respect to signal y. Finally, n is the number of samples of the considered windows of x and y. cc_{xy} lies in the interval [-1,1]. Identical waveforms result in cc_{xy} = 1; two time-series with no correlation produce cc_{xy} = 0; waveforms which are identical except reversed polarities generate cc_{xy} = -1. In the cross-correlation analysis every single event is compared with every other event of the whole dataset. Once the correlation functions are calculated, the CC matrix is built. This matrix consists of maximum correlation coefficient values between the couples of events (e.g. seismic or infrasound events) that are obtained by changing the lag between them (**Fig. 3.4**).

For the purpose of event classification, the events need to be grouped into families. In this work, we choose the method of Green and Neuberg (2006), whose grouping approach allows to identify gradual waveform variations among the families. In this waveform classification the event with the largest number of cross-correlation value above a fixed threshold is selected and is called the "master event". Successively, a waveform stacking is performed by averaging the waveforms of all the events well correlated with the master event. This waveform stacking is then cross-correlated with the original dataset of events, allowing to group all the events, that have cross-correlation coefficient largest than the threshold, into a family. This procedure is then repeated iteratively until the entire matrix is grouped into families. The cross-correlation threshold is chosen as a trade-off between classification accuracy and event detection, and the window length is to be fixed according to the event features.

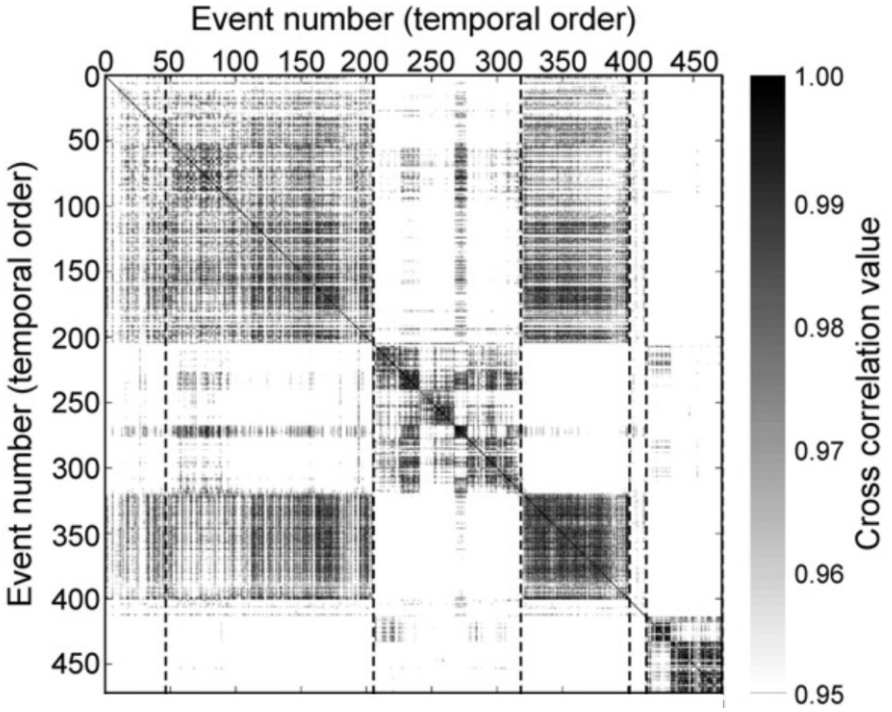

Fig. 3.4 *Example of the cross correlation matrix of infrasound events recorded at Mt. Etna. The dashed vertical lines show the main waveform variations. From Cannata et al. (2011a).*

Further more, one of the most powerful and useful output measures resulting from cross-correlation analysis is the temporal shift or lag (l) of one signal relative to the other. The lag can provide information about when signal events are happening relative to each other in each of the signals used for the cross-correlation.

3.3.2. Subspace detector

As aforementioned, the most common trigger algorithm used in seismology is the STA/LTA since it is able to detect signal with no specific characteristic and no a priori information about the events to be detected. However, a disadvantage of an energy detector, is the high false alarm rate when thresholds are set aggressively to detect smaller signals. An alternative algorithm is the matched filter, which correlates a template waveform against a continuous data stream to detect occurrences of that waveform. Cross-correlation based detectors are highly sensitive and have high probabilities of detection at low false alarm rates (Gibbons and Ringdal, 2006). They revealed to be very useful to strictly repetitive sources, but require perfect knowledge of the signal. However, repeating sources frequently produce varied waveforms not well represented by a single template (Harris, 2006). Broadband subspace detectors are introduced for seismological applications that require the detection of repetitive

sources that produce similar, yet significantly variable seismic signals (Harris, 2006). Subspace detectors operate by correlating a linear combination of a set of orthonormal basis waveforms (developed from the reference template waveforms produced by a particular source) against an incoming data stream to detect signals that lie in the subspace spanned by the basis (hence the name "subspace detector") (Harris, 2006). Doing so, it can detect both identical events and events that exhibit small variations with respect to the reference templates. Hence, the subspace detector turns out to be powerful for the detection of explosive infrasonic events occurring in a volcanic area. Indeed, during an eruption a single crater usually produces similar but not identical infrasonic events due to temporal variation in explosion dynamics, in vent geometry or in location (e.g. two or more vents inside a single crater). Similar to other detectors, the subspace implements a binary hypothesis test on the presence or absence of a signal in a data observation window (Van Trees, 1968). The signal is assumed to be deterministic, but dependent upon a vector of unknown parameters, and is specified as an unknown linear combination of basis waveforms. The unknown signal and noise parameters are estimated from the data as a generalized likelihood ratio test. To calculate the basis, reference waveforms (templates) are organized as columns of a data matrix and a singular value decomposition (SVD) is computed (Maceira et al., 2010). The basis consists of the left singular vectors corresponding to the most significant singular values in the decomposition. The subspace detector operates by projecting the data in a detection window into a subspace spanned by the column of the subspace representation matrix (U) (**Fig. 3.5**).

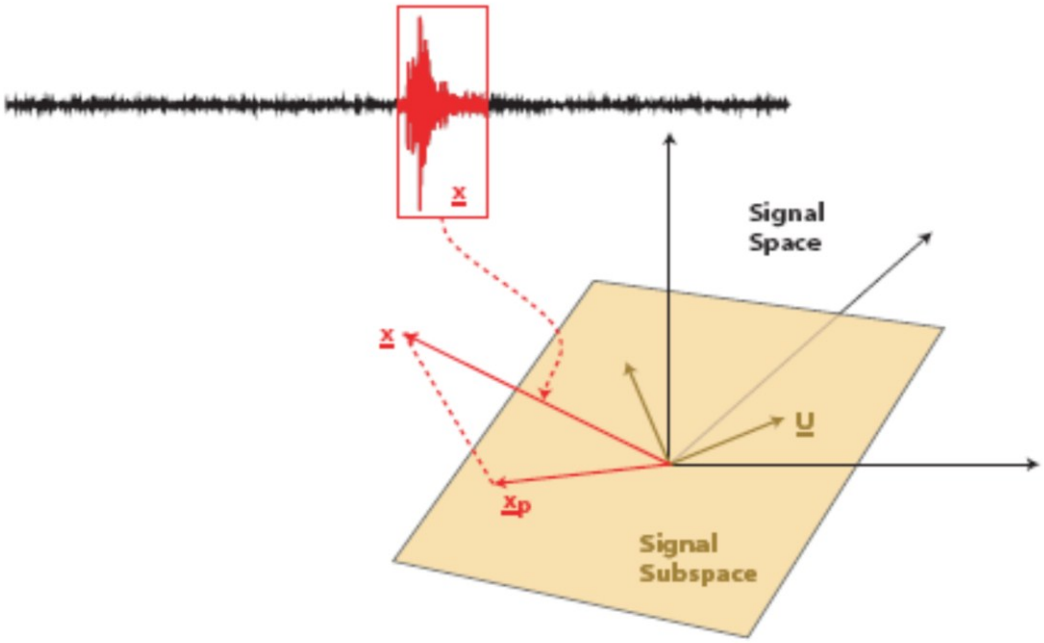

Fig. 3.5 *x_p results from the projection of the windowed signal (x vector) into a subspace (U) spanned by the columns of the subspace representation matrix. From Harris (2006).*

A detection statistic (z) is then computed continuously as the data window slides down the continuous data (x) (Maceira et al., 2010 and references therein):

$$z = \frac{x^T U U^T x}{x x^T} \tag{3.9}$$

The detection statistic ranges between 0 and 1, and is given by the ratio of the energy in the projected data to the total energy in the original windowed data. It is equal to if the waveform in the detection window is exactly a linear combination of basis waveforms (Harris and Dodge, 2011).

The essential parameters controlling the trade-off between sensitivity and flexibility are the detection threshold and the dimension of the subspace, i.e. the number of basis waveforms (Harris, 2006). The selected template or subspace should depend on the data set under study.

3.4. Source location

In order to locate the source of seismic volcanic tremor, LP and infrasound events it is impossible to use techniques based on first arrival phase picking inversion, similar to those used to calculate hypocenters of earthquakes, because of their non-impulsive character. Further, since each signal is characterised by different features, distinct techniques have been developed to locate their sources.

3.4.1. Infrasound source location

Commonly used techniques to locate infrasound events are based on cross-correlation and semblance functions (e.g. Ripepe and Marchetti, 2002; Matoza et al., 2007; Jones and Johnson, 2010). These methods allow to locate the surface projection of the infrasonic sources. A new location technique has been proposed by Cannata et al. (2011a). This new method is based on the joint of semblance (Neidel and Tarner, 1971) and brightness functions (Kao and Shan, 2004), and turned out to be accurate in locating closely spaced eruptive vents (Cannata et al., 2011a). For U traces acquired at a number N of sensors, the semblance function is given by (Neidel and Tarner, 1971):

$$S_0 = \frac{\sum_{j=1}^{M}\left(\sum_{i=1}^{N} U_i\left(\tau_i + j\Delta t\right)\right)^2}{N\sum_{j=1}^{M}\sum_{i=1}^{N} U_i\left(\tau_i + j\Delta t\right)^2} \tag{3.10}$$

where Δt is the sampling interval, τ_i is the origin time of the window sampling the *i-th* trace, $U_i(\tau_i + j\Delta t)$ is the *j-th* time sample of the *i-th* U trace, and M represents the number of samples in the window. The semblance function is a measure of the similarity among waveforms recorded at different sensors and is a number between 0 and 1. S_0 can be normalized in order not to consider the amplitude of the signal (Almendros and Chouet, 2003). Concerning the brightness function, introduced by Kao and Shan (2004), it has been modified as follows (Cannata et al., 2011a):

$$B_0 = \frac{1}{N}\sum_{i=1}^{N}\left(\max\left(W_i\right)\right) \tag{3.11}$$

where W_i is a time window of the signal U_i multiplied by a hanning window:

$$W_i = hanning\left|U_i\left(\tau_i + j\Delta t\right)\right| \qquad \text{with j=1,…,M} \qquad (3.12)$$

In this case the signals U_i have to be normalized such that, if all the largest amplitudes are aligned at the centre of the considered time windows, B_0 is equal to 1 (Cannata et al., 2011a). In practice, the brightness of a point at a time is calculated by summing the normalized amplitudes from all stations at the predicted arrival times (Kao and Shan, 2004). The method is based on a grid search over a surface and the source is located in the grid node with the largest composite semblance-brightness value.

A start time t_s is fixed as the time of first arrival at a reference station (generally chosen on the basis of the highest signal to noise ratio). The source is assumed to be in each node of the grid, and for each node the origin time to is calculated, assuming a certain value of propagation velocity of the infrasonic waves v:

$$t_0 = t_s - \frac{r}{v} \qquad (3.13)$$

where r is the distance between the station and the node assumed to be the source. The theoretical travel time (t_i) is calculated for each of the N stations ($t_i = r_i/v$) and for each node of the grid. Then, taking into account these theoretical travel times and the origin time, signals at different stations are delayed and values of semblance and brightness functions are computed. The two distributions obtained are successively normalized and then summed node by node by assigning the same weight to semblance and brightness functions (**Fig. 3.6**).

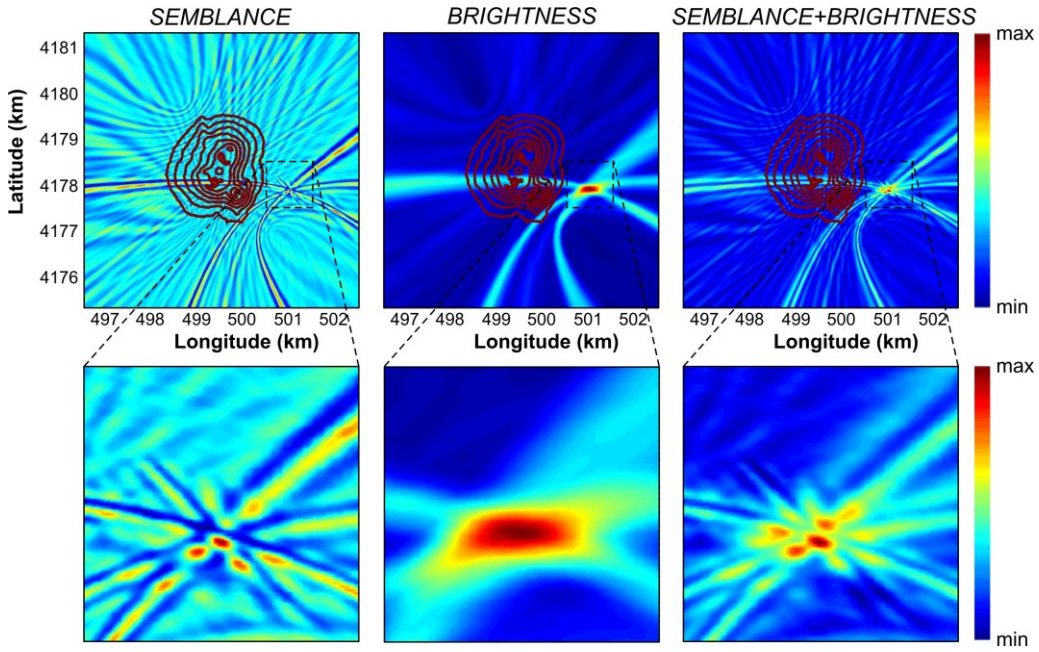

Fig. 3.6 *Example of semblance, brightness and semblance+brightness space distribution for an infrasound event at Mt. Etna. The concentric lines are the altitude contour lines from 3 to 3.3 km a.s.l.. From Cannata et al. (2011a).*

The source is located in the node where the delayed signals show the largest composite semblance-brightness value. This joint method not only shows the high location resolution of the semblance method, but also, by the brightness function, strongly reduces the side lobes generally characterising semblance locations (Jones and Johnson, 2010; Montalto et al., 2010; Cannata et al., 2011a).

3.4.2. Volcanic tremor source location

Most of the methods applied on signals recorded by sparse seismic stations to locate volcanic tremor worldwide are based on amplitude decay (e.g. Battaglia and Aki, 2003; Kumagai et al., 2010; Jones et al., 2011). A method based on amplitude decay is also applied at Mt. Etna to locate the source of volcanic tremor (Di Grazia et al., 2006; Patanè et al., 2008). It assumes the propagation in a homogeneous medium and is based on a grid-search approach. The amplitude decay is expressed by the general law:

$$A(f,r) = A_0(f) r^{-b} e^{-\alpha r}, \quad \alpha = \frac{\pi f}{Qc} \tag{3.14}$$

where f is the frequency, c the velocity, the term r^{-b} accounts for the amplitude decay due to the geometrical spreading (b = 1 or 0.5, for body and surface waves, respectively). α is the

absorption coefficient and depends on the ray-path-averaged quality factor (Q), on frequency and velocity c. The equation can be linearized taking the logarithm on both sides as (Di Grazia et al., 2006; Cannata et al., 2010a):

$$\ln A_i + \alpha r_i = \ln A_0 - b \ln r_i \tag{3.15}$$

where A_i is the RMS of amplitude measured at the *i-th* station, r_i is the corresponding source-to-receiver distance and A_0 is the amplitude at the source. Then, the source location of tremor is found on the basis of the goodness of the linear regression fit (hereafter referred to as R^2) obtained for each point on a spatial 3D grid (Di Grazia et al., 2006). In particular, the centroid position of all the 3D grid points, whose R^2 values do not differ more than 1% from the maximum R^2, is considered as the tremor source location. Time evolution of volcanic tremor source location centroids can be plotted in map and section (**Fig. 3.7a, b,** respectively**).**

Although the attenuation factor (α) should not have a large influence on the source locations (Battaglia et al., 2005), Patanè et al. (2008) and Cannata et al. (2010a) iteratively computed several values of α in the equation (3.15) ($0 \leq \alpha \leq 0.4$ with step of 0.01) and observed how the best values of R^2 were achieved with very low α values, mainly between 0 and 0.02.

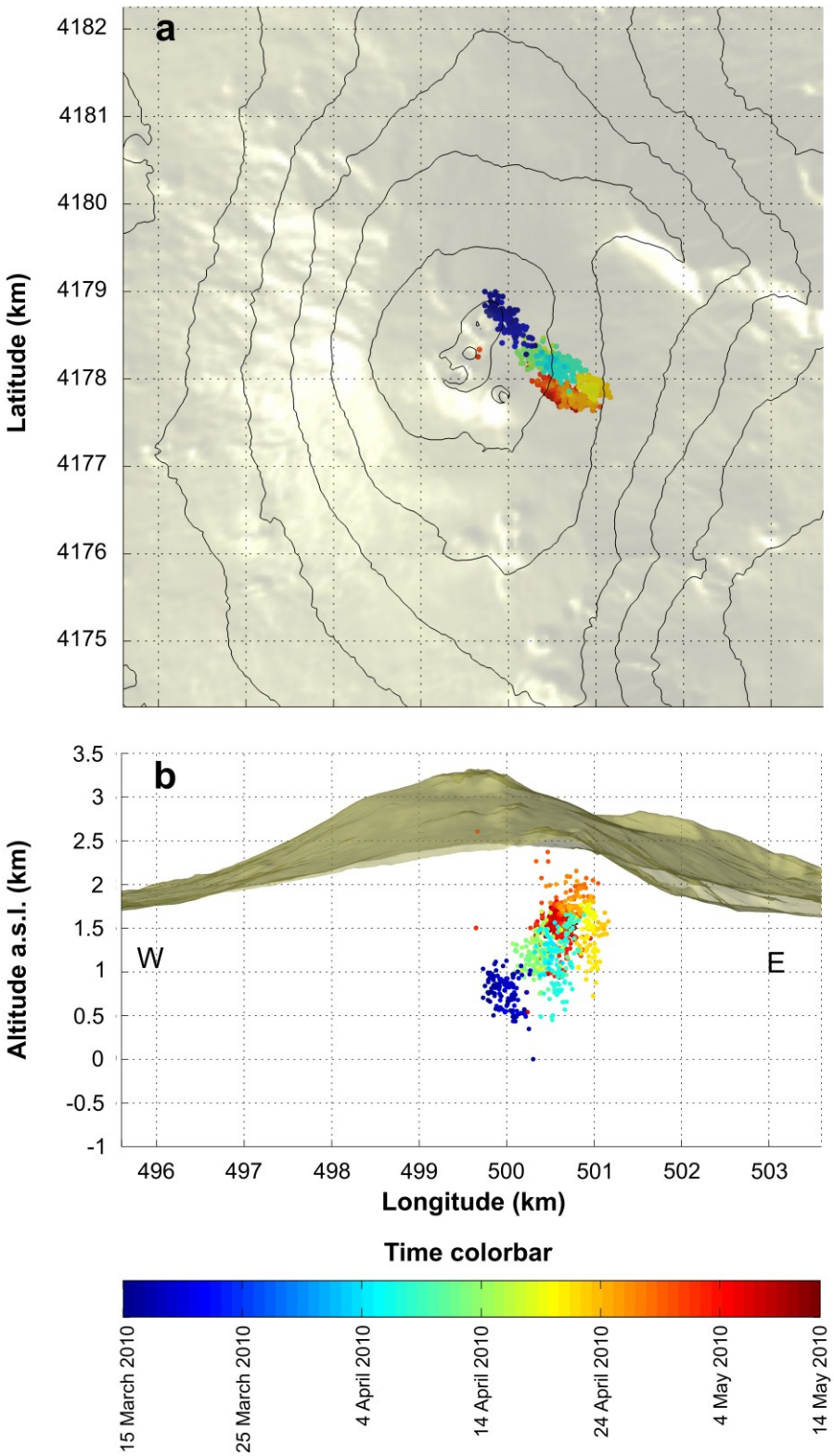

Fig. 3.7 *Space distribution of centroids of R^2 values for volcanic tremor at Mt. Etna. Time evolution of source locations are shown in map* ***(a)*** *and section* ***(b)*** *(see the bottom time color bar).*

3.4.3. LP source location

The methods generally used to locate LP events are based on seismic amplitude decay (e.g Battaglia et al., 2003) and on cross-correlation coefficient (e.g Saccarotti et al., 2007). LP events analyzed in this work are located by means of a composite method based on semblance function and R^2 value, above described. This joint technique takes therefore advantage of both LP waveform comparison among the different stations and space amplitude distribution (Patanè et al., 2011). Similar to the volcanic tremor and infrasound events location methods, this technique is based on a grid-search and consists in finding a set of arrival times, that yields a maximum joint semblance-R^2 value for the data (Patanè et al., 2011).

3.5. Methods of analysis for seismo-acoustic signals

In this work investigations of volcanic activity have been mainly performed by analyzing infrasound signal and comparing it with seismic signal. The conjunction of acoustic observations with seismic ones allows to separate shallow or subaerial processes from deeper (purely seismic) processes (Lees et al., 2008; Zobin, 2012). Recent studies have demonstrated how in volcano monitoring the infrasound analysis is very efficacious in supporting seismic surveillance (e.g. Johnson and Ripepe, 2011). One of the advantage lies in the fact that during shallow volcanic activity, acoustic and seismic waves are radiated in the same spectral band.
Besides the comparison between infrasound and seismic signal, a powerful tool in volcano-seismology is the study of seismo-acoustic source. These kinds of sources are characterized by the excitation of mechanical waves both in the solid earth and atmosphere, and are therefore located at or near the solid earth-atmosphere boundary (Arrowsmith et al., 2010). Several volcanic processes are able to generate seismo-acoustic signals such as inflation at the surface of magma inside the conduit (e.g. Kobayashi et al., 2005), explosive degassing (e.g. Ripepe et al., 1996), resonance phenomena (e.g. Garces and McNutt, 1997).

3.5.1. Energy partitioning analysis: Volcano Acoustic Seismic Ratio

In order to characterize seismo-acoustic data an analysis of the energy partitioning can be performed. To this aim, the Volcano Acoustic Seismic Ratio (VASR) has been adopted (Johnson and Aster, 2005). This parameter evaluates the elastic coupling of the eruptive source with the volcano and atmosphere and is useful to investigate the conduit condition.

Many authors have acknowledged the utility of a quantitative analysis of the relative partitioning of acoustic and seismic energy to compare eruptive dynamics both between different volcanoes (e.g. Johnson and Aster, 2005) and at a single volcano among different explosive episodes (e.g. Rowe et al., 2000; Sahetapy-Engel et al., 2008).
We calculated the VASR, as presented by Johnson and Aster (2005), to evaluate the relative partitioning of acoustic and seismic energy during the explosive activity. It is defined as:

$$VASR = \frac{E_{ac}}{E_{seism}} \tag{3.16}$$

where E_{ac} and E_{seism} are acoustic and seismic energy, respectively. This parameter is useful to characterize eruption sources and their elastic coupling with the volcano and atmosphere. The acoustic energy was estimated on the basis of the excess pressure (ΔP) assuming linear propagation of sound (infinitesimal excess pressure with respect to ambient pressure) by means of (Johnson and Aster, 2005 and references therein):

$$E_{ac} = \frac{2\pi r^2}{\rho_{atm} c_{atm}} \int \Delta P(t)^2 dt \tag{3.17}$$

where r is the microphone-source distance, ρ_{atm} and c_{atm} are the density and sound velocity of atmosphere. Acoustic propagation in the atmosphere (with time dependent conditions of temperature and wind) can cause acoustic energy to refract. Despite this, for infrasonic microphones located at short distances (roughly within 5 km of the vent) these effects are generally negligible. However, wind generates noise in the form of a broadband tremor-like signal lasting from tens of seconds to hours (Johnson et al., 2003) which could overlap and hide volcanic infrasonic activity.
To obtain VASR, seismic energy (E_{seism}) was computed on the resultant vector of the three component traces of the recorded velocity (U) by the following equation (Boatwright, 1980; Johnson and Aster, 2005):

$$E_{seism} = 2\pi r^2 \rho_{volc} c_{volc} \frac{1}{A} \int S^2 U(t)^2 dt \tag{3.18}$$

where ρ_{volc} and c_{volc} are the volcano density and P wave velocity, respectively. A accounts for the attenuation and S is the site response. Concerning the seismic wave radiation we adopted the assumptions discussed by Johnson and Aster (2005). At Etna literature data demonstrated

that frequency-dependent absorption coefficient has a small influence on energy dissipation (Di Grazia et al., 2006; Patanè et al., 2008; see **section 3.4.2**). On the basis of this consideration and taking into account the small station-source distance (Johnson and Aster, 2005), we fixed *A* equal to 1. The site response is another parameter that could be a potential cause of biases in the seismic energy evaluation. Site correction factors for ECPN, EBEL and EBCN stations were evaluated and found to be equal to ~ 1 (Di Grazia et al., 2006; Andrea Cannata, personal communications).

Nevertheless, some limitations are due to the assumptions and the parameters fixed for the energy estimations. Focusing on each parameter, the error in the measure of source-station distances is low enough to be neglected, while, concerning P-wave velocity, density of volcano edifice we refer to literature data (Gresta et al., 2004; Lokmer et al., 2007b). Regarding the acoustic wave velocity and density in the atmosphere, they are largely dependent on the temperature, but unfortunately we do not have any measure of this parameter at such altitude. In order to evaluate to what degree the variation of the fixed parameters affects VASR values, we calculated the VASR by systematically converting them to reasonable ranges (assumed on the basis of several literature data). In particular, for seismic energy computation, we adopted P-wave velocity in the range 1.7-2 km/s, and volcano edifice density from 2.3 to $2.5*10^3$ kg/m^3. Then, in order to compute the acoustic energy, we evaluated the acoustic wave velocity and density on the basis of different temperature conditions (from -15 to 30 °C), obtaining ranges of 322-350 m/s and 0.83-0.99 kg/m^3, respectively. Finally, we found minimum and maximum values for the VASR, which differ from the values calculated by about 20 %.

It is noteworthy that we will show analysis of seismo-acoustic signal occurring at the same volcano, and therefore any eventual uncertainties on some aforementioned parameters (e.g. ρ_{volc} and c_{volc}), that remain unchanged during the episodes, are not able to strongly affect the relative comparison among values obtained for the studied episodes.

The VASR parameter has been evaluated in this thesis both on discrete seismo-acoustic events and continuous seismic and infrasonic signal. Several mechanisms can be invoked for variable VASR (**Fig. 3.8**). The plume density is inversely proportional to the volumetric perturbation of the atmosphere: for example, high VASR values can be due to pressurized volatiles expanding explosively without entraining much ash, and on the contrary, the acoustic radiation can be reduced if a cap rock obstructing the conduit is present (Johnson and Aster, 2005 and references therein). Partitioning of energy can also reflect the position of the source, indeed a deep explosion will impart high energy to the wall of the conduit, with

respect to a shallow one (Johnson and Aster, 2005). Furthermore, seismic and acoustic efficiency can depend on impedance contrast (Garces et al., 1998; Rowe et al., 2000) between the fluid filling the conduit and the wall rock.

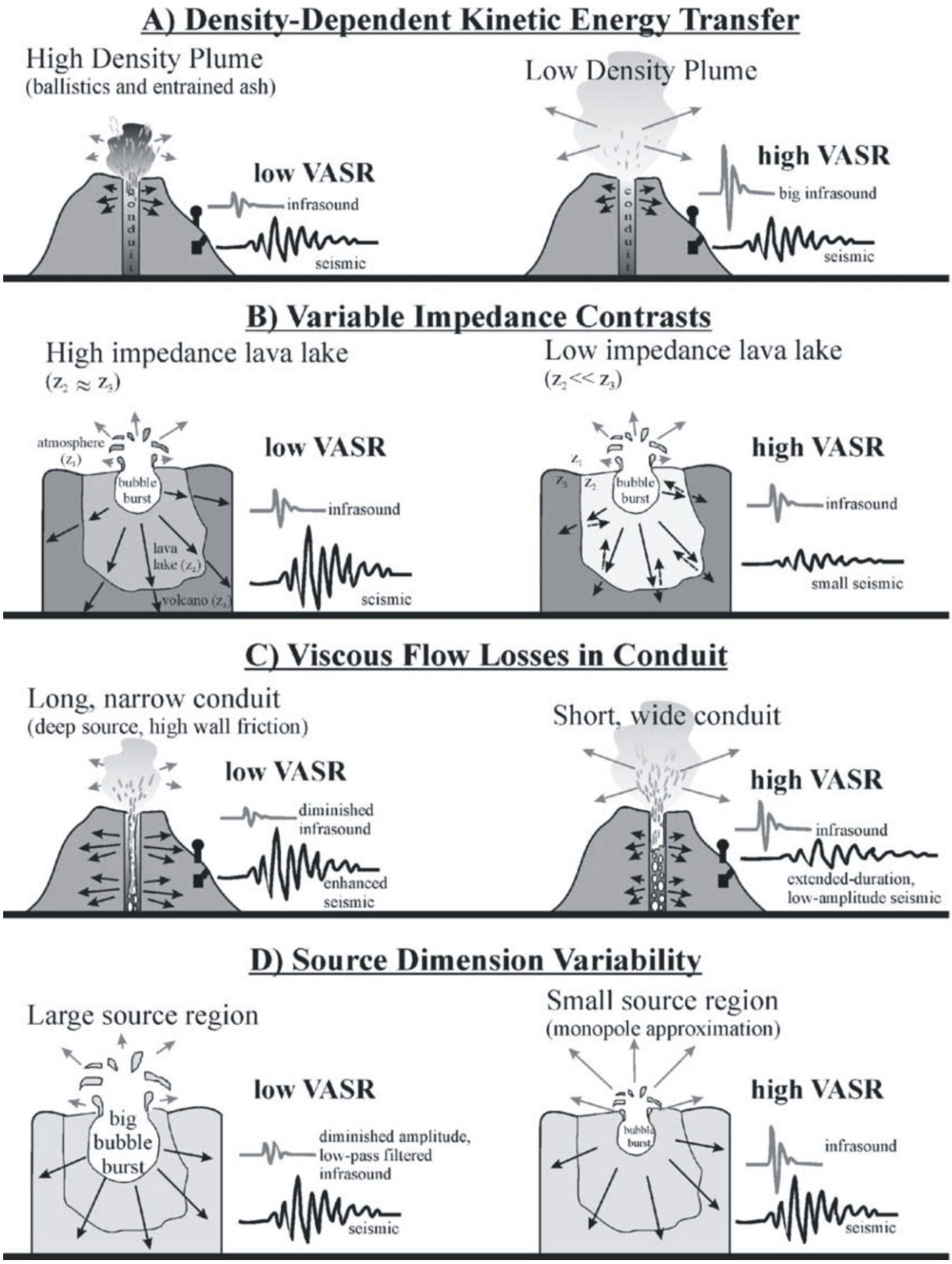

Fig. 3.8 *Mechanisms for variable VASR. Energy repartitioning depends on infrasonic and seismic radiation propagation (grey and black arrows, respectively). From Johnson and Aster (2005).*

3.5.2. Time lag estimation

Seismic and infrasound waves, once generated, will propagate towards the sensors at different speeds. In particular, due to its lower speed, an infrasound event will arrive with a delay time (hereafter called lag) with respect to the seismic event. Lag times have been used in literature to infer the depth of sources within a volcanic conduit and propagation medium properties (Ripepe et al., 2001a, Ripepe et al., 2002; Kobayashi et al., 2005; Petersen and McNutt, 2007). Lags between infrasound and seismic events have been here evaluated using cross-correlation analysis. Once the window containing the infrasonic event is selected, the cross-correlation analysis tracks down the seismic window including the similar seismic event. Thus, the lag is calculated between the windows which show the maximum cross-correlation coefficient (a similar method was used by Ripepe et al., 2001b). Nevertheless, the high level of volcanic tremor, affecting sometimes the recordings of the summit seismic stations, can prohibit the use of cross-correlation function. To overcome this drawback, lag has been also measured by means of an accurate manual procedure, by picking the onset of infrasonic and seismic events.

In order to estimate the depth of the source the approach of Petersen and McNutt (2007) has been adopted. Seismic and infrasonic sources can be considered whether co-located (**Fig. 3.9a**), generally coinciding with the free magma surface inside the conduit, or not (**Fig. 3.9b**). In the latter case, the delay between seismic and infrasonic onsets is related to a seismic pressure wave ascending through the conduit (Ishihara, 1985) or to a rising gas slug (Ripepe et al., 2001a). In particular, in this thesis, because of the similarity between the waveform and spectral contents of seismic and infrasonic signals, suggesting a common source (e.g. Ripepe et al., 1996; Matoza et al., 2010), we considered the case in which seismic and infrasound sources are co-located at the free magma surface. Infrasound waves cover the distance between the source and the crater rim with speed cc, depending on the property of the fluid filling the conduit, then they propagate in the atmosphere as far as the infrasonic station with acoustic speed equal to 340 m/s (c). On the other hand, the seismic waves travel in the rocks in between the source and the seismic station with velocity v. Therefore, the lag is given by:

$$time\ lag = \frac{x}{c} + \frac{z}{c_c} - \frac{d}{v} \tag{3.19}$$

where x is the distance between the crater rim and the microphone, z is the depth of the magma free surface (source) in respect to the crater rim, and d is the distance between the

source and the seismic station (**Fig. 3.6a**). Based on this equation temporal variations of the lag between seismic and infrasound events are mainly related to changes in the ratio z/c_c.

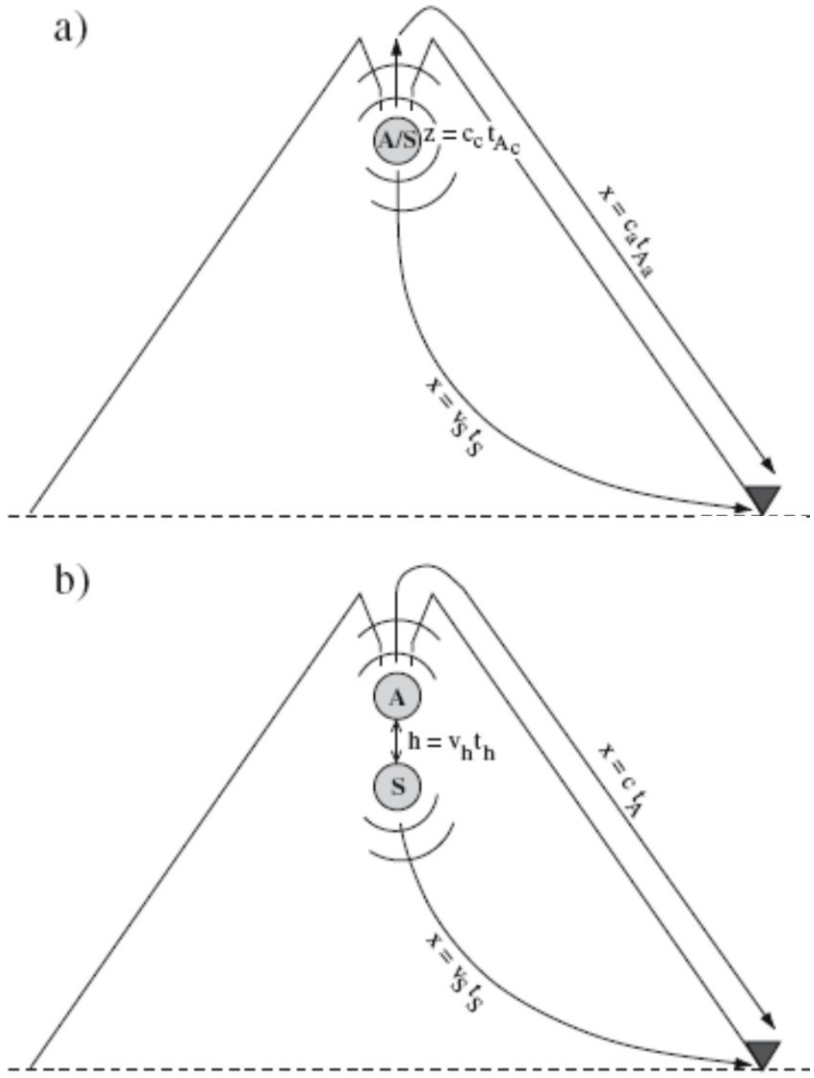

Fig. 3.9 ***(a)*** *Sketch of co-located seismic (S) and acoustic source (A) inside the conduit of a volcano. In sketch* ***(b)*** *seismic and acoustic source are located at different depth. From Petersen and McNutt (2007).*

4. DATASET OF ANALYSES

4.1. Eruptive activity at Mt. Etna volcano

Sixteen months after the end of 2004-2005 flank eruption, on 14 July 2006, an eruptive fracture opened on the eastern side of SEC. It was characterized by the presence of two eruptive vents and lasted 10 days. After 37 days of quiescence the eruptive activity resumed on 31 August and proceeded almost constantly up to 15 December 2006. The main thrust of the activity switched between the summit and peripheral vents of SEC at different times. The entire 2006 summit eruption consisted of 18 paroxysmal episodes and was characterized by Strombolian explosions, short-term eruptive plumes and lava fountains (**Fig. 4.1**; Andronico et al., 2008). The 16 November paroxysmal episode was associated with the largest increase in seismic volcanic tremor amplitude (Andronico et al., 2008). Other very high seismic tremor amplitudes were observed during the 19, 21, 24 and 27 November eruptive episodes.

Fig. 4.1 *Pictures of 20 July (from www.pa.ingv.it) and 16 November 2006 (courtesy of Laura Spina) eruptive episodes in the area of South-East-Crater.*

Since January 2007, an inflation pattern was recorded by the local GPS network (Aiuppa et al., 2010; Bonaccorso et al., 2011), suggesting a magma recharge phase. Volcanic activity during 2007 was marked by 6 paroxysmal episodes (Langer et al., 2011), among which two (29 April and 6-7 May 2007) were characterized by Strombolian activity at the summit of SEC, whereas the other four exhibited sustained lava fountaining, located at SEC (29 March and 10-11 April) and at a vent in the lower E slope of the cone (4-5 September and 23-24 November). All the explosive events had variable duration and were accompanied by lava effusion (Langer et al., 2011). Thereafter, until the beginning of May 2008, the eruptive activity at Mt. Etna consisted of discontinuous and mild explosive activity at SEC.

On 10 May 2008 a new vent opened at the eastern base of SEC generating a violent explosive eruption. It lasted from about 14:00 to 19:00 UTC and was characterized by intense lava fountaining and lava effusion (Bonaccorso et al., 2011). After three days of no volcanic activity, an eruption started on 13 May 2008, from an eruptive fissure that opened on the upper eastern flank of the volcano. A NW-SE trending eruptive fissure opened at 09:30 (~3000 m a.s.l.; Behncke and Neri, 2008a in Cannata et al., 2011a) and fed lava fountaining and lava flows. Late in the morning the rupture propagated downslope to the ESE, towards the upper eastern flank between ~2900 and 2650 m a.s.l.. Here the activity consisted of lava fountains, strombolian activity and lava flows from several vents (**Fig. 4.2**; Bonaccorso et al., 2011). This eruption lasted about 14 months, during which lava effusion from the aforementioned system of fissure was continuous. During these months phases of intensification of activity, followed after few days by a gradual decline, were observed. In particular, periods of increase were characterized by the renewal of explosive activity, the reactivation of the topographically higher vents and an increase in effusion rate (Cannata et al., 2011a and reference therein). They were accompanied by increase of the volcanic tremor amplitude and were attributed to new input of gas-rich magma within the system (Bonaccorso et al., 2011; Cannata et al., 2011a). According to Aloisi et al. (2009) and Bonaccorso et al. (2011) the 2008-2009 eruption was fed by an intrusion departed from the central conduit system at a depth of ~ 1.6 km and broke off toward the east in the shallow part.

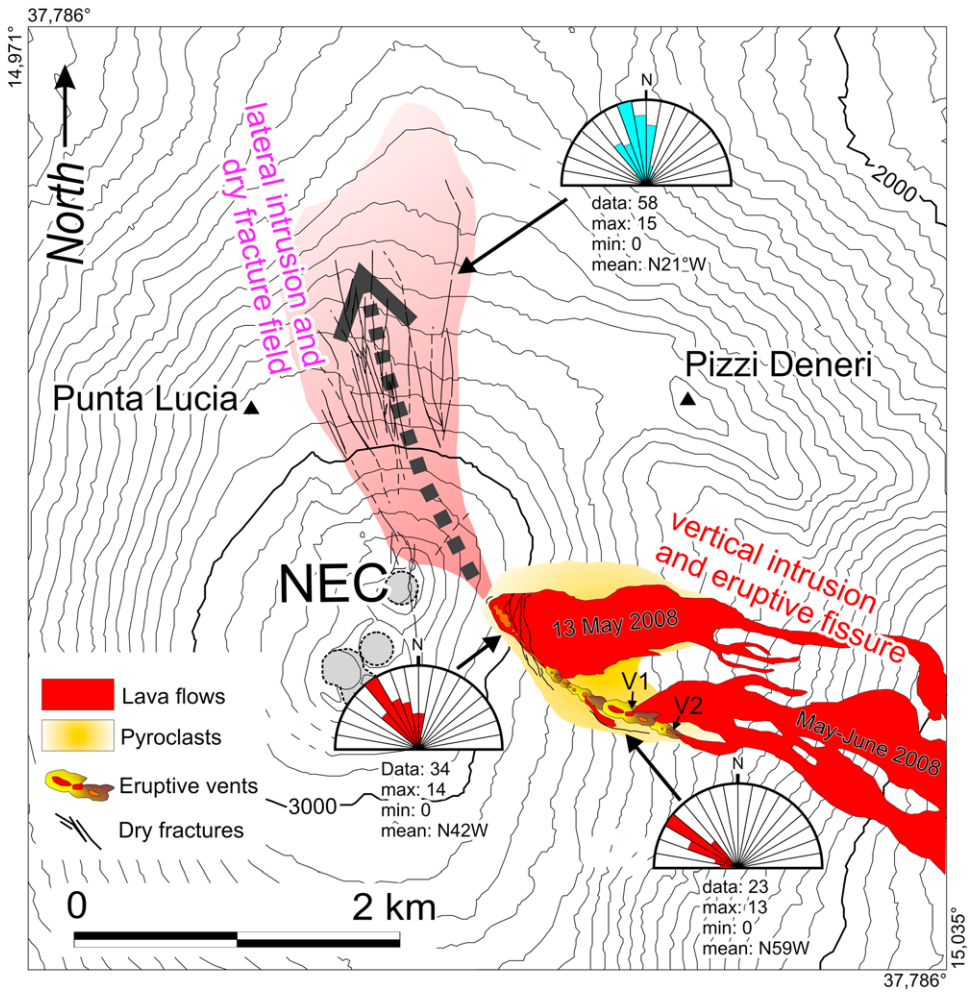

Fig. 4.2 *Map of the lava flows, eruptive vents, dry fracture field during the initial phase of the 2008-2009 eruption on Mt. Etna. From Bonaccorso et al. (2011).*

This eruption represented the conclusion of the recharge process begun in 2007 (Aloisi et al., 2009). The last episode of explosive activity of the 2008-2009 eruption was recorded on 11-14 March, then gradually effusive activity diminished until ending on 6 July 2009. Successively, for 4 months Mt. Etna remained silent. On 6 November 2009, a new vent (a few meters wide and depth) within the depression in the lower E slope of the cone (pit-crater) formed. This vent produced pulsing degassing at high temperature and sometimes weak ash emissions (Corsaro, 2009). Degassing activity and intracrater collapses carried on causing the enlargement of the new vent until the end of February 2010 (Andronico et al., submitted). On mid-March degassing resumed at pit-crater. After this date and throughout the 2010 the pit-crater and BN crater were characterized by numerous weak and short-lasting ash emissions (Andronico et al., submitted). Among them the three main episodes occurred on 8 April at pit-crater, and on 25 August and 22 December at BN. Further, at NEC on 14-15 November a weak eruption column, produced by a continuous but weak ash emission and steam release, was observed (Andronico et al., submitted). On 11 January 2011 a lava fountain episode

occurred at the pit-crater. This episode gave rise to a new eruptive phase at Etna which produced 18 paroxysmal episodes during 2011 (**Fig. 4.3**) and 7 during 2012.

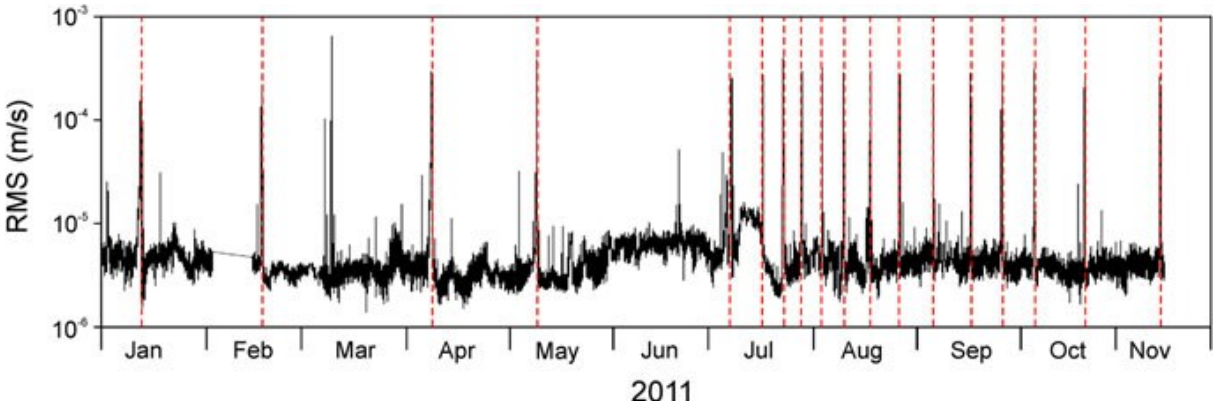

Fig. 4.3 *Seismic RMS during January-November 2011 period, showing the 18 lava fountain episodes (vertical dashed red lines). From Cassisi et al. (2012).*

Due to this eruptive activity (**Fig. 4.4a**), the cone on the eastern flank of SEC grew and reached at the end of December of 2011 ~ 3200 m a.s.l. becoming the "New SEC" (**Fig. 4.4b**).

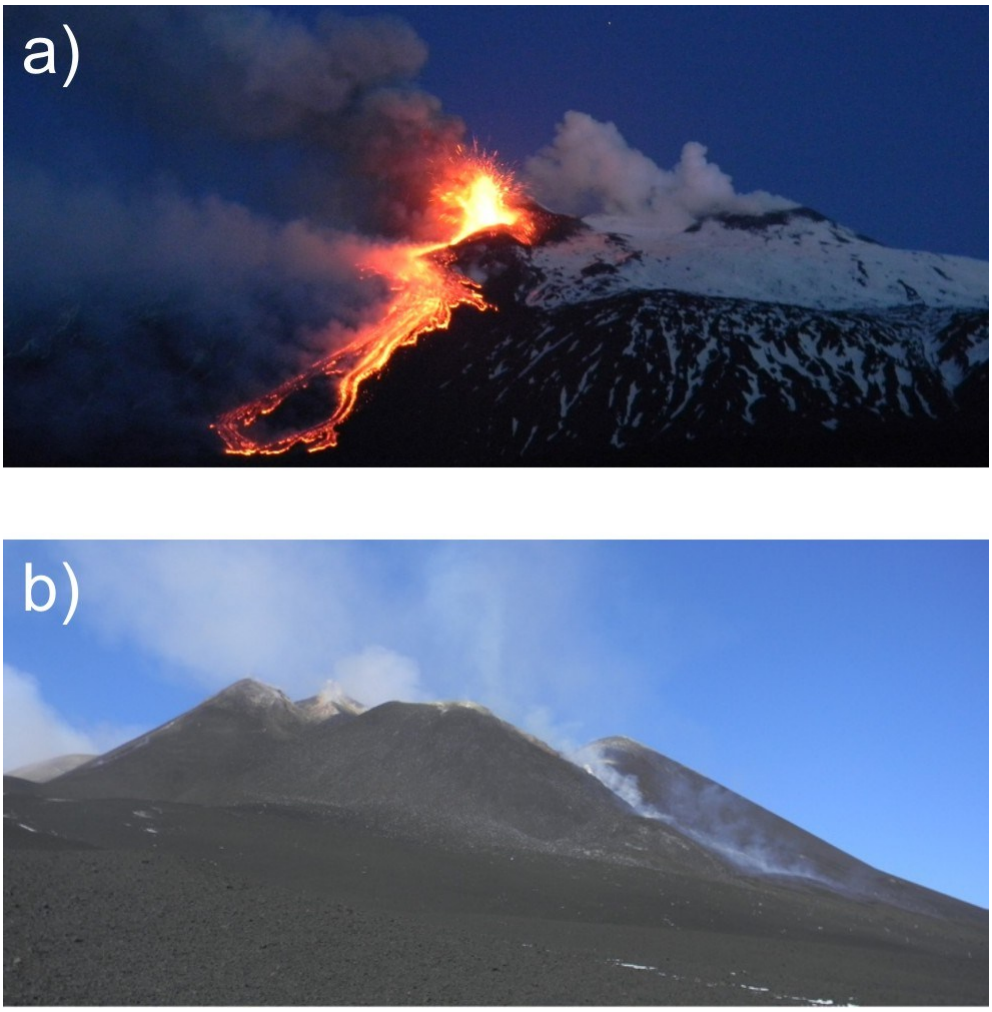

Fig. 4.4 ***(a)*** *Picture of 12 May 2011 paroxysmal episode at New South-East-Crater.* ***(b)*** *The New South-East-Crater on 15 November 2011 (ahead) compared with the South-East-Crater (behind) (Photos of Boris Behncke from www.ct.ingv.it).*

The time interval between the paroxysmal episodes varied from 8 weeks to ~ 6 days. The early phases of these energetic episodes consisted of weak Strombolian explosions and lava flows and lasted from few hours to two days. Strombolian explosions exhibited successively increasing strength and frequency, accompained by a volcanic tremor amplitude increase (Etna updates available at www.ct.ingv.it). The paroxysmal phase was reached when vigorous Strombolian activity evolved into lava fountaining, which lasted from about half an hour to five hours. During the time interval of no eruption the summit craters were characterized by pulsating degassing.

Furthermore, during 2011 and since 2 July of 2012 BN exhibited intracrateric eruptive activity. In particular Strombolian explosions and intermittent lava effusion were observed in a intracrateric vent at the base of the south-eastern crater wall (Etna updates available at www.ct.ingv.it).

5. SEISMO-ACOUSTIC SIGNAL INVESTIGATIONS: CASE STUDIES

In this chapter a few case studies on how infrasound signal can help investigating eruption dynamics in detail, with a focus on degassing and explosive activity, will presented. The dataset of analysis includes infrasound and seismic signal recorded in association with paroxysmal activity (16 November 2006 and lava fountains of 2011), during the hours preceding the 2008-2009 flank eruption, and during minor ash emission episodes occurred during 2010. In particular seismo-acoustic signal will be explored with the aim of shed a light on the shallower portion of the plumbing system of Etna. In addition, modelling of infrasound source mechanism and inferences on conduit condition of summit craters of Etna will be faced.

A multi-parametric approach, integrating analysis of infrasound signal with video camera recording and other volcanological data, has been used.

5.1. Seismo-acoustic investigations of paroxysmal activity at Mt. Etna volcano: New insights into the 16 November 2006 eruption

On 16 November 2006, a one-day-long paroxysmal eruption occurred at Mt. Etna volcano. The 16 November eruptive activity was one of the 18 paroxysmal episodes occurred during 2006 summit eruption. It took place in the area of SEC and was characterized by Strombolian explosions, lava effusions, pyroclastic flows and rock avalanches. Therefore, the variegated volcanic phenomena taking place on 16 November, the high amplitude of seismic and infrasound signals, together with the great abundance of the other data, make this eruptive episode suitable for a multi-parametric study.

In this work, the infrasound and seismic signals were analyzed, together with the video recordings acquired during the explosive activity taking place at Mt. Etna on 16 November 2006, with the aim of better understanding the relationship between these data and the related eruptive dynamics.

5.1.1. Volcanic framework

On the basis of volcanological observations, we divided the eruptive episode into three phases (**Fig. 5.1**). At 5:07 (all times are GMT) a dense ash plume was observed at the summit of SEC. It reached a few hundred meters in height and at 05:13 (onset of the first phase) it was replaced by an intense Strombolian activity.

The second phase, starting roughly at 06:40, was characterized by a decrease in Strombolian activity and the beginning of activity on the SE flank of SEC, where, besides Strombolian explosions, rockfalls and debris avalanches took place. At the same time, lava began to spill out from several fractures on the summit of the SEC cone, on the saddle between BN and SEC and, unlike the other paroxysmal events of the 2006 summit eruption, also on the southern slope of BN (Andronico et al., 2008). Owing to cloudy weather, the video-camera did not follow the volcanic activity after ~09:00. Thanks to direct observations, Behncke et al. (2009) report that a few hours after the onset of the eruptive activity the aforementioned volcanic phenomena had carved a deep and wide trench into the SE flank of the SEC cone. Lava issued from a vent high in the headwall of the trench and from its lower end, forming cascades that flowed down the trench. Periodic emission of white steam, rockfalls, and avalanches with rolling ash clouds continued to take place from various portions of the trench.

Major collapses occurred within the trench at ~13:45 - 14:00 and produced a large mixed ash-steam plume (Behncke et al., 2008; Norini et al., 2009; Ferlito et al., 2010).

The eruption culminated in the third phase starting at ~14:00, when a series of explosions at the SE base of SEC cone produced jets of dark ash and white steam. Behncke et al. (2008) explained the explosions as the result of the mixing of hot lava and fluid-soaked rocks, constituting a block that was forced out from the lower flank of SEC cone. On the other hand, according to Ferlito et al. (2010) the explosions originated from the opening of a fracture and magma injection at the base of the cone. An eruptive column developed and suddenly collapsed forming a pyroclastic flow that spread eastward at 14:25. Another smaller pyroclastic flow occurred at 14:54. Successively, the activity continued with Strombolian explosions and ash emissions from the SEC vents.

There are different interpretations of this volcanic phenomenon by various authors (pyroclastic density currents, Behncke et al., 2009; gravity-driven granular flow, Norini et al., 2009; gravity-driven pyroclastic flow, Ferlito et al., 2010). Explosive activity gradually decreased and ended at around 16:30, whereas the lava flow continued for several hours (Andronico et al., 2008; Behncke et al., 2009).

Due to numerous and different phenomena taking place at SEC (Strombolian explosions, lava effusions, pyroclastic flows, rock avalanches), many authors have investigated the eruption of 16 November through seismological and volcanological studies, deposit samplings and simulations of tephra dispersion (Andronico et al., 2008; Behncke et al., 2008, 2009; Behncke, 2009; Norini et al., 2009; Ferlito et al., 2010).

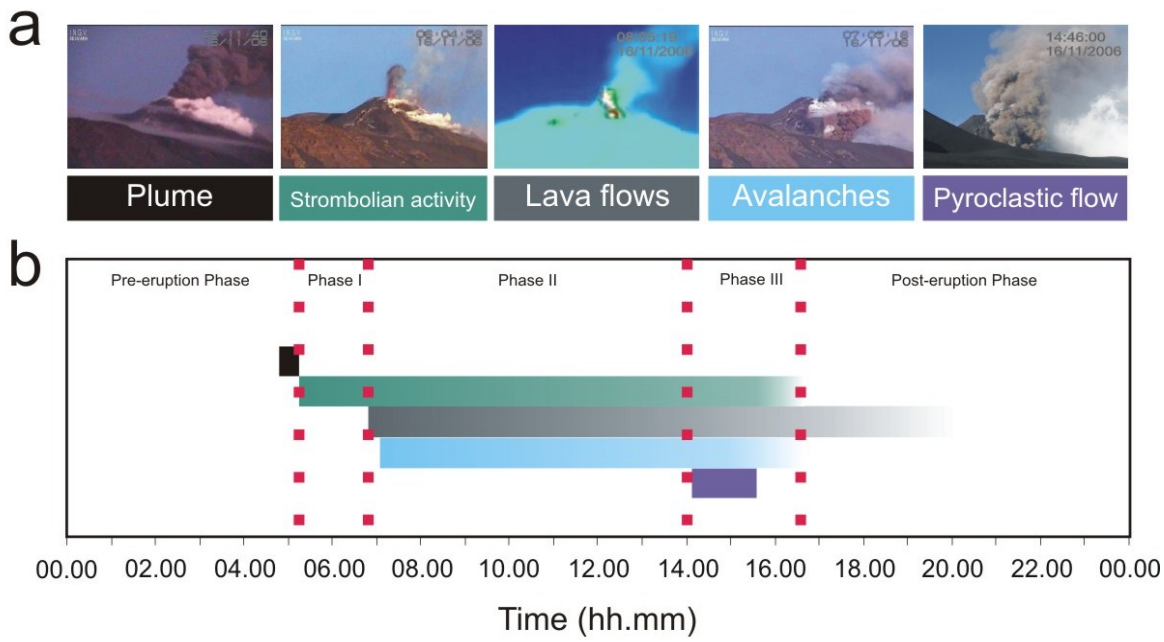

Fig. 5.1 *Volcanic activity evolution on 16 November 2006.* ***(a)*** *Frames of several volcanic phenomena occurring in the area of SEC.* ***(b)*** *Temporal sequence of eruptive phenomena. Colors of horizontal bars in* ***(b)*** *correspond to colors at the base of photos in* ***(a)***.

5.1.2. Data acquisition

During 2006, the Mt. Etna seismic permanent network consisted of 16 stations equipped with broadband (40 s cut-off period), 3-component Trillium seismometers (Nanometrics™) and acquired at a sampling rate of 100 Hz. In this work, we used the data from the 13 stations located at elevations ranging between 1100 and 3000 m a.s.l. (**Fig. 5.2a**). Among those deployed near the summit craters, ECPN station was equipped in August 2006 with a pressure sensor, consisting of a Monacor condenser microphone with a sensitivity of 80 mV/Pa in the 1–20 Hz infrasound band (**Fig. 5.2a**). The infrasound signal is acquired at a sampling rate of 100 Hz. Finally, we also used continuous video recorded by two of the four surveillance video-cameras operating in the visible and thermal radiation fields (**Fig. 5.2a, b**).

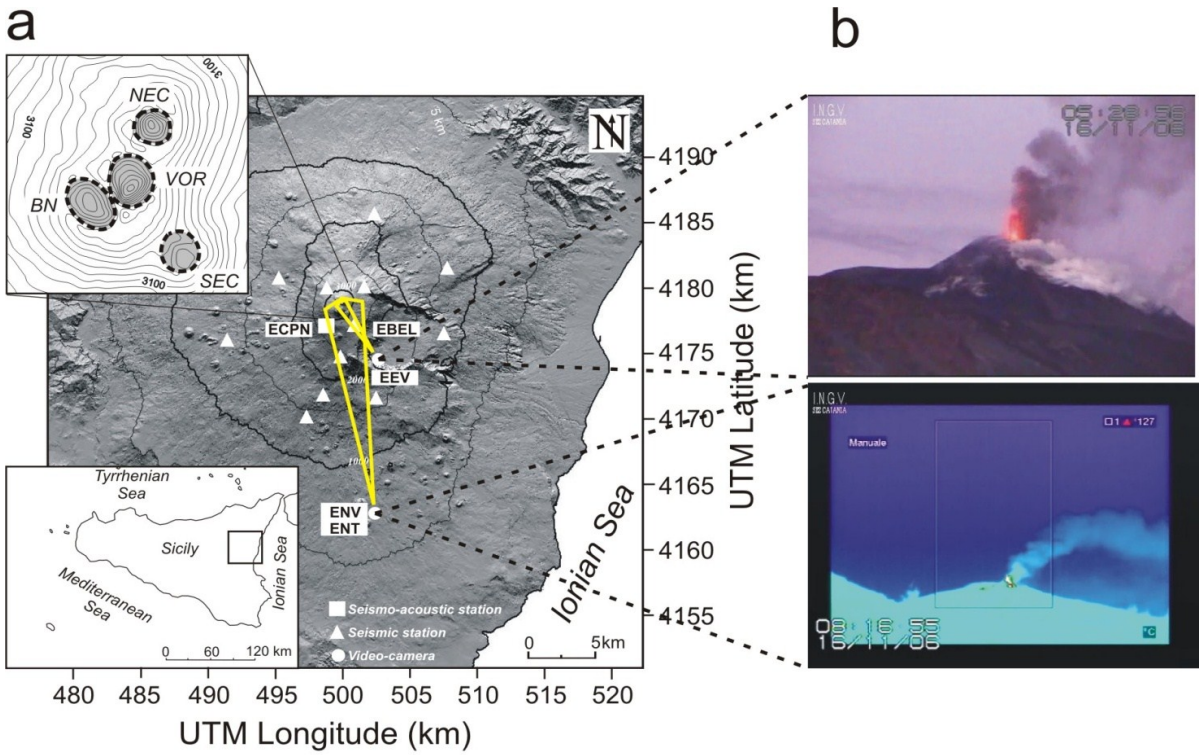

Fig. 5.2 ***(a)*** *Map of Mt. Etna with location of the seismic-acoustic sensor (square) and the seismic stations (triangles) used in this work. In yellow, the field of view of the two video-cameras (circles), operating in visible and thermal radiation fields are shown. In the upper left inset, the position of the summit craters (VOR= Voragine; BN= Bocca Nuova; NEC= North-East Crater; SEC= South-East Crater) is shown.* ***(b)*** *Examples of frames from the visible (EEV) and thermal (ENT) video-cameras recordings.*

5.1.3. Analysis of continuously acquired signals

In order to study the continuously recorded seismic and infrasound signals, shown in the helicorders in **Fig. 5.3a, b**, we calculated: i) root-mean-square envelope (RMS); ii) volcanic acoustic-seismic ratio (VASR); iii) spectrograms; iv) coherence function between seismic and infrasound signals; v) seismic volcanic tremor source location and vi) reduced displacement (RD) of seismic volcanic tremor amplitude.

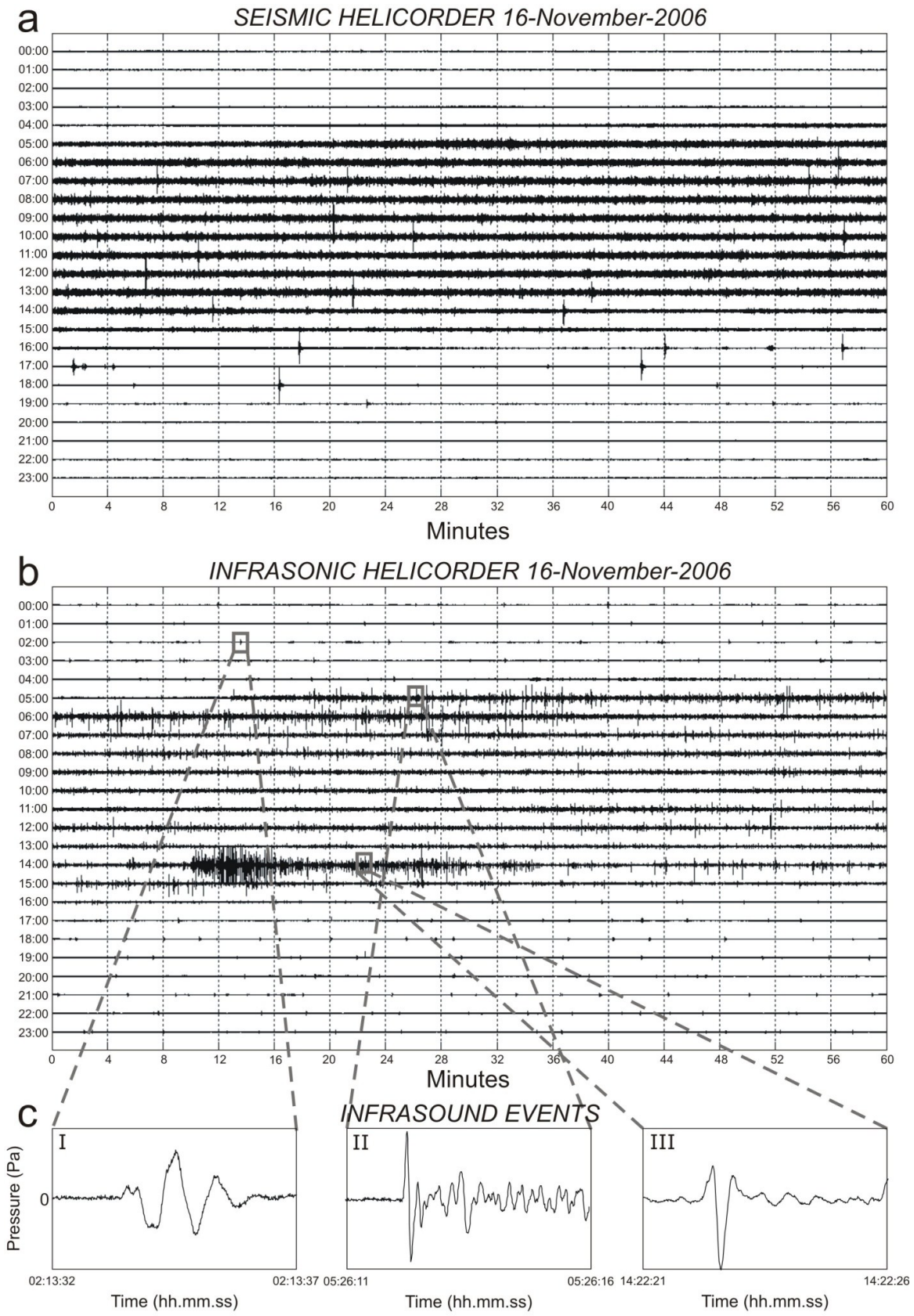

Fig. 5.3 ***(a)*** *Helicorder of seismic signal recorded at ECPN station during 16 November 2006.* ***(b)*** *Helicorder of infrasound signal recorded at ECPN station during 16 November 2006.* ***(c)*** *Examples of NEC infrasound events* ***(I)*** *and SEC infrasound events* ***(II*** *and* ***III)*** *recorded at ECPN station.*

For such analyses we used infrasound signals recorded by ECPN and seismic signals by ECPN and EBEL stations. Time variations of infrasound and seismic amplitude were obtained by calculating the RMS on non-overlapping 5-second-long windows (**Fig. 5.4a, b** and **c**). Both the infrasound and seismic signals indicate the beginning and end of the eruptive episode, but they also show different and apparently contrasting trends.

Due to the large number of infrasound events in succession during the explosive activity, VASR was calculated on the continuously recorded infrasound and seismic signals acquired by ECPN station located at 1300 m far from SEC. Indeed, this parameter represents a standardized method for comparing discrete explosive events, but it can be used as a time-varying quantity for extended-duration events (Johnson and Aster, 2005). In particular, the energy values were computed for each sample of seismic and infrasound signals. Then, the total energy within 10-s-long moving windows (overlapped by 50%) was calculated. The VASR time series were calculated by **equations 3.16, 3.17** and **3.18** (**Fig. 5.4d**) setting ρ_{atm} and c_{atm} equal to 0.9 kg/m^3 and 340 m/s and ρ_{volc} and c_{volc} equal to 2500 kg/m^3 and 1800 m/s (Gresta et al., 2004; Lokmer et al., 2007b). The infrasound signal during 16 November is not affected by significant wind noise. Wind intensity should not have introduced errors on the evaluation of acoustic energies. Indeed, as testified by several people in the summit area during the eruptive episode, the wind was absent or very moderate (< 5 m/s).

The time variation of spectral content of seismic and infrasound signals is displayed as spectrogram in **Fig 5.4e, f**. Spectrograms were obtained calculating an average spectrum per minute by 10.24-second-long sliding windows (overlapped by 50%).

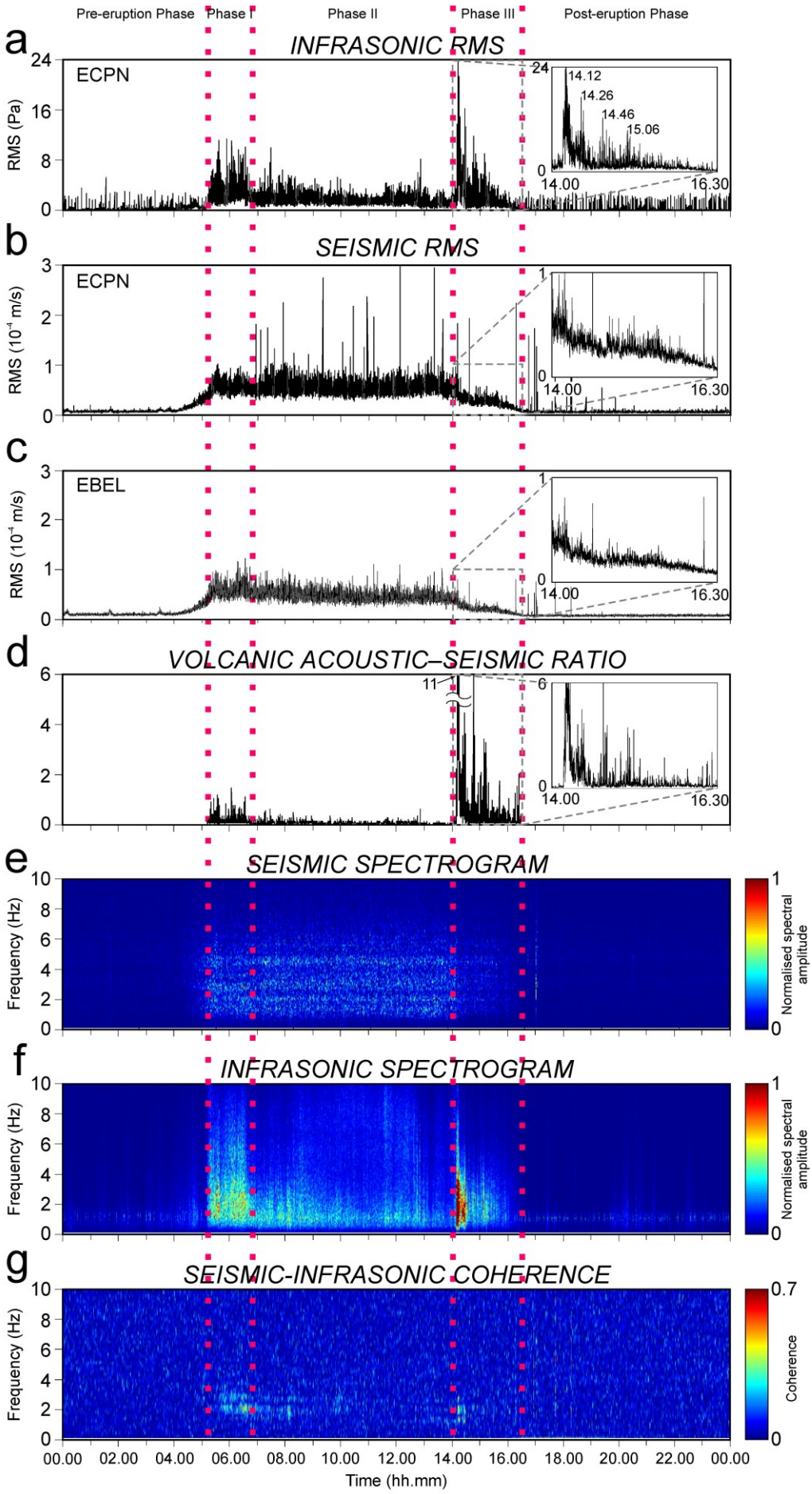
Pre-eruption Phase
Phase I
Phase II
Phase III
Post-eruption Phase
a
INFRASONIC RMS
ECPN
RMS (Pa)
14.12
14.26
14.46
15.06
14.00
16.30
b
SEISMIC RMS
ECPN
RMS (10⁻⁴ m/s)
c
EBEL
d
VOLCANIC ACOUSTIC–SEISMIC RATIO
e
SEISMIC SPECTROGRAM
Frequency (Hz)
Normalised spectral amplitude
f
INFRASONIC SPECTROGRAM
g
SEISMIC-INFRASONIC COHERENCE
Coherence
00.00
02.00
04.00
06.00
08.00
10.00
12.00
14.00
16.00
18.00
20.00
22.00
00.00
Time (hh.mm)

Fig. 5.4 *Features of continuously acquired seismic and infrasound signals on 16 November 2006.* ***(a)*** *RMS of infrasound signal recorded at ECPN station.* ***(b, c)*** *RMS of seismic signal recorded at ECPN and EBEL stations, respectively.* ***(d)*** *Volcano acoustic-seismic ratio calculated by the signals recorded by the seismic and infrasonic sensors at ECPN station during the explosive activity.* ***(e)*** *Spectrogram of seismic signal recorded at ECPN station.* ***(f)*** *Spectrogram of infrasound signal recorded at ECPN station.* ***(g)*** *Coherence between seismic signal recorded by EBEL and infrasound signal recorded by ECPN. The vertical dashed lines* ***(a-g)*** *indicate the time boundaries among the different phases of eruptive activity (see text for details). Insets in* ***(a)***, ***(b)***, ***(c)*** *and* ***(d)*** *show in detail the variations occurring during the third phase.*

Figure 5.4g shows the result of the coherence analysis between seismic and infrasound signal. The coherence function was calculated by moving windows of 5.12 s (overlapped by 50%) of infrasound signal at ECPN and seismic signals recorded by both ECPN and EBEL. Due to the smaller distance of EBEL from the explosive activity area with respect to ECPN (hence less attenuation), we displayed the coherence between infrasound signal and seismic signal acquired at EBEL (**Fig. 5.4g**).

The interval spanning from the beginning of the studied period to ~3:15 was characterized by low RMS values of both infrasound and seismic signals (**Fig. 5.4a, b,** and **c**). Furthermore, some peaks in the infrasound RMS highlight the occurrences of infrasound events radiated by NEC. From ~3:15 to the beginning of the explosive activity, seismic energy gradually increased. During the same interval the infrasonic energy also showed an increasing trend, interrupted at ~5:00 by a decrease roughly coinciding with the onset of plume emission (**Fig. 5.1**). In order to investigate the relationship between the seismic volcanic tremor and 16 November volcanic activity, source location was performed by means of the method based on the seismic amplitude decay explained in **section 3.4.2** (**Figs. 5.5** and **5.6**).

Signals recorded by 10-14 seismic stations, belonging to the broadband network at elevations between 1100 and 3000 m a.s.l., were used. We measured the RMS amplitudes of the 25-*th* percentile on 5 minute windows filtered in the band 1-5 Hz, instead of average values. This enables us to efficiently remove undesired transients in the signal and to consider continuous recordings (Di Grazia et al., 2006; Patanè et al., 2008). We considered a grid of 6x6x6 km^3 volume with a spacing between nodes of 250 m.

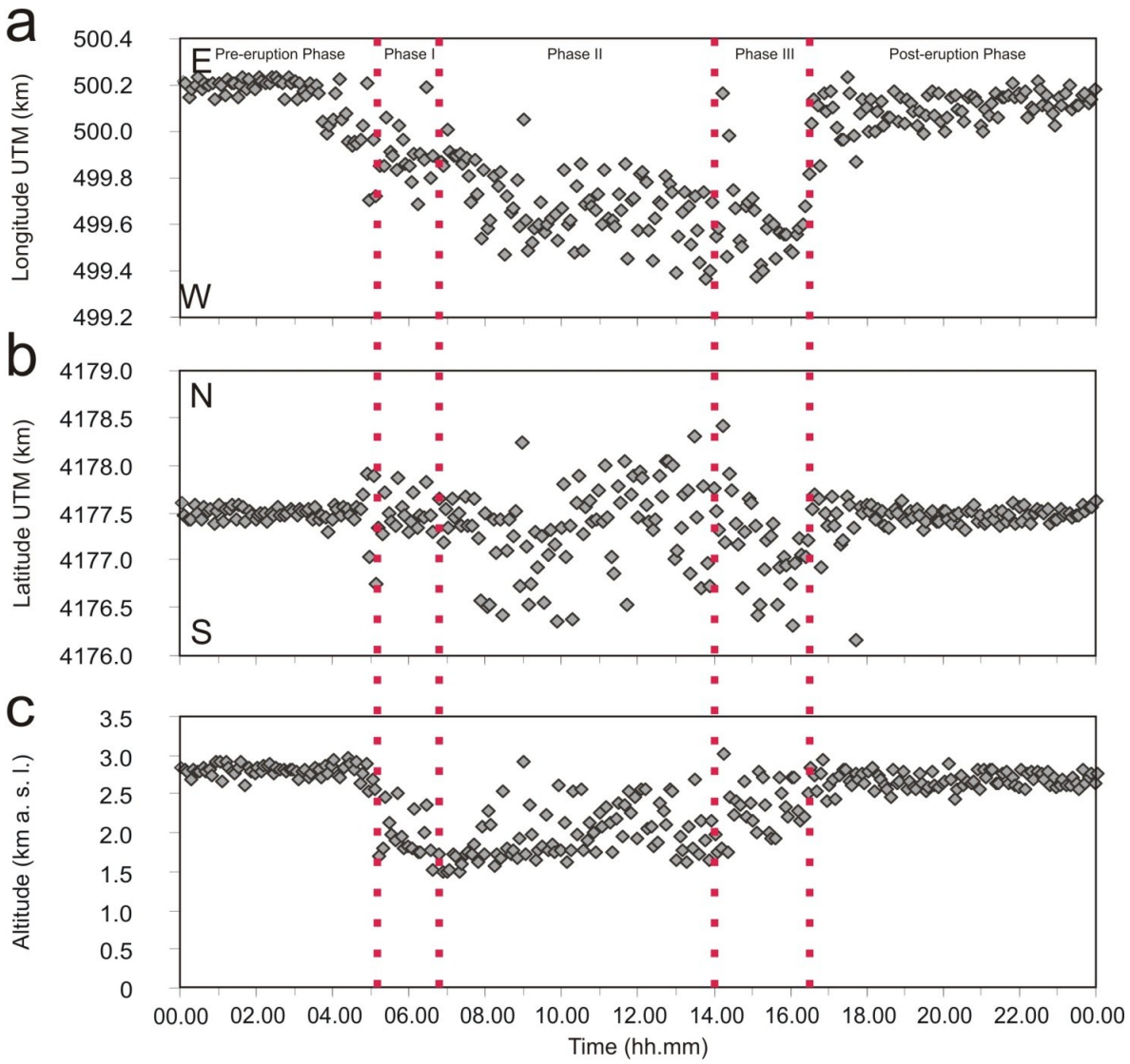

Fig. 5.5 *Time evolution of seismic volcanic tremor centroids obtained by amplitude decay in the frequency band 1-5 Hz during 16 November 2006. Seismic volcanic tremor locations plotted as function of longitude* ***(a)****, latitude* ***(b)*** *and altitude* ***(c)****.*

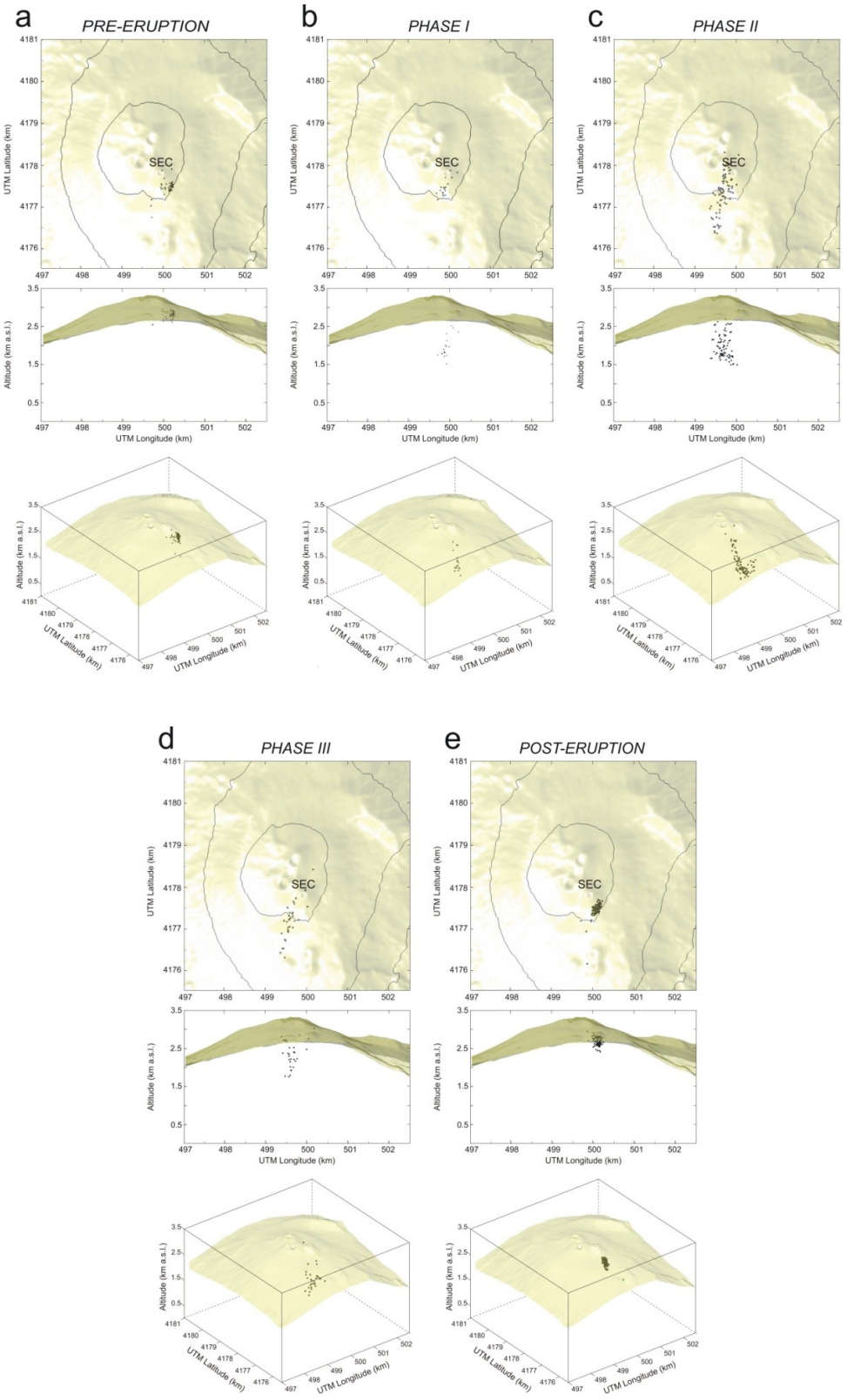

Fig. 5.6 *Source locations of seismic volcanic tremor plotted in map, section and 3D view, before the explosive activity (00.00-05:13;* ***a****), during the three phases of activity* ***(b-d)*** *and after (16:30-24.00;* ***e****).*

In this pre-eruption phase, the seismic volcanic tremor centroids were located at shallow depth (2.5-3.0 km a.s.l.) below SEC (**Figs. 5.5** and **5.6a**).

During the first phase, starting at 5:13, coinciding with the onset of intense Strombolian explosions (**Fig. 5.1**), both infrasound and seismic RMS became fairly stable (**Fig. 5.4a, b** and **c**). The VASR showed values of ~0.2 (**Fig. 5.4d**). Both infrasonic and seismic energies were radiated in the frequency band 0.7-5.0 Hz, as exhibited by spectrograms in **Fig. 5.4e, f**. In the frequency band 1.5-3.0 Hz coherence values increased up to 0.5 (**Fig. 5.4g**). The seismic volcanic tremor centroids shifted westward and deepened reaching a depth of about 1.5 km a.s.l. (**Figs. 5.5** and **5.6b**).

The second phase was characterized by a decrease in infrasound amplitude, while seismic signal recorded at ECPN station showed a slight increase **(Fig. 5.4a, b)**. These different seismic and infrasound behaviors gave rise to a decrease of VASR (~0.1; **Fig. 5.4d**), as well as to a clear reduction in coherence values (**Fig. 5.4g**). During this second phase, the dominant spectral components of infrasound shifted toward lower frequencies and were comprised in a narrower band than the previous phase (**Fig. 5.4f**). The hypocentres of seismic volcanic tremor indicated a further westward migration, accompanied by an opposite trend of the centroid depths (that gradually shallowed) with respect to the previous phase (**Figs. 5.5** and **5.6c**). At the same time, lava outpoured from two fissures located in the saddle between SEC and BN and south of BN **(Fig. 5.1)**.

The third phase was the most intense from the infrasound point of view and was characterized by various volcanic phenomena (pyroclastic flows, jets of dark ash and white steam). As shown in **Fig. 5.4a,** at 14:12 the infrasound RMS reached the highest value of about 24 Pa, successively showing at least another three peaks at 14:26, 14:46 and 15:06. From 14:13, seismic amplitude gradually decreased **(Fig. 5.4b, c)**. During this short interval, VASR highlighted these contrasting behaviors of the two signals reaching values of ~11 (**Fig. 5.4d**) and coherence showed the highest values of the whole studied period in the band 1.0-2.5 Hz, reaching the maximum value of ~0.6 at ~14:10-14:30 (**Fig. 5.4g**). After 14:20, the infrasound amplitude started decreasing and together with the seismic RMS reached the pre-eruption levels at 16:30 (**Fig. 5.4a, b,** and **c**), when the explosive activity ended. During this third phase, seismic volcanic tremor locations underwent a further westward migration and became shallower (**Figs. 5.5** and **5.6d**). Moreover, it is worth noting that the tremor source location calculated for the interval 14:10-14:15, roughly coinciding with the maximum values of the infrasound RMS, sharply shifted below SEC at very shallow depth (~3000 m a.s.l.; **Fig. 5.5**).

Finally, after 16:30 some peaks in the infrasound RMS related to NEC events again became visible (**Fig. 5.4a**) and the seismic volcanic tremor centroids shifted towards the same rock volume as during the pre-eruption phase (**Figs. 5.5** and **5.6e**).

During the 16 November eruptive activity at SEC, RD (calculated from body waves and every 5 minutes) exhibited a mean value of about 26 cm^2 and reached the highest peak (45 cm^2) during the intense Strombolian activity of the first phase (**Fig. 5.7**).

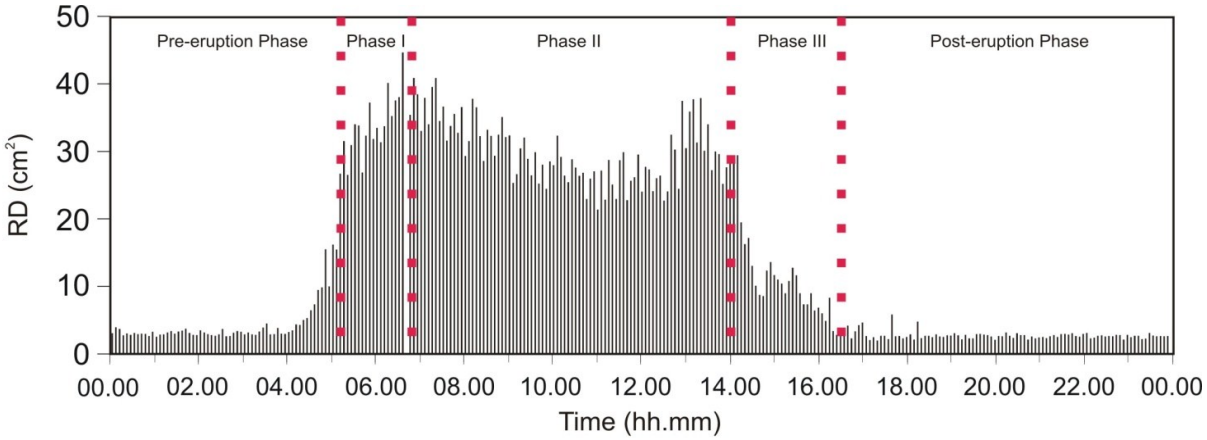

Fig. 5.7 *Reduced displacement of seismic volcanic tremor amplitude recorded at ECPN station. The vertical dashed lines indicate the time boundaries among the different phases of eruptive activity (see text for details).*

5.1.4. Analysis of infrasound events

Both the summit craters SEC and NEC have been recognized to be active from the infrasound point of view, even if they show different "infrasonic" behaviors. In addition, SEC radiates both infrasound events and infrasonic volcanic tremor only during explosive activity (see the infrasound recording and the video-camera frames in **Fig. 5.8**), whereas NEC generates infrasound events almost continuously associated to degassing activity and deep explosions observed constantly since summer 2006 (e.g. Cannata et al., 2009b, c).

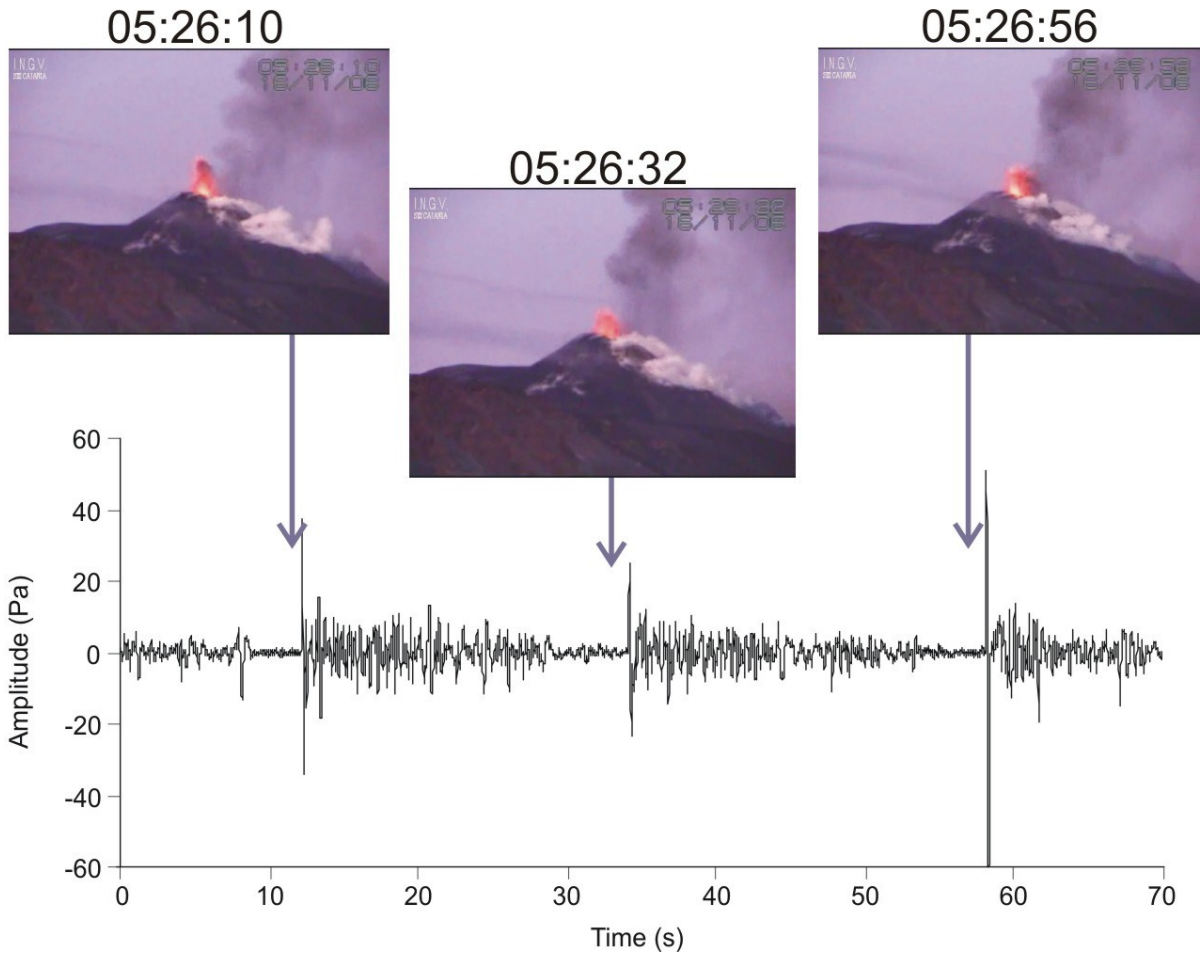

Fig. 5.8 *Seventy seconds of infrasound signal recorded at ECPN station showing three infrasound events and frames of the corresponding explosions recorded by EEV video-camera.*

Even the waveforms of the infrasound events radiated by NEC and SEC are very different. Indeed, the NEC events are characterized by waveforms resembling decaying sinusoids, either monochromatic or with some harmonic spectral peaks (**Fig. 5.3cI**), whereas SEC events show a first energetic part roughly composed of one cycle or one cycle and a half, followed by a second part with various weaker oscillations (**Fig. 5.3cII, III**; e.g. Cannata et al., 2009b, c).
We detected infrasound events in the signal recorded at ECPN during 16 November 2006, by STA/LTA algorithm by fixing a short window of 0.4 s and a long window of 4 s, and found 1904 events (**Fig. 5.9a**).

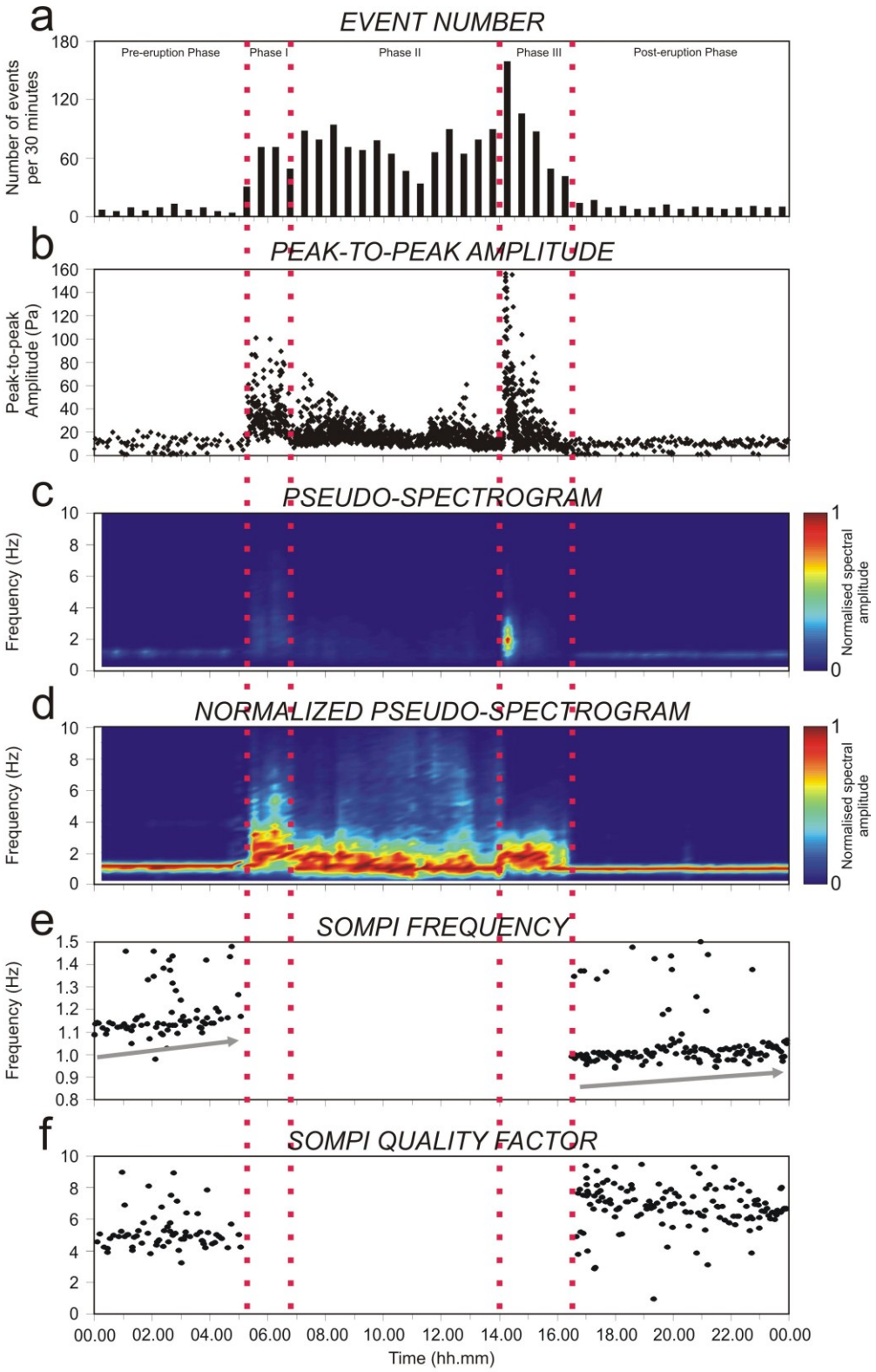

Fig. 5.9 *Features of infrasound events.* ***(a)*** *Rate of occurrence of events in 30-minute windows.* ***(b)*** *Peak-to-peak amplitude.* ***(c)*** *Pseudo-spectrogram of infrasound events recorded at ECPN station.* ***(d)*** *Normalized pseudo-spectrogram of infrasound events recorded at ECPN station.* ***(e, f)*** *Dominant frequency and quality factor of infrasound events calculated by Sompi method. The grey arrows in* ***e)*** *indicate the frequency increasing trend. The vertical dashed lines indicate the time boundaries among the different phases of activity (see text for details).*

First of all, we calculated the peak-to-peak amplitudes of the 1904 infrasound events plotted in **Figure 5.9b**. In order to study the variation of the spectral features of the infrasound events, we performed two different frequency domain analyses: Fast Fourier Trasform (FFT) and Sompi analysis addressed in **sections 3.2.1-3.2.3.**

With FFT, we calculated one spectrum for each event by using roughly 5-s-long windows, containing the event and a pre-event of roughly 0.5 s. Then, we averaged the spectra of the events occurring during 15-minute time spans and the obtained average spectra were visualised as pseudo-spectrograms, both non-normalized and normalized (**Fig. 5.9c**, **d** respectively).

Since the NEC events show monochromatic waveforms resembling decaying sinusoids, like the event in **Figure 5.3cI**, we applied the Sompi method to obtain information about their damping features. Therefore, for this analysis we took into account only the pre-eruption and the post-eruption phases, characterized by the occurrence of the NEC events alone. Sompi analysis was performed on 2-s-long windows of infrasound signal, coinciding with the tails of the NEC events, and frequency and Q were calculated for AR order of 2 (**Fig. 5.9e, f**). The evident monochromatic nature of the investigated signals justifies the choice of these low orders (Lesage, 2008).

In the time domain we performed a waveform classification, based on cross-correlation coefficient, to obtain information on the variability of the source. Cross-correlation analysis was carried out on the 1904 infrasound events of our dataset, filtered in the frequency range 0.7–5.0 Hz. In order to reach a good balance between the classification accuracy and the event detection capability a 0.85 cross-correlation coefficient threshold value was chosen.

We found 9 families with more than 852 events, whose time distribution and stacked waveforms are reported in **Figures. 5.10a** and **5.11**, respectively. Furthermore, by using roughly 5-s-long windows, we calculated the dominant frequencies of the stacked waveforms of each family, which are reported in the insets in **Figure 5.11**. In order to evaluate the repeatability and stationarity of the infrasound source, in 30-minute-long windows we counted both all the detected events and only the events belonging to the nine families (called "classified events"). Then, we calculated the percentages of the classified events with respect to the detected events in 30-minute-long windows and plotted them in **Figure 5.10b**.

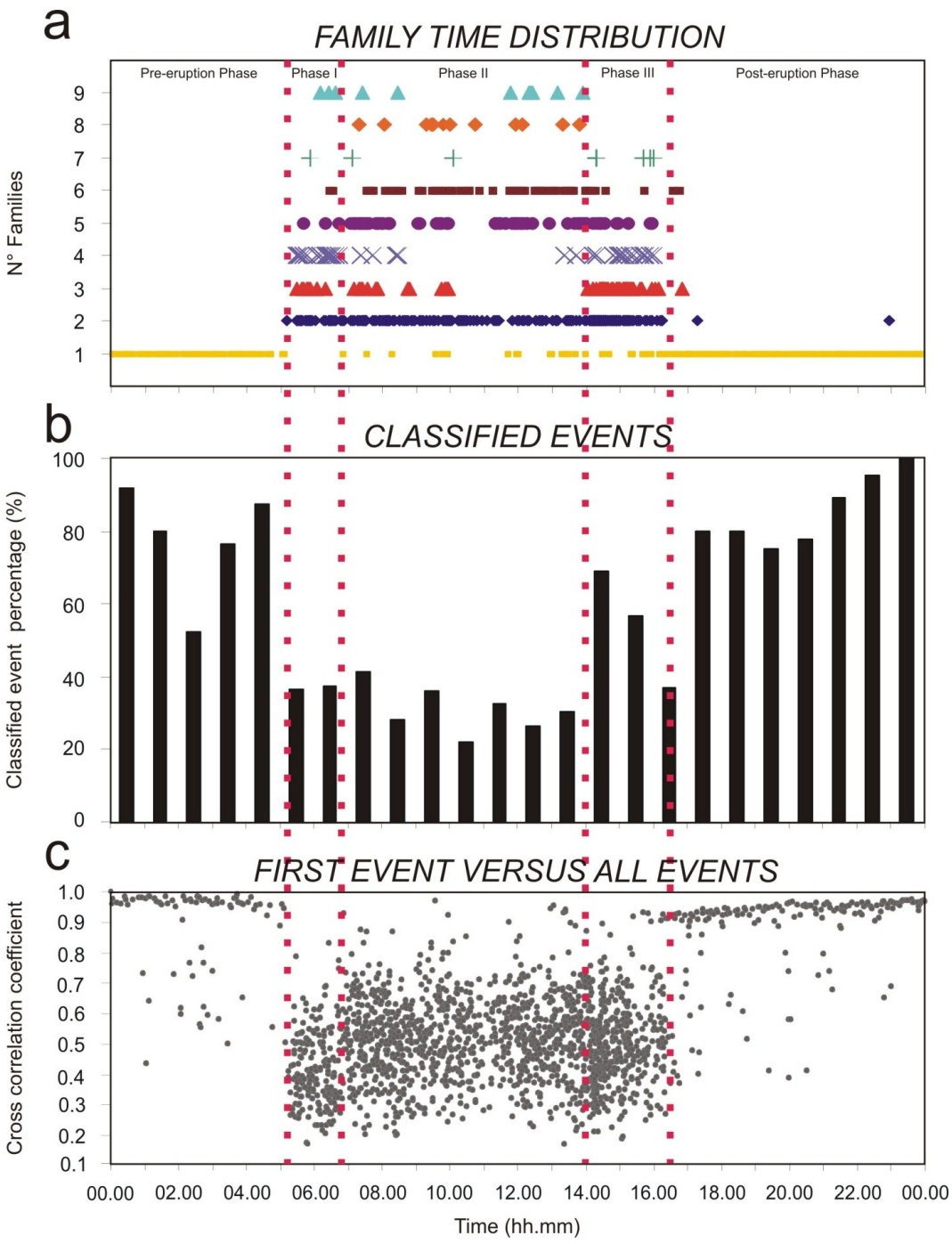

Fig. 5.10 *Cross-correlation analysis of infrasound events.* ***(a)*** *Time distribution of the events grouped in nine families.* ***(b)*** *Time variation of classified event percentage with respect to all the detected events.* ***(c)*** *Time evolution of cross-correlation coefficient between the first event and all the others.*

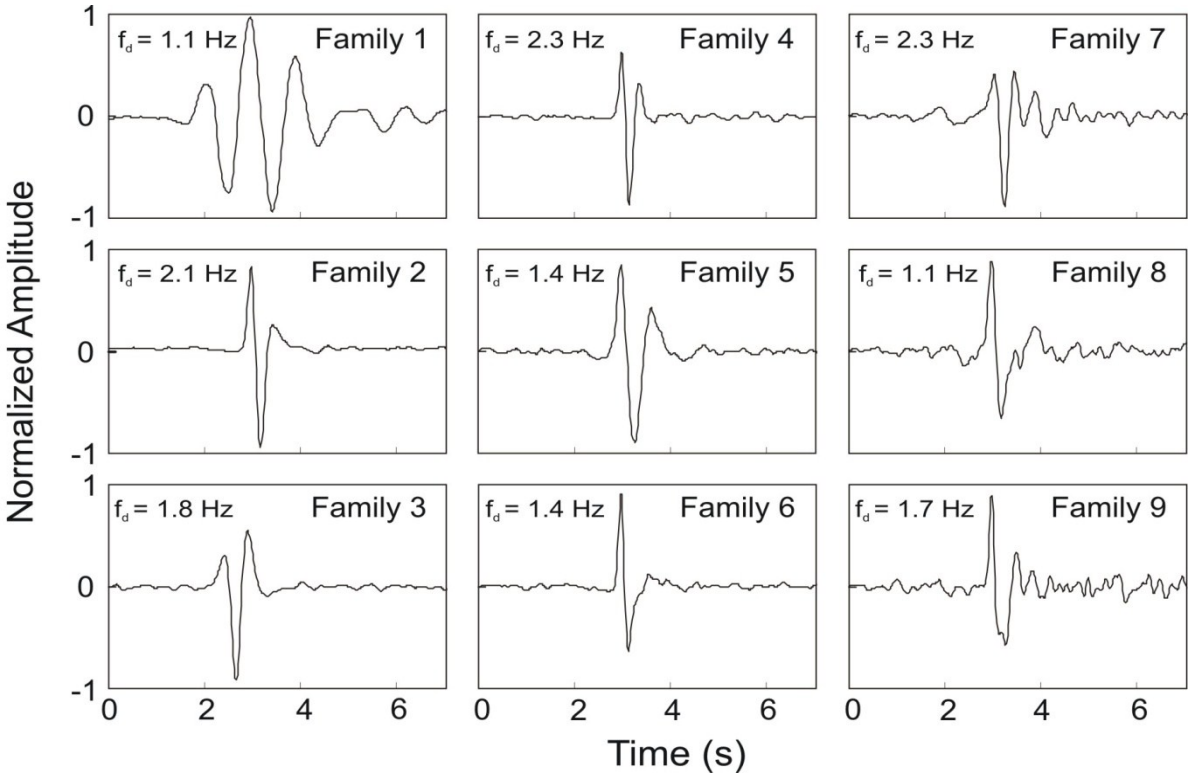

Fig. 5.11 *Stacked waveforms of each of the nine families obtained by cross-correlation analysis. The dominant frequency is indicated by f_d.*

In the pre-eruption phase the triggering algorithm allowed recognizing infrasound events that, thanks to the similarity to the infrasound transients identified and localized by Cannata et al. (2009b, c), were attributed to the activity of NEC. They exhibited peak-to-peak amplitude from a few up to 20 Pa (**Fig. 5.9b**). By pseudo-spectrograms and Sompi analysis, we found evidence of a dominant frequency of ~1.2 Hz (**Fig. 5.9d, e**) and a *Q* value of ~5 (**Fig. 5.9f**). In this phase all the detected events were grouped by cross-correlation analysis in the family 1 (**Fig. 5.10a**), whose stacked waveform is reported in **Figure 5.11**. The repeatability of the NEC events, inferred by cross-correlation analysis, is confirmed by the high percentage of classified events with respect to the detected events (**Fig. 5.10b**). Further, a slightly increasing trend of dominant frequency was noticed before the onset of the activity (**Fig. 5.9e**).

From 05:13 on, we recorded a different type of infrasound event (**Fig. 5.3cII**) with respect to those recorded in the previous phase (**Fig. 5.3cI**). During this first eruptive phase infrasound signal characteristics reflect the strongly explosive nature of the activity. Indeed, in **Figure 5.9a** we noticed a high rate of infrasound events, accompanied by an increase of peak-to-peak amplitudes, corresponding to Strombolian explosions on summit vents of SEC (**Fig. 5.8**). The normalized pseudo-spectrogram shows a frequency content in the band 1.5-4.0 Hz (**Fig. 5.9d**). The infrasound events in this phase were mostly grouped in families 2, 3 and 4 (**Fig. 5.10a**) and the stacking of their waveforms is shown in **Figure 5.11**. The variability of infrasound

events during the explosive activity is supported by the low percentage of classified events (**Fig. 5.10b**). It should be noted that by using a lower threshold the percentage of classified events would increase. However, our aim is to investigate the variability of infrasound events through the three phases of the eruptive activity at SEC and compare it with the high stability of the NEC events.

As described before, at ~06:40 (onset of the second phase of the eruption), the explosive activity decreased in intensity and rockfalls, as debris-avalanches, took place (**Fig. 5.1**). However, as shown in **Figure 5.9a** the triggering algorithm detected a slightly higher number of events with respect to the first phase (**Fig. 5.9a**). A possible reason for the greater number of detected events is the decrease in background noise level (testified by the lowered infrasound RMS; **Fig. 5.4a**) and then in the dynamic triggering threshold allowing the detection of a larger number of events. This is confirmed by the generally lower peak-to-peak amplitude of the events (**Fig. 5.9b**). The temporal evolution of volcanic phenomena is also highlighted by the decreasing dominant frequency and the narrowing frequency band (**Fig. 5.9d**). Such decreasing dominant frequency is also clearly visible in stacked waveforms and dominant frequencies of families 6, 8 and 9, into which most of the events of this second phase were grouped (**Figs. 5.10a** and **5.11**). However, it should be noted that the families did not always switch between each other; for instance, families 2, 5 and 7 are spread out through all the phases (**Fig. 5.10a**). As in the first phase, the percentage of classified events with respect to all the detected events is low (**Fig. 5.10b**). In other words, the data display a great deal of variability, suggesting that conditions are unstable.

Most infrasonic energy was radiated in the third phase, between the 14:10 and 14:20, as proved by the largest number of infrasound events (**Fig. 5.9a**) and by the highest peak-to-peak and spectral amplitudes (**Fig. 5.9b, c**) during this interval. The events during the third phase showed frequency content in the band 1-3 Hz. Most infrasound events of the third phase were grouped into families 2, 3, 4 and 5 (**Fig. 5.10a**) and were characterized by a fairly good repeatability, as shown by the high percentage of classified events (in particular during 14:10-14:20 interval; **Fig. 5.10b**). It is interesting to note that families 3 and 4 were also observed during the first phase.

After the explosive activity at SEC (~16:30), only NEC events were again recorded. In this post-eruption phase, peak-to-peak amplitude values were similar to the pre-eruption phase (**Fig. 5.9b**). The pseudo-spectrogram shows a decrease in frequency content, more clearly highlighted by Sompi analysis, from 1.2 to 1.0 Hz (**Fig. 5.9d, e**), while Q underwent an increase with a mean value of 7 (**Fig. 5.9f**). This means that infrasound events during the post-

eruption phase had a slower amplitude decay with respect to the pre-eruption phase. Also in this phase, NEC events were grouped in family 1 (**Fig. 5.10a**) and exhibited a high clustering (**Fig. 5.10b**). The time distribution of the family 1 shows how NEC events also occurred during the eruptive episode (**Fig. 5.10a**), albeit in small numbers.

To further investigate such a difference we performed the waveform classification again by increasing the threshold up to 0.95 and focusing on NEC events.

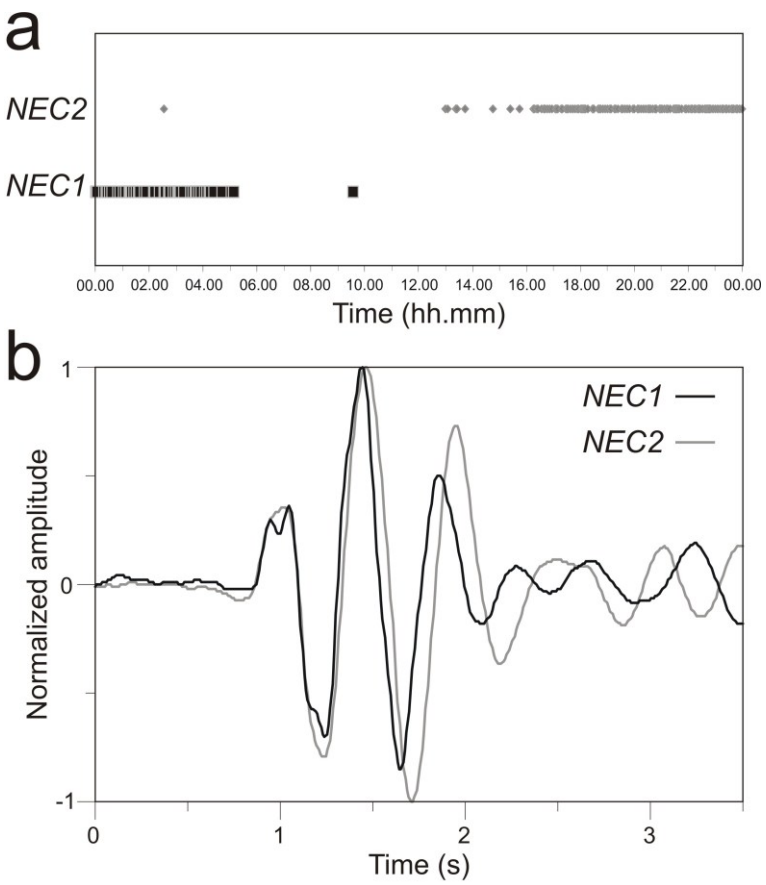

Fig. 5.12 ***(a)*** *Time distribution of the two families of NEC events (NEC1 and NEC2) recognized by the cross-correlation analysis using a threshold of 0.95.* ***(b)*** *Normalized stacked waveforms of the traces of the NEC1 and NEC2 events.*

Thus, two different families of NEC events have been found, called NEC1 and NEC2. The former preceded and the latter followed the eruptive activity (**Fig. 5.12a**). The stacked waveforms of NEC1 and NEC2, reported in **Figure 5.12b**, confirm the results from the frequency domain analyses: NEC2 events are characterized by lower dominant frequency and higher *Q* values than NEC1 events.

Finally, we extracted from the cross-correlation matrix the cross-correlation coefficient values calculated by comparing the first event with all the others (**Fig. 5.10c**). This kind of plot, also used by some authors to investigate the variations of LP and VLP events (e.g. Stephens and

Chouet, 2001; Cannata et al., 2009a), shows the time evolution of all the detected infrasound events with respect to a reference one. Before the onset of the eruptive activity, most of the cross-correlation values were high and fairly stable. Therefore, since the first event is a NEC event, the infrasound NEC source seemed to remain fairly steady during this interval. During the eruptive activity we noted a sharp decrease in the cross-correlation values, suggesting the activation of different infrasound sources (the active vents in the SEC area). After the eruptive activity the cross-correlation coefficient increased but did not immediately reach the values obtained before the activity. The cross-correlation coefficient gradually increased, reaching values comparable to those obtained in the pre-eruption phase only at the end of the investigated period. This variation in waveforms is due to the increasing trend of dominant frequencies, similar to the one observed during the pre-eruption phase (**Fig. 5.9e**).

In summary, on the basis of the results of the cross-correlation analysis, the infrasound activity at NEC shows much more stable features than the activity at SEC. Furthermore, waveform changes of NEC events, observed after the eruptive activity at SEC, evidenced a gradual return to the stable conditions of the first hours of the day.

5.1.5. Discussion

Investigations on the dynamics of the 16 November 2006 paroxysmal eruption were previously carried out through observation of seismic volcanic tremor and live-cameras, tephra sampling and analysis (Andronico et al., 2008; Behncke et al., 2009; Norini et al., 2009; Ferlito et al., 2010). In order to obtain further insights into the explosive mechanisms during this eruptive episode, we applied a multi-disciplinary approach, integrating seismic and video-camera data with infrasound signals (**Fig. 5.2**).

The 16 November eruptive activity was one of the 18 paroxysmal episodes during the 2006 summit eruption. It was characterized by complex volcanic phenomena. On the basis of volcanological observations, we divided the eruptive episode into three phases (**Fig. 5.1**). During the first phase, intense Strombolian activity and lava effusion from vents on the summit area of SEC were observed. The second phase was mainly characterized by a decrease in explosive activity and the occurrence of rockfalls and debris avalanches on the south-eastern flank of the SEC cone. During the third phase, the singularity of this eruptive episode was the occurrence of two pyroclastic flows taking place on the eastern flank of SEC. In particular, the pyroclastic flow at 14:24 caused the formation of an 1.2 km-long block-and-ash deposit downslope from SEC (Behncke et al., 2009; Norini et al., 2009). No evident ground

deformations were recognized by the tiltmeter network during the whole eruptive episode (S. Gambino, personal communication, 2011).

The onset of the eruptive episode was heralded by the increase in seismic signal amplitude ~ 03:15 (**Fig. 5.4b**). Thanks to its close relationship with the evolution of volcanic activity, variations in seismic volcanic tremor amplitude were used to forecast paroxysmal explosive activity at Etna during 2000 and 2001 (Alparone et al., 2007b). In spite of the good correspondence, there are some cases where increases in seismic volcanic tremor amplitude did not match eruptive activity (e.g. Cannata et al., 2010a). The increase in seismic volcanic tremor amplitude of the studied eruptive episode was accompanied by an increase of infrasound amplitude (**Fig. 5.4a**). Explosive volcanic activity is controlled by the violent release in the atmosphere of large volumes of gas in overpressure conditions. This produces large pressure perturbations which can be detected as infrasound waves (e.g. Ripepe et al., 2009). For this reason, infrasound investigation appears to be a simple and useful method for explosive activity detection. At the distances considered here, scattering/dissipitation of atmospheric acoustic waves is less pronounced than for seismic waves (Ripepe et al., 2009), but weather-dependent effects like wind noise are not easily filtered out, especially if only one acoustic sensor is used. Therefore, the best monitoring would seem to be the joint analysis of video-camera, infrasound and seismic data. This multi-parametric approach allows us to observe and correlate the eruptive activity evolution with both the infrasound and seismic signal.

Figure 5.13 shows a sketch of the magma dynamics inside the conduit for the aforementioned three phases, based not only on the different "volcanological" features, but also on the different seismic and infrasound features.

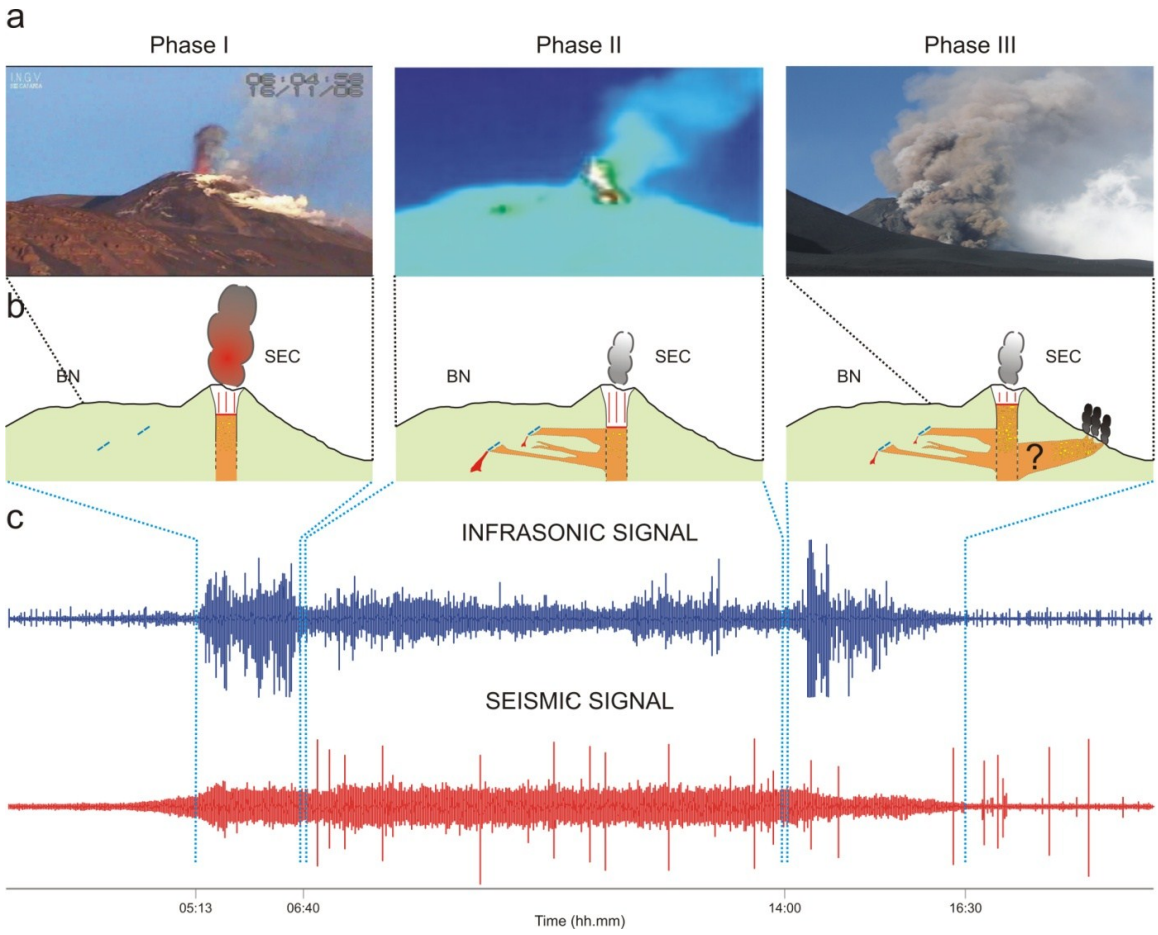

Fig. 5.13 *Sketch model representing the observed volcanic phenomena, the recorded seismic and infrasound signals and interpretations of the 16 November 2006 eruptive episode.* ***(a)*** *Images of the eruptive activity: intense strombolian activity (phase I); weak strombolian activity and lava effusion from several vents (SEC, two fissures located on the saddle between BN and SEC and south of BN) (phase II); pyroclastic flow (phase III).* ***(b)*** *Cartoon of magma dynamics evolution inside the conduit for the different phases. Cartoon shows the evolution of magma fragmentation level height during the three analyzed phases, the opening of the effusive fissures (phase II), the inferred gas-rich magma batch arrival and the debated fracture opening at the base of SEC hypothesized by Ferlito et al. (2010) (phase III).* ***(c)*** *Infrasound and seismic signals recorded during the three phases.*

The first phase showed high values of infrasonic and seismic volcanic tremor RMS amplitudes (**Fig. 5.4a, b**), high peak-to-peak amplitudes (**Fig. 5.9b**) and occurrence rate of infrasound events (**Fig. 5.9a**), corresponding with visible Strombolian explosions (**Fig. 5.8**). Furthermore, similarly to infrasound data, thermal data, reported by Behncke et al. (2009), exhibited very high values during the first hours of the eruption. Unfortunately, the limited range of this kind of data, and then the saturated thermal measurements, did not allow to verify if the highest value of apparent temperature was reached during the first or the second phase. All these evidences reflect the highly explosive nature of this first phase.

The three recognized families of infrasound events suggest the presence of simultaneously active sources (**Figs. 5.10a** and **5.11**). Indeed, sometimes a vent has a unique signature and can be distinguished visually from the waveform character of infrasound waves (McGreger and Lees, 2004; Cannata et al., 2009b, c). During the studied eruptive episode, at least three vents at the summit area of SEC produced Strombolian explosions and ash emissions (Behncke et al., 2009).

Before the onset of the paroxysmal episode, the seismic volcanic tremor centroids were located below SEC probably because of the on-going eruption (**Figs. 5.5c** and **5.6a**). At the beginning of the explosive activity, the seismic volcanic tremor centroids deepened (**Figs. 5.5c** and **5.6b**). A similar pattern was noticed during lava fountains at SEC in 2000 (Alparone et al., 2003) and at VOR in 1999 (Cannata et al., 2008). As suggested by these authors, we infer that the intense Strombolian activity at summit vents of SEC would have enabled a depressurization process, causing the involvement of deeper magma and then the deepening of the seismic volcanic tremor source centroids.

The VASR ratio, taking into account the coupling between volcanic activity and both the volcanic edifice and the atmosphere, was ~0.2 (**Fig. 5.4d**) and the coherence between seismic and infrasound signals reached a maximum value of 0.5 (**Fig. 5.4g**). Such coherence values lead us to hypothesize that in the first phase at least the shallowest component of seismic volcanic tremor was well-coupled with explosive activity, and then seismic and infrasound signals shared a common source. During the first phase, RD exhibited a mean value of 34 cm^2, reaching the maximum value of 45 cm^2, which at Mt. Etna, in literature, is associated to intense Strombolian activity and lava fountain (e.g. Privitera et al., 2003; Alparone et al., 2003).

Successively, during the second phase, changes in the infrasound sources were observed, testified by both lower infrasound RMS (**Fig. 5.4a**) and event peak-to-peak amplitudes (**Fig. 5.9b**), in agreement with the decreasing explosive activity. Furthermore, slightly different infrasound waveforms were detected. It is worth noting that a clear-cut switching of families from first to second phase was not found, though infrasound events certainly underwent a decrease in frequency and increased variations in the waveform characteristics (**Figs. 5.10a** and **5.11**).

The westward migration of seismic volcanic tremor centroids (**Figs. 5.5a** and **5.6c**), leading to the slight seismic RMS increase at ECPN station (**Fig. 5.4b**), occurred at the same time as the re-activation of two effusive fissures located on the saddle between BN and SEC and south of BN (**Fig. 5.1**). The opposite behaviors of infrasound and seismic RMS caused a decrease in

VASR values (**Fig. 5.4d**). Moreover, the very low values of coherence (up to 0.25; **Fig. 5.4g**) suggest the decoupling between seismic and infrasound sources during this phase.

Late in the second phase, the temporal evolution of thermal data (Behncke et al., 2009) followed a similar trend to infrasound RMS, undergoing a decrease until ~12:00 and a slight increase for the rest of the second phase.

The decrease in the explosive activity and the resulting reduction of infrasonic energy were likely due to the opening of the two aforementioned effusive fissures. Indeed, according to the model by Ripepe et al. (2005, 2009) for the 2003 and 2007 Stromboli eruptions, the opening of effusive fractures might cause a reduction in magma column height. The lower level of magma within the conduit and the consequent deepening of the fragmentation level led to a decrease in gas overpressure and therefore in the explosive activity.

In the light of this interpretation, we can formulate hypotheses about the observed changes in the infrasound event waveforms. Assuming propagation effects are negligible, changes in waveforms mainly imply variations in source mechanisms. For instance, taking into consideration the Strombolian bubble vibration model (Vergniolle et al., 2004), then infrasound waveforms depend closely on overpressure and bubble dimension, linked to vent/conduit geometry. In view of this, the inferred deepening of fragmentation level and hence the different conditions of the infrasound generation (e.g. conduit geometry and overpressure) could have caused variations in the infrasound event waveforms from the first to the second phase. On the other hand, as suggested by Johnson and Aster (2005), also the VASR decrease could be related to such a deepening of the fragmentation level.

During the third phase, the contrasting behaviour between infrasound and seismic signal became more pronounced: indeed, at the onset of this phase the infrasound signal underwent a very sharp increase from 14:05, reaching the highest RMS values of the whole episode at 14:12, while the seismic amplitude from 14:13 gradually decreased (**Fig. 5.4a, b**). In addition, at least another three RMS peaks were observed at 14:26, 14:46 and 15:06. Owing to the cloud cover a comparison with thermal data was not possible during the whole of the third phase. Most infrasonic energy of this phase was radiated between the 14:10 and 14:30, as also testified by the largest number (**Fig. 5.9a**) and highest peak-to-peak amplitudes (**Fig. 5.9b**) of infrasound events. These showed highly comparable waveforms to the infrasound events detected during the first phase (**Figs. 5.10a** and **5.11**), but were characterized by a higher repeatability (**Fig. 5.10b**), suggesting the presence of very similar stationary and repeatable infrasound sources to those observed during the first phase. During this short time span 14:10-14:30, coherence exhibited the highest value (**Fig. 5.4g**) of the paroxysmal episode, again

indicating a good coupling between the two signals. Indeed, at 14:10 – 14:15, at the same time as the maximum peak of the infrasound activity was reached, the tremor source centroids shifted below SEC at very shallow depth. The progressive shallowing of the seismic volcanic tremor centroids during the third phase testified the reduced activity of the deeper sources not directly associated with infrasound sources. Apparently in contrast with coherence results, VASR reached the highest value (**Fig. 5.4d**). Assuming a coupling of infrasound and seismic signals, such high VASR, together with the very high recorded infrasonic energy, could be due to pressurized volatiles which expand explosively without entraining much ash and/or to a shallowing of fragmentation level, which would allow for an unimpeded explosion (Johnson and Aster, 2005). Both these phenomena could be caused by the arrival of a batch of gas-rich magma, below the SEC, that is likely due to the depressurization of the shallow plumbing system as suggested by Ferlito et al. (2010). In fact, the acceleration of the collapse phenomena of the SEC flank, taking place at 13:45−14:00, just before the RMS infrasound major peak, could have favoured gas exolution of the upper part of the magma column. Then, such an increase in the magma gas content may have intensified infrasound activity and caused the pressure rise in the shallow part of magma column. The pressurization of shallow parts of SEC plumbing system may have led to the opening of a short fissure in the weakened part of the cone, as often observed on the SEC flanks during paroxysmal episodes (e.g. Alparone et al., 2003; Behncke, 2009; Andronico and Corsaro, 2011). The opening of an eruptive fissure just before the pyroclastic flow at 14:25, also inferred by Norini et al. (2009) and Ferlito et al. (2010), could have caused the interaction between intruding magma and fluid-soaked rocks with a similar mechanism to that hypothesized by Behncke et al. (2009).

On the other hand, besides the depth of the explosive source and the overpressure inside the bubble, the acoustic energy increase during the third phase could also be due to changes in the typical time associated with film bursting (Divoux et al., 2008; Vidal et al., 2010). According to experiments carried out by Vidal et al. (2010), film rupture time is mainly affected by viscosity, temperature and volatile content of the magma film layer above the bubbles. In particular, with a decreasing viscosity the film rupture velocity should be faster and consequently the amplitude of the recorded acoustic signal larger. Also in this case, the above cited increase in magma gas content can lead to a viscosity decrease, which can be considered an additional cause for the very high values of both infrasonic energy and VASR.

It is noteworthy that the pyroclastic flow at 14:25 was accompanied by no detectable infrasound transients.

The remaining part of the phase was characterized by a gradual decrease in the energy of seismic and infrasound signals, accompanying the weakening explosive activity at the end of the eruptive episode (**Fig. 5.4a, b**).

Infrasound activity before and after the paroxysmal episode at SEC consisted mainly of amplitude transients, related to NEC activity, as displayed in the infrasound helicorder and RMS (**Figs. 5.3b** and **5.4a**, respectively). With respect to the SEC events, the NEC ones were characterized by steadier waveforms suggesting a highly repeatable source (**Fig. 5.10b**). However, slight waveform changes in the NEC events, highlighted by cross-correlation and spectral analyses and consisting of both decrease of dominant frequency (from ~1.2 to 1.0 Hz) and increase of Q values (from ~5.0 to 7.0), were observed after the eruptive activity (**Figs. 5.9e, f**, **5.10c** and **5.12**). It is noteworthy that during the few hours of the post-eruption phase, cross-correlation coefficient, frequency and Q values showed gradual trends towards the pre-eruption conditions (**Figs. 5.9e, f** and **5.10c**). Spectral changes in NEC infrasound events after an explosive activity at SEC had already been observed at Etna after the lava fountain of 10 May 2008 (Di Grazia et al., 2009). The hypothesis of a branched shallow system feeding Etna summit craters has already been suggested by Marchetti et al. (2009b) in an array analysis carried out during September-November 2006. These authors noted a switching of infrasound source location between NEC and SEC until October 27. Thus, the detection of NEC events during the eruptive activity at SEC is in agreement with the behavior observed by Marchetti et al. (2009b) after 27 October 2006.

To further investigate the aforementioned spectral variations we modeled the source mechanism of NEC events as the acoustic resonance of a fluid-filled conduit (Garces and McNutt, 1997). Such a mechanism of acoustic generation has also been demonstrated with laboratory experiments (e.g. Vidal et al., 2006). We assumed that NEC infrasound events are generated by longitudinal acoustic resonance, and did not take into account radial modes (e.g. Hagerty et al., 2000; De Angelis and McNutt, 2007). In fact, at the frequency considered, the wavelengths of the acoustic waves in the fluid are greater than the width of the conduit and consequently the longitudinal modes are dominant (Garces and McNutt, 1997). Moreover, during May 2008 some NEC infrasound events were characterized by a fundamental mode and an integer harmonic, supporting the acoustic resonance model (Cannata et al., 2009b).

The sound speed inside the conduit is subject to strong variations depending on the chemical/physical property of fluid filling the conduit. Morrissey and Chouet (2001) suggest c_c values from ~400 to 1000 m/s for a pure gas mixture. If the fluid is a bubbly magma, c_c can range between 300 and 2500 m/s (Murase and McBirney, 1973; Aki et al., 1977). Assuming

300 and 2500 m/s as the lower and the upper limit, respectively, and for a frequency equal to 1.2 Hz, the conduit length ranges between ~150 and 1050 m.

On the basis of the decrease in frequency of 0.2 Hz, we inferred i) a length increase of ~20%, or ii) a sound speed decrease of ~20%, or finally iii) both these variations with different percentage. In light of this, the observed spectral changes could be related to either variations in the fluid chemical/physical property (such as changes in gas concentrations, temperature and pressure; e.g. Kumagai and Chouet, 2000; Morrissey and Chouet, 2001) or conduit geometry/size variations (e.g. Garces and McNutt, 1997; Kumagai and Chouet, 2000, 2001).

If we consider the conduit portion above the fragmentation level, filled with a gas mixture, as the resonating part, a length increase would mean a drop in magma column, while a sound speed decrease would mean a variation in the geochemical/physical properties of this gas mixture (e.g. changes in density and composition of the volatile phases). The former hypothesis is consistent with the withdrawal of magma and the subsequent emptying of the shallow portion of the plumbing system due to the eruption. In this case, assuming a value of sound speed of 500 m/s (used also in Fee et al., 2010a), a decrease in frequency of 0.2 Hz would imply a drop in magma level of 40 m (in particular a conduit length increase from 210 to 250 m). As a consequence, the magma fragmentation level should be situated at a depth of 210-250 m. This value is consistent with depths estimated at Etna (Gresta et al., 2004) and other volcanoes (e.g. Shishaldin, Petersen and McNutt, 2007; Stromboli, Marchetti et al., 2008). The drop in the magma column (e.g. the length increase of the resonating part of the conduit) would also explain the Q value increase of the NEC infrasound events. Q parameter can be considered a measure of the decay time. Experiments carried out by Vidal et al. (2006) demonstrated that the damping time increases when the fundamental frequency decreases as a function of the conduit length.

Concerning the latter hypothesis (sound speed decrease), Morrissey and Chouet (2001), assuming a gas-gas mixture fluid (H_2O-CO_2 or H_2O-SO_2) at 800° K, obtained a decrease in sound speed of ~20% by adding 50% of CO_2 or SO_2. Moreover, such a decrease in sound speed would also imply an increase of the impedance contrast between the resonating fluids and the surrounding rocks (e.g. Sturton and Neuberg, 2006), with a consequent slower amplitude decay testified by the Q value increase (**Fig. 5.9f;** e.g. Sturton and Neuberg, 2006).

If the resonating part of the conduit is filled with bubbly magma, a length increase would imply a shallowing of the fragmentation level, while sound speed decrease could mean an increase in gas volume fraction. On the basis of recent studies (e.g. Fee et al., 2010a) that modelled infrasound signals as due to gas filled cavities/conduits resonance, we disregard the

last hypothesis and consider the conduit portion above the magma fragmentation level as the resonating infrasound source.

Following this assumption and taking into account the intense explosive activity occurring at summit area of the SEC, we believe the idea that the frequency decrease observed at the end of the eruptive episode is more likely due to a drop in the magma column, caused by the emission of a large amount of gas-rich magma, than to an increase of CO_2 or SO_2. In support of this hypothesis is the frequency increase observed during both the pre and post-eruption phases (**Fig. 5.9e**), which could be explained by a rise of the magma column because of the oncoming eruption and a return to the pre-eruption condition, respectively.

The occurrence of such variations of the NEC events at the same time as SEC activity leads us to infer the existence of a link in the plumbing systems feeding these two craters.

5.1.6. Conclusions

The paroxysmal Etnean eruption of 16 November 2006 at SEC was investigated by a multi-parametric analysis of seismic, infrasound and video-camera recordings. The waveform characterization of infrasound events, by means of cross-correlation and spectral analyses, confirmed the existence of different vents, either contemporaneously active or switching from one to the other in the summit area of SEC. On the basis of infrasound, a gas enrichment of the shallow magma column, preceding the pyroclastic flows by a few minutes and likely causing them, was clearly inferred. Such an enrichment was probably triggered by a depressurization phenomenon. Finally, we related the source of NEC infrasound events to the acoustic resonance of the conduit portion filled with gas mixture. In light of this model, the observed spectral changes in the NEC infrasound events confirm the existence of a link in the plumbing systems feeding NEC and SEC.

The present work is an example of the ability of the joint analysis of infrasound, seismic and video-camera data to track the evolution of volcanic activity in detail, demonstrating the utility of a multi-parametric approach that could be used in any active volcanic environment.

5.2. *Modelling of North-East Crater Conduit and its Relation with the Feeding System of the 2008-2009 Eruption at Mt. Etna Inferred from Seismic and Infrasound Signals*

On 13 May 2008, an eruption started at Mt. Etna from an eruptive fissure that opened on the upper eastern flank of the volcano. During 12-13 May, 157 infrasound events, together with the related seismic transients, were collected.

Many authors have already studied this eruption, investigating the evolution of activity and magma ascent dynamics through ground deformation, magnetic variations, as well as infrasound and seismic data (Napoli et al., 2008; Aloisi et al., 2009; Cannata et al., 2009b; Di Grazia et al., 2009; Bonaccorso et al., 2011; Langer et al., 2011).

The aim of the work is to track the changes in the characteristics of seismo-acoustic events (occurring during 12 and 13 May) and to examine the links to the impending eruption. Further, infrasound source mechanism will also be investigated to acquire new insights into the shallower portion of the Mt. Etna plumbing system.

5.2.1. Volcanic framework

On 13 May 2008, a new eruption started at Mt. Etna with the opening of a system of eruptive fissures in the upper eastern flank of the volcano. Since January 2008, more evident extensions of GPS baselines, located at relatively low altitude, and the occurrence of deep earthquakes were further evidence of the volcanic system recharging (Di Grazia et al., 2009). About two months before the eruption onset there was significant deformation also at higher altitude. The seismicity increased and was located on the NE, E and S flanks of the volcano. Further, a violent explosive eruption started at about 14:00 of 10 May 2008 (all times are GMT) and was preceded and accompanied by an increase in volcanic tremor amplitude (Patanè et al., 2011). Strombolian activity took place at the vent in the lower E flank of the cone and was rapidly replaced by a lava fountain. This paroxysmal episode ceased at about 18:00 on the same day and preceded by three days the beginning of the 2008-2009 flank eruption. At 08:39 on 13 May, the occurrence of a seismic swarm, located NE of the summit craters between -1.5 and 1.5 km a.s.l. (Cannata et al., 2009b), together with significant ground deformation (Aloisi et al., 2009), heralded the ascent of magma in the shallower portion of the volcano and the impending eruption. The magma intrusion caused, at about 09:30, the

opening of an N140°E eruptive fissure extending between 3050 and 2950 m a.s.l. and fed both a lava fountain from its northern part and lava flows (Bonaccorso et al., 2011; Cannata et al., 2011a). The fissure propagated, successively, downslope to ~2650 m a.s.l. in south-eastward direction (see EF in the inset of **Fig. 5.14**), where Strombolian activity and lava effusion took place (Bonaccorso et al., 2011). A few hours later, an asymmetric graben (2300 m long) formed north of NEC, with NNW-SSE and N-S dry fractures (Bonaccorso et al., 2011; **Fig. 5.14**). The eruption continued until July 2008, with alternating periods of decrease and renewal of Strombolian activity and lava effusion (Cannata et al., 2011a). Successively, the eruption was mainly effusive and continued until 6 July 2009.

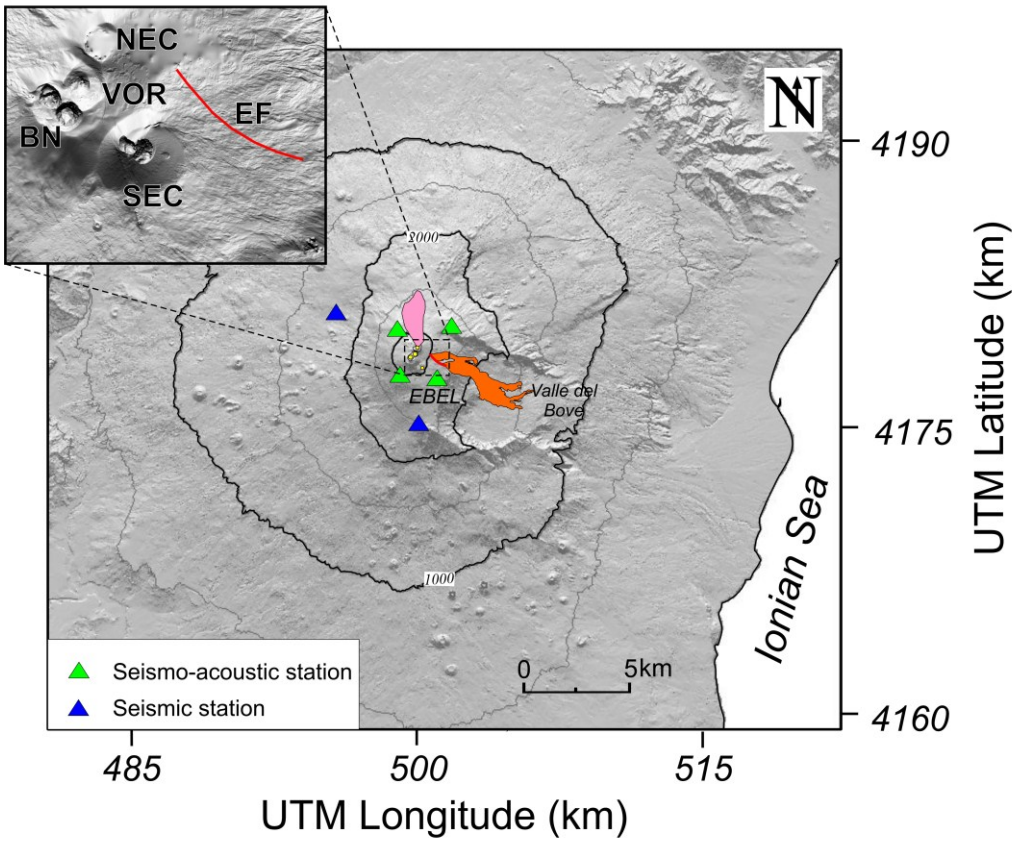

Fig. 5.14 *Digital elevation model of Mt. Etna with location of the seismo-acoustic sensor (green triangles) and the seismic stations (blue triangles) used in this work. In the upper left inset, the digital elevation model of the summit area with the four summit craters (VOR= Voragine; BN= Bocca Nuova; NEC= North-East Crater; SEC= South-East Crater) and the position of the 13 May 2008 eruptive fissure (EF red line). The pink and orange areas indicate the dry fracture field (Bonaccorso et al., 2011) and the lava flows from the 2008–2009 eruption (Behncke et al., 2009), respectively. The position of EBEL reference station is also indicated.*

5.2.2. Data acquisition

We used data from 6 seismic stations located between 1500 and 3000 m a.s.l. and 4 infrasonic stations sited around summit craters with altitude in the range ~2800-3000 m a.s.l. (**Fig. 5.14**). The stations, belonging to the permanent seismic and infrasonic networks, are run by Istituto Nazionale di Geofisica e Vulcanologia, Osservatorio Etneo - Sezione di Catania. Seismic stations are equipped with broadband (40 s cut-off period), 3-component Trillium seismometers (Nanometrics™) and infrasonic stations are equipped with Monacor condenser microphone with a sensitivity of 80 mV/Pa in the 1-20 Hz infrasound band. Seismic and infrasound signals were acquired at a sampling rate of 100 Hz.

Since Monacor microphones do not have flat response in the whole frequency range of interest, (generally 0.3-6 Hz), laboratory tests were performed on recording ambient noise at both Monacor and a G.R.A.S. 40AN microphone. The G.R.A.S. 40AN sensor shows a flat response with sensitivity of 50 mV/Pa in the frequency range 0.3-20,000 Hz, and ±3 dB in the range 0.1-0.3 Hz. Thus, on the basis of the response of G.R.A.S. sensor the "experimental" response curve of the Monacor microphone was calculated to correct the amplitude values, spectra and pseudo-spectrograms (reported further on).

5.2.3. Data analysis

To carefully investigate the volcano dynamics just a few hours before the beginning of the eruption, seismic and infrasound signals, recorded during 12-13 May 2008, were studied.

Since the deployment of the permanent infrasonic network and till 12 May 2008, during a non-eruptive period, infrasound activity consisted of amplitude transients with dominant frequency between 1 and 2.5 Hz, recorded almost continuously and related to the degassing activity of NEC (Spina et al., submitted).

The amplitude of infrasound signal recorded on 12 and 13 May (**Fig. 5.15a**) and the related RMS values gradually increased from ~20:00 on 12 May, until the onset of the eruption (9:30 on 13 May, **Fig. 5.15b**) when they sharply reached the maximum value.

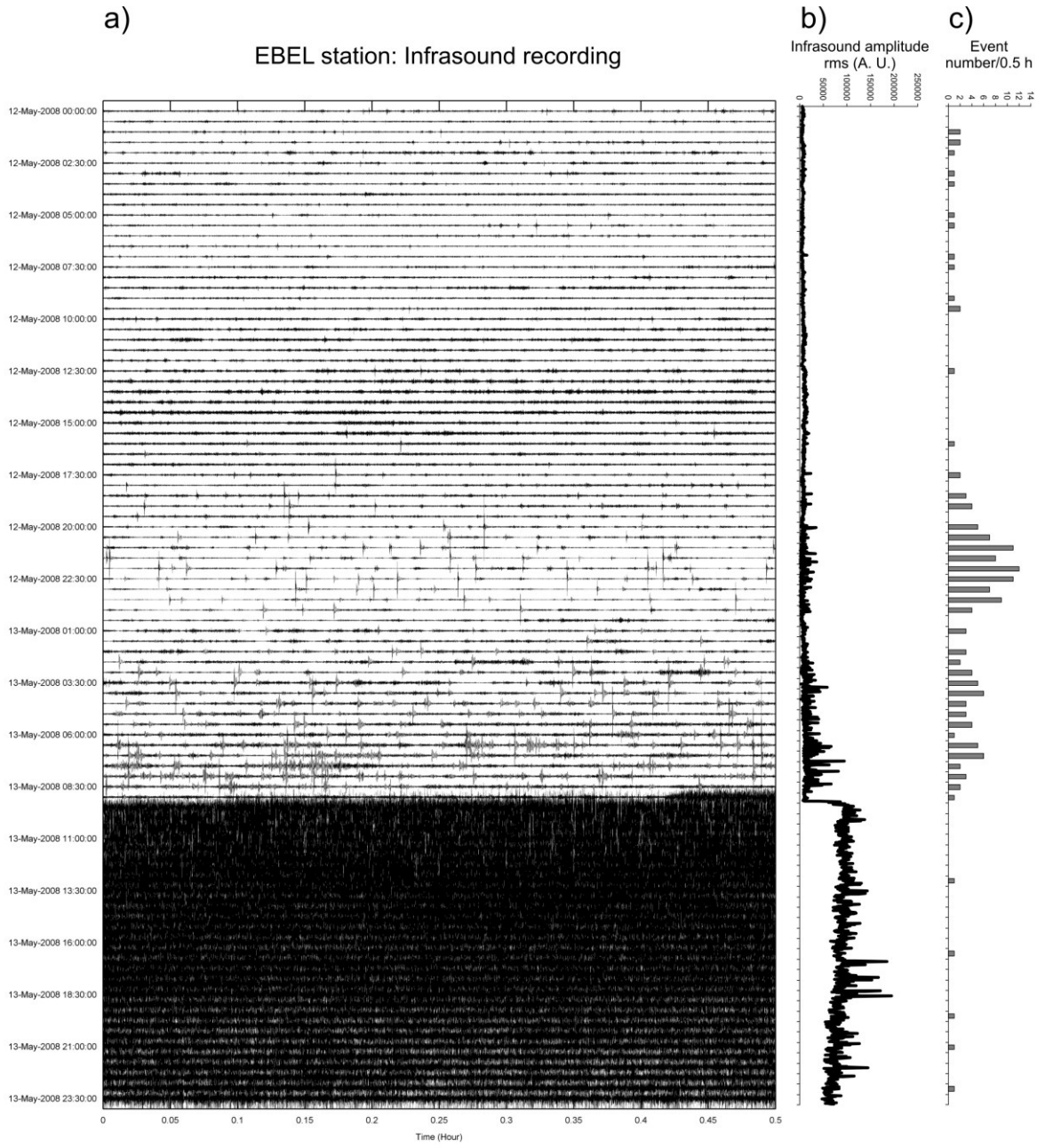

Fig. 5.15 ***(a)*** *Helicorder of infrasound signal recorded at EBEL station during 12 and 13 May 2008.* ***(b)*** *Amplitude RMS of infrasound signal recorded at EBEL station.* ***(c)*** *Time evolution of occurrence rate of infrasound events in 30-minute-long windows.*

The infrasound events were extracted by applying the STA/LTA trigger algorithm (Withers et al., 1998) on the signal recorded at EBEL (**Fig. 5.14**), the reference station in this study, since less affected by noise. On the basis of the infrasound event features, we fixed the short and the long window of trigger algorithm equal to 0.6 s and 6 s, respectively, and filtered the signal in the frequency band 0.2-2 Hz, thus detecting 157 events. We evaluated the time evolution of the occurrence rate (**Fig. 5.15c**) by tallying the number of infrasound events in a 30-minute-long window. The occurrence rate showed a maximum around 22:00 on 12 May (13 events

per 30 minutes), whereas it underwent a slight decrease in the hours preceding the onset of the eruption, partly due to the higher background signal level. Such infrasound events lasted 10-15 s and were characterized by an impulsive and energetic first pulse followed by decaying sinusoidal oscillations (**Fig. 5.16**).

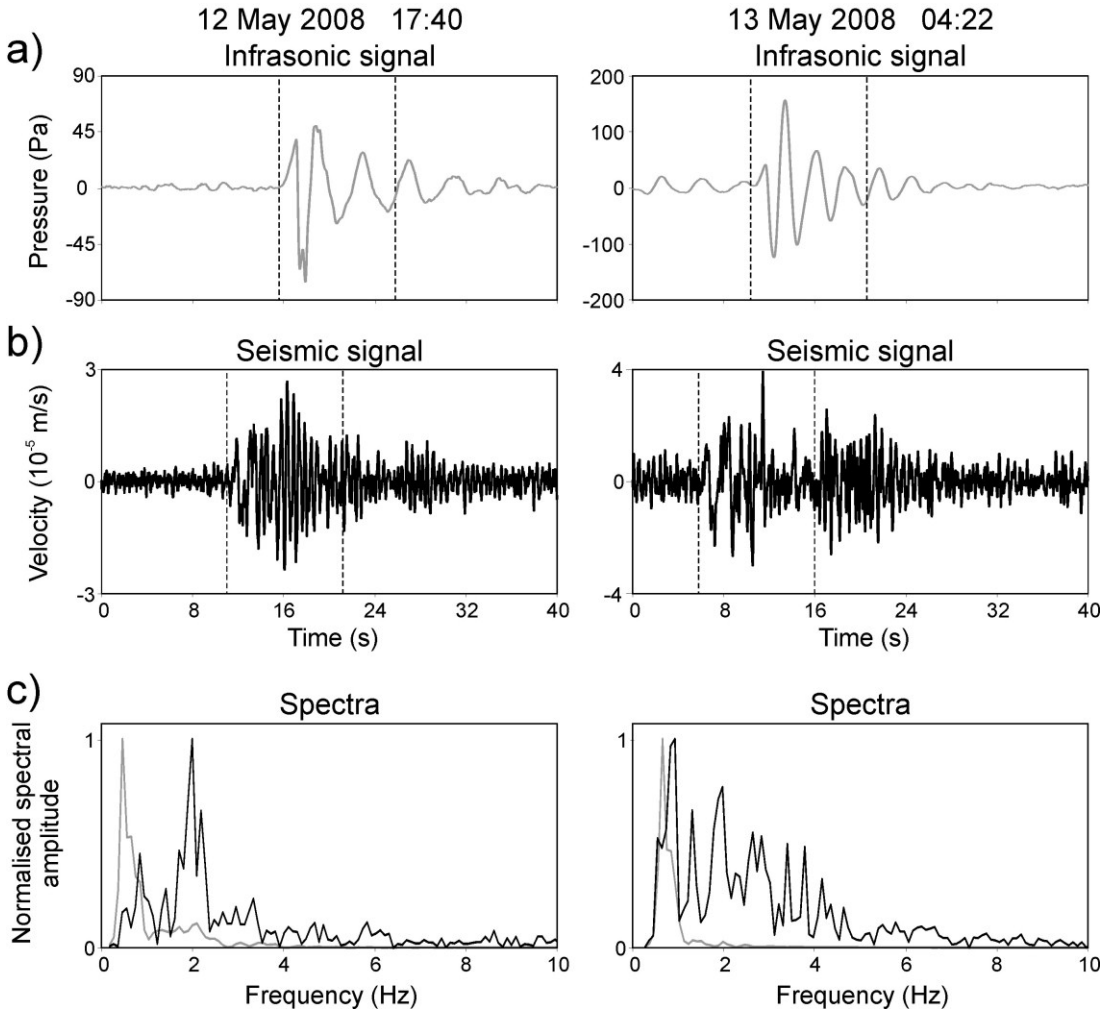

Fig. 5.16 ***(a)*** *Infrasound and* ***(b)*** *vertical seismic components of two seismo-infrasonic events recorded by EBEL station, and* ***(c)*** *corresponding spectra, calculated on the signal windows comprised between the dashed vertical lines in* ***(a, b)****. The grey and black lines in* ***(c)*** *indicate the spectra of the infrasound and seismic signals, respectively.*

We analyzed such events in the frequency domain, and visualized the time evolution of the spectral content by means of the pseudo-spectrogram (**Fig. 5.17a**). It is made up of 48 spectra, each of which was obtained averaging the spectra (calculated by applying FFT on roughly 5-s-long windows) of the events occurring during 1-hour-long time spans. The white areas in the pseudo-spectrogram represent time spans with complete or almost complete lack of events. Indeed, to be drawn, each column of the pseudo-spectrogram needs at least one event occurring in each of the two contiguous 1-hour-long windows.

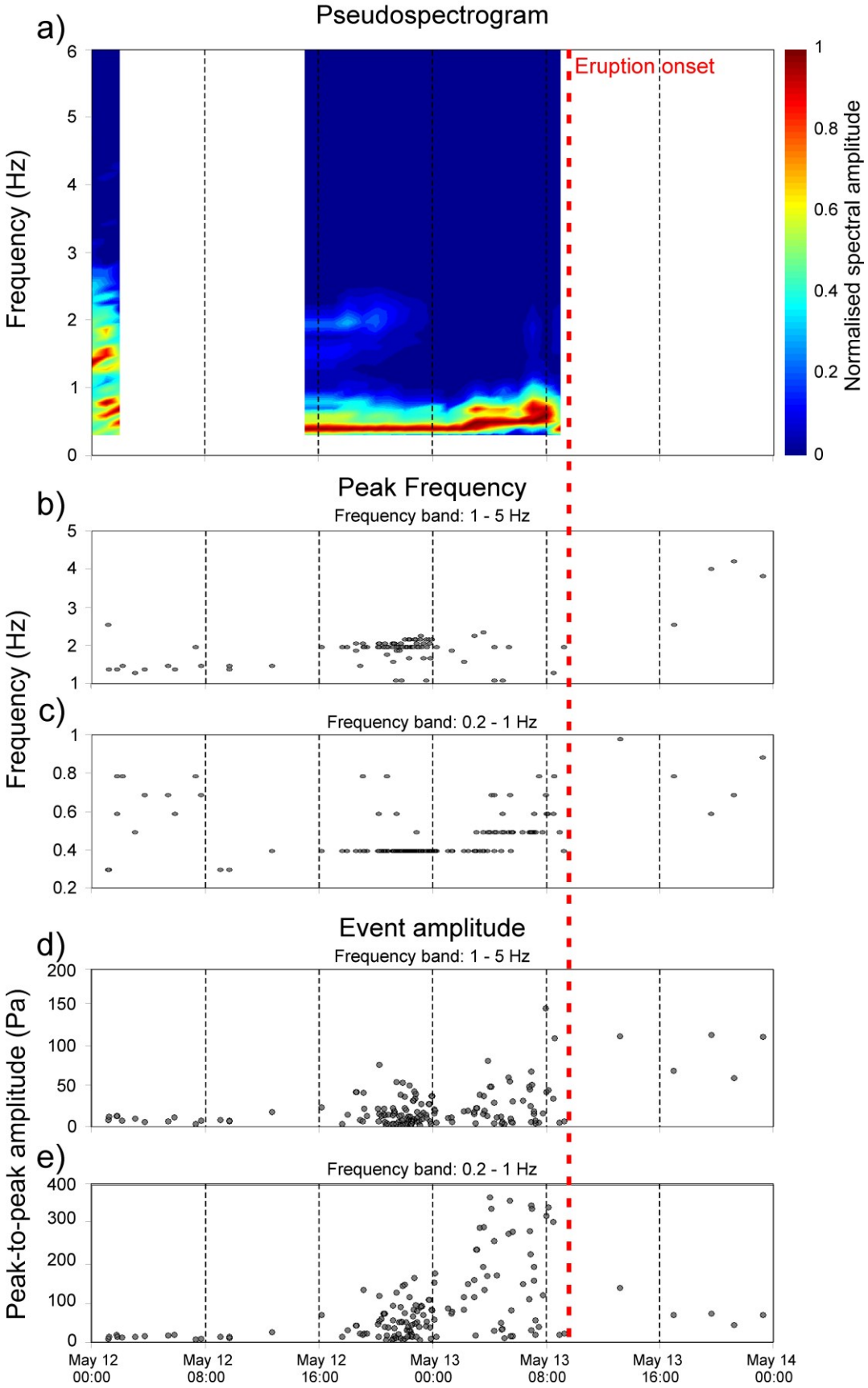

Fig. 5.17 *Analyses of 157 infrasound events.* ***(a)*** *Pseudospectrogram made up of 48 spectra of infrasound events recorded at EBEL station.* ***(b, c)*** *Temporal evolution of peak frequencies*

calculated into the frequency bands 1-5 Hz and 0.2-1 Hz, respectively. ***(d, e)*** *Peak-to-peak amplitudes evaluated into the frequency bands 1-5 Hz and 0.2-1 Hz, respectively.*

The pseudo-spectrogram highlighted how the infrasound events radiated energy mostly in the frequency band 0.4-2.5 Hz. In particular, two spectral peaks were dominant in the frequency bands 0.4-0.7 and 1.5-2.0 Hz. The main temporal variations are the frequency increase of the higher spectral peak and the coincident appearing of the lower frequency peak roughly at 16:00 on 12 May. A slight frequency increase of the lower spectral peak occurred a few hours before the onset of the eruption.

To better investigate these two frequency bands and their temporal variations, by using a 10s-long signal window we calculated the dominant peak frequencies separately in two frequency bands: 0.2-1 and 1-5 Hz. Analysing the higher band, we noticed that the peak frequency gradually increased from 1.5 to about 2.0 Hz during 12 May, while on 13 May it remained fairly steady until the onset of the eruption (**Fig. 5.17b**). The lower band exhibited an increase in the peak frequency from 0.4 to 0.7 Hz from 00:00 on 13 May to the onset of the eruption (**Fig. 5.17c**). Moreover, for the infrasound event characterization we estimated the peak-to-peak amplitudes in both the spectral bands. From 13 May the peak-to-peak amplitudes showed a gradually increasing trend, which was more pronounced for the lower frequency band (**Fig. 5.17d, e**).

While in most cases NEC events lacked any seismic counterpart or were accompanied by very weak seismic signals (Spina et al., submitted), clear long-period seismic events are associated with the NEC events preceding the eruption (**Fig. 5.16**). It is noteworthy that a few infrasound events with the associated seismic events had also been recorded in the hours preceding the lava fountain on 10 May 2008. They exhibited similar frequency content but lower peak-to-peak amplitudes.

Figure 5.18a, **b** shows an example of an infrasound event of 13 May with the coupled seismic one (raw traces). Both the events exhibit similar spectral content, especially at low frequency (< 1 Hz; **Fig. 5.18c**, **d**).

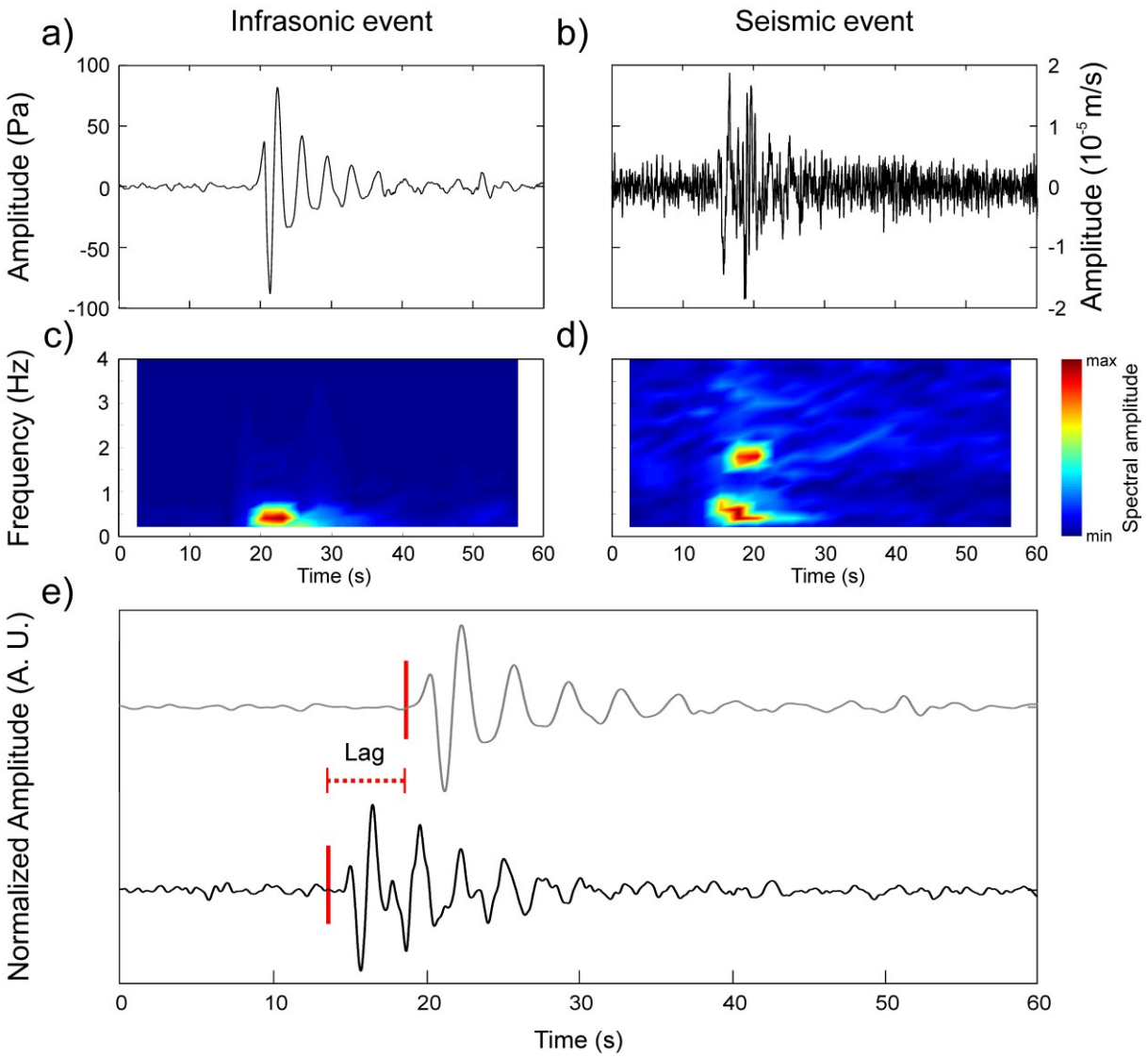

Fig. 5.18 *Example of infrasound event* ***(a)*** *and the associated seismic trace* ***(b)*** *recorded at EBEL station.* ***(c, d)*** *Short Time Fourier Transform (STFT), calculated on 5.12-second-long windows, of infrasound and seismic event, respectively.* ***(e)*** *Low-pass filtered traces (<1 Hz) of infrasound (grey) and seismic (black) signal, and the time lag between the two events.*

All the four stations were used to locate the infrasound event source by applying a composite method based on semblance and brightness functions (see **section 3.4.1**) on a grid of 6x6 km^2 with spacing between nodes of 50 m. **Figures 5.19a, b** and **5.20a** show how the locations are well aligned along the NEC coordinates (red dotted lines in **Fig. 5.19**) for the whole period.

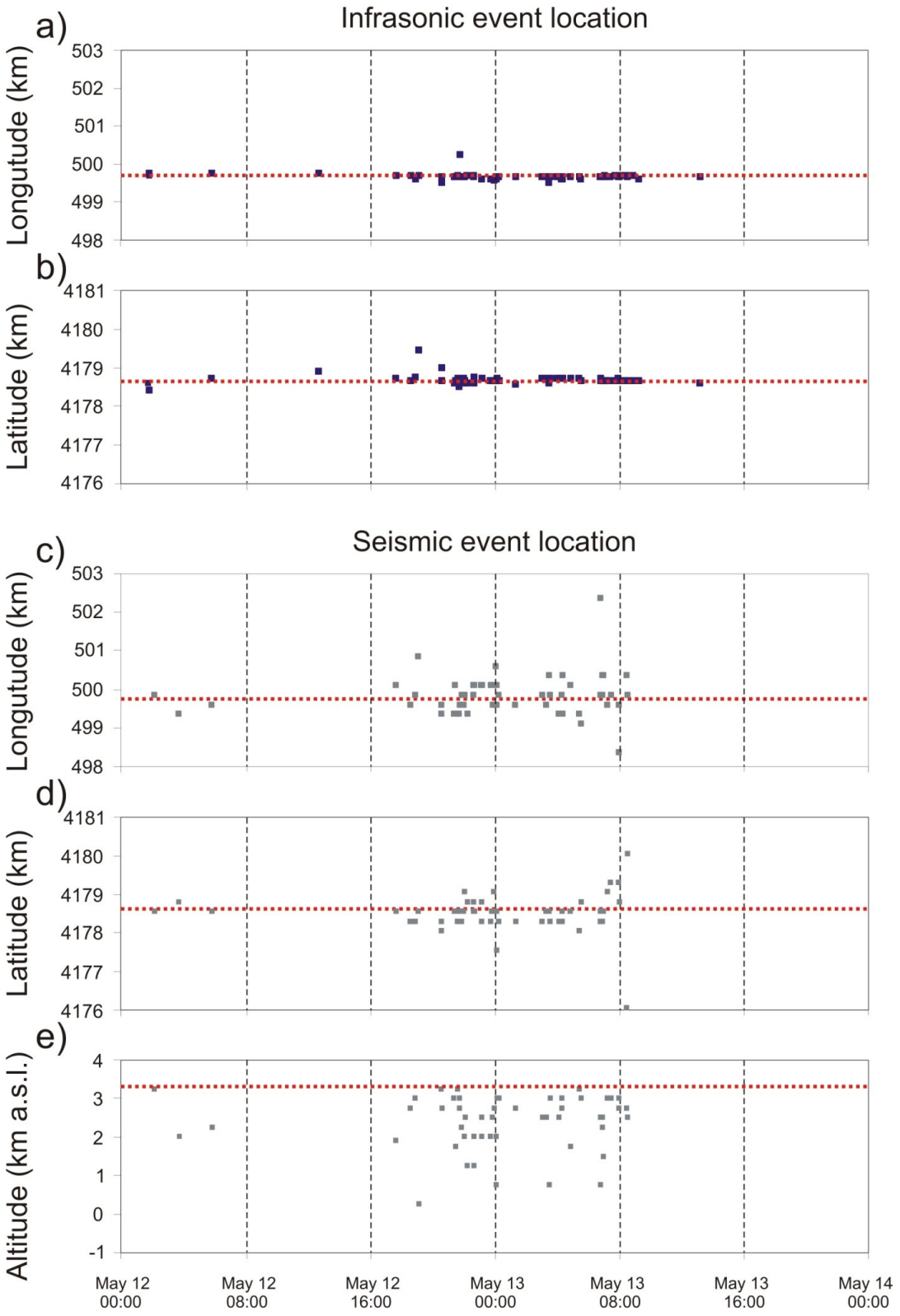

Fig. 5.19 *Locations of infrasound* ***(a, b)*** *and seismic* ***(c-e)*** *events plotted as a function of time. Red dotted line indicates NEC coordinates.*

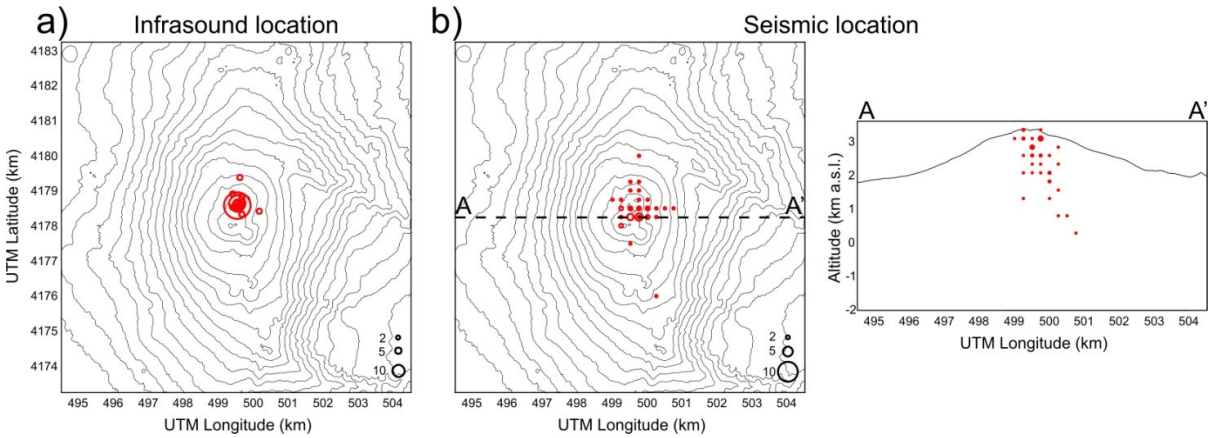

Fig. 5.20 ***(a)*** *Map of Mt. Etna with the source locations of the infrasound events, indicated by red circles.* ***(b, c)*** *Map and section of Mt. Etna with the source locations of the seismic events, indicated by red circles. The radii of the circles in* ***(a, b)*** *are proportional to the number of the locations in each grid node (see symbol legend in the lower right corner of the maps).*

Moreover, we located the seismic events associated with the infrasound ones. We performed the location analysis by using the composite method based on semblance function and R^2 value described in **section 3.4.3** using a grid of 6x6x4 km^3 with spacing of 250 m. 54 seismic events were located (see **Figs 5.19c-e** and **5.20b**). Similarly to the infrasound events, the seismic events are roughly located below NEC and did not exhibit significant time variations. It is also evident how the seismic locations are more scattered than the infrasound ones (**Fig. 5.19**). This is mainly due to the lower velocity of infrasound waves, with respect to the seismic ones, and the simpler velocity structure of the atmosphere (which can generally be considered homogeneous for short propagation distances) than the volcano edifice velocity structure (Johnson, 2005). Thanks to these differences, the infrasound source locations have higher resolution than the seismic ones. This is also clearly evidenced in **Figure 5.21**, showing the space distribution of semblance-brightness and semblance-R^2 of the infrasound and seismic components, respectively, of a selected seismo-infrasonic event.

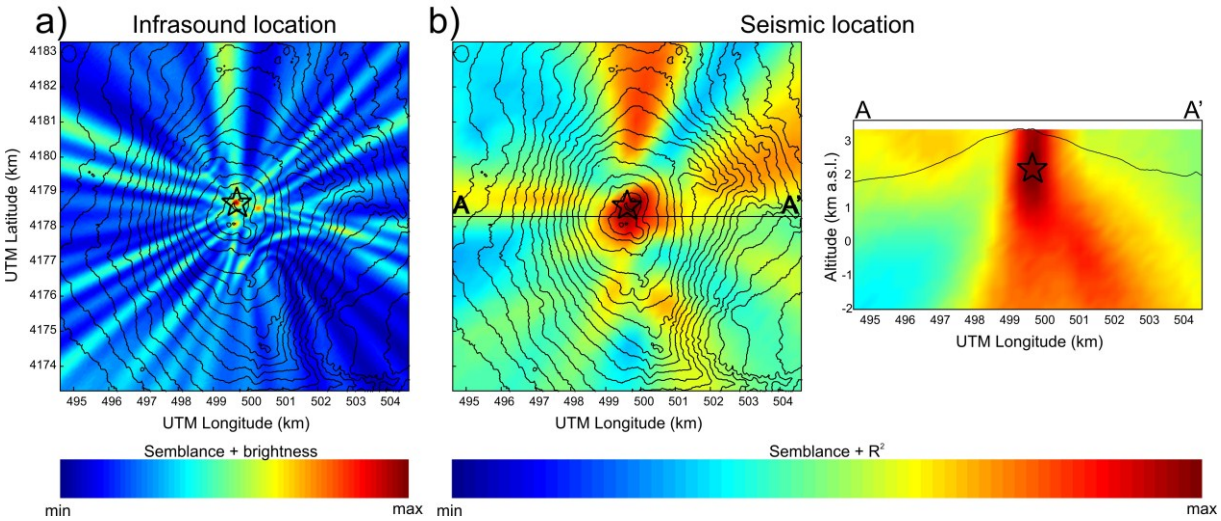

Fig. 5.21 ***(a)*** *Map of Mt. Etna showing an example of the space distribution of semblance-brightness values.* ***(b)*** *Map and section of Mt. Etna showing an example of the space distribution of semblance-R^2 values. The stars indicate the grid node with the largest semblance-brightness value* ***(a)*** *and semblance-R^2 value* ***(b)****, respectively, for the selected seismo-acoustic event.*

Unlike the semblance-brightness distribution, exhibiting a very narrow area with high values, the semblance-R^2 distribution highlights a much larger high-value volume, and then a less resolved source location.

The comparison between the seismic and infrasonic traces (filtered in the band 0.2-1 Hz) in **Figure 5.18e** highlights the similarity of their waveforms and their time lag. On the basis of the seismic-infrasonic lag several authors estimated the source depth (e.g., Ripepe and Braun, 1994; Ripepe et al., 2001a; Gresta et al., 2004; Petersen and McNutt, 2007). In the matter of small variations of the lag, they can give information about the changes in source location and propagation medium properties (e.g. Kobayashi et al., 2005). To this end, we evaluated the temporal evolution of the lag at station EBEL as described in **section 3.5.2**. We chose 4-second-long windows, a window shift step of 0.05 s and a cross-correlation coefficient threshold of 0.7. The results are shown in **Figure 5.22** (orange dots). Following this procedure we were able to calculate the lag only for ~30 events of the whole dataset due to the high level of volcanic tremor affecting the seismic recordings. To overcome this drawback, we measured the lag between the rest of the events by picking the onset of infrasound and seismic events and we found the lag values shown in **Figure 5.22** (blue dots).

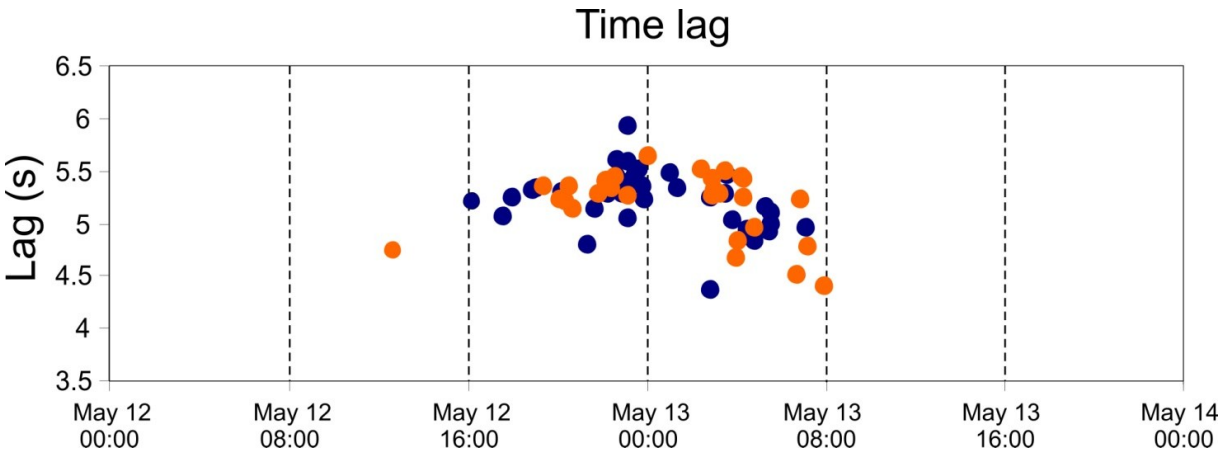

Fig. 5.22 *Temporal evolution of the time lag between infrasound traces and the associated seismic ones using cross-correlation function (orange dots) and a manual procedure (blue dots) (see text for details).*

The results obtained by the two procedures were comparable and highlighted a decreasing trend in the lag a few hours preceding the eruption. In particular, the average lag is equal to 5.4 s before 03:00 on 13 May, reaching an average value of 4.7 s a few hours before the beginning of the eruption.

5.2.4. NEC conduit model

NEC is the most active crater of Mt. Etna from the acoustic point of view, whereas it exhibited almost no eruptive activity in the last decade. Infrasound activity has been continuously recorded since the installation of the permanent network in 2006 even during non-eruptive periods. There is no visible eruptive activity at NEC during the occurrence of infrasound events. Since NEC infrasound events show coda composed of regularly decaying sinusoidal waveforms and sometimes harmonics (Cannata et al., 2009b; Spina et al., submitted), resonance mechanisms are considered more appropriate than other models such as a Strombolian bubble vibration model. On the other hand, no unambiguously detectable infrasound associated to explosive sources, was recognized (**Fig. 5.16**). Sources related to degassing processes close to the free magma surface are likely to excite the resonance phenomena, as already hypothesised by other authors to explain resonance triggering processes (e.g. Garces and McNutt, 1997; Fee et al., 2010a).

Thus, information on conduit geometry and physical properties of the fluid filling the conduit can be inferred. We hypothesized a portion of the NEC conduit behaving as a pipe resonator. Similarly to other authors (e.g. Petersen and McNutt, 2007; Fee et al., 2010a), we considered as the resonating portion of the conduit the one above the free magma surface, filled with a

gas-mixture. The interface between the gas-mixture and the magma column acts as a closed termination due to the impedance contrast between the two phases. As regarding the upper end of the pipe resonator, NEC morphology should be taken into consideration.

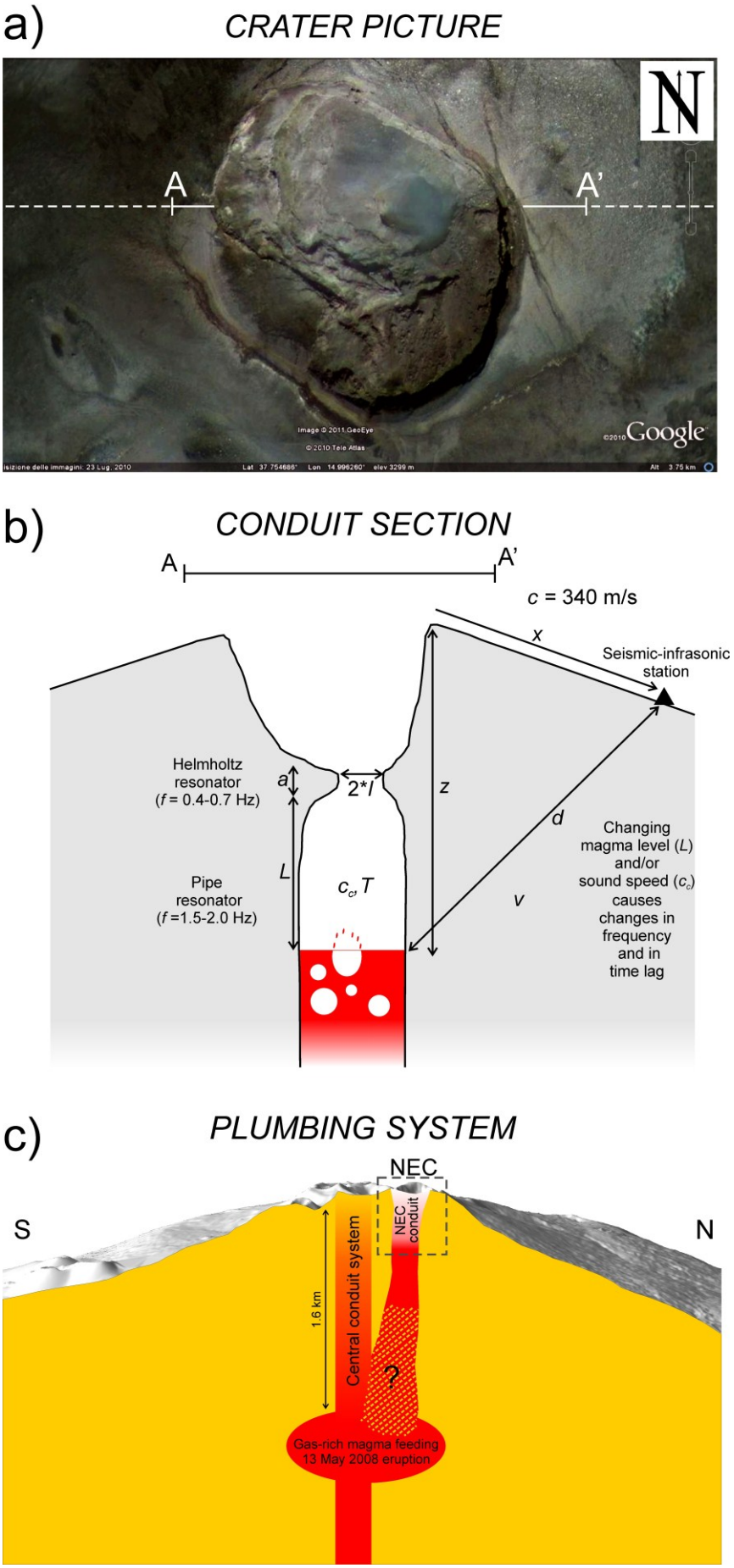
a)
CRATER PICTURE
N
A
A'
Image © 2011 GeoEye
© 2010 Tele Atlas
©2010 Google
b)
CONDUIT SECTION
A
A'
c = 340 m/s
x
Seismic-infrasonic station
Helmholtz resonator (f = 0.4-0.7 Hz)
a
2*l
z
d
Changing magma level (L) and/or sound speed (c_c) causes changes in frequency and in time lag
L
Pipe resonator (f =1.5-2.0 Hz)
c_c, T
v
c)
PLUMBING SYSTEM
NEC
S
N
NEC conduit
1.6 km
Central conduit system
?
Gas-rich magma feeding 13 May 2008 eruption

Fig. 5.23 ***(a)*** *Picture of NEC (viewed by GoogleEarth) where the upper part of the conduit is visible at the bottom of the funnel-shaped crater.* ***(b)*** *Section showing the model of NEC conduit. Higher frequencies of infrasound events are generated by the pipe resonance of the conduit. Further, the inferred narrowing in the upper part of the conduit makes possible Helmholtz resonance, which is responsible of the lower frequencies. All the letters reported inside the sketch indicate different physical parameters (see* ***equations 3.19****,* ***2.3****, and* ***2.10****).* ***(c)*** *Cartoon showing a S-N section of Mt. Etna volcano with the central conduit system through which the gas-rich magma, feeding the 2008-2009 eruption, initially rose and then broke off to the east. The link between the NEC conduit and the reservoir with the gas-rich magma (located at depth of 1.6 km; Bonaccorso et al., 2011), proposed in this work, is also reported. The dashed area and the question mark highlight the unknown depth of the link between NEC conduit and the central conduit system.*

NEC shows a funnel-shaped crater at the bottom of which the upper part of the conduit is open and clearly visible (**Fig. 5.23a**). Nevertheless, the lack of an obstruction does not imply that it is an acoustically opened termination, as observed by several authors (e.g. Garces and McNutt, 1997; De Angelis and McNutt, 2007). Analyses of NEC infrasound events (Spina et al., submitted), recorded during the whole period 2007-2009, highlighted the presence of integer harmonics of the fundamental mode. Spectra with integer harmonics can be modeled by a closed-closed (or open-open) pipe resonator. For this reason, assuming that the bottom end is a closed termination, the upper end of the resonating conduit should be a closed termination, too. The parameter, which the behavior of the termination depends on (closed or open), is the impedance contrast, that is function of cross-sectional area variations (if any) of the termination and changes in fluid properties (Garces and McNutt, 1997). Therefore, if the impedance contrast in the upper end of the conduit is high, for instance due to a narrowing, this could make the termination closed. In light of this, the little hole (with respect to the crater dimension) at the bottom of the crater could be the opening of the narrowing (**Fig. 5.23b**). Because of the small dimension of the conduit radius with respect to the observed infrasound wavelengths, only longitudinal modes were taken into account (Garces and McNutt, 1997). By means of the **equation 2.3,** introduced in **section 2.3.1,** and taking into account a wide range of values for both c_c and L, we calculated the theoretical frequencies. As aforementioned, the higher frequency peak of infrasound events ranges in the frequency band 1.5-2.0 Hz. **Figure 5.24** shows the range of variation of c_c and L for the frequency values observed.

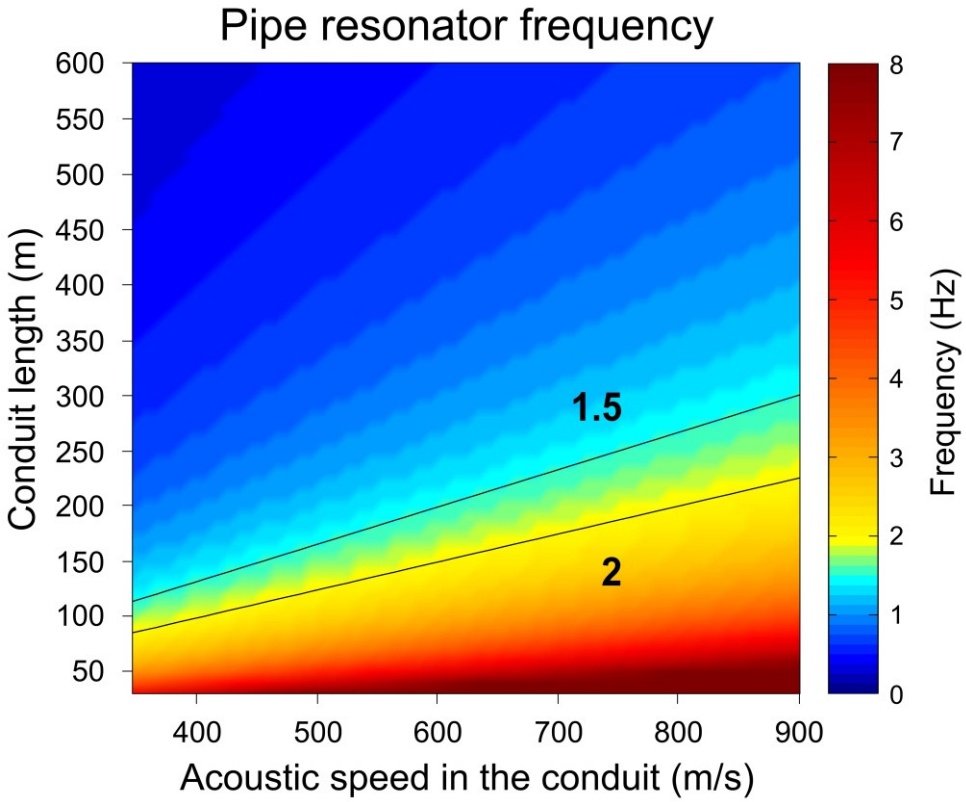

Fig. 5.24 *Variation of theoretical frequency (visualized with the colour scale), obtained by applying the pipe resonator model (**equation 2.3**), as a function of conduit length and acoustic speed in the conduit. Values of the higher frequency peaks observed during the analyzed period are plotted by black contours on the graph.*

For the purpose of the modeling, the acoustic speed in the conduit was constrained as argumented in **section 2.2.** Therefore, applying **equation 2.1**, we obtained an acoustic speed ranging between 400 and 750 m/s. We took into consideration the time interval in which infrasound events were characterized by both the higher and lower frequency components (16:00-24:00 of 12 May; **Fig. 5.17a**). Therefore, taking into account the above calculated range of acoustic speed and the observed higher frequency peak in this time interval (2 Hz), the length of the resonating conduit portion ranges roughly between 100 and 200 m (**Fig. 5.24**).

As aforementioned, infrasound events recorded during 13 May also contain a lower frequency band at 0.4-0.7 Hz. In this case, since the wavelength (~820-1430 m, with an acoustic speed of 575 m/s, the mean value of the aforementioned c_c range) is much longer than the dimension of the conduit, we modeled this lower frequency band as due to a Helmholtz resonance. We consider the conduit as the rigid walled cavity and the narrowing in its upper part acting as a neck (**Fig. 5.23b**).

Most of the parameters, which the Helmholtz resonator frequency depends on (**equation 2.10**), are unknown. We only have a measure of the neck radius, estimated as equal to 15 m. First, we calculated the Helmholtz resonator theoretical frequencies fixing the acoustic speed in the conduit and the conduit length (575 m/s and 150 m, respectively), but systematically changing both neck length and conduit radius. Results are shown in **Figure 5.25**, which demonstrates that the frequency variation is more influenced by the conduit radius with respect to the neck length.

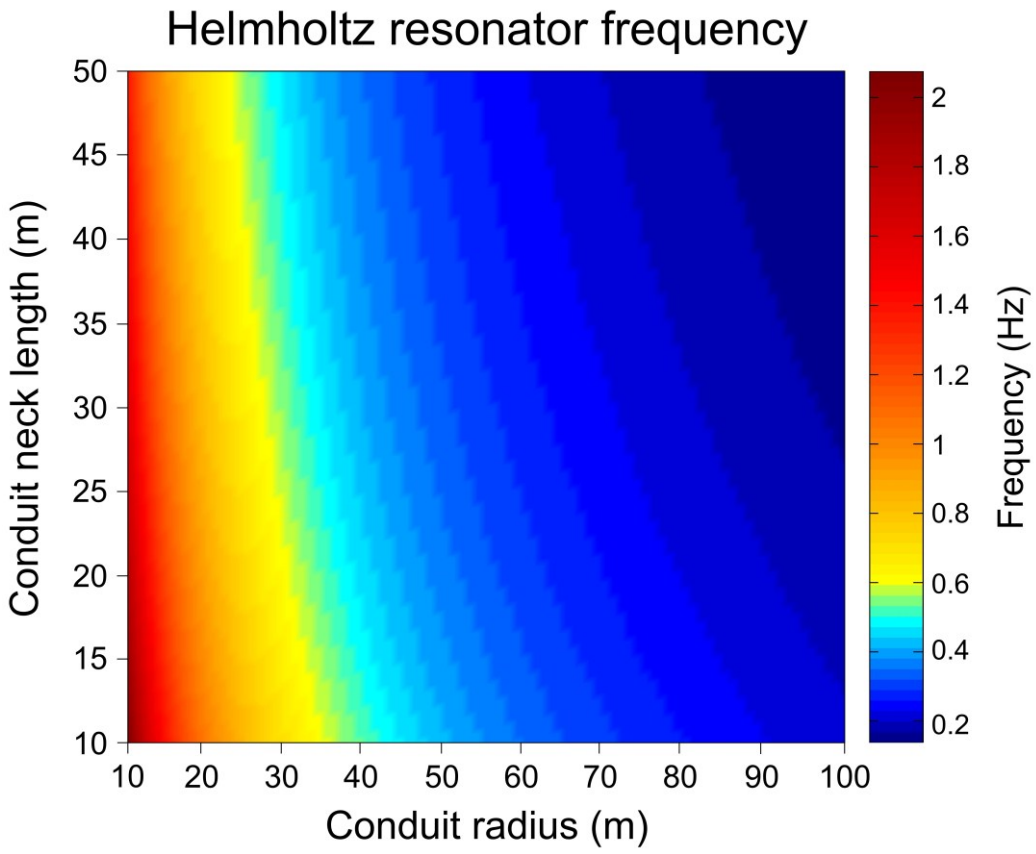

Fig. 5.25 *Variation of theoretical frequency (visualized with the colour scale), obtained by Helmholtz resonator model (**equation 2.10**), as a function of the conduit neck length and conduit radius.*

In consequence of this, the next step was the attempt to estimate the conduit radius. As aforementioned, the higher spectral peak observed on 12 May between 16:00 and 24:00, modeled as a pipe resonator frequency, led us to obtain a range of probable conduit length of 100-200 m. On the basis of this observation, we applied the Helmholtz resonator model to the lower frequency peak (0.4 Hz), observed during the same interval (16:00-24:00 on 12 May). Therefore, we solved the **equation 2.10** for the conduit radius and, fixing S and l at ~700 m^2 and 15 m, respectively, obtained a range of values (25-75 m) in function of the inferred

conduit length and acoustic speed. Successively, we performed the calculation for the following period (00:00-08:00 on 13 May), where the frequency peak reached 0.7 Hz, obtaining a radius ranging from 15 to 45 m. The overlap between these value intervals (25-75 m and 15-45 m) is 25-45 m and should represent a reasonable range for the conduit radius. Bonaccorso and Davis (1999; and references therein) assumed a radius of 25 m to model the ground deformation for an explosive eruption occurring in December 1995 at NEC.

Therefore, on the basis of our interpretation of the NEC events, both the spectral components of which they are made are due to propagation effect (the lower and the higher ones to Helmholtz and pipe resonances, respectively). The source likely triggering the resonance (releases of gas at the free magma surface) does not generate clear infrasound signals. In the proposed model the upper end of the pipe resonator is considered closed because of the conduit narrowing. Such a narrowing, equal to ~10-35% of the conduit section (considering conduit radius of 45-25 m, respectively), allows the atmosphere coupling and the infrasound radiation. The portion of acoustic energy transmitted and reflected through the narrowing can be quantified by estimating the power transmission (T_p) and reflection (R_p) coefficients (Raichel, 2006):

$$T_p = \frac{4}{4\cos^2 ka + \left(\frac{S}{A} + \frac{A}{S}\right)^2 \sin^2 ka} \tag{5.1}$$

$$R_p = 1 - T_p \tag{5.2}$$

where k is the wave number which equals to $2\pi/\lambda$ (λ is the wavelength), A is the cross-sectional area of the conduit. Such coefficients range from 0 to 1 and depend on the neck length, the ratio between the cross-sectional areas of the conduit and the narrowing, as well as on the acoustic frequency. In **Figure 5.26** the variation of T_p and R_p with frequency, assuming c_c equal to 575 m/s and conduit radius of 25 and 45 m (**Fig. 5.26a**, **b**, respectively), is plotted.

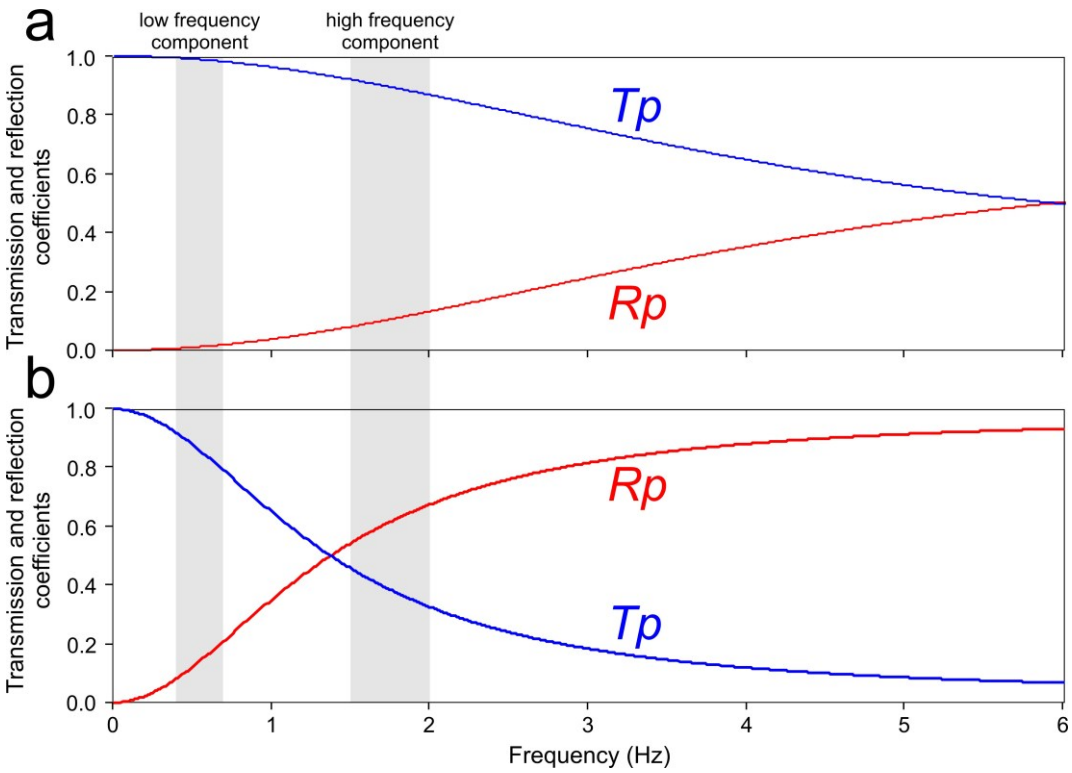

Fig. 5.26 *Frequency dependence of power transmission (T_p blue lines) and reflection (R_p red lines) coefficients through the narrowing, assuming a conduit radius of 25* ***(a)*** *and 45* ***(b)*** *m. The grey areas highlight the two frequency components characterising NEC events during the studied period. See text for details.*

It can be noted how at the NEC event frequencies a good amount of acoustic energy is transmitted through the narrowing. Further, since the transmission coefficient decreases with increasing frequency, such a structure behaves as a low-pass filter. Perhaps for this reason, we can only sometimes record the harmonics of the pipe resonance.

Figure 5.27 shows the relationship between Helmholtz / pipe resonance frequency peaks and the conduit length assuming a fixed c_c value of 575 m/s.

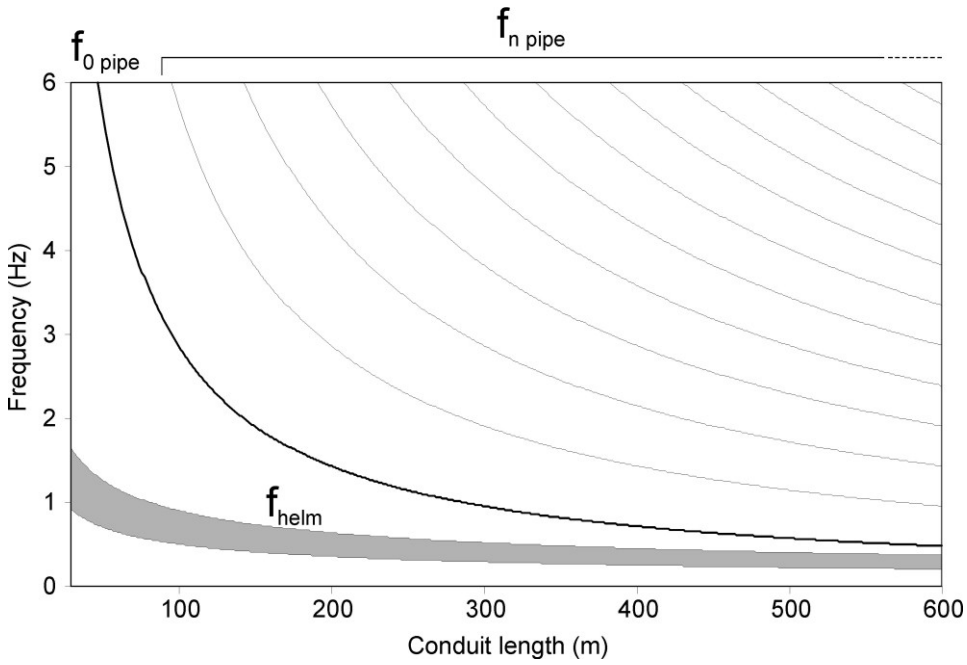

Fig. 5.27 *Conduit length dependence of frequency of Helmholtz resonator frequency (f_{helm}, grey area) and of fundamental frequency (f_0 pipe, black thick line) and harmonics (f_n pipe, black narrow line) for closed-closed pipe resonator. In particular, the upper and the lower limits of the grey area represents the conduit length dependence of frequency of Helmholtz resonator in case of conduit radius of 25 and 45 m, respectively. See text for details.*

As above described, in the proposed model a conduit portion works contemporaneously as a Helmholtz cavity and a closed-closed pipe, to explain the coexistence of two spectral components. A well-known natural system can behave in a similar way: the vocal tract. Indeed, in the case of the vowel "i" the jaw and the tongue body are raised, creating a narrow front cavity, and the tongue body is moved forward, enlarging the back cavity (e.g. Diehl, 2008). Therefore, this configuration, with a constriction in the middle, gives rise to two cavities: the front cavity behaving as a open-closed pipe, and the back cavity as both closed-closed pipe and Helmholtz resonator (e.g. Johnson, 1997; Diehl, 2008). The coexistence of the three resonance peaks creates the vowel "i" spectrum.

Successively, we analyzed temporal variations of seismo-infrasonic event features, taking place during the 12 hours before the eruption beginning. During this time interval the higher frequency component of infrasound events disappeared, hence we focused on the frequency increase of the lower peak (**Fig. 5.17a, c**) and on the decrease of the time lag between seismic and infrasound events (**Fig. 5.22**). We applied the Helmholtz resonator model, using for the conduit radius the mean value of the aforementioned range (25-45 m), and calculated the theoretical frequencies in function of L and c_c. **Figure 5.28** shows that both decrease of L and/or increase of c_c can be responsible for the observed frequency increase (from 0.4 to 0.7 Hz).

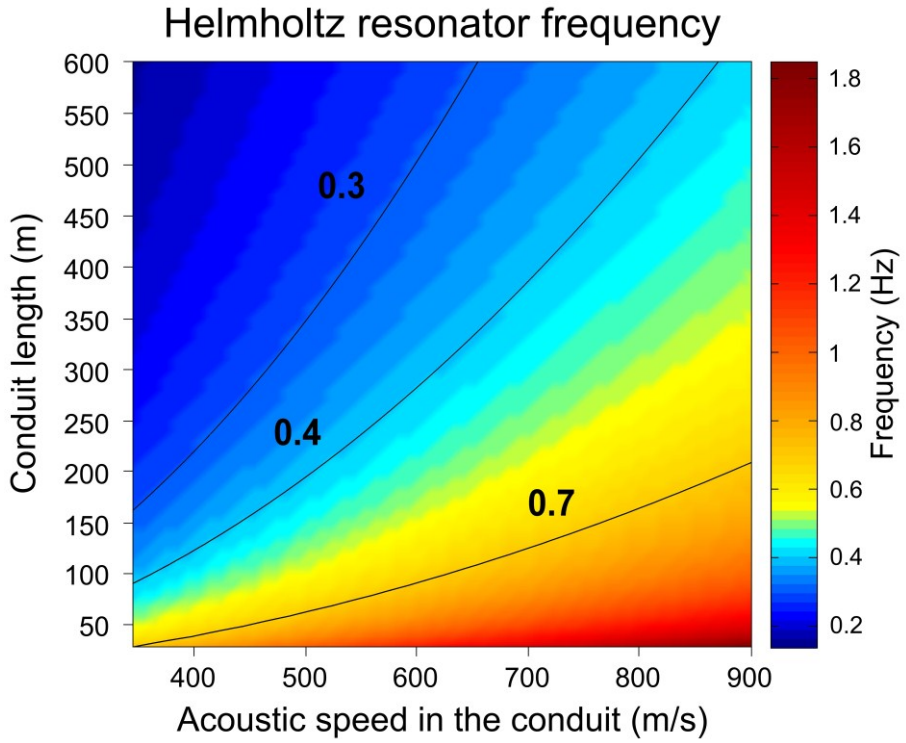

Fig. 5.28 *Variation of theoretical frequency (visualized with the colour scale), obtained by applying the Helmholtz resonator model (**equation 2.10**), as a function of conduit length and acoustic speed in the conduit. Values of the lower frequency peaks observed during 12 May (0.4 Hz) and before the eruption beginning on 13 May (0.7 Hz) are plotted by black contours on the graph, together with 0.3 Hz value. See text for details.*

We tend to discard the lower values of the range of c_c shown in **Figure 5.28** because they imply such low conduit length values (down to 30 m) that, assuming the conduit radius comprised between 25 and 45 m, pipe resonance could not be plausible.

As addressed in **section 3.5.2** the lag between seismic and infrasound events and its temporal variation have been used in literature to determine the depth of the source triggering the resonance (e.g. Ripepe and Braun, 1994; Ripepe et al., 2001a; Gresta et al., 2004; Petersen and McNutt, 2007).

The similarity between the waveform and spectral contents of seismic and infrasound signals suggest a common source (e.g. Ripepe et al., 1996; Matoza et al., 2010). These features makes more reasonable the model with co-located seismic-infrasound sources. In order to investigate the time lag decrease from 5.4 to 4.7 s, occurring between 00:00 and 08:00 on 13 May, we used the approach of Petersen and McNutt (2007) (**Fig. 3.9** in **section 3.5.2**).

Considering the seismo-infrasound events recorded at station EBEL, located ~2000 m far from NEC, we calculated the theoretical time lags changing systematically source altitude (z), c_c values and v (**Fig. 5.29**).

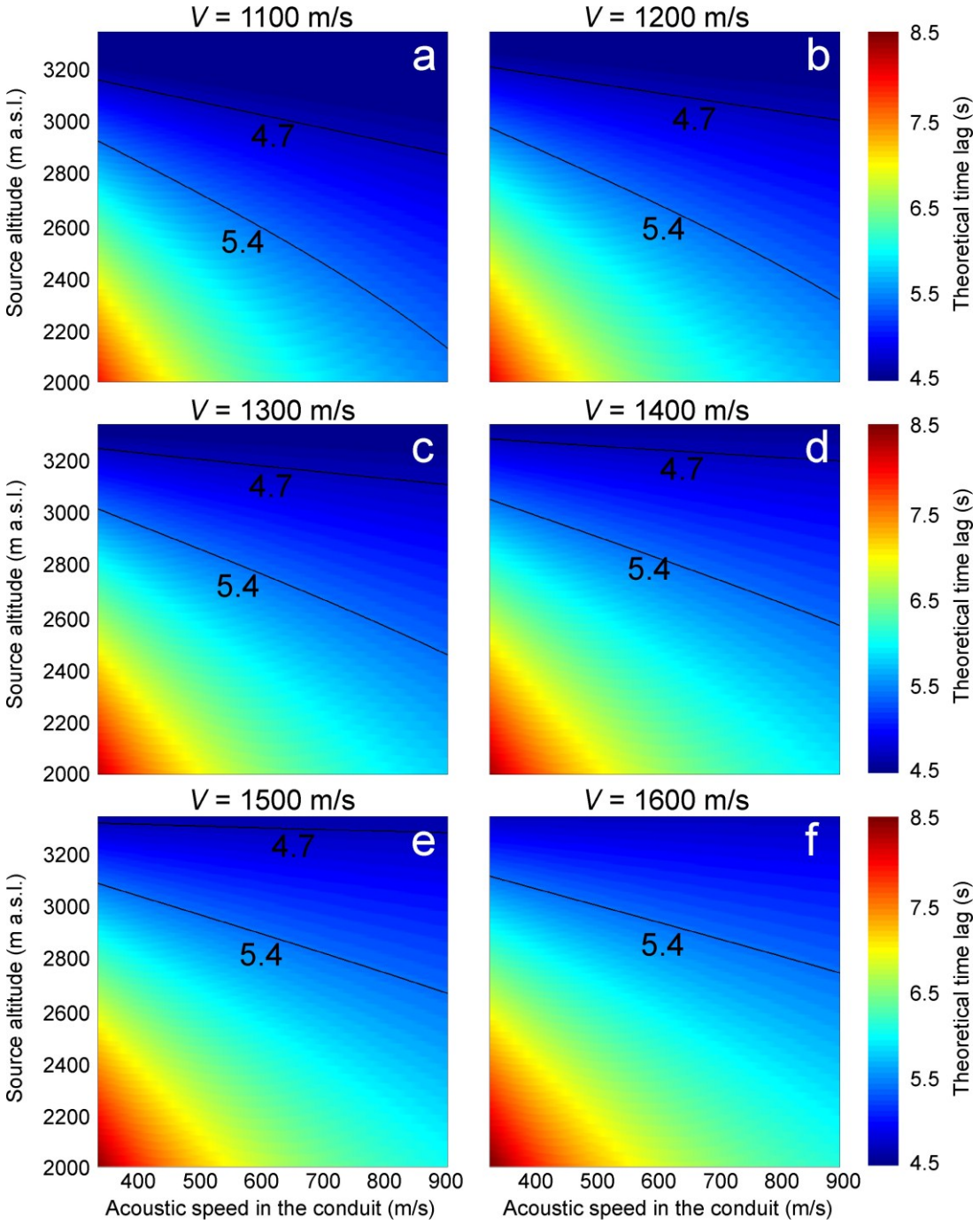

Fig. 5.29 *Variation of theoretical time lag (visualized with the colour scale), obtained by means of* ***equation 3.19****, as a function of source altitude, acoustic speed in the conduit and seismic velocity (v). Values of time lag observed during 12 May (5.4 s) and before the eruption beginning on 13 May (4.7 s) are plotted by black contours on the graph.*

First of all, it was noted how the maximum seismic velocity, on the basis of which a seismic-infrasonic time lag of 4.7 s can be obtained, is ~1500 m/s. Indeed, the contour line representing 4.7 s disappeared in **Figure 5.29f**. Because of the expected shallowness of the seismic-infrasonic sources in this study, we cannot use results from tomographic studies at

Mt. Etna to constrain the seismic velocity. In any case, the obtained seismic velocity upper limit (~1500 m/s) is in agreement with the evidences of near-surface (few hundred meters) low seismic velocities common in volcanic environments, reported in many papers (e.g. Saccorotti et al., 2004; Bean et al., 2008). In all the considered cases in **Figure 5.29**, it is evident that a time lag decrease from 5.4 to 4.7 s cannot be due only to an increase of c_c, but necessary implies a shallowing of the source. For instance, if we consider the mean value of the range of c_c above mentioned (575 m/s) and a seismic velocity of 1300 m/s, and take into account the time lag value shortly before the beginning of the eruption (4.7 s), we obtain a source altitude equal to 3180 m a.s.l. (**Fig. 5.29c**). Successively, for the same time interval, and hence considering a peak frequency equal to 0.7 Hz, we used the same value of c_c to extract a value of conduit length by means of the Helmholtz resonator (**Fig. 5.28**), obtaining a 90 m long resonator. Assuming 3330 m a.s.l. as the crater rim altitude and a ~70 m deep funnel-shaped crater, a 90 m long resonator is equivalent to a source altitude of 3170 m a.s.l.. It is noteworthy that the depth value of the source of the seismo-infrasonic events calculated by means of the Helmholtz resonance model is consistent with the one obtained using the time lag. Under the assumption that the lag variation observed few hours before the eruption is mainly due to a shallowing of the magma column level, and considering a constant value of sound velocity (575 m/s), the fragmentation level altitude inside the conduit should have changed from ~2800 (during 12 May) to 3180 m a.s.l. (morning of 13 May) (**Fig. 5.29c**). Finally, we evaluated the fragmentation level altitude during 12 May also by applying the Helmholtz resonator equation: taking into account 0.4 Hz we obtained a conduit length of 260 m, which, considering a ~70 m deep crater, corresponds to ~3000 m a.s.l. Nevertheless, the mismatch between this value and the previous one computed by the lag could simply be due to inaccuracy of the peak frequency estimation. Since the duration of the infrasound events is about 10-15 s, the window length used to estimate the peak frequency was fixed to 10 s, and consequently the spectral resolution was roughly equal to 0.1 Hz. Indeed, if 0.3 Hz, in place of 0.4 Hz, is used in the calculation of the Helmholtz resonator length, we obtain a value of 460 m (**Fig. 5.28**), and therefore a fragmentation level altitude of 2800 m a.s.l., in agreement with the one evaluated by lag approach.

Finally, it is worth noting that, although the estimated depth values of the fragmentation level depend on several assumptions (e.g. seismic velocity, acoustic speed in the conduit) and hence can be imprecise, the waveform and spectral variations of the NEC events undoubtedly suggest a shallowing of the magma level inside the NEC conduit a few hours before the beginning of the eruption.

5.2.5. Discussion

In this work we analyzed 157 infrasound events and the corresponding seismic signals detected during 12-13 May 2008, and preceding the 2008-2009 eruption begun in the morning of 13 May.

The recharging phase preceding the 2008-2009 flank eruption, started in 2007 and was evidenced by a positive areal dilatation and several lava fountain episodes (Bonaccorso et al., 2011). From January 2008 to the beginning of the eruption, the energy release related to volcano-tectonic earthquakes was subjected to a speed up, initially due to deep earthquakes (focal depth of 10-20 km b.s.l.) and successively to shallower ones. In the same period, the GPS network measured inflation processes, first at relatively low altitude before reaching the higher altitude in March (Di Grazia et al., 2009).

Changes in seismo-volcanic signals occurred during the two weeks preceding the onset of the eruption. The LP events, located from January beneath BN crater, after 4 May became deeper and underwent an increase in both number and amplitude. In the same period the volcanic tremor, located beneath the central craters, deepened as well, and changed becoming monochromatic (Patanè et al., 2011). All the LP and volcanic tremor variations preceded and heralded the lava fountain taking place on 10 May at SEC (Patanè et al., 2011). Such seismo-volcanic changes were interpreted as the arrival of gas-rich magma up to the shallower portion of plumbing system (Patanè et al., 2011).

Focusing on the time period after the lava fountain and before the beginning of the eruption, further changes of seismo-volcanic signals were observed. From the early afternoon on 12 May, a gradual migration of the volcanic tremor epicentres from BN toward NEC and the NE Rift took place (Patanè et al., 2011). In particular, the source of the volcanic tremor was located under the NEC at about 1.5 km below the crater (Patanè et al., 2011).

The infrasound and seismic signals, making up our data-set, are likely to be generated by the same source as suggested by the similar frequency content, waveforms and epicentral location (**Figs. 5.18, 5.19** and **5.20**). The importance of these events is related to both the peculiar infrasound low frequency component (<0.7 Hz), rarely recorded at Etna before, and the significant changes (mainly affecting infrasound spectral content and time lag between seismic and infrasound signals) taking place a few hours before the eruption onset (**Figs. 5.17** and **5.22**). Concerning the low frequency component, Vergniolle and Ripepe (2008) described ~0.5 Hz infrasound signals, attributed to sloshing waves, recorded in 2001 at Mt. Etna.

However, the 2001 waveforms show substantial difference respect to NEC events, consequently such an interpretation of this low frequency component is not suited to our case.
It is noteworthy that volcanic tremor source migration occurred at the same time as the occurrence rate of seismo-infrasound events reached the maximum value (22:00 on 12 May, **Fig. 5.15c**). All these features suggest that the seismo-infrasonic events are closely linked to the impending eruption, even if they are located at NEC and the eruptive activity occurred at a fissure opened on the upper eastern flank of the volcano.
The infrasound component of these seismo-infrasonic events is characterized by two frequency bands, 0.4-0.7 and 1.5-2.0 Hz, whose sources were attributed to resonance phenomena inside the conduit. The conduit portion, responsible for such signals, is likely bounded by the magma fragmentation level, at the bottom, and a narrowing, at the top, and is filled with a gas-mixture. Sources close to the free magma surface related to degassing processes, trigger propagation effects (such as resonance phenomena) because of the interaction with the conduit. In particular, on the basis of the waveform and spectral features of the two aforementioned frequency bands, we inferred the superposition of two resonance phenomena: a closed-closed pipe resonance, producing the higher frequency peak (1.5-2.0 Hz); a Helmholtz resonance, generating the lower frequency peak (0.4-0.7 Hz) (**Fig. 5.23b**). On the basis of both spectral features and time lag between seismic and infrasound components, inferences on the geometrical features of NEC conduit were made. In particular, ranges for the conduit radius values and for the depth of the magma free surface, where the source triggering the resonance is supposed to be sited, were inferred. Furthermore, variations of such seismo-infrasonic events, can provide information on the magma column dynamics inside the shallow part of NEC conduit. The aforesaid spectral variations, together with the decreasing seismic-infrasonic time lag, occurring during 12-13 May, are clearly included in the framework of the seismo-volcanic signal changes sometimes observed before and during volcanic eruptions, at Etna and other volcanoes as well (e.g. Kobayashi et al., 2005; **section 5.1**). The decreasing pattern of the time lag measured a few hours before the eruption is to be ascribed to the magma free surface shallowing, even if we cannot exclude that c_c changes could contribute to the variation. Similarly, also the increase of the infrasound dominant frequencies was interpreted to result from the shortening of both pipe and Helmholtz resonators.
According to Aloisi et al. (2009) and Bonaccorso et al. (2011) the 2008-2009 eruption was fed by an intrusion following the path of the central conduit in the first part of the intrusion up to a shallow storage zone (below 1.5-2.0 km a.s.l.) and then breaking off toward the east in

the shallow part. As aforementioned, on the basis of the fact that both occurrence and variations of the analyzed seismo-infrasonic events are closely time-related to the eruption onset, we can infer that the NEC conduit is directly linked to some portions of such plumbing system (such as to the shallow storage zone at 1.5-2.0 km a.s.l.) feeding the 2008-2009 eruption (**Fig. 5.23c**). Proof of a branched shallow plumbing system has already been found at Etna by Marchetti et al. (2009b), La Spina et al. (2010) and **section 5.1**. In particular, La Spina et al. (2010) modelled a shallow plumbing system in which NEC conduit is a branch of the central feeding conduit.

In light of this connection, the change in the magma level inside the NEC conduit, inferred on the basis of spectral and time lag variations, can be linked to the pressure increase inside this plumbing system. Indeed, if we consider a simple plumbing system composed of a magma chamber connected to a vertical open-conduit, in equilibrium conditions the pressure inside the chamber has to be balanced by the magmastatic pressure of the conduit (e.g. Witham and Llewellin, 2006). Therefore, a pressure increase inside the shallow storage zone at 1.5–2.0 km a.s.l. can cause the magma flow from the chamber into NEC conduit, with a consequent magma level increase inside it. Taking into account the fragmentation level increase, estimated equal to ~ 200-400 m (see **section 5.2.3**), and considering a constant value of magma density inside the conduit in the range 700-2700 kg/m^3 (gas-magma foam and bubble-free magma, respectively; e.g. Pinkerton et al., 2002), we obtain a pressure increase inside the plumbing system of ~1.5-11 MPa, preceding the onset of the eruption by a few hours. Although there are major uncertainties in this evaluation, mainly related to the above assumptions, the magnitude order of such a pressure increase value can be considered reliable. Such a pressure increase is able to fracture rocks (e.g. Tait et al., 1989) and is also roughly consistent with the driving pressure value of 13 MPa, considered responsible for the intrusive process preceding the 2008-2009 eruption by Currenti et al. (2011).

A pressure increase inside the plumbing system can be caused by different mechanisms, such as magma input from a deeper source, gas exsolution and dynamical stress transfer (e.g. McLeod and Tait, 1999; Cannata et al., 2010b). These processes may be related to each other, too. For instance, the heating of the original magma by new hot input lowers the volatile solubility, hence promoting gas exsolution (McLeod and Tait, 1999). Similarly, small pressure changes, associated with dynamic stresses in a crystallizing magma that is close to critical supersaturation, should be able to trigger a significant increase in bubble nucleation leading to a marked pressure increase (Cannata et al., 2010b). On the basis of the data shown in this work, we cannot pinpoint the exact phenomenon leading to the plumbing system

pressure increase. However, since such a variation took place in a relatively short interval (a few hours), slow processes, such as crystallization increasing the concentration of volatile in the melt, can be excluded.

Finally, it is noteworthy that the above analyzed variations of seismo-infrasonic events, occurring during the night between 12 and 13 May, preceded the VT seismic swarm, located NE of the summit craters, and the accelerating ground deformation starting from 08:39 on 13 May. Such phenomena, that similarly to the seismo-infrasonic event variations were caused by a pressure increase inside the plumbing system, were followed at ~9:30 by the opening of an eruptive fissure and then by the beginning of the 2008-2009 eruption.

5.2.6. Concluding remarks

The seismo-volcanic events, occurring a few hours before the beginning of the May 2008 eruption, have been analyzed in this study. The following points summarize the main findings:

- By seismic and infrasound data the shallower portion of the plumbing system feeding NEC was modelled. Pipe and Helmholtz resonances were proposed to be contemporaneously active at NEC, giving rise to a higher and a lower frequency component in the infrasound signal, respectively.
- The occurrence of seismo-infrasonic events located at NEC during the hours preceding the eruption, together with the variation of their features, led us to infer a link between NEC conduit and the plumbing system feeding the activity at the eruptive fissure on 13 May 2008.
- On the basis of variations over time of both spectral features and seismic-infrasonic time lag, shallowing phenomena of the free magma surface inside NEC conduit were inferred.
- The upraise of the magma column is likely due to pressure increase in the plumbing system that preceded/accompanied the VT seismic swarm and acceleration of ground deformation in the summit area.

In conclusion, analyses of seismo-infrasonic events, preceding the 13 May 2008 eruption, proved to be a useful tool to detect instability in the shallow plumbing system in advance with respect to other geophysical parameters. Such multi-parametric approaches may be valuable techniques to be integrated in the monitoring of open conduit volcanoes throughout the world.

5.3. The 2010 ash emission at the summit craters of Mt. Etna: Relationship with seismo-acoustic signals

During 2010 Mt Etna was characterized by an high occurrence rate of minor explosive activity, especially at pit-crater of SEC and BN. Where, with minor explosive activity we mean episode producing ash emission more or less diluted with a relatively low height of the eruptive column (~ 1 km; Andronico et al., submitted). Three ash emission episodes, occurring at three of the summit craters, were taken into account: 8 April at the pit-crater of SEC, 25 August at BN and 14-15 November at NEC. In these time intervals seismic and infrasound events were recorded. **Figure 5.30** shows source location of infrasound events for each of the studied ash emission episodes. To locate infrasound events the new location technique explained in **section 3.4.1** was applied. We used a grid of 4x4 km^2, with a spacing of 25 m, coincident with the topographical surface and centered below the summit craters.

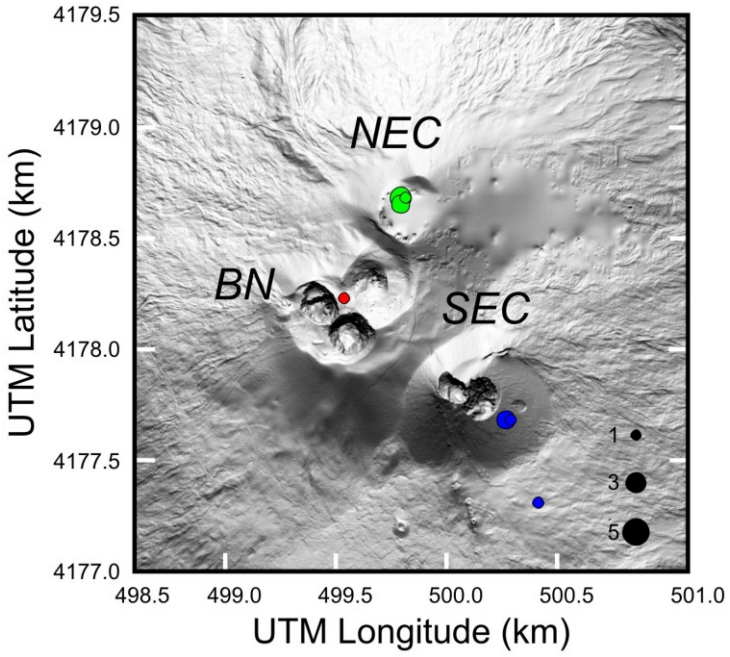

Fig. 5.30 *Digital elevation model of Mt. Etna summit with source locations of the infrasound events occurring during 8 April (blue dots), 25 August (red dots) and 14-15 November (green dots) eruptive episodes. The radii of the dots are proportional to the number of the locations in each grid node (see black dots and numbers reported in the lower right corner of the map).*

A multidisciplinary study was carried out by a joint analysis of seismic and infrasound signals recorded during such ash emission episodes, volcanological data (video-camera recordings) and dispersal and texture of the deposit. The aim of this study is to investigate the mechanism

of the ash emission episodes and the condition of the three craters. Indeed, componentry and morphological analysis may be used to investigate the origin of the ash.

5.3.1. Data acquisition

During the studied period the permanent infrasound network comprised 10 stations, distributed along two rings (**Fig. 5.31**). Among them, 6 stations were equipped with G.R.A.S. 40-AN microphones characterized by a flat response of 50 mV/Pa in the 0.3-20000 Hz band. We prefer to use only these stations in order to improve the quality of the analysis. The seismic data used in this work were recorded by 19 stations equipped with broadband (40 s cutoff period) three-component Trillium seismometers (Nanometrics). Infrasound stations are located at the same place as some seismic stations.

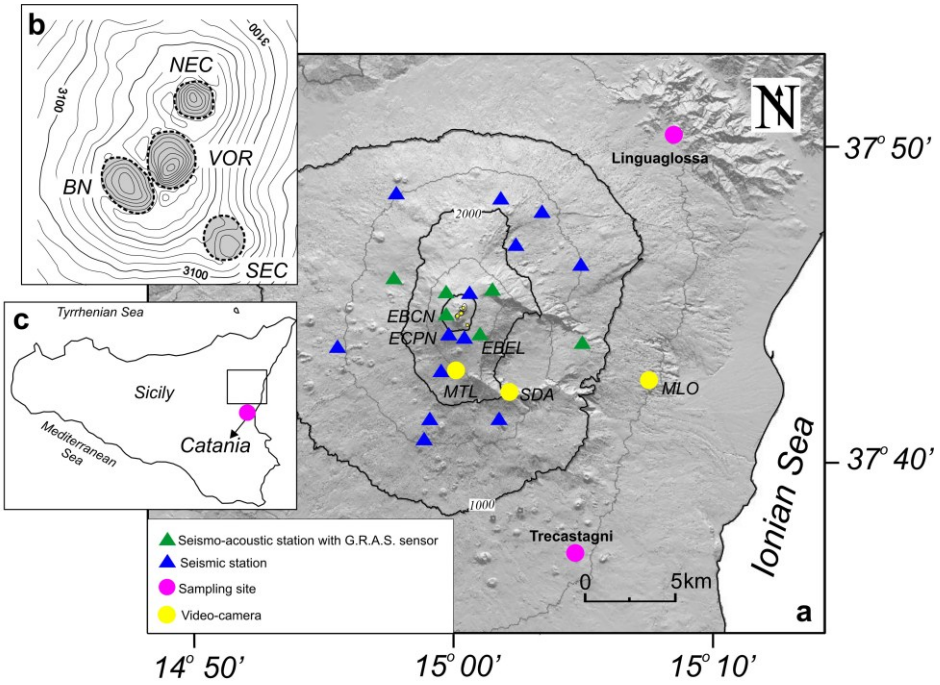

Fig. 5.31 ***(a)*** *Digital Elevation Model of Mt. Etna with location of the seismic (solid blue triangles) and seismo-acoustic (G.R.A.S. sensor; solid green triangles) stations used in this work (see the key in the lower left corner). MLO, MTL and SDA (solid yellow circles) are the Milo, Montagnola and Schiena dell'Asino cameras, respectively. Solid red circles: main localities reported in the text.* ***(b)*** *Distribution of the summit craters.* ***(c)*** *Location of the Sicily in the regional context.*

5.3.2. 8 April ash emission

5.3.2.1. Volcanological data

On 8 April, at 04:36 a seismic sequence, located below the SEC, was recorded. During these seismic events no volcanic activity was observed. Nevertheless, episodic puffs of reddish ash occurred from the late morning. At around 15:58 the first of numerous ash emissions took place at the pit-crater. The main and last ash emission occurred at 16:28, and produced a dark and thick plume reaching ~ 700 m in height (Andronico et al., submitted); a few minutes after the ash emission episode ended. It is noteworthy that the ash emissions were accompanied by infrasound events and the seismic counterparts. 4 samples of ash were collected between Linguaglossa and the slopes of the volcano. On volcanic ash, samples grain-size, componentry and morphologic analyses were carried out (Andronico et al., submitted). As regarding the grain-size analysis (**Fig. 5.32**), two of the proximal samples were characterized by more than 90% of particles with dimensions ranging from 0.125 mm to 1 mm showing a modal value of 0.25 mm, and a third one with a secondary mode peaked at 8 mm (Andronico et al., submitted). While the sample 16 km far from the vent was unimodal at 0.25 mm with 60 % of particles ranging between 0.25 and 0.5 mm. Successively, componentry was evaluated (for details on method of analysis see Andronico et al., submitted) in order to identify the proportion of the different ash components (e.g. sideromelane, tachylite, lithics and crystals: Taddeucci et al., 2002; Andronico et al., 2009a,b). From componentry analysis, performed on the highest frequency size class for every sample, results that the 4 samples of 8 April were characterized by a high percentage of lithic fraction (~ 50 and 82 %) with respect to the juvenile particles (15 – 45 %) and crystals (2 – 5 %) (**Fig. 5.32**). In particular three of them had percentages of lithics between 71 and 82 % (Andronico et al., submitted).

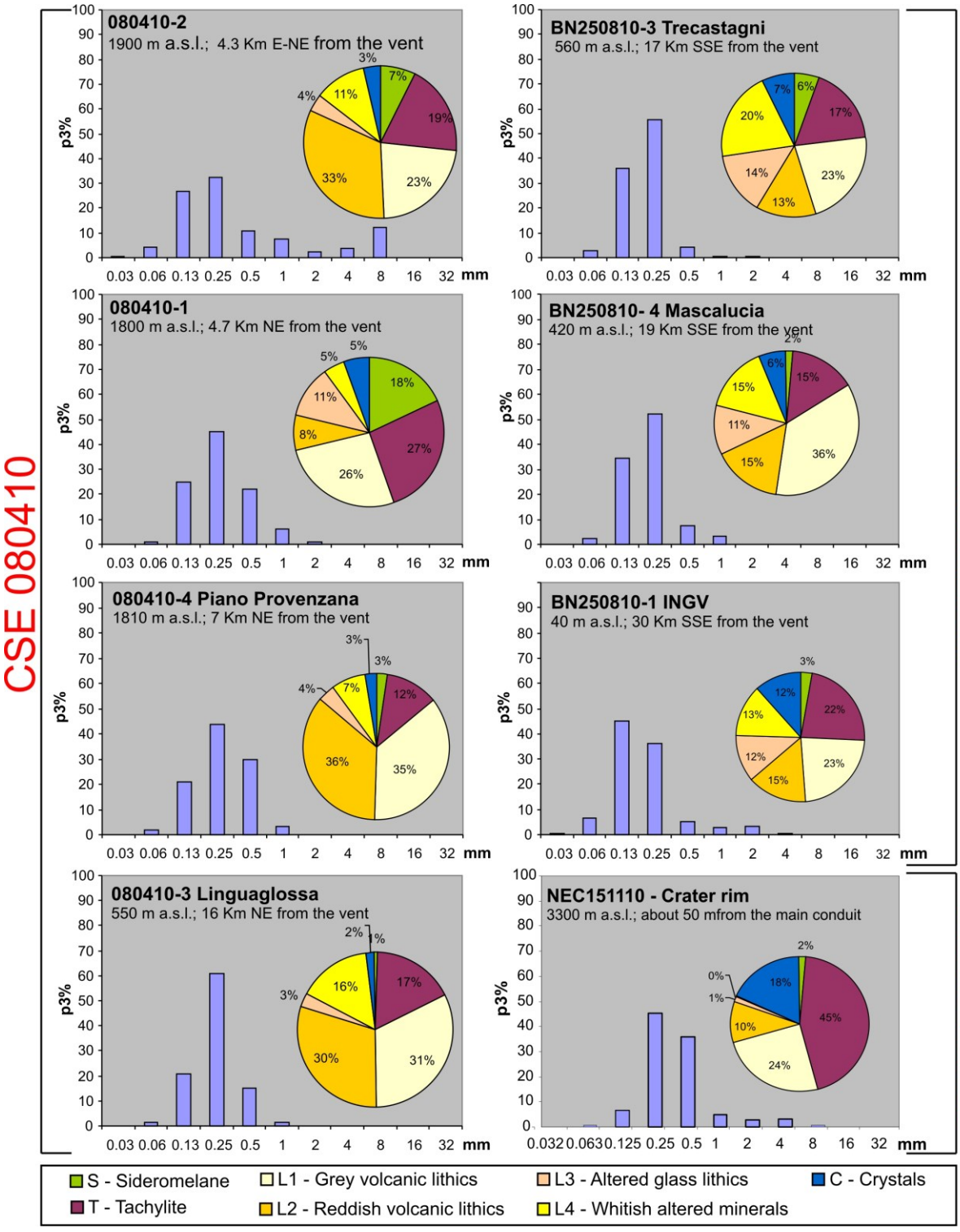

Fig. 5.32 *Grain-size distribution (histogram) and component percentage (pie diagram) of samples related to the three analyzed ash emission episodes (Andronico et al., submitted).*

5.3.2.2. Seismo-acoustic data analysis

In order to characterize seismo-acoustic data collected during the 2010 explosive events of Mt. Etna, we adopted the VASR, addressed in **section 3.5.1** (parameter proposed by Johnson

and Aster, 2005). In this case, VASR was calculate for each seismo-acoustic event. Regarding the seismic events, energy (E_{seism}) was computed on the resultant vector of the three component traces of the recorded velocity, and ρ_{volc} and c_{volc} were fixed equal to 2500 kg/m^3 and 1800 m/s, respectively. Acoustic energy (E_{ac}) was estimated on the basis of the excess pressure taking into account a ρ_{atm} equal to 0.9 kg/m^3 and c_{atm} equal to 340 m/s. Carefully checking the weather-conditions during the three analyzed episodes, wind intensities were found lower than 7 m/s, and, consequently, could not have introduced errors on the evaluation of acoustic energies. More than 25 seismo-acoustic events were recorded during the ash emission episode (between 15:58 and 16:30), 19 of those were selected and analyzed.

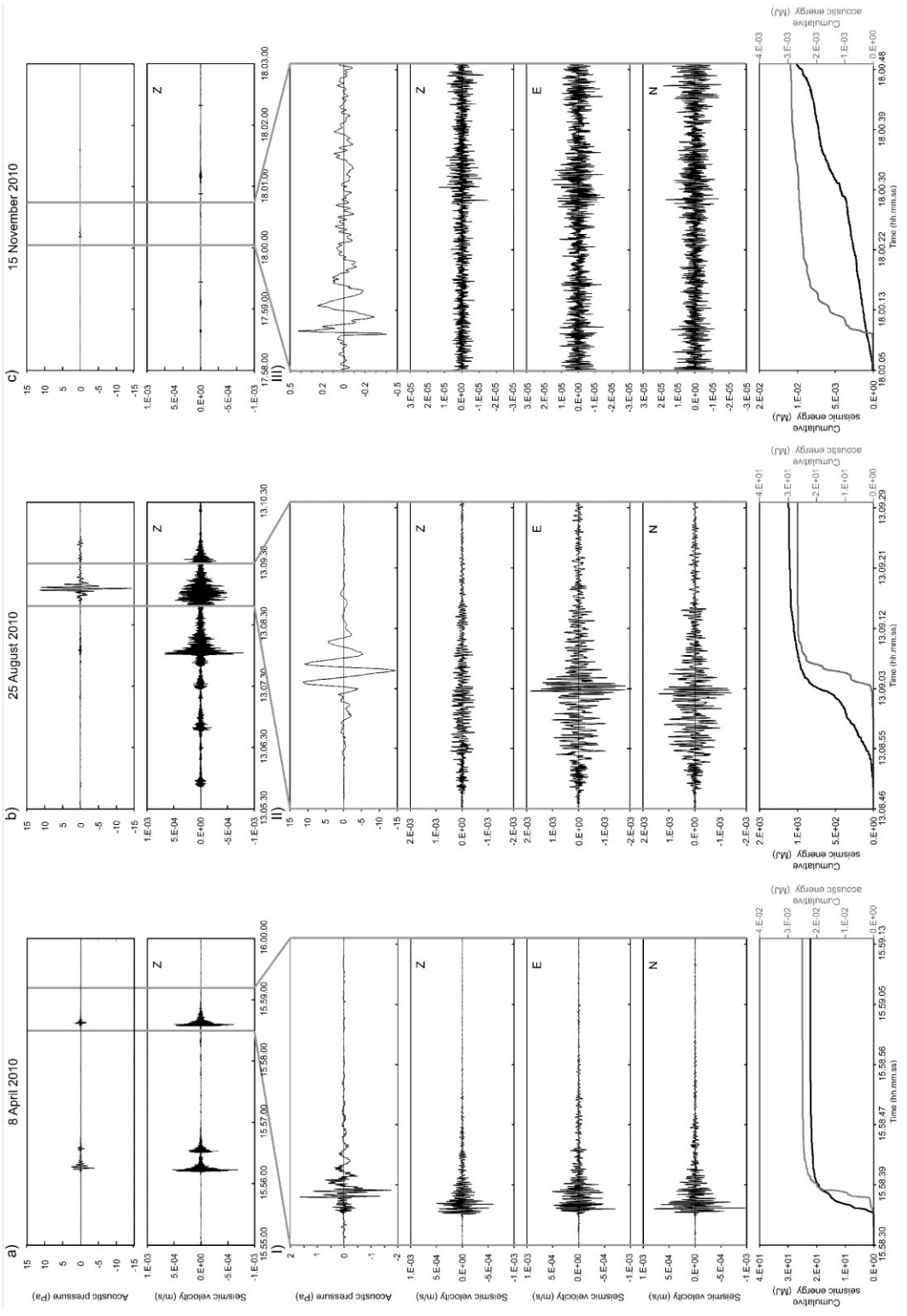

Fig. 5.33 *Infrasound signals, three component seismic signals and relative cumulative energies for events recorded at EBEL station during the three analyzed eruptive episodes. In particular, the events shown in* ***(a)****,* ***(b)*** *and* ***(c)*** *were recorded during explosive activity at the pit crater of SEC, BN and NEC, respectively.*

They were characterized by a duration of about 15 s as shown in **Figure 5.33aI**. Explosive events recorded on 8 April are mainly characterized by VASR between 0.001 and 0.1 (**Fig. 5.34,** blue dots) and the respective acoustic and seismic energies display a fairly positive correlation (i.e. increasing seismic energy, acoustic energy increases, too), except for the event of 16:18. This last one, indeed, exhibited a lower seismic energy and a VASR value of about 2.

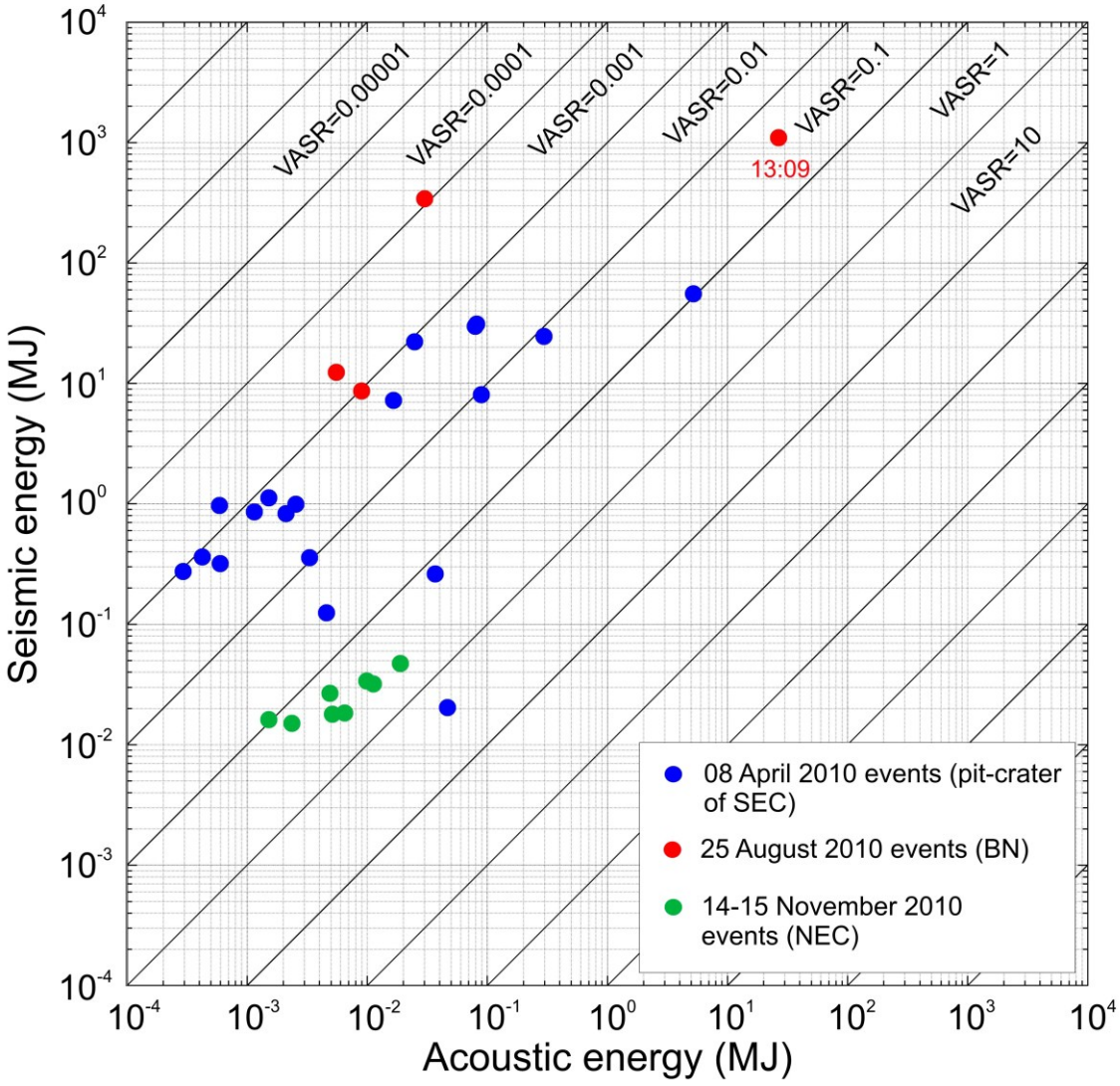

Fig. 5.34 *VASR values calculated for seismo-acoustic events recorded during 8 April (blue dots), 25 August (red dots) and 14-15 November (green dots) eruptive episodes. Please note that an error of 20 % due to the uncertainties of the fixed parameters could affect VASR values (see* ***section 3.5.1*** *for further details).*

5.3.3. 25 August ash emission

5.3.3.1. Volcanological data

During 2010 BN was characterized by numerous episodes of explosive and failures events producing ash emissions. One of the most powerful explosion occurred on 25 August at BN-1 (one of the two sub-circular pit-craters in the BN crater) at 13:09. The explosion generated a thick, dense volcanic plume which reached more than 1 km in height. It lasted ~ 10 minutes and then was gradually replaced by pulsating degassing (Andronico et al., submitted).
During 25 August and in the following days other weaker ash emissions occurred at the same vent. The 13:09 explosion was associated with acoustic and seismic radiation and was preceded by a sequence of seismic events started at ~ 13:05 (**Fig. 5.33b**). It is noteworthy that on 24 August a low frequency seismic sequence located at BN was recorded, while no volcanic activity was observed at the vent. Three samples of the 25 August eruptive plume deposit were collected in the sites of Trecastagni, Mascalucia and at 30 km from the vent (Andronico et al., submitted and reference therein). Similar to the ash emission deposit of the 8 April episode at the pit-crater, the highest percentage of the samples was represented by lithic particles (**Fig. 5.32**). In particular, the content of lithic was between 63 and 77%, while the sideromelane fraction was of 2-6% and tachylite from 15 to 22% (Andronico et al., submitted). As shown in **Figure 5.32** the three samples exhibited a quasi-unimodal distribution and similar proportion of component fractions.

5.3.3.2. Seismo-acoustic data analysis

Focusing on ash emission of 25 August, between 13:05 and 13:10, 6 main seismic events occurred. The last two of them were accompanied by infrasound radiation and corresponded to the eruptive plume at ~ 13:09. Seismic and infrasound events were recorded even during the weak ash emissions of the following days. The main infrasound event of 25 August was characterized by duration of about 30 s (**Fig. 5.33bII**). In order to characterize the eruptive episode from the seismo-acoustic point of view, energy partitioning analysis was carried out. As regarding the events recorded before the ash emission of 13:09, they presented only the seismic traces and exhibited VASR values between ~0.0001 and 0.001 (**Fig. 5.34**, red dots). While, for the event recorded during the main explosion of 13:09, presenting both the seismic and infrasound trace, a VASR value equal to 0.02 was obtained (**Fig. 5.34**, red dot labeled "13:09").

5.3.4. 14-15 November ash emission

5.3.4.1. Volcanological data

Since about a decade volcanic activity at NEC has been mainly made up of a steady, continuous pulsating degassing and deep explosions with very rare pyroclastic ejection beyond the crater rim (INGV internal report available at www.ct.ingv.it). Indeed, during periods of no eruptive activity, this crater represents the biggest gas producer of Etna (Andronico et al., submitted). On 12 November 2010 volcanic activity changed, and an intermittent emission of reddish ashes and steam was clearly visible at the NEC vent. This phenomenon gradually evolved from pulsating to quasi continuous, generating on 14 November a weak eruptive plume of ~ 100-300 m. It was characterized by a thin diluted column of ash and lasted 2 days. Concerning the deposit, which covered a limited area of the volcano, a single sample was collected. It was taken over the rim of NEC and was formed, for the 80%, by particles ranging from 0.25 to 1 mm (**Fig. 5.32**). The sample pertaining to the NEC ash emission activity, contrary to the samples of pit-crater and BN, exhibited an higher percentage of juvenile material, with respect to the lithic one. In particular, it consisted of 45% of tachylite, 2% of sideromelane, 35% of lithic particles and for the remaining percentage of crystals (see **Fig. 5.32**; Andronico et al., submitted).

5.3.4.2. Seismo-acoustic data analysis

Since the deployment of infrasound permanent network at Etna, during the regular degassing activity of NEC, infrasound events have been usually recorded (Cannata et al., 2009b, c; Spina et al., submitted; **sections 5.1**, **5.2**). Concerning the ash emissions of November 2010 from NEC, we analyzed infrasound and seismic signals recorded during 14-15 November. Seismic and infrasound traces are shown in **Figure 5.33cIII**, and, in particular, the latter were similar to the peculiar NEC events in terms of waveform and spectral content. These kinds of infrasound events are characterized by duration up to tens of seconds, waveforms resembling decaying sinusoids and usually have two frequency bands: one lower than 0.5 Hz, the other comprised between 0.8-2.5 Hz. NEC ash emission on 14-15 November was associated to the solely infrasound wave radiation and no evident seismic events were observed (**Fig. 5.33cIII**).

It is noteworthy that the transients in the seismic signal (**Fig. 5.33c**), due to their time lag with respect to the infrasound events, cannot be attributed to the NEC activity.

For this ash emission episode, VASR was calculated between the window containing the infrasound event and the corresponding seismic window aside from the presence of any evident seismic event. Results are reported in **Figure 5.34** (red dot label) and show VASR values comprised between 0.1 and 1.

5.3.5. Volcanic Tremor Analysis between March and December 2010

Successively, seismic volcanic tremor, continuously recorded between March and December 2010, was analyzed. To build the RMS (Root Mean Square) amplitude time series, 5-second-long moving window of the seismic signal (recorded by the vertical component of ECPN station and filtered in the 0.5-2.5 Hz) was taken into account, then, a value of 25th percentile was obtained for each 1-minute-long RMS series (**Fig. 5.35**). Such a percentile value allows to remove from the signal the seismic transients such as volcano-tectonic earthquakes and long period events.

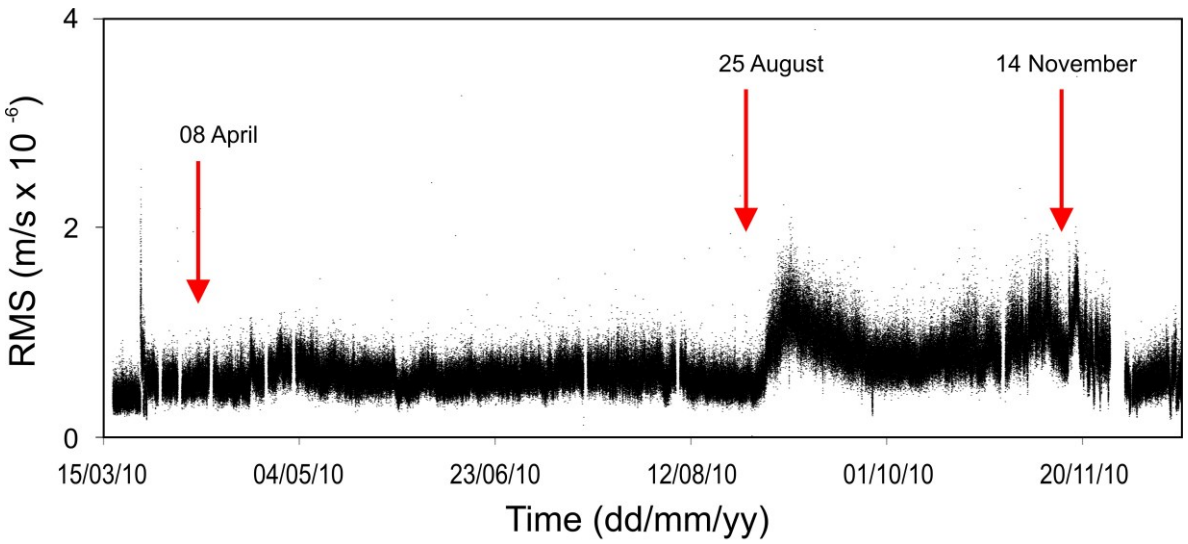

Fig. 5.35 *Variation over time of the 25th percentile calculated on RMS (Root Mean Square) amplitude time series of seismic signal.*

The main significant increase in amplitude occurred during the second period on the last days of August. Then, the RMS amplitude sharply decreased in mid-November (**Fig. 5.35**).

Furthermore, seismic volcanic tremor source location was performed using the method reported in **section 3.4.2**. The 3D grid used for this work is 6x6x6 km^3, with spacing between

nodes of 250 m and centered beneath the summit craters. Source location of volcanic tremor is plotted against time in **Figure 5.36.**

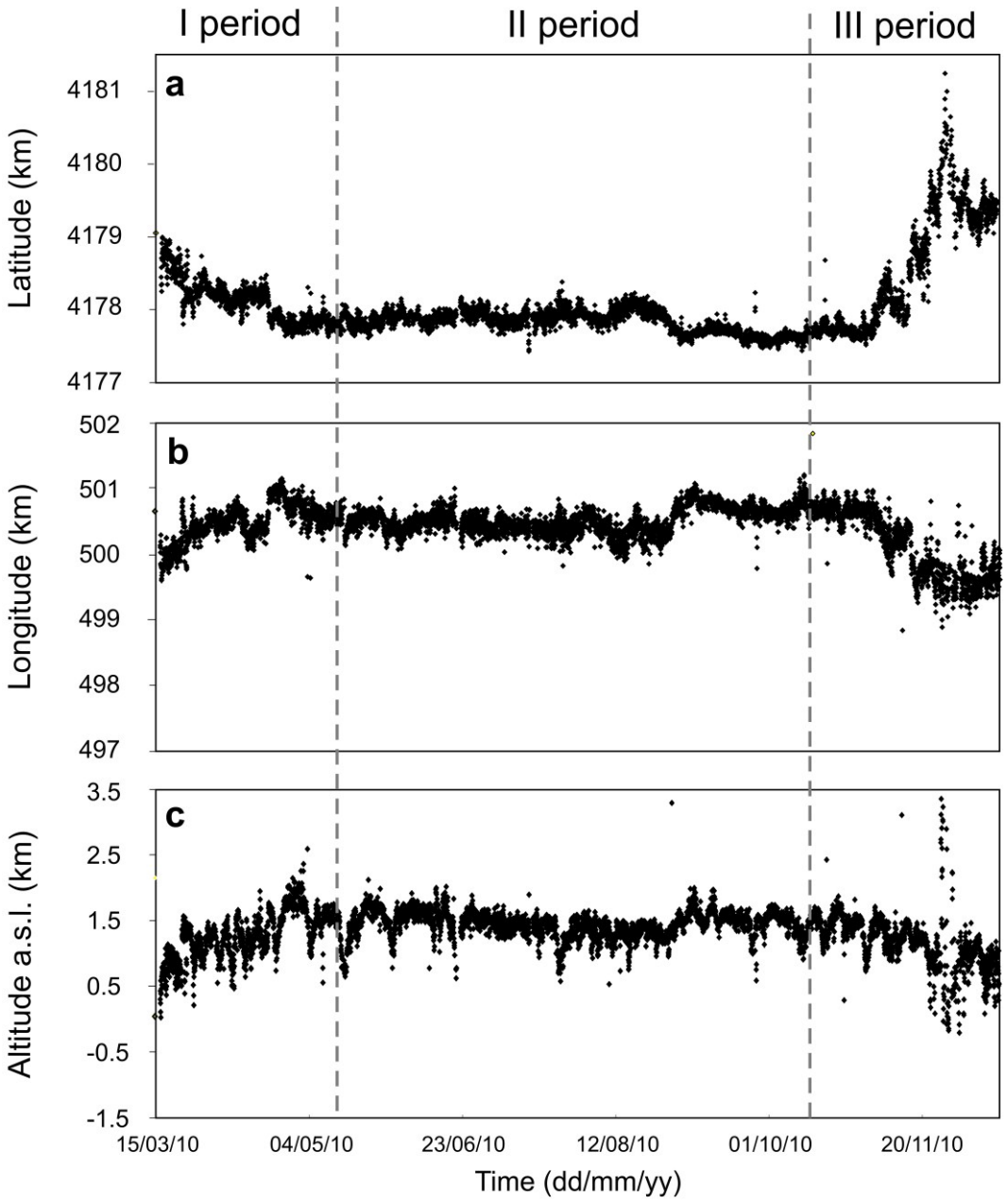

Fig. 5.36 *Temporal variation of latitude* ***(a)****, longitude* ***(b)*** *and altitude* ***(c)*** *of volcanic tremor source location. The dashed grey lines bound the three periods characterized by different volcanic tremor location trends.*

Successively, in order to highlight the occurrence of migration of volcanic tremor sources, the analyzed period was subdivided into three intervals as shown in **Figure 5.36** (15 March-14 May; 15 May-14 October; 15 October-15 December) and locations were plotted in map and section view (**Fig. 5.37**).

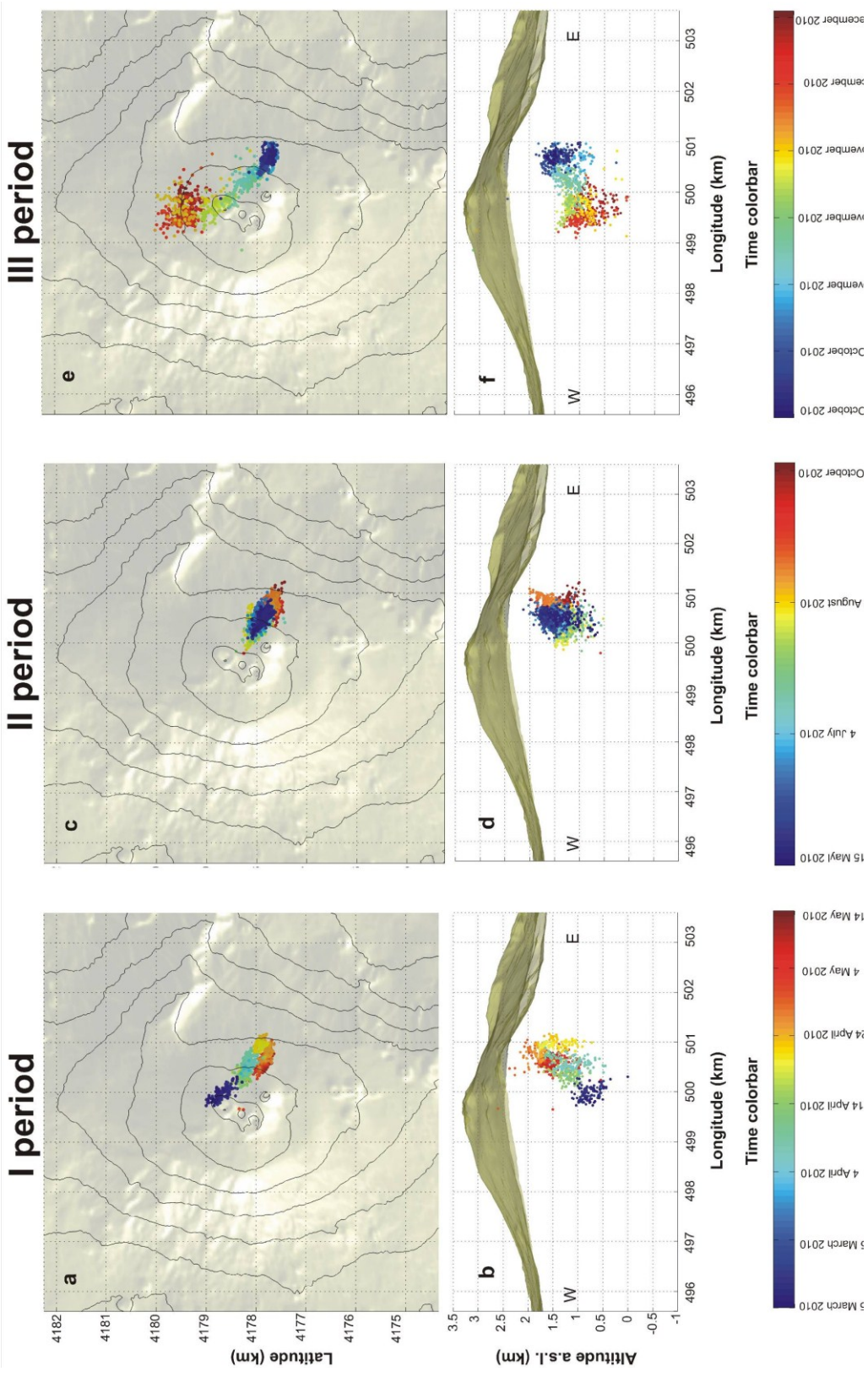

Fig. 5.37 *Maps and sections of Mt. Etna with volcanic tremor source locations calculated during three periods (see the bottom time color bar). In particular, period I lasts from 15 March to 14 May* ***(a)****, period II from 15 May to 14 October* ***(b)****, finally period III from 15 October to 15 December* ***(c)****, 2010.*

At the beginning of the first period volcanic tremor was located below the NEC between 0.5 and 1 km a.s.l. (**Fig. 5.37a, b**). From April it underwent a gradually shallowing (1.5-2.0 km a.s.l.), and moved south-eastward, toward SEC (**Fig. 5.37c, d**), where it remained for the rest of the second period. Tremor locations progressively returned to their original position (North East of the summit area) and deepened from the beginning of November (**Fig. 5.37e, f**).

5.3.6. Discussion and modeling

We investigated three minor episodes of ash emission by means of analysis of seismic and acoustic signal and the study of the dispersion and the texture of the erupted products.

The results led us to group the explosive events into two main types (*type a* and *type b*) of ash emission. The features of the *type a* are: emission of a ~ 1 km sustained eruption plume, whose product reached up to 20-30 km of distance from the vent; and radiation of evident seismic events beside the infrasound ones. Explosive events at BN and pit-crater of SEC were included in *type a* ash emission. On the contrary, *type b* is characterized by a continuous and prolonged in time ash emission producing a dilute and weak eruptive plume. During this kind of activity no evident seismic events were recorded. Resuming, concerning seismo-acoustic radiation, both *type a* and *type b* ash emissions were characterized by the infrasound wave radiation, but they can be distinguished on the base of the presence or the absence of evident seismic counterpart.

Based on the volcanic activity of summit craters in the recent years (see **section 4.1**), it is reasonable to suppose that in 2010 the volcanic conduit below the pit-crater of SEC was the location of cooling magma, caused by the frequent volcanic activity. Concerning the BN its bottom was quiescent and practically inactive since 2006 and was covered up to mid-2010 by a growing, relatively cold layer of debris mostly produced by failures of the inner walls and involved only by low fumarolic and degassing activity (Andronico et al., submitted).

On the contrary, NEC has been characterized in recent years by intense degassing suggesting continuous clearing of the conduit and the lack of old material on the top of the magma column residing in the conduit.

The morphological features (shape, surface and vesicularity) of sideromelane in the tephra deposits suggest the involvement of "fresh" magma during all the studied volcanic events, and hence the activity at the three craters (pit-crater of SEC, BN and NEC) was magmatic (Andronico et al., submitted).

Each ash emission episode was investigated evaluating seismo-acoustic energy partitioning. As previously specified in **section 3.5.1**, there are many different parameters affecting energy partitioning and therefore VASR value of seismo-acoustic events. The seismo-acoustic events, recorded during the numerous ash emissions of 8 April, were characterized by VASR values ranging between 0.001 and 0.1 (15 events out of 19 have VASR roughly in the 0.001-0.01 range). Such low values of VASR can be due to either a deep source or the presence of a dense cap rock topping the conduit. On the basis of the aforementioned conduit condition of pit-crater and the higher percentage of lithic particles with respect to the low quantity of sideromeloane, between the described possibilities we prefer the latter. Indeed, overlying material capping the vent causes an inefficient displacement of the atmosphere thus decreasing the radiated acoustic energy (Johnson and Aster, 2005). On the other hand, when ejected during explosive activity, the old material (volumetrically larger than the low amount of magma involved) may significantly dilute the percentage of juvenile particles (sideromelane and tachylite) (Andronico et al., submitted). Furthermore, the hypothesis of a cap obstructing the vent is also supported by the aforementioned occurrence of a sequence of seismic low frequency events with no acoustic emissions, taking place in the early morning of 8 April and suggesting the lack of coupling of the shallow plumbing system with the atmosphere before the main ash emission episode. **Figure 5.34** shows how seismic and acoustic energies (blue dots) have roughly a positive correlation: increasing seismic energy, acoustic energy increases, too. This general trend of correlated acoustic and seismic energies is typical of a fairly steady source and has been attributed to variations in explosive yield, likely related to eruption magnitude (Johnson and Aster, 2005). Nevertheless, there are few VASR values scattered with respect to the general positive trend of the data. Taking into account the short time-span in which the events occurred and the characteristics of the eruptive episode, variations in seismo-acoustic energy partitioning may likely be due to changes in plume density and/or in source depth. Indeed, density of the plume is inversely proportional to the volumetric perturbation of the atmosphere (Johnson and Aster, 2005).

Regarding the eruptive episode on 25 August, it consisted in a sequence of seismic events (started at 13:05) and culminated at 13:09 with the emission of a dense and dark cloud above the BN-1 crater. At the same time as the ash emission, a high energy infrasound event, accompanying the seismic event, was recorded. Three events recorded before the ash emission exhibited VASR values between ~0.0001 and 0.001, while during the main explosion, at 13:09, VASR reached a value of 0.02. The temporal evolution of volcanic phenomena, together with the absence of the infrasound events before the ash emission,

makes the changing condition of the crater the most probable reason for such a variable VASR. In particular, an obstruction of the conduit would have prevented the explosion from radiating infrasound signals before the main ash emission of 13:09. Once the conduit has become open, radiation of infrasound events would occur during the ash emission at 13:09. This hypothesis is supported by the low quantity of sideromelane together with the high percentage of lithics observed in BN ash samples. Also in this case the sequence of seismic low frequency events preceding the explosions supports such a hypothesis.

During the ash emission on 14-15 November 2010, no meaningful changes of NEC infrasound events, compared to their general features observed in the previous days, were found. No evident seismic events were associated with 14-15 November ash emission, thus, in this case, VASR was calculated by using seismic windows mostly containing noise, and then overestimating seismic energies. As a consequence, on the basis of the **equation 3.16** the VASR values should be even higher. VASR values obtained for this episode are well clustered between 0.1 and 1. Such higher values with respect to the VASR values obtained for *type a* ash emission are related to the low coupling of the seismo-acoustic source with the medium, likely due to the absence of a cap rock obstructing the NEC top conduit. Furthermore, sample of NEC plume consisted of an higher percentage of juvenile component with respect of lithic one. Both the results confirm the hypothesis of a relatively free or at least permeable surface at the top of the residing active magma column inside NEC thanks to the efficient degassing, as mentioned in **section 5.3.4.1.** The idea of considering NEC conduit the main branch of degassing for the volcano was also highlighted by other acoustic studies (Marchetti et al., 2009b; Cannata et al., 2009c).

It is noteworthy that the difference of several orders of magnitude among VASR values (**Fig. 5.34**) of the main episodes, occurring at different vents, is not due to the variability of the parameters, which were fixed in order to compute seismic and acoustic energies. Indeed, uncertainties in the aforementioned parameters could produce an error of 20 %, despite taking into account precautionary range of variation. Thus, such wide variability of VASR should be due to changes in the mechanisms at the base of explosive activity, likewise the presence/absence of a plug in the conduit, which could prevent acoustic waves from coupling with atmosphere. For the same reason, the variability observed among explosions occurring at the same vent are likely due to changes in the explosive dynamics. In particular, during the 8 April eruptive episode, as previously said, we believe the variation in VASR value to be caused by changes in the source depth and/or plume density. During the 25 August eruptive episode, the main variation of VASR is directly reflecting the transition from the closed

conduit condition to the disruption of the plug and the consequent opening of the system. Finally, the 14-15 November episode exhibits low variability of VASR, in agreement with the hypothesis we made of a steady-state open system.

Concerning the analysis of volcanic tremor, no correlation between variations in its amplitude and the three minor ash emission episodes (**Fig. 5.35**) was evidenced. On the other hand, in two of the three cases, changes in volcanic tremor location were observed. In particular, in the first days of April volcanic tremor location became shallower and migrated southeastward toward the SEC, where on 8 April the explosive event occurred. Then, a few days before the 14-15 November ash emission volcanic tremor source moved below the eruptive vent. This correlation between the renewal of volcanic activity and volcanic tremor source location can have implications for early warning. Indeed, such a link between volcanic tremor and eruptive activity at Etna has been observed in other cases (e.g. Schick and Riuscetti, 1973; Patanè et al., 2008, 2011).

It is noteworthy that ash emissions of *type a* were preceded by some hours by a sequence of low frequency seismic events, not accompanied by any infrasound evidence. In accordance with the literature associating such seismic low frequency events with the dynamics of fluids within the plumbing system (e.g. Chouet, 1996; Almendros et al., 2002), we hypothesize that they are related to the pressure transients excited by gas slugs rising and pushing at the top of the plugged conduit. Increases in amplitude and occurrence rate of low frequency events have also preceded eruptive activities at other volcanoes such as Redoubt (Chouet et al., 1994), Mount St. Helens (Moran et al., 2008) and Colima (Varley et al., 2010). It is noteworthy that no seismic sequence preceded the eruptive episode at NEC.

5.3.7. Concluding remarks on modeling and hazard implications

The study of the 2010 ash emissions at Etna allowed us to distinguish two main *types*, *a* and *b*, the former characterized by relatively powerful explosivity and impulsive nature, the latter by low explosivity and long-duration. Based on the joint analysis of seismo-acoustic signals and volcanological data, we propose a model about eruption dynamics of *type a* and *type b* ash emission (**Fig. 5.38**).

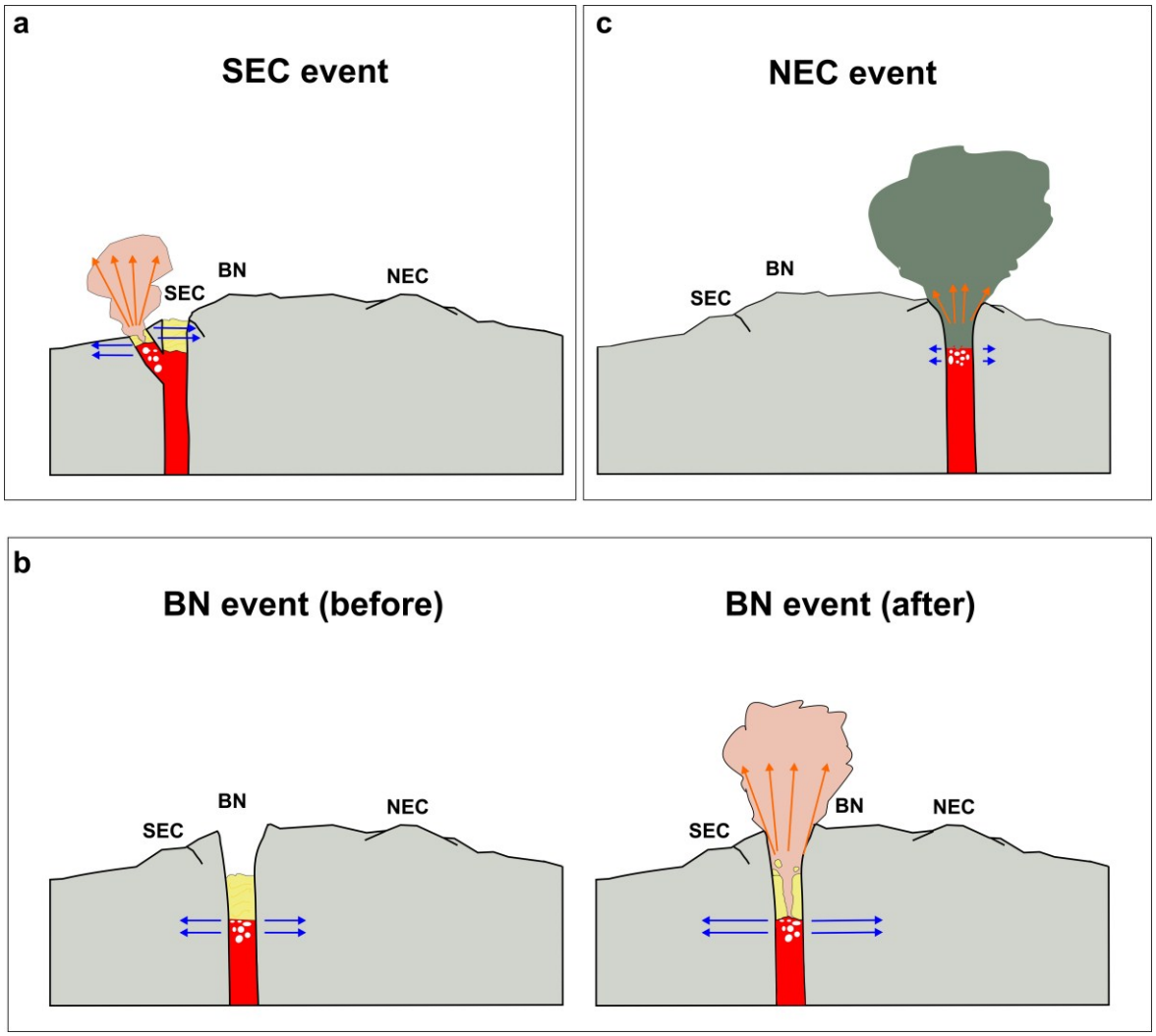

Fig. 5.38 *Sketches of eruptive events at pit-crater of SEC* ***(a)****, BN* ***(b)*** *and NEC* ***(c)****. Distances in the sketches are not in scale. The length of the orange and blue arrows represents qualitatively infrasonic and seismic energy, respectively. Orange color in the SEC and BN conduits (sketches* ***a*** *and* ***b****) point to the cap rock at the top of the magma system; conversely the green color in the sketch* ***(c)*** *suggests the relative clearing of the NEC conduit.*

Analysis results suggest, for *type a* ash emission, the accumulation of gas below the involved craters, followed by its release through minor explosive events, and culminating in the main explosive event generating an eruption plume. The model assumes the presence of a cap rock plugging the upper portion of the conduit, that causes a good coupling with rocks and thus radiating seismic signals. When the cap is removed during the explosive event, infrasound is finally generated because of the coupling with the atmosphere (**Fig. 5.38a, b**). This mechanism is better clear in the BN ash emission episode, where the evolution over time of seismo-acoustic signals is well correlated with temporal variation of conduit conditions.

On the contrary, for NEC ash emission episode (*type b*) a different eruptive dynamic was invoked. Based on the radiation of the solely infrasound energy and the abundance of juvenile material, the absence of a cap rock, thus an open condition conduit, was inferred (**Fig. 5.38c**).
In conclusion, we suppose that *type a* minor events are more hazardous because of their impulsive and short-lived nature with respect to the *type b* (Andronico et al., submitted). The shift of the volcanic tremor source, together with the occurrence of seismic sequences of energetic low frequency events, seem to be promising to issue warnings for this minor explosive activity. Resuming, the multidisciplinary study of both seismic and acoustic signals preceding and accompanying ash emission, together with the texture analysis of the deposits proved to be an important tool for better understanding the related eruptive dynamics.

5.4. Subspace detector: lava fountain episodes at Mt. Etna volcano

The current eruption of Mt. Etna, which began in January 2011, has produced numerous energetic episodes of lava fountaining. The source vent of these events was the New South-East Crater (NSEC).

The subspace method has promised to outperform standard STA/LTA methods for real-time event detection in cases where similar events can be expected (see **section 3.3.2**). We present an analysis of acoustic signals wherein we apply the method of subspace detection in order to verify the trigger potentiality of such an algorithm during Strombolian and lava fountain activity. Further, the analysis has the aim to determine whether the explosive source exhibits a temporal evolution within or between fountaining events, or otherwise produces repeating, classifiable events occurring through the continuous explosive degassing.

5.4.1. Data acquisition

Since the first days of January 2011 Mt. Etna has produced a new eruptive cycle. Between January and November, 18 lava fountains occurred at the NSEC. Three paroxysmal eruptions were selected: 9-10 April, 11-12 May and 8-9 July. We used continuous acoustic signals recorded by EBEL station, which in 2011 was equipped with a condensator microphone G.R.A.S. with sensitivity of 50mV/Pa in the frequency range 0.3-20000 Hz (**Fig. 5.39**).

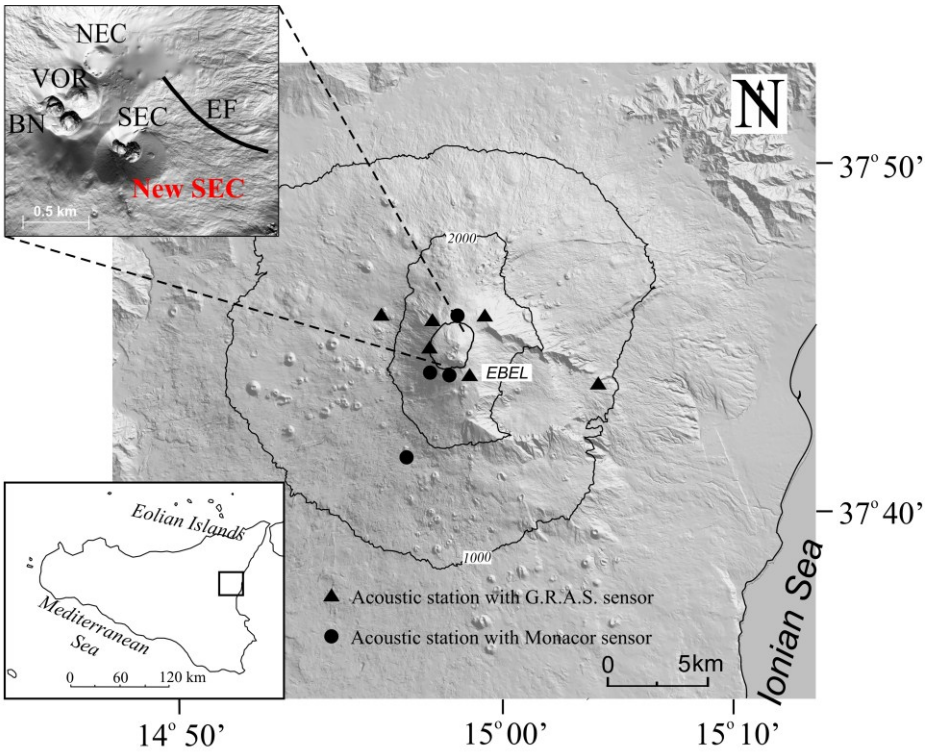

Fig. 5.39 *Digital elevation model of Mt. Etna with location of the acoustic station equipped with G.R.A.S. (triangles) and Monacor (circles) sensors. In the upper left inset, the digital elevation model of the summit area with the four summit craters and the position of the 13 May 2008 eruptive fissure (EF red line) and the NSEC. The position of EBEL station used in this work is also indicated. In the lower left location of Etna in the regional context.*

5.4.2. Volcanic framework

5.4.2.1. 8-10 April 2011 eruption

The paroxysmal episode of 10 April was the third lava fountain since the beginning of the last eruptive period. It occurred 51 days after the previous paroxysm and was characterized by lava flow and an intense lava fountain (INGV internal report available at www.ct.ingv.it). The weak Strombolian activity started on the morning of 8 April from two vents inside NSEC. It successively increased during the forenoon of 9 April until 18:00, when a lava flow was emitted and Strombolian activity rapidly decreased. A gradual increase of both intensity and rate of Strombolian explosions again took place in the night between 9 and 10 April. Between 06.00 and 08.00 on 10 April, the frequency of explosions from the two vents rapidly increased. Strombolian activity became almost continuous between 8:00 and 9:00 forming a lava fountain reaching in less than one hour ~300 m in height. After 11:30 the lava fountaining activity decreased in intensity and at about 13:10 started rapidly to diminish

(INGV internal report available at www.ct.ingv.it). From 13:30 the lava fountain was replaced by discontinuous jets activity (few tens of meters high), which ended at about 14:00.

5.4.2.2. 8-11 May 2011 eruption

Four weeks after April paroxysm, mild and discontinuous Strombolian activity renewed on morning of 8 May and remained weak but constant until 11 May. At about 15:00 volcanic tremor amplitude progressively increased and a few hours later the activity intensified. Around 21:00 Strombolian explosions were more intense and higher in rate. The Strombolian activity evolved into lava fountaining at ~1:20 reaching about 200-300 m at ~2:00. The acme of lava fountain lasted about 2 hours, then showed a gradually decline at ~3:45. The eruptive activity ended at 4:10, at the same time as a drop in the volcanic tremor amplitude (INGV internal report available at www.ct.ingv.it).

5.4.2.3. 7-9 July 2011 eruption

7-9 July eruptive episode was the fifth of the year, and, although shorter in duration with respect to the previous lava fountain, it produced a dense eruption column several kilometres high that reached Catania. Strombolian explosions preceding the July paroxysmal episode started to increase at 21:00 on 7 July and tapered off until ~9:00 on 8 July. The Strombolian activity resumed at ~6:00 on 9 July and gradually increased in intensity until 13:50, when it was replaced by a lava fountain. The most energetic phase of the lava fountain lasted till 15:15 when it evolved again into Strombolian activity. It is noteworthy that at 15:20 a roughly waveform-stable acoustic signal was recorded. The whole paroxysmal episode ended at about 15:40 (INGV internal report available at www.ct.ingv.it).

5.4.3. Data analysis

We examined two days of unfiltered infrasound signal for each of the three paroxysmal episodes, to detect both Strombolian and lava fountaining activities. As explained in **section 3.3.2,** subspace detector operates a projection of continuous data into a subspace developed from the reference template waveforms produced by a particular source. Therefore, sets of templates were chosen from the signal to build the subspace basis vectors. The templates were

manually selected from the raw signal and then aligned. Regarding April and May eruptive episodes, two sets of templates were chosen. The first set of templates (25, **Fig. 5.40a**) consisted of infrasound events extracted during Strombolian activity occurring usually hours before the beginning of the fountaining, while the second set of templates (18, **Fig. 5.40b**) comprised infrasound events related to the lava fountain activity. In particular, the choice of two sets of templates is related to the intent of detecting in the signal Strombolian activity and lava fountain, separately. To characterize the subspace, between 8 and 15 SVD (see **section 3.3.2** for details) values were used. For each paroxysmal episode two days of data were scanned with the subspace developed from these two sets of templates to detect infrasound events generated by the particular sources.

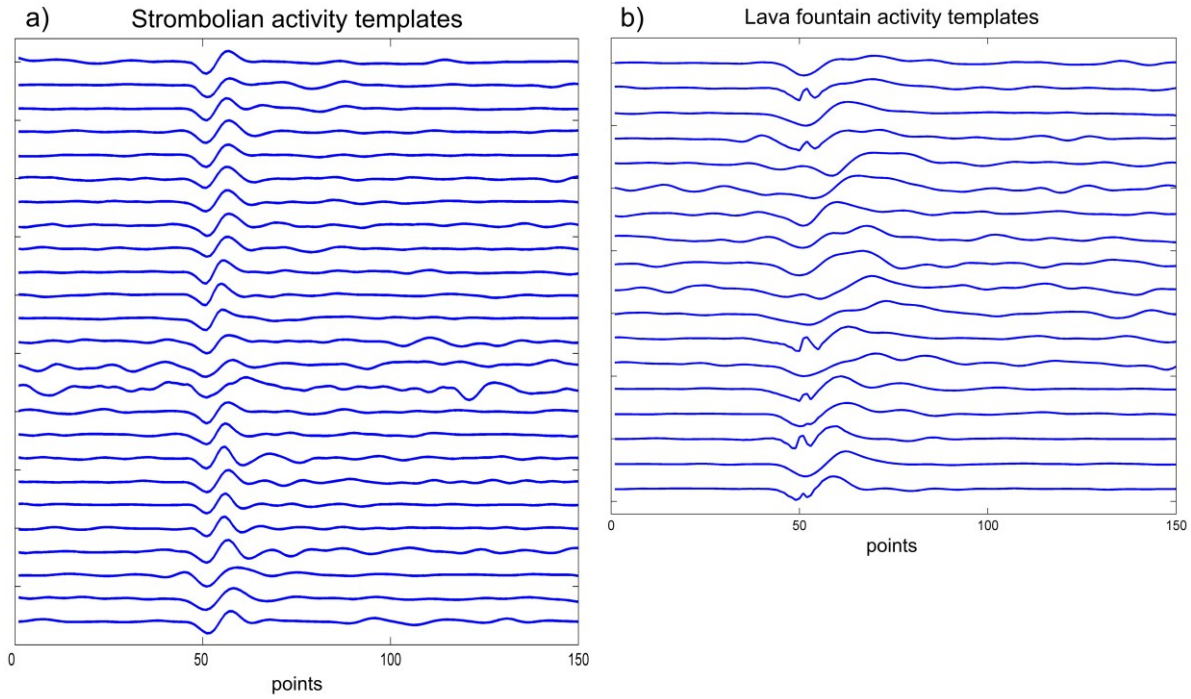

Fig. 5.40 *Example of reference templates 150 points long extracted from infrasound signal used to build the subspace matrix.* ***(a)*** *Templates pertaining Strombolian activity on 9-10 April.* ***(b)*** *Templates identified during lava fountain on 10 April.*

A *z* statistic value is calculated for each sliding window position (with a step of 1 point) as the windowed data is projected into the subspace (see **section 3.3.2**). The meaning of the *z* parameter is similarity degree between the collected reference templates and the continuous signal. Regarding paroxysmal episode of 8-10 April, templates of the first set were chosen from signal recorded during Strombolian activity occurring between 09:00 on 09 April and 09:00 on 10 April (**Fig. 5.40a**), while templates of the second set were extracted during the time interval between 09:40 and 13:15 on 10 April during the lava fountain (**Fig. 5.40b**).

Subspace was first applied taking into consideration templates of Strombolian activity (red "x" in **Fig. 5.41a**) and the results are shown in **Figure 5.41a.** It must be said that in this preliminary phase of the study, a detection statistic (*z*) threshold value has not been fixed, thus we can only interpret the results in a relative way. Indeed a statistical analysis should be carried out for a great number of eruptive episodes in order to estimate the critical *z* threshold value for which the detection can be considered reasonable. Several procedures exist in literature providing criteria to set the optimum threshold value, since it has to satisfy the trade-off between sensitivity and flexibility (Harris, 2006 and reference therein). Furthermore, this analysis represents a first attempt to apply the subspace detector to acoustic data recorded during volcanic eruption. By comparing the obtained *z* values (**Fig. 5.41a**) with video camera recordings and infrasound signal (**Fig. 5.41c**), it results that the subspace detector, using the first set of templates, was able to detect the Strombolian activity on 9 April.

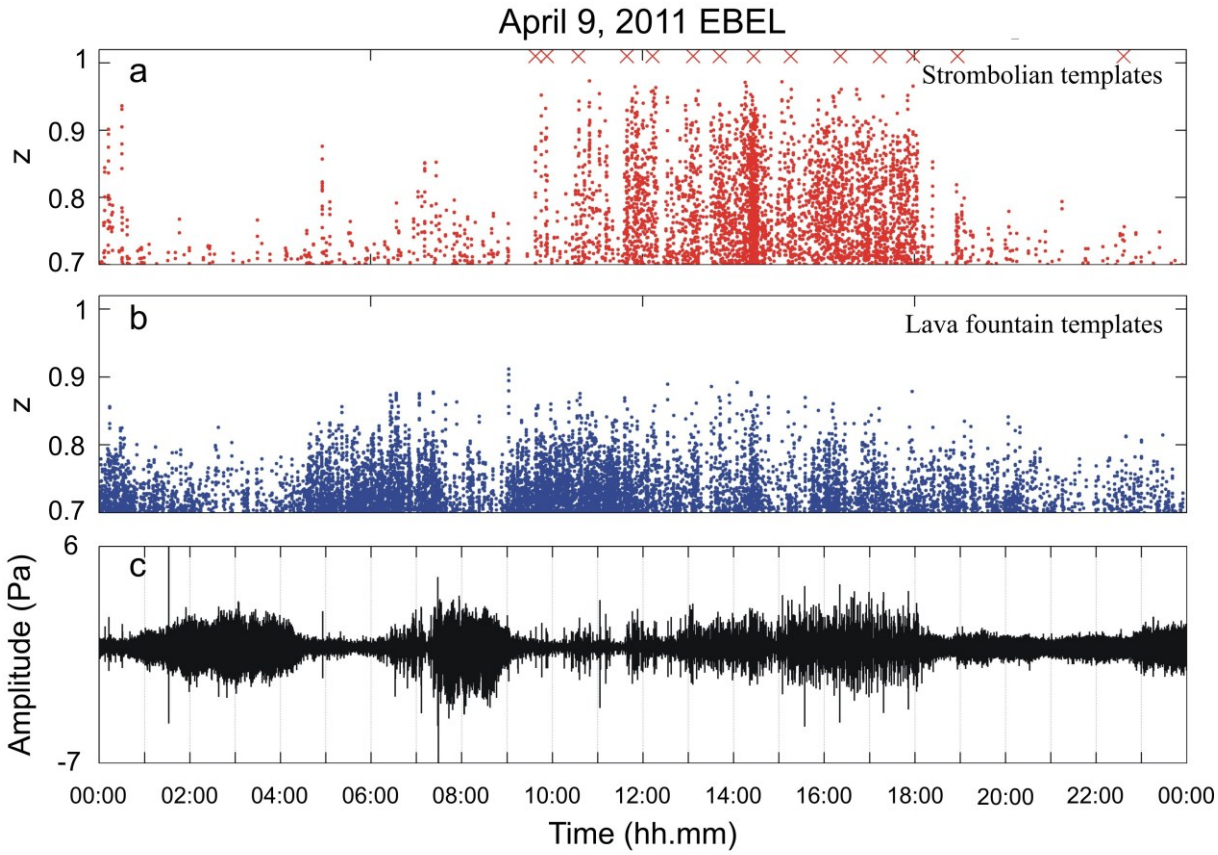

Fig. 5.41 *Event detection by means of subspace method on 9 April 2011 data. z statistic values obtained using Strombolian activity* ***(a)*** *and lava fountain* ***(b)*** *templates.* ***(c)*** *Continuous infrasound signal recorded at EBEL station.*

During Strombolian activity *z* values reached values from 0.9 up to 0.97 (**Fig. 5.41a**). The weak increase of infrasound signal amplitude before 10:00 and after 18:00 is noise, likely caused by wind.

Secondarily, subspace was applied on 9 April continuous data using templates of lava fountain activity. In this case, no particularly high values of *z* were obtained in agreement with volcanic activity (**Fig. 5.41b**).

On 10 April 2011 the transition from Strombolian activity to lava fountain occurred between 08:00 and 09:00. Indeed, after 08:00 high frequency rate Strombolian explosions were replaced by a small lava fountain (INGV internal report available at www.ct.ingv.it). Subspace detector applied to 10 April infrasound data was able to detect both the Strombolian activity and the lava fountain. This is clear in **Figure 5.42a,** where, applying subspace detector using Strombolian templates, we observe, starting from the first hours of 10 April, a gradual increase of *z* values together with the growth of Strombolian explosions.

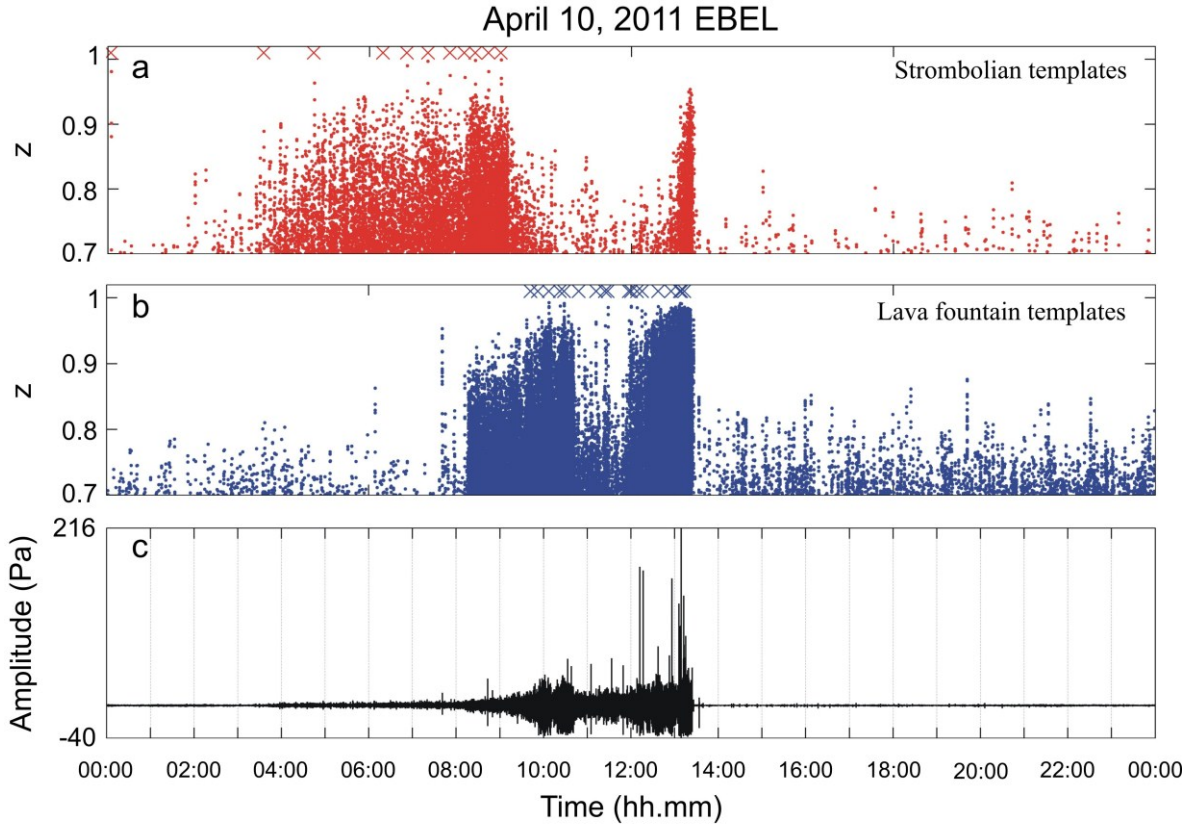

Fig. 5.42 *Event detection by means of subspace method on 10 April 2011 data. z statistic values obtained using Strombolian activity* ***(a)*** *and lava fountain* ***(b)*** *templates.* ***(c)*** *Continuous infrasound signal recorded at EBEL station.*

The *z* parameter remained on high values (up to 0.95) till around 09:10, when it abruptly dropped (**Fig. 5.42a**). Successively, the subspace detector recognized Strombolian activity between 13:10 and 13:20 (see peak of *z* value in **Fig. 5.42a**). **Figure 5.42b** shows the results of subspace using lava fountain templates on 10 April. The subspace method detected the onset of the lava fountain at around 08:15 (*z* values of ~0.9). From 08:15 to 13:20 *z* values gradually increased up to almost 1, with the exception of a time interval between 10:45 and 12:00 when a few events were detected (**Fig. 5.42b**). As for the case of the subspace with Strombolian templates, even here *z* value sharply dropped around 13:20 (**Fig. 5.42b**). It is interesting to point out that during the transition period from Strombolian activity to lava fountain and a few minutes before the end of the paroxysm (around 13:10-13:20; **Fig. 5.42c**), infrasound signals ascribable to both Strombolian explosions and lava fountain were detected by subspace detector (**Fig. 5.42a, b**).

The same procedure was applied to the May eruptive episode. The subspace with Strombolian and lava fountain templates was applied to 11 and 12 May infrasound data (**Figs. 5.43** and **5.44)**. Results show how the subspace technique detected the Strombolian explosions preceding the lava fountain (**Fig. 5.43a**). Around 21:00 the similarity between infrasound events and the subspace developed from the first set of templates gradually increased (*z* values from 0.9 to 0.98) together with increase in amplitude of infrasound signal (**Fig. 5.43a, c**).

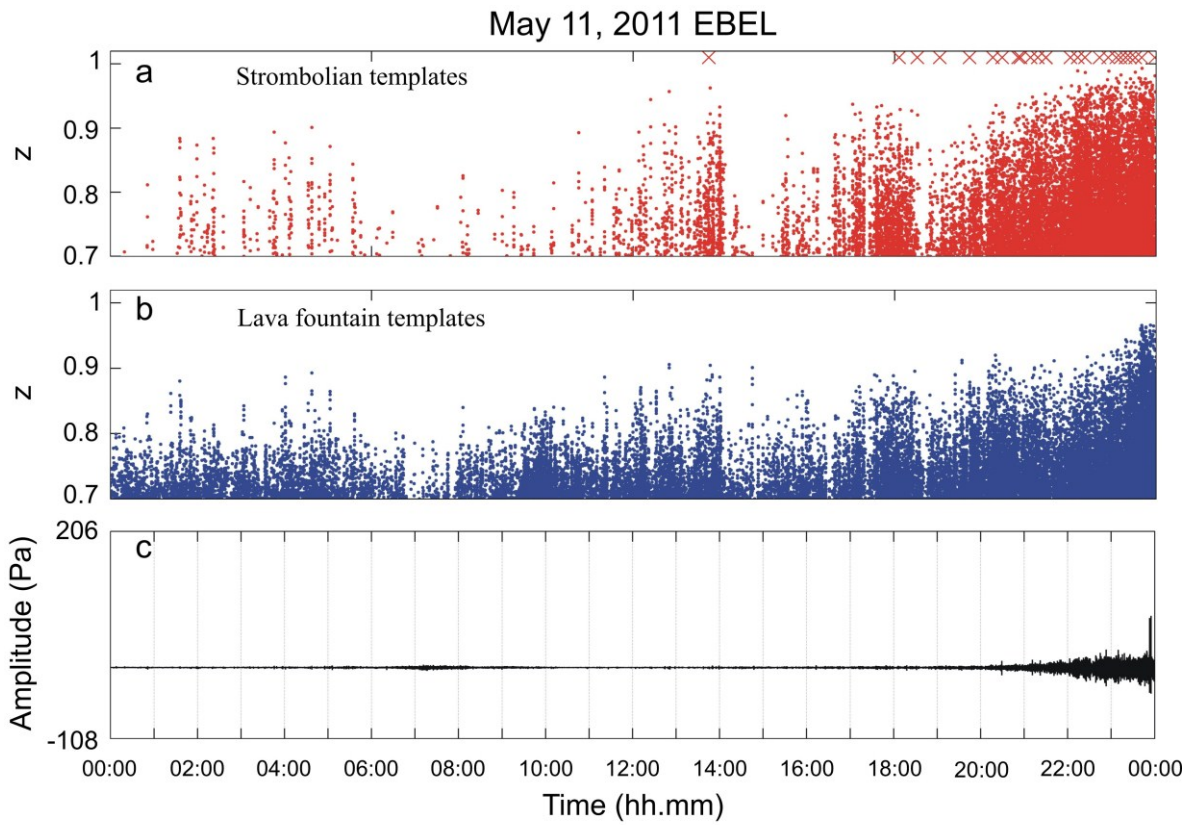

Fig. 5.43 *Event detection by means of subspace method on 11 May 2011 data. z statistic values obtained using Strombolian activity* ***(a)*** *and lava fountain* ***(b)*** *templates.* ***(c)*** *Continuous infrasound signal recorded at EBEL station.*

z statistic values remained high until shortly before 01:00 on 12 May, then decreased and again reached values of about 0.97 during the last phase of the paroxysm (**Fig. 5.44a**). On the other hand, using lava fountain templates, *z* values exhibited high values (higher than 0.9) starting from 23:00 on 11 May (**Fig. 5.43b**). By means of these templates, the subspace was able to detect the most intense phase of the paroxysm (**Fig. 5.44b**). Indeed, according to the report of the eruptive episode (**section 5.4.2.2.**), the lava fountain developed at ~01:20 and gradually declined at ~3:45 (**Fig. 5.44c**). After 04:00 on 12 May, in line with the cessation of the eruptive activity, no Strombolian and lava fountain infrasound events were detected by the subspace. Indeed, z values dropped and remained below 0.8 for the rest of the day (**Fig. 5.44a, b**).

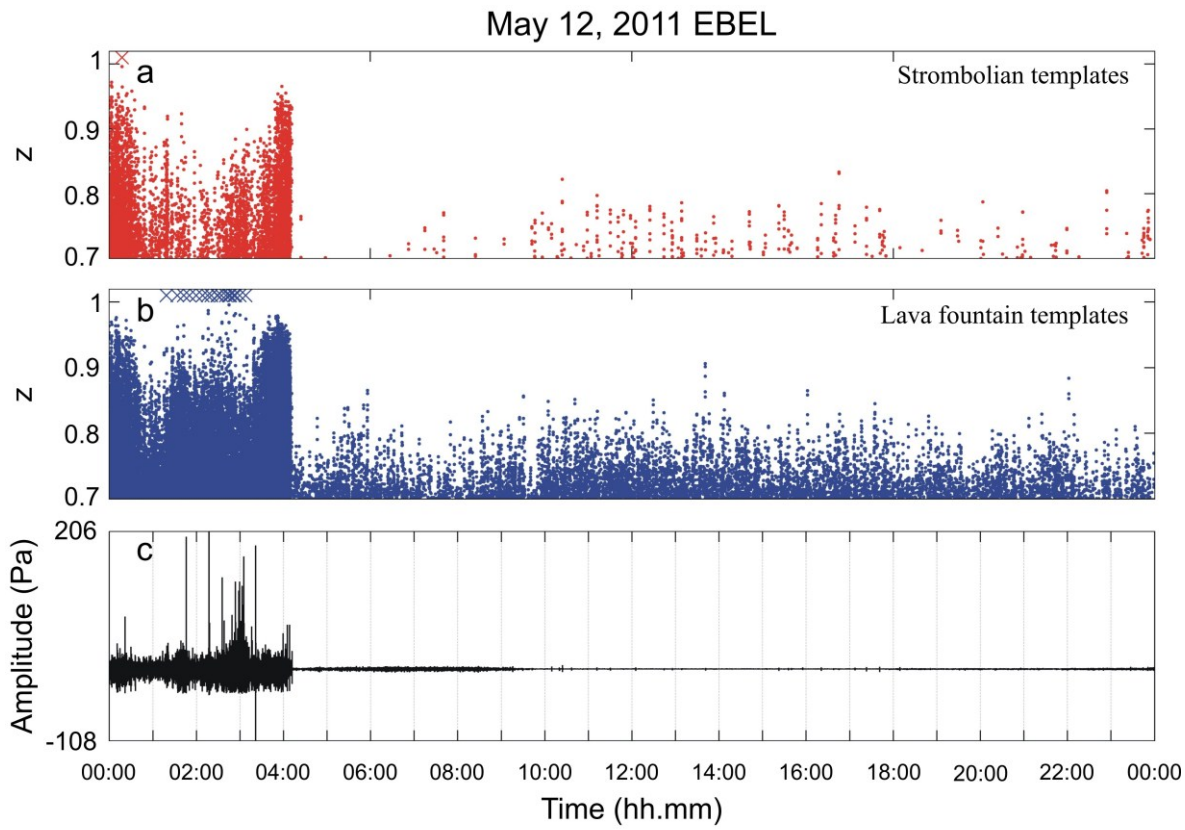

Fig. 5.44 *Event detection by means of subspace method on 12 May 2011 data. z statistic values obtained using Strombolian activity* ***(a)*** *and lava fountain* ***(b)*** *templates.* ***(c)*** *Continuous infrasound signal recorded at EBEL station.*

Successively, we focused on the 7-9 July eruptive episode. On 9 July, during the last stage of the paroxysm (**Fig. 5.45b**) we observed a particular infrasound signal (**Fig. 5.45d**), whose onset coincided with the end of the lava fountain (~15:15).

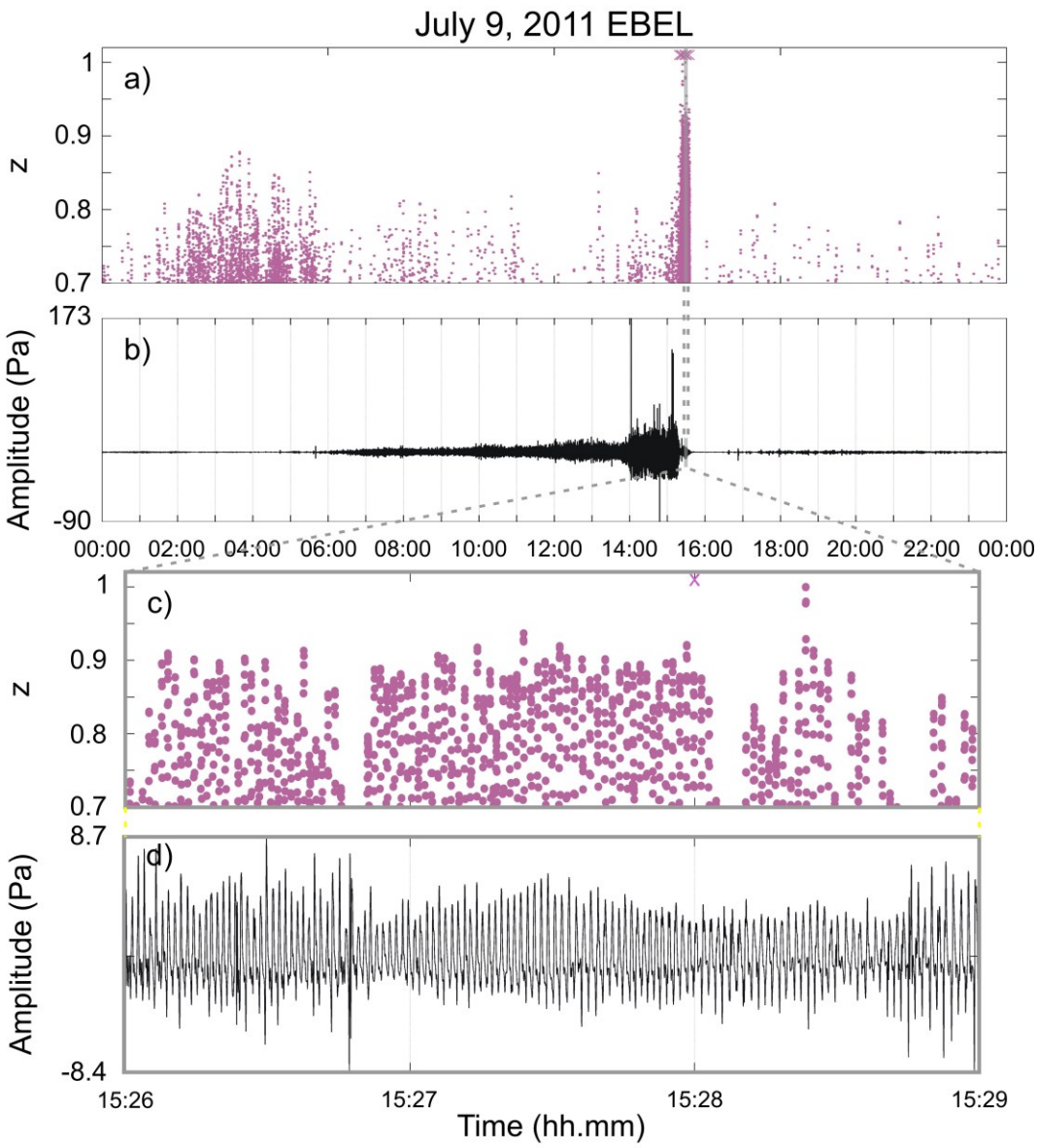

Fig. 5.45 *Event detection by means of subspace method on 9 July 2011 data. z statistic values obtained using "chugging" signal templates* ***(a)*** *and the related zoom* ***(b)****. **(c)** Continuous infrasound signal recorded at EBEL station and the related zoom* ***(d)****.*

This signal lasted until 15:38 and was very similar in waveform to a kind of harmonic infrasonic tremor called "chugging" (see **section 2.1**; Lees and Ruiz, 2008). The subspace used to scan 9 July infrasound data was built by a few templates extracted from the signal recorded during the time interval 15:15-15:38 (**Fig. 5.45b**). Results show how by means of this set of templates the algorithm detected precisely (*z* values > 0.9) "chugging" signal (**Fig. 5.45c**). On the contrary, the subspace detector, in such a way built, did not identify infrasound signals related to either Strombolian or lava fountaining activity (**Fig. 5.45a, b**).

The subspace application just shown is a retroactive event detection, since we processed stored continuous data. In particular we selected reference templates within specific time

periods of a given eruptive episode to seek similar signal throughout the whole paroxysm. Results show how the subspace detector is able to detect infrasound events from a given source (**Figs. 5.41-5.44**).

For a hypothetical real-time detection, reference templates of incoming eruptive activity are not available. In the light of this we explored the application of subspace method to an eruptive episode using reference templates collected during a previous one. In particular, subspaces developed from the two sets of templates, extracted from infrasound signal recorded on 8-10 April during Strombolian and lava fountain activity were used to scan continuous data recorded during the May eruptive episode (**Figs. 5.46-5.47**). Beside real-time and automatic monitoring purposes, this test was performed with the aim of identifying similarity between infrasound event waveforms during different eruptive episodes. Concerning 11 May, the comparison between **Figures 5.43** and **5.46** show how the detection of May Strombolian and lava fountain events using May templates is similar to the detections obtained using April templates.

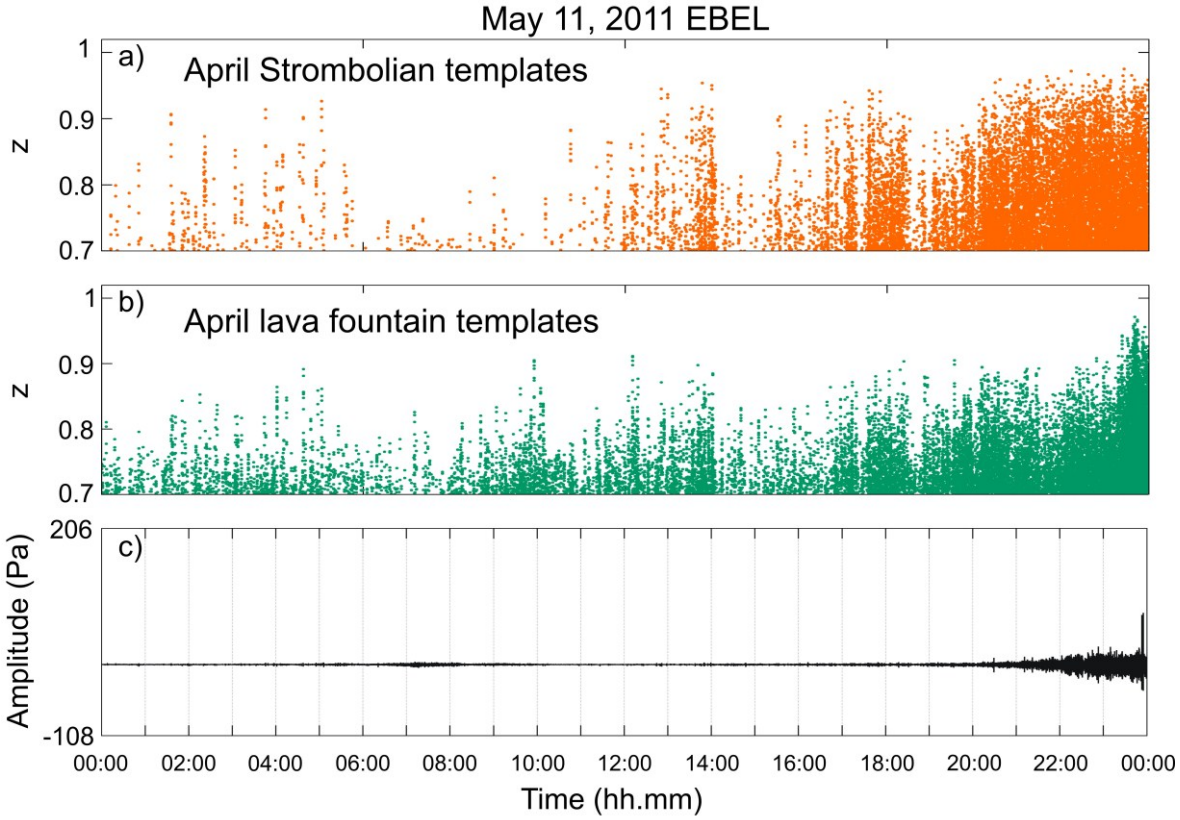

Fig. 5.46 *Event detection by means of subspace method on 11 May 2011 data adopting templates extracted from April eruption signal. z statistic values obtained using Strombolian activity* ***(a)*** *and lava fountain* ***(b)*** *templates.* ***(c)*** *Continuous infrasound signal recorded at EBEL station.*

The same can be said regarding 12 May, when the lava fountain occurred: we observed similar detection distribution and *z* values, using both Strombolian and lava fountain templates (**Fig. 5.44a, b** and **Fig. 5.47a, b**).

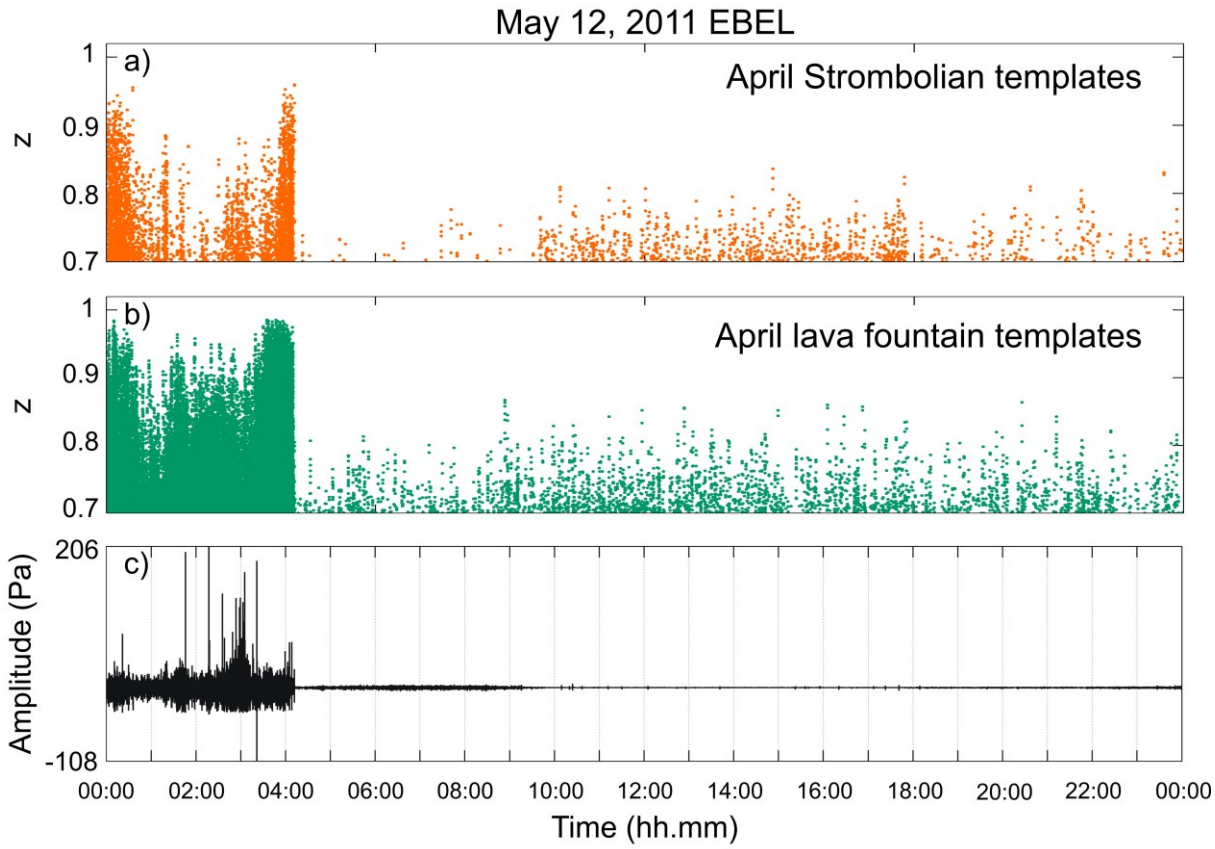

Fig. 5.47 *Event detection by means of subspace method on 12 May 2011 data adopting templates extracted from April eruption signal. z statistic values obtained using Strombolian activity* ***(a)*** *and lava fountain* ***(b)*** *templates.* ***(c)*** *Continuous infrasound signal recorded at EBEL station.*

Furthermore, by means of the accurate observation of infrasound events, we noted variability among waveforms, particularly during lava fountaining. The complexity of waveforms during the lava fountain, for the analyzed episodes, seemed to be due to the superposition of Strombolian events. To investigate this hypothesis, the approach of Rowe et al. (2000) was applied. According to this procedure we extracted a simple infrasound waveform from signal recorded during Strombolian activity, which can be considered as empirical Green's function, and duplicated it. Successively, the two identical waveforms were first time-lagged and multiplied for different amplification factors (1, 2 and 3) and finally summed. The synthetic shifted and scaled events in this way obtained are reported in **Figure 5.48.**

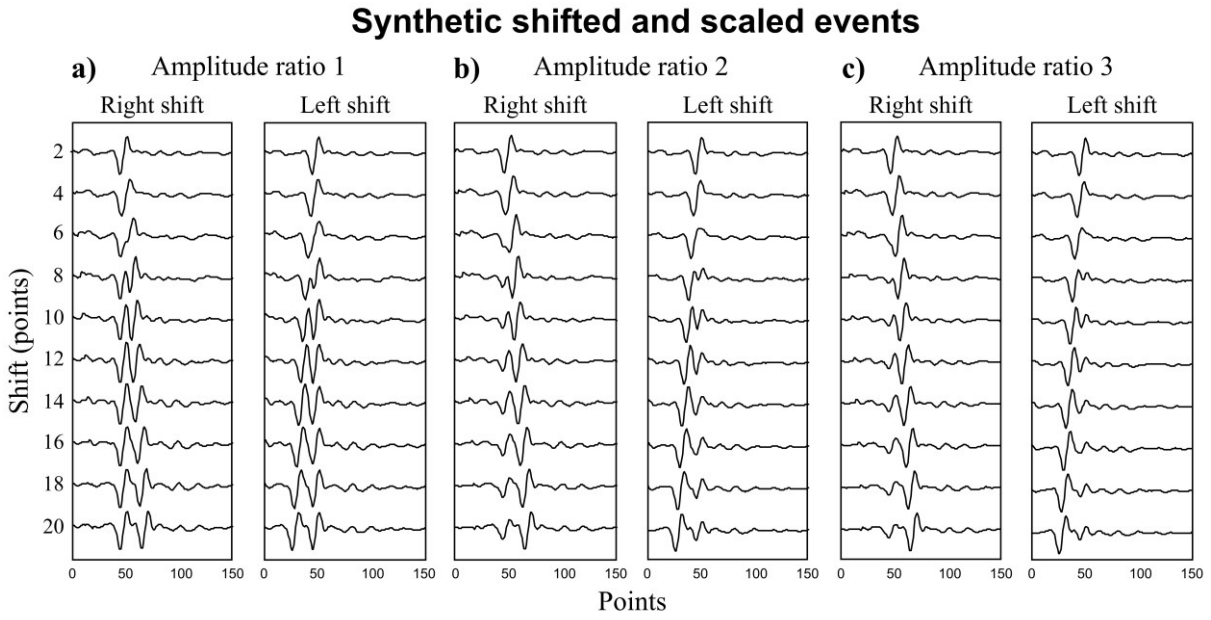

Fig. 5.48 *Synthetic events generated by summing two identical infrasound 150 point-long Strombolian events. Three sets of synthetic events were derived by superposing to the original waveform the second one scaled by amplitude factors equal to 1* ***(a)****, 2* ***(b)****, 3* ***(c)****. For each set the second waveform was time-lagged with shifts between 2 and 20 points (y axes), both on the right and left side.*

The next step consisted of using these collections of synthetic waveforms to build three sets of templates, which differ for the amplitude ratio between the two identical infrasound events (**Fig. 5.48**). Then, we applied subspaces developed from these template sets to scan 11 and 12 May infrasound data. **Figures 5.49** and **5.50** show a comparison between event detection obtained with synthetic templates (**Figs. 5.49a** and **5.50a**) and with the Strombolian and lava fountain real ones (**Figs. 5.49b** and **5.50b,** respectively). It is clearly visible in **Figure 5.50** that using synthetic events generated from a simple Strombolian event we were able to detect not only Strombolian explosions but also the lava fountain activity, as opposed to the real Strombolian templates recorded during the same eruptive episode. The distribution and values of *z* parameter in **Figures 5.49a** and **5.50a,** if compared with **Figures 5.49b** and **5.50b,** seem to have been obtained by using both the two sets of real Strombolian and lava fountain templates.

The results obtained running the subspace with such synthetic templates support the hypothesis that lava fountain events are a sort of combination in space and/or time of Strombolian events.

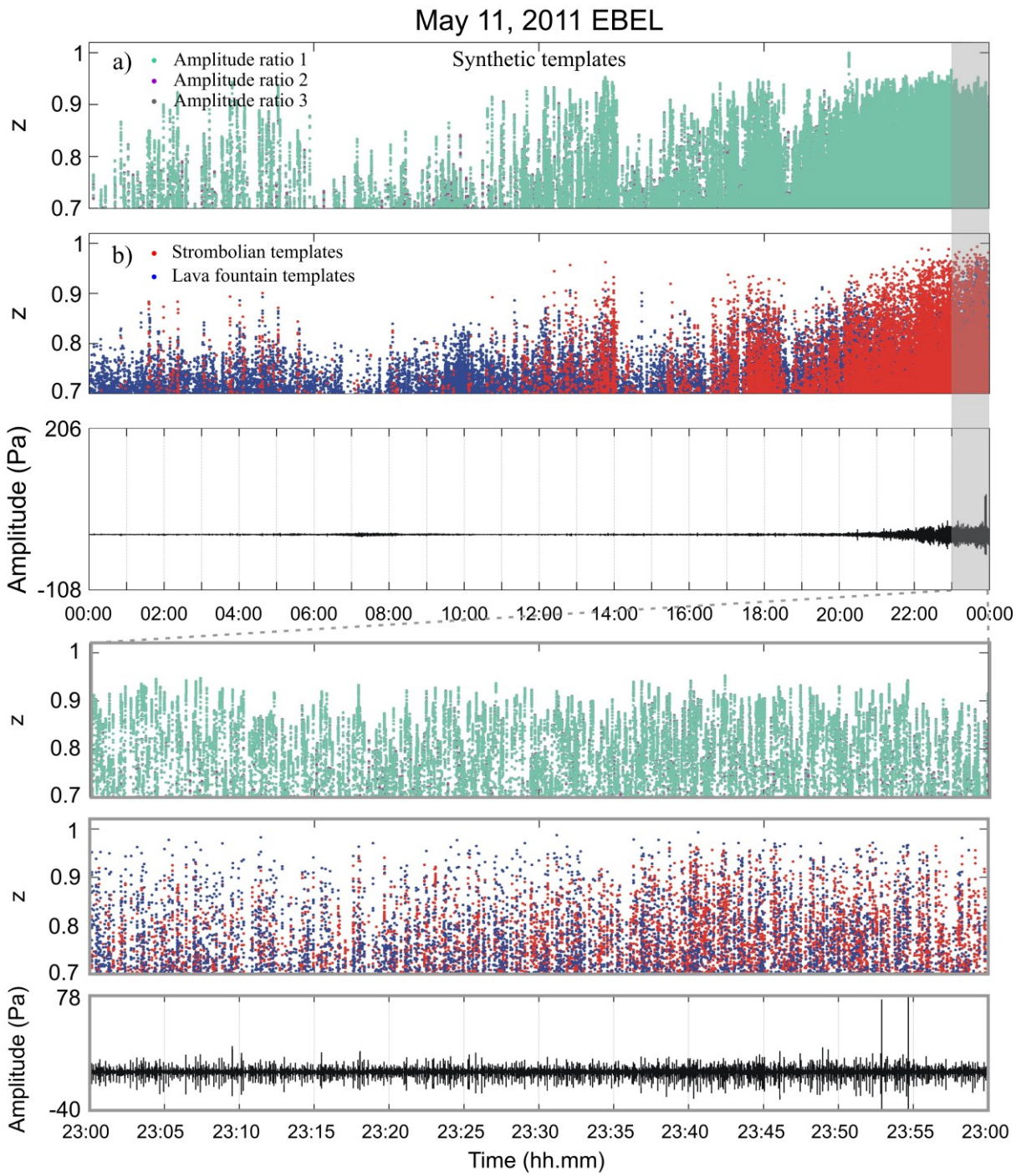

Fig. 5.49 *Event detection by means of subspace method on 11 May 2011 data adopting synthetic templates. z statistic values obtained using three different sets of templates (amplitude ratio between the two identical waveforms equal 1,2 and 3)* ***(a)****, real Strombolian activity and lava fountain templates* ***(b)*** *and relative 1-hour-long zoom.*

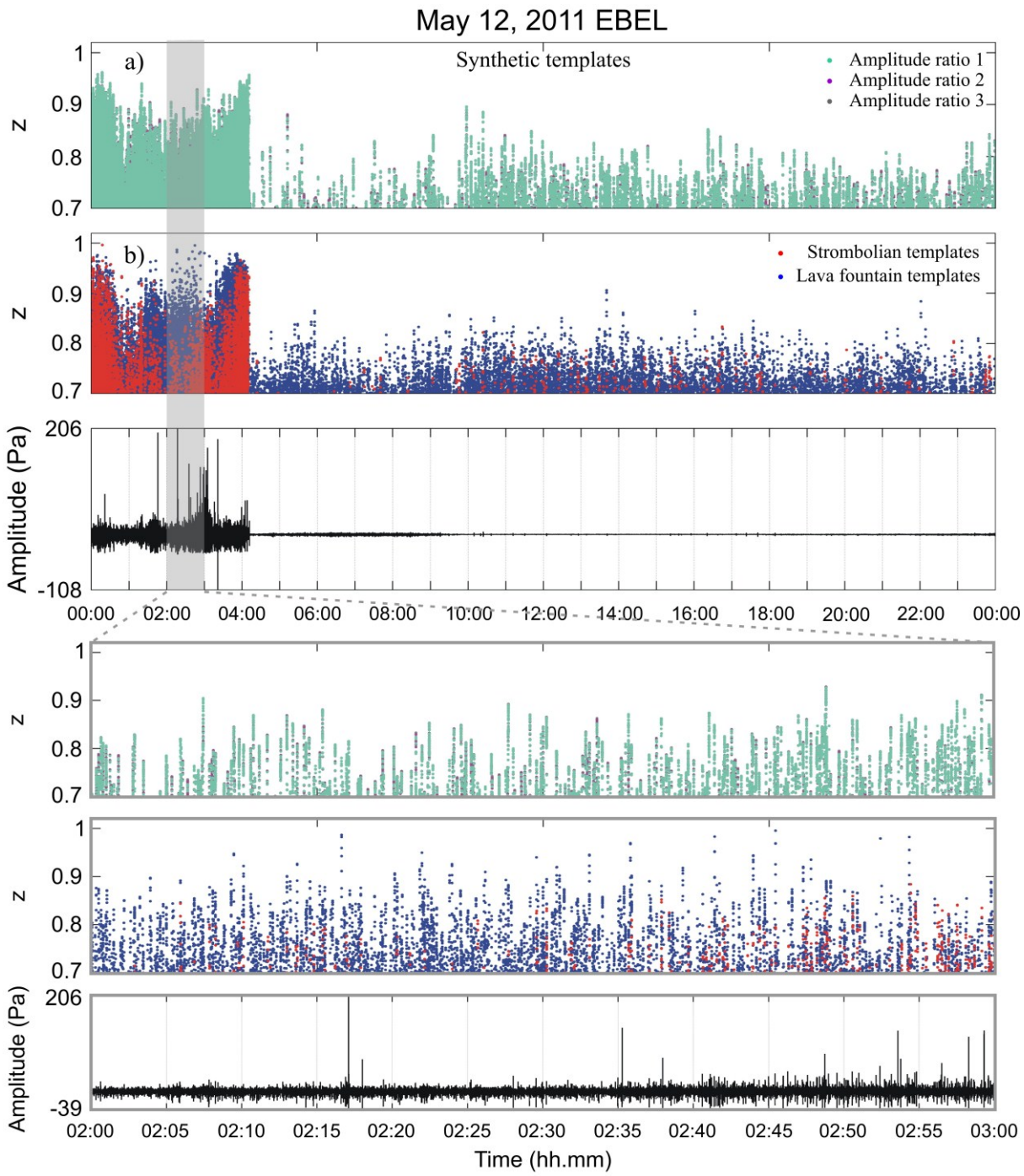

Fig. 5.50 *Event detection by means of subspace method on 12 May 2011 data adopting synthetic templates. z statistic values obtained using three different sets of templates (amplitude ratio between the two identical waveforms equal 1,2 and 3)* ***(a)****, real Strombolian activity and lava fountain templates* ***(b)*** *and relative 1-hour-long zoom.*

5.4.4. Discussion and conclusions

A dataset consisting of three different paroxysmal eruptive episodes occurring during 2011 was taken into account to test out the applicability of a subspace-based method for event detection aim. Infrasound continuous data for each episode were scanned using subspaces developed from several set of templates. As addressed in **section 3.3.2.** STA/LTA trigger algorithm reveals inefficient when amplitude transients are close in space and in time. On the contrary results obtained in this study demonstrated that subspace detector is able to detect infrasound events from a given source, being it strombolian, lava fountain or "chugging source" (**Figs. 5.41-5.45**). In particular, event detections using reference templates relative to Strombolian activity are well-correlated with Strombolian explosions observed during both April and May eruptive episode. This led us to infer that Strombolian activity produces repeating events occurring through the continuous explosive degassing. As concerning the detection of lava fountain activity, it was clearer for 10 April lava fountain (sharp increase of *z* values) with respect to 12 May, likely due to the different evolution from Strombolian to lava fountain activity.

The results, obtained by applying subspace developed from templates of April eruption to May eruption, suggest a high similarity between infrasound waveforms recorded during both the paroxysms. Assuming that the source mechanism of all the eruption infrasound events is the same (Strombolian explosions), the presence or absence of variation in the degree of similarity among infrasound waveforms (inferred from *z* values) can give indication on source dynamics and characteristics.

Resuming, due to the capability in detecting temporally close events, the subspace detector promises to be a powerful technique for automatic detection purposes. Further, based on preliminary analyses carried out on this dataset, the analysis of eruptive episodes by means of subspace detector seems to be an attractive tool to investigate the temporal evolution of explosive activity during a paroxysmal episode and among eruptive episodes (**Figs. 5.49-5.50**).

This work was a first promising attempt to apply the subspace detector to acoustic data recorded during volcanic eruption, and hence further work needs to be done.

6. CONCLUSIONS

The present thesis describes the results of the analysis of infrasound and seismo-acoustic signals produced by different types of volcanic activity at Mt. Etna, such as lava fountains, Strombolian explosions, degassing activity and short-lived ash emissions.

Recent literature has proved the importance of integrating data and adopting multidisciplinary approaches to understand volcanic phenomena (e.g., Johnson and Ripepe, 2011 and references therein).

Investigation on eruptive activity has been performed by the joint analysis of infrasound signal with seismic and video-camera data, as well as texture analysis of the deposits. The case studies taken into account have demonstrated how the multi-parameter approach is the most valuable method to track the evolution of volcanic activity and characterize the source dynamics.

Analysis techniques applied to characterize infrasound and seismo-volcanic signals have included source location, evaluation of spectral content, cross-correlation and coherence analysis, subspace detector and estimation of seismo-acoustic energy partitioning, which is related to explosive dynamics and evaluates how seismic and infrasound radiation is coupled with volcano edifice and the atmosphere.

Infrasound waves have been proved to be more suitable to address explosive and degassing dynamics during eruptive activity with respect to seismo-volcanic signals (Johnson et al., 2003). Indeed, during paroxysmal eruptions, as inferred investigating the 16 November 2006 eruptive episode, as well as during simple degassing activity, seismic signal can be affected by deeper sources (not directly related to the explosive/degassing activity), contrary to the infrasound signal which is caused by the perturbation of the atmosphere caused by the release of pressurised gas at the surface. On the other hand, during volcanic explosions, coupled seismo-acoustic signals have allowed to constrain the explosive source depth into the conduit (e.g., Gresta et al., 2004; Kobayashi et al., 2005; Petersen and McNutt, 2007) and the acoustic properties of the fluid filling conduit (Hagerty et al., 2000). The analysis of seismo-acoustic events collected during 12-13 May 2008, before the onset of 2008-2009 eruption, and their variations (in both spectral content and lag time between seismic and infrasound signal) have revealed to be fundamental to understand the eruption dynamics.

One of the main findings of the thesis lies in the modelling of North-East Crater (NEC) conduit, achieved by exploring spectral features of infrasound from this crater. NEC represents the most active crater from an infrasound point of view. Indeed, since 2006,

infrasound events, related to degassing activity at NEC, have been regularly recorded. The analysis of NEC infrasound events recorded before and after the 16 November 2006 paroxysmal activity at South-East Crater (SEC), as well as on 12-13 May 2008 a few hours before the eruption onset, provided information on both NEC shallow plumbing system and connections among the summit craters. First, the coexistence of two spectral components characterizing these infrasound events has been explained by modelling the portion of the NEC conduit above the free magma surface with the superposition of two resonance mechanisms: pipe and Helmholtz resonances. The closed-closed pipe resonance occurs in the conduit portion above the free magma level filled with a gas-mixture and produces the higher frequency peak, while the Helmholtz resonance is due to a narrowing hypothesized at the top of it and generates the lower frequency peak. Resonance mechanisms of fluid-filled conduit have been proposed in literature to explain acoustic and seismic signal behaviour at several volcanoes (e.g. Shishaldin, Petersen and McNutt, 2007; Villarrica, Goto and Johnson, 2011). In particular, the coexistence of two source mechanisms responsible for multiple frequency components has also be founded at Kilauea (Fee et al., 2010a) and at Arenal (Lesage et al., 2006) volcanoes. Fee et al. (2010a) hypothesized pipe and Helmholtz resonances inside the gas-filled cavity of the Halema`uma`u Crater producing infrasound bursts and tremor.

It is worth noting that the spectral features of the NEC infrasound events changed over time. Different interpretations were given in literature to explain the infrasound spectral changes. For instance, Fee et al. (2010a) attributed the variations of the infrasound events recorded at Halema`uma`u to an enlargement of the crater through collapses. Lesage et al. (2006) explained spectral features of seismic tremor at Arenal, which is often accompanied by acoustic waves with the same spectral band, with intermittent pressure pulses caused by intermittent gas flow through fractures in the conduit plug (acting like a clarinet reed), and the presence of pipe resonance of the portion of conduit filled with bubbly magma underneath the plug. This demonstrates how modelling of seismic and acoustic signal features strictly depends on the characteristics of volcano conduit and magma and/or gas dynamics.

Based on the NEC conduit model, the frequency decrease of NEC infrasound events observed at the end of the 16 November 2006 eruptive episode at SEC was ascribed to a lengthening of the conduit, which means a drop in the magma column. This deepening of the magma column was justified by hypothesizing a link in the plumbing systems feeding NEC and SEC. NEC is considered a branch of the central feeding conduit lying beneath Bocca Nuova (BN) and Voragine (VOR) (Burton et al., 2003; La Spina et al., 2010). Evidence of interconnected plumbing system at Etna and, in particular, of a geometrical connection between the conduits

of the central craters and SEC has been inferred by geochemical analysis of volcanic gas plume during 2007-2008 activity (Aiuppa et al., 2010) and infrasound signal investigation in September-November 2006 (Marchetti et al., 2009b). Nevertheless, Corsaro and Pompilio (2004), based on observations of the volcanic activity and petrological studies, showed how during 1995-1998 SEC erupted products exhibited different composition with respect to the central craters. On the contrary, on January 1999 the compositions were the same, thus evidencing how distinct flows and thermal regimes controlling the cooling and crystallisation of Etna magmas at SEC can develop.

Similarly, we ascribed the frequency increase of NEC infrasound events a few hours before the eruption onset at the 2008-2009 eruptive fissure to shallowing phenomena inside the NEC (free magma level raising) and possibly to variation of acoustic speed in the conduit. The occurrence of these infrasound events at NEC during 12-13 May 2008 and their temporal variations led us to infer a connection between NEC conduit dynamics and the activity at the eruptive fissure. This connection lies in a physical link between the NEC conduit and the magma storage feeding the activity at the eruptive fissure, and thus supports the results obtained by Aloisi et al. (2009). Indeed, these authors modelled an intrusion following the path of the central conduit up to a shallow storage zone (below 1.5-2.0 km a.s.l.) and then breaking off toward the east in the shallow part. In the light of this connection, variations of spectral features of infrasound events, together with time lag between seismic and infrasound events, imply shallowing phenomena of the magma level inside the NEC conduit and can be thus linked to a pressure increase inside the plumbing system. Hence, inferences on the geometrical features of NEC conduit and on the extent of the shallowing of the magma level were made. It is noteworthy that, in spite of uncertainties associated with the parameters used in the equations, depth values of the magma level and its shallowing were obtained from two independent observations (frequency increase and time lag decrease) and were in agreement.

Furthermore, this kind of an approach, consisting of the solely analysis of the frequency content changes of NEC infrasound events (16 November 2006 episode) or combined with time lag variation between these events and their seismic counterparts (12-13 May 2008 episode), can allow to monitor the condition of shallow plumbing system in terms of pressure variations. Indeed, based on the value of shallowing of magma level occurring a few hours before the 13 May 2008 activity at the eruptive fissure, a pressure increase equal to ~1.5-11 MPa was estimated, and was consistent with the driving pressure value of 13 MPa obtained by Currenti et al. (2011) for the intrusion preceding the 2008-2009 eruption.

Therefore, results arising from the thesis confirm the complexity of the shallow plumbing system of Etna and point out the involvement of NEC into the eruptive dynamics at the volcano. This is also supported by the fact that, although no eruptive activity occurred at this crater since several years, at least since 2004 its volcanic activity consists of a steady, continuous to pulsating degassing.

Focusing on minor ash emissions taking place during 2010, seismo-acoustic energy partitioning, evaluated by means of VASR, joined with analysis of the erupted products and volcanic tremor, has been used to group the explosive episodes into two types. *Type a* includes ash emissions taking place at BN and the pit-crater of SEC and implies, before the explosive event, the presence of a cap rock plugging the conduit underneath which gas accumulates. On the contrary, regarding the continuous and prolonged in time ash emission at NEC, belonging to *type b*, open conditions of the conduit were inferred. VASR values obtained for *type a* ash emission suggest that conduit conditions are temporally variable and can reflect the presence or absence of an obstruction and/or changing fragmentation depth as also observed at Karymsky (Johnson and Aster, 2005). On the contrary, clustered and higher VASR values characterizing *type b* ash emission indicate stable and efficient coupling with the atmosphere, which is in agreement with results obtained at Erebus (Johnson and Aster, 2005), where seismo-acoustic signals are generated by repeatable explosions at the surface of a persistent lava lake. Summarizing, this multi-disciplinary approach led us to infer the conduit conditions of the pit-crater of SEC, BN and NEC, during minor ash emissions in 2010, and to obtain indications about hazard.

Finally, the application of the subspace detector method to infrasound data, recorded during the paroxysmal eruptions taking place at New South-East Crater (NSEC) in 2011, have revealed to be a promising tool both to detect temporally close events from a given source and to investigate the temporal evolution and dynamics of explosive activity during a paroxysmal episode as well as for automatic detection purposes.

ACKNOWLEDGEMENTS

It would not have been possible to prepare this doctoral thesis without the help and support of many. I would like to express my deep gratitude to my supervisor Professor Stefano Gresta, who introduced me to the field of volcano seismology, his guidance and his advices taught me how to do research. I wish to sincerely thank my tutors, Dott. Andrea Cannata and Dott. Eugenio Privitera, their constructive comments and wide scientific knowledge have been of great value for me. They helped me focus my ideas throughout the PhD study and supported me with motivation and enthusiasm on both a scientific and a personal level. Especially I am grateful to the patience and perseverance of Dott. Andrea Cannata that supported me overcome many crisis situations in all the time of research and writing of this thesis.

I owe my thanks to INGV of Catania for providing me the chance to work on data and an excellent atmosphere for doing research. I also thank the infrasonic-network team of INGV for their technical support.

During this work I have collaborated with many researchers, Laura Spina, Daniele Andronico, Deborah Lo Castro, Giuseppe Di Grazia, and I wish to extend my thanks to them and to all those who have involved me in interesting and insightful discussions about volcanology and seismology.

I am thankful to Charlotte Rowe, Jeffrey Johnson, and Stephen Arrowsmith, who, during my stage in USA at Los Alamos National Laboratory and at New Mexico Tech, helped me with suggestions in seismology and field work related issues and for giving me the opportunity to work with them.

I warmly thank my officemates and colleagues whose valuable advices about technological and computer related skills and friendly help have been fundamental all the way through the PhD. Finally my invaluable thank goes to my friends and my loved ones.

REFERENCES

Acocella, V., Neri, M. (2003). What makes flank eruptions? The 2001 Etna eruption and its possible triggering mechanism. Bull. Volcanol., 65, 517-529, doi:10.1007/s00445-003-0280-3.

Aiuppa, A., Cannata, A., Cannavò, F., Di Grazia, G., Ferrari, F., Giudice, G., Gurreri, S., Liuzzo, M., Mattia, M., Montalto, P., Puglisi, G. (2010). Patterns in the recent 2007–2008 activity of Mount Etna volcano investigated by integrated geophysical and geochemical observations. Geochem. Geophys. Geosyst., 11, Q09008, doi:10.1029/2010GC003168.

Aki, K., Fehler, M., Das, S. (1977). Source mechanism of volcanic tremor: Fluid driven cracks models and their application to the 1963 Kilauea eruption. J. Volcanol. Geotherm. Res., 2, 259–287, doi:10.1016/0377-0273(77)90003-8.

Allard, P., Behncke, B., D'Amico, S., Neri, M., Gambino, S. (2006). Mount Etna 1993- 2005: Anatomy of an evolving eruptive cycle. Earth Sci. Rev., 78, 85-114, doi:10.1016/j.earscirev.2006.04.002.

Almendros, J., Chouet, B., Dawson, P., Bond, T. (2002). Identifying elements of the plumbing system beneath Kilauea Volcano, Hawaii, from the source locations of very-long-period signals. Geophys. J. Int., 148, 303–312.

Almendros, J., Chouet, B. (2003). Performance of the radial semblance method for the location of very long-period volcanic signals. Bull. Seismol. Soc. Am., 93, 1890–1903.

Aloisi, M., Cocina, O., Neri, G., Orecchio, B., Privitera, E. (2002). Seismic tomography of the crust underneath the Etna volcano, Sicily. Phys. Earth Planet. Inter., 134, 139–155, doi:10.1016/S0031-9201(02)00153-x.

Aloisi, M., Bonaccorso, A., Cannavò, F., Gambino, S., Mattia, M., Puglisi, G., Boschi, E. (2009). A new dike intrusion style for the Mount Etna May 2008 eruption modelled through continuous tilt and GPS data. Terra Nova 21, 316–321, doi:10.1111/j.1365-3121.2009.00889.x.

Alparone, S., Andronico, D., Lodato, L., Sgroi, T. (2003). Relationship between tremor and volcanic activity during the Southeast Crater eruption on Mount Etna in early 2000. J. Geophys. Res., 108(B5), 2241, doi:10.1029/2002JB001866.

Alparone, S., Cannata, A., Gresta, S. (2007a). Time variation of spectral and wavefield features of volcanic tremor at Mt. Etna (January–June 1999). J. Volcanol. Geotherm. Res., doi:10.1016/j.jvolgeores.2006.12.012.

Alparone, S., Andronico, D., Sgroi, T., Ferrari, F., Lodato, L., Reitano, D. (2007b). Alert system to mitigate tephra fallout hazards at Mt. Etna Volcano, Italy. Nat. Hazards, 43, 333–350, doi 10.1007/s11069-007-9120-7.

Alster, M. (1972). Improved calculation of resonant frequencies of Helmholtz resonators. J. Sound Vib., 24, 63–85.

Andronico, D., Lodato, L. (2005). Effusive Activity at Mount Etna Volcano (Italy) During the 20th Century: A Contribution to Volcanic Hazard Assessment. Natural Hazard, 36, 407-443. doi:10.1007/s11069-005-1938-2.

Andronico, D., Scollo, S., Cristaldi, A., Ferrari, F. (2008). Monitoring ash emission episodes at Mt. Etna: 16 November 2006 case study. J. Volcanol. Geotherm. Res., 180, 123-134, doi:10.1016/j.jvolgeores.2008.10.019.

Andronico, D., Scollo, S., Cristaldi, A., Ferrari, F. (2009a). Monitoring ash emission episodes at Mt. Etna: the 16 November 2006 case study. J. Volcanol. Geotherm. Res., 180 (2–4), 123–134, doi:10.1016/j.jvolgeores.2008.10.019.

Andronico, D., A. Cristaldi, , P. Del Carlo, and J. Taddeucci (2009b). Shifting styles of basaltic explosive activity during the 2002-03 eruption of Mt Etna, Italy. J. Volcanol. Geotherm. Res., 180 (2–4), 110–122, doi:10.1016/j.jvolgeores.2008.07.026.

Andronico, D., Corsaro, R.A. (2011). Lava fountains during the episodic eruption of South–East Crater (Mt. Etna), 2000: insights into magma-gas dynamics within the shallow volcano plumbing system. Bull. Volcanol., doi:10.1007/s00445-011-0467-y.

Andronico, D., Lo Castro, D., Sciotto, M., Spina, L.. The 2010 ash emissions at the summit craters of Mt Etna: Relationship with seismo-acoustic signals. Submitted to J. Geophys. Res..

Apuani, T., Corrazzato, C., Merri, A., Tibaldi, A. (2012). Understanding Etna flank instability through numerical models. J. Volcanol. Geotherm. Res., doi:10.1016/j.jvolgeores.2012.06.015.

Arrowsmith, S., Johnson, J., Drob, D., Hedlin, M. (2010). The Seismo-Acoustic Wavefield: A new paradigm in studying geophysical phenomena. Review of Geophysics, doi:10.1029/2010RG000335.

Bailey, J., Harris, A., Dehn, J., Calvari, S., Rowland, S. (2006). The changing morphology of an open lava channel on Mt. Etna. Bull. Volcanol., 68, 497–515.

Barreca, G., Bonforte, A., Neri, M. (2012). A pilot GIS database of active faults of Mt. Etna (Sicily): A tool for integrated hazard evaluation. J. Volcanol. Geotherm. Res., http://dx.doi.org/10.1016/j.jvolgeores.2012.08.013.

Battaglia, J., Aki, K. (2003). Location of seismic events and eruptive fissures on the Piton de la Fournaise volcano using seismic amplitudes. J. Geophys. Res., 108 (B8). doi:10.1029/2002JB002193.

Battaglia, J., Aki, K., Ferrazzini, V. (2005). Location of tremor sources and estimation of lava output using tremor source amplitude on the Piton de la Fournaise volcano: 1. Location of tremor sources. J. Volcanol. Geotherm. Res. 147, 268-290, doi:10.1016/j.jvolgeores.2005.04.005.

Bean, C., Lokmer, I., O'Brien, G. (2008). Influence of near-surface volcanic structure on long-period seismic signals and on moment tensor inversions: Simulated examples from Mount Etna. J. Geophys. Res., 113, B08308, doi:10.1029/2007JB005468.

Behncke, B., Neri, M. (2008). Eruzione dell'Etna del 13–14 Maggio 2008, Sopralluoghi con elicottero, Aggiornamento delle ore 13:00 (tempi espressi in ora locale). INGV-Open file report.

Behncke, B., Calvari, S., Giammanco, S., Neri, M., Pinkerton, H. (2008). Pyroclastic density currents resulting from the interaction of basaltic magma with hydrothermally altered rock: an example from the 2006 summit eruptions of Mount Etna, Italy. Bull. Volcanol., 70, 1249-1268, doi:10.1007/s00445-008-0200-7.

Behncke, B. (2009). Hazards from pyroclastic density currents at Mt. Etna (Italy). J. Volcanol. Geotherm. Res., 180, 148–160, doi:10.1016/j.jvolgeores.2008.09.021.

Behncke, B., Falsaperla, S., Pecora, E. (2009). Complex magma dynamics at Mount Etna revealed by seismic, thermal, and volcanological data. J. Geophys Res., 114, B03211, doi:10.1029/2008JB005882.

Benson, P.M., Vinciguerra, S., Meredith, P.G., Young, R.P. (2010). Spatio-temporal evolution of volcano seismicity: A laboratory study. Earth Planet. Sci. Lett., 297, 315-323.

Boatwright, J. (1980). A spectral theory for circular seismic sources: simple estimates of source dimension, dynamic stress drop, and radiated seismic energy. Bull. Seismol. Soc. Am., 70 (1), 1-27.

Bonaccorso, A., Davis, P.M. (1999). Models of ground deformation from vertical volcanic conduits with application to eruptions of Mount St. Helens and Mount Etna. J. Geophys. Res., 104, 10531–10542.

Bonaccorso, A., Bonforte, A., Calvari, S., Del Negro, C., Di Grazia, G., Ganci, G., Neri, M., Vicari, A., Boschi, E. (2011). The initial phases of the 2008–2009 Mount Etna eruption: A multidisciplinary approach for hazard assessment. J. Geophys. Res., 116, doi:10.1029/2010JB007906.

Bonforte, A., Guglielmino, F., Coltelli, M., Ferretti, A., Puglisi, G. (2011). Structural assessment of Mt. Etna volcano from Permanent Scatterers analysis. Geochem. Geophys. Geosyst., 12, doi:10.1029/2010GC003213.

Borgia, A., Ferrari, L., Pasquarè, G. (1992). Importance of gravitational spreading in the tectonic and volcanic evolution of Mount Etna. Nature, 357, 231– 235.

Borgia, A., Lanari, R., Sansosti, E., Tesauro, M., Berardino, P., Fornaro, G., Neri, M., Murray, J. B. (2000). Actively growing anticlines beneath Catania from distal motion of Mount Etna's decollement measured by SAR interferometry and GPS. Geophys. Res. Lett., 27, 3409–3412, doi:10.1029/1999GL008475.

Bouche, E., Vergniolle, S., Staudacher, T., Nercessian, A., Delmont, J.C., Frogneux, M., Cartault, F., Le Pichon, A. (2010). The role of large bubbles detected from acoustic measurements on the dynamics of Erta 'Ale lava lake (Ethiopia). Earth Planet. Sci. Lett., 295, 37-48.

Bousquet, J.C., Lanzafame, G. (2001). Nouvelle interprètation des fracture des éruption latérales de l'Etna: conséquences pour son cadre tectonique. Bull. Soc. Geol. Fr., 172, 455-467.

Branca, S., Carbone, D., Greco, F. (2003). Intrusive mechanism of the 2002 NE-Rift eruption at Mt. Etna (Italy) inferred through continuous microgravity data and volcanological evidences. Geophys. Res. Lett., 30, doi:10.1029/2003GL018250.

Branca, S., Coltelli, M., & Groppelli, G. (2004). Geological evolution of Etna volcano. In: Mt. Etna: Volcano Laboratory, Bonaccorso, A., Calvari, S., Coltelli, M., Del Negro, C., Falsaperla, S., 49-63, American Geophysical Union, Geophysical Monograph, 143.

Branca, S., Coltelli, M., De Beni, E., Wijbrans, J. (2007). Geological evolution of Mount Etna volcano (Italy) from earliest products until the first central volcanism (between 500 and 100 ka ago) inferred from geochronological and stratigraphic data. Int. J. Earth Sci., doi:10.1007/s00531-006-0152-0.

Burton, M., Allard, P., Mure`, F., Oppenheimer, C. (2003). FTIR remote sensing of fractional magma degassing at Mt. Etna, Sicily, in Volcanic Degassing, edited by C. Oppenheimer, D. Pyle, and J. Barclay, Geol. Soc. Spec. Publ., 213, 281- 293.

Campbell B., Peatross, J. (2011) Experimental methods in Physics, Phys 145. Brigham Young University.

Cannata, A., Catania, A., Alparone, S., Gresta, S. (2008). Volcanic tremor at Mt. Etna: Inferences on magma dynamics during effusive and explosive activity. J. Volcanol. Geotherm. Res., 178, 19-31, doi:10.1016/j.jvolgeores.2007.11.027.

Cannata, A. (2009). Location and modelling of the magma plumbing system at Mt. Etna by analysing seismic long period signals. PhD Thesis.

Cannata, A., Hellweg, M., Di Grazia, G., Ford, S., Alparone, S., Gresta, S., Montalto, P., Patanè, D. (2009a). Long Period and Very Long Period events at Mt. Etna volcano: evidence of strong time variability and strict interrelationship. J. Volcanol. Geotherm. Res., 187, 227-249, doi:10.1016/j.jvolgeores.2009.09.007.

Cannata, A., Montalto, P., Privitera, E., Russo, G., Gresta, S. (2009b). Tracking eruptive phenomena by infrasound: May 13, 2008 eruption at Mt. Etna. Geophys. Res. Lett., 36, L05304, doi:10.1029/2008GL036738.

Cannata, A., Montalto, P., Privitera, E., Russo, G. (2009c). Characterization and location of infrasonic sources in active volcanoes: Mt. Etna, September-November 2007. J. Geophys. Res., 114, B08308, doi:10.1029/2008JB006007.

Cannata, A., Di Grazia, G., Montalto, P., Ferrari, F., Nunnari, G., Patanè, D., Privitera, E. (2010a). New insights into banded tremor from the 2008–2009 Mt. Etna eruption. J. Geophys. Res., 115, B12318, doi:10.1029/2009JB007120.

Cannata, A., Di Grazia, G., Montalto, P., Aliotta, M., Patanè, D., Boschi, E. (2010b). Response of Mount Etna to dynamic stresses from distant earthquakes. J. Geophys. Res., 115, B12304, doi:10.1029/2010JB007487.

Cannata, A., Sciotto, M., Spina, L., Spampinato, L. (2011a). Insights into explosive activity at eruptive fissure closely-spaced vents by infrasound signals: example of Mt. Etna 2008 eruption. J. Volcanol. Geotherm. Res., 208, 1–11.

Cannata, A., Montalto, P., Aliotta, M., Cassisi, C., Pulvirenti, A., Privitera, E., Patanè, D. (2011b). Clustering and classification of infrasonic events at Mount Etna using pattern recognition techniques. Geophys. J. Int., 185, 253-264, doi: 10.1111/j.1365-246X.2011.04951.x.

Caplan-Auerbach, J., Bellesiles, A., Fernandes, J.K. (2009). Estimates of eruption velocity and plume height from infrasonic recordings of the 2006 eruption of Augustine Volcano, Alaska. J. Volcanol. Geotherm. Res., 189, 12-18, doi:10.1016/j.jvolgeores.2009.10.002.

Cassisi, C., Aliotta, M., Cannata, A., Montalto, P., Patanè, D., Pulvirenti, A., Spampinato, L. (2012). Motif Discovery on Seismic Amplitude Time Series: The Case Study of Mt Etna 2011 Eruptive Activity. Pure Appl. Geophys., doi 10.1007/s00024-012-0560-y.

Chouet, B. (1981). Ground motion in the near field of a fluid-driven crack and its interpretation in the study of shallow volcanic tremor. J. Geophys. Res., 86, 5985–6016.

Chouet, B. (1992). A seismic model for the source of long period events and harmonic tremor, In "Volcanic seismology" (Gasparini, Scarpa and Aki Eds.), Springer Verlag, Berlin, 133-156.

Chouet, B.A., Page, R.A., Stephens, C.D., Lahr, J.C., Power, J.A. (1994). Precursory swarms of long-period events at Redoubt Volcano (1989-1990), Alaska: their origin and use as a forecasting tool. J. Volcanol. Geotherm. Res., 62, 95–135.

Chouet, B. (1996). Long-period volcano seismicity: its source and use in eruption forecasting. Nature, 380, 309–316.

Chouet, B. (2003). Volcano seismology. Pure Appl. Geophys., 160, 739–788, doi:10.1007/PL00012556.

Chouet, B., Dawson, P., Ohminato, T., Martini, M., Saccorotti, G., Giudicepietro, F., De Luca, G., Milana, G., Scarpa, R. (2003). Source mechanism of explosions at Stromboli

Volcano, Italy, determined from moment-tensor inversions of very-long-period data. J. Geophys. Res., 108(B1), doi:10.1029/20042JB001919.

Chouet, B., Dawson, P., Arciniega-Ceballos, A. (2005). Source mechanism of Vulcanian degassing at Popocate´petl volcano, Me´xico, determined from waveform inversions of very long period signals. J. Geophys. Res., 110, B07301.

Cocina, O., Neri, G., Privitera, E., Spampinato, S. (1998). Seismogenic stress field beneath Mt. Etna (South Italy) and possible relationships with volcano-tectonic features. J. Volcanol. Geotherm. Res., 83, 335-348.

Coltelli, M., Del Carlo, P., Vezzoli, L. (2000). Stratigraphic constraints for esplosive activity in the last 100 ka at Etna volcano, Italy. Int. J. Earth Sci., 89, 665-677.

Cooley, J.W., Tukey, J.W. (1965). An algorithm for the machine calculation of complex Fourier series. Math. Comput., 19, 297-301.

Corsaro, R.A., Pompilio, M. (2004). Magma dynamics in the shallow plumbing system of Mt. Etna as recorded by compositional variations in volcanics of recent summit activity (1995-1999). J. Volcanol. Geotherm. Res., 137, 55-71.

Corsaro, R.A., Miraglia, L., Pompilio, M. (2007). Petrologic evidence of a complex plumbin system feeding the July–August 2001 eruption of Mt. Etna, Sicily, Italy. Bull. Volcanol., 69 (4), 401–421. doi:10.1007/s00445-006-0083-4.

Corsaro, R.A. (2009). Rapporto settimanale sull'attività eruttiva dell'Etna (16 – 22 novembre 2009). Report UFVG2009/87, INGV, Catania, Italy.

Corsaro, R.A., Di Renzo, V., Distefano, S., Miraglia, L., Civetta, L. (2012). Relationship between petrologic processes in the plumbing system of Mt. Etna and the dynamics of the eastern flank from 1995 to 2005. J. Volcanol. Geotherm. Res., doi:10.1016/j.jvolgeores.2012.02.010.

Cristofolini, R., Ghisetti, F., Riuscetti, M., Vezzani, L. (1979). Neotectonic seismicity and volcanic activity in northeastern Sicily. VI Colloquium on the geology of the Aegean Region, 757– 766.

Currenti, G., Napoli, R., Di Stefano, A., Greco, F., Del Negro, C. (2011). 3D integrated geophysical modeling for the 2008 magma intrusion at Etna: Constraints on rheology and dike overpressure. Physics of the Earth and Planetary Interiors, 185, 44-52.

De Angelis, S., McNutt, S.R. (2007). Observations of volcanic tremor during the January-February 2005 eruption of Mt. Veniaminof, Alaska. Bull. Volcanol., 69, 927-940, doi: 10.1007/s00445-007-0119-4.

De Barros, L., Bean, C.J., Lokmer, I., Saccorotti, G., Zuccarello, L., O'Brien, G.S., Métaxian, J.-P., Patanè, D. (2009). Source geometry from exceptionally high resolution long period event observations at Mt. Etna during the 2008 eruption. Geophys. Res. Lett., 36, L24305, doi:10.1029/2009GL041273.

De Beni, E., Branca, S., Coltelli, M., Groppelli, G., Wijbrans, J. (2011). 40Ar/39Ar isotopic dating of Etna volcanic succession. Ital. J. Geosci. (Boll. Soc. Geol. It.), 130 (3), 292-305. doi:10.3301/IJG.2011.14.

Di Grazia, G., Falsaperla, S., Langer, H. (2006). Volcanic tremor location during the 2004 Mount Etna lava effusion. Geophys. Res. Lett., 33, L04304, doi:10.1029/2005GL025177.

Di Grazia, G., Cannata, A., Montalto, P., Patanè, D., Privitera, E., Zuccarello, L., Boschi, E. (2009). A multiparameter approach to volcano monitoring based on 4D analyses of seismo-volcanic and acoustic signals: the 2008 Mt.Etna eruption. Geophys. Res. Lett., 36, L18307, doi:10.1029/2009GL039567.

Diehl, R.L. (2008). Acoustic and auditory phonetics: the adaptive design of speech sound systems. Phil. Trans. R. Soc., B 363, 965–978.

Divoux, T., Vidal, V., Melo, F., Géminard, J.C. (2008). Acoustic emission associated with the bursting of a gas bubble at the free surface of a non-newtonian fluid. Phys. Rev., E, 77, 056310, doi:10.1103/PhysRevE.77.056310.

Doglioni, C., Innocenti, F., Mariotti, G. (2001). Why Mt. Etna? Terra Nova, 13, 25-31.

Falsaperla, S., Cara, F., Rovelli, A., Neri, M., Behncke, B., Acocella, V. (2010). Effects of the 1989 fracture system in the dynamics of the upper SE flank of Etna revealed by volcanic tremor data: The missing link? J. Geophys. Res., 115, B11306, doi:10.1029/2010JB007529.

Fee, D., Garcés, M., Patrick, M., Chouet, B., Dawson, P., Swanson, D. (2010a). Infrasonic harmonic tremor and degassing bursts from Halema'uma'u Crater, Kilauea Volcano, Hawaii. J. Geophys. Res., 115, B11316, doi:10.1029/2010JB007642.

Fee, D., Garces, M., Steffke, A. (2010b). Infrasound from Tungurahua Volcano 2006–2008: Strombolian to Plinian eruptive activity. J. Volcanol. Geotherm. Res., 193 (1–2), 67–81, doi:10.1016/j.jvolgeores.2010.03.006.

Fee, D., Matoza, R.S. (2013). An overview of volcano infrasound: From hawaiian to plinian, local to global. J. Volcanol. Geotherm. Res., 249, 123-139, .doi:10.1016/j.jvolgeores.2012.09.002.

Ferlito, C., Viccaro, M., Nicotra, E., Cristofolini, R. (2010). Relationship between the flank sliding of the South East Crater (Etna, Italy) and the paroxysmal event of November 16, 2006. Bull. Volcanol., 72, 1179-1190, doi:10.1007/s00445-010-0384-5.

Firstov, P.P., Kravchenko, N.M. (1996). Estimation of the amount of explosive gas released in volcanic eruptions using air waves. Volcanol. Seismol., 17, 547–560.

Garces, M.A., McNutt, S.R. (1997). Theory of the airborne sound field generated in a resonant magma conduit. J. Volcanol. Geotherm. Res., 78, 155–178.

Garces, M.A., Hagerty, M.T., Schwartz, S.Y. (1998). Magma acoustics and time-varying melt properties at Arenal Volcano, Costa Rica. Geophys. Res. Lett., 25 (13), 2293-2296.

Garces, M.A. (2000). Theory of acoustic propagation in a multi-phase stratified liquid flowing within an elastic-walled conduit of varying cross-sectional area. J. Volcanol. Geotherm. Res., 101 (1–2), 1–17.

Garcés, M.A., Harris, A., Hetzer, C., Johnson, J.B., Rowland, S., Marchetti, E., Okubo, P. (2003). Infrasonic tremor observed at Kilauea volcano, Hawaii. Geophys. Res. Lett., 30(20), 2023, doi:10.1029/2003GL018038.

Gibbons, S., Ringdal, F. (2006). The detection of low magnitude seismic events using array-based waveform correlation. Geophys. J. Int., 165:149–166.

Gibert, D., Beauducel, F., Déclais, Y., Lesparre, N., Marteau, J., Nicollin, F., Tarantola, A. (2010). Muon tomography: Plans for observations in the Lesser Antilles. Earth Planets Space, 62, 153-165.

Gilbert, J.S., Lane, S.J. (2008). The consequences of fluid motion in volcanic conduits, In Fluid Motions in Volcanic Conduits: A source of seismic and Acoustic Signals (Lane, S.J. and Gilbert, J.S. Eds), Geological Society, London, Special Publications, 307, 1-10, doi:10.1144/SP307.1.

Gomez, D.M., Torres, R.A. (1997). Unusual low-frequency volcanic seismic events with slowly decaying coda waves observed at Galeras and other volcanoes. J. Volcanol. Geoth. Res., 77, 173–193.

Gonnermann, H.M., Manga, M. (2007). The Fluid Mechanics Inside a Volcano. Annu. Rev. Fluid Mech., 39, 321–356, doi:10.1146/annurev.fluid.39.050905.110207.

Goto, A., Johnson, J.B. (2011). Monotonic infrasound and Helmholtz resonance at Volcan Villarrica (Chile). Geophys. Res. Lett., 38, L06301, doi:10.1029/2011GL046858.

Green, D., Neuberg, J. (2006). Waveform classification of volcanic low-frequency earthquake swarms and its implication at Soufrière Hills Volcano, Monserrat. J. Volcanol. Geotherm. Res., 153, 51-63, doi:10.1016/j.jvolgeores.2005.08.003.

Gresta, S., Montalto, A., Patanè, G. (1991). Volcanic tremor at Mt. Etna (January 1984–March 1985): its relationship to the eruptive activity and modelling of the summit feeding system. Bull. Volcanol., 53, 309–320.

Gresta, S., Ripepe, M., Marchetti, E., D'Amico, S., Coltelli, M., Harris, A.J.L., Privitera, E. (2004). Seismoacoustic measurements during the July August 2001 eruption at Mt. Etna volcano, Italy. J. Volcanol. Geotherm. Res., 137, 219–230, doi:10.1016/j.jvolgeores.2004.05.017.

Gvirtzman, Z., Nur, A. (1999). The formation of Mount Etna as the consequence of slab rollback. Nature, 401, 782–785.

Hagerty, M.T., Schwartz, S.Y., Garces, M.A., Protti, M. (2000). Analysis of seismic and acoustic observations at Arenal Volcano, Costa Rica, 1995-1997. J. Volcanol. Geotherm. Res., 101, 27-65, doi:10.1016/S0377-0273(00)00162-1.

Harris, A., Dehn, J., Patrick , M., Calvari, S., Ripepe, M., Lodato, L. (2005). Lava effusion rates from hand-held thermal infrared imagery: an example from the June 2003 effusive activity at Stromboli. Bull. Volcanol., 68, 107–117.

Harris, D. (2006). Subspace Detectors: Theory, Lawrence Livermore National Laboratory Internal Report UCRL-TR-222758, 46. (http://www.llnl.gov/tid/lof/documents/pdf/335299.pdf).

Harris, D.B, Dodge, D.A. (2011). An Autonomous System for Grouping Events in a Developing Aftershock Sequence. Bull. Seism. Soc. Am., 101 (2), 763–774.

Hedlin, M.A.H., Walker, K., Drob, D.P., de Groot-Hedlin, C.D. (2012). Infrasound: Connecting the Solid Earth, Oceans, and Atmosphere. Annu. Rev. Earth Planet. Sci., 40, 327–354, doi: 10.1146/annurev-earth-042711-105508.

Houlie, N., Montagner, J.P. (2007). Hidden Dykes detected on Ultra Long Period seismic signals at Piton de la Fournaise volcano? Earth Planet. Sci. Lett., 261, 1-8.

Ishihara, K. (1985). Dynamical analysis of volcanic explosion. J. Geodyn., 3, 327–349.

Johnson, K. (1997). Acoustic and Auditory Phonetics. Malden, MA, Blackwell Publishers.

Johnson, J.B., Lees, J.M. (2000). Plugs and chugs: Seismic and acoustic observations of degassing explosions at Karymsky, Russia and Sangay, Ecuador. J. Volcanol. Geotherm. Res., 101, 67–82, doi:10.1016/S0377-0273(00)00164-5.

Johnson, J.B. (2003). Generation and propagation of infrasonic airwaves from volcanic explosions. J. Volc. Geotherm. Res., 121, 1-14.

Johnson, J.B., Aster, R.C., Ruiz, M.C., Malone, S.D., McChesney, P.J., Lees, J.M., Kyle, P.R. (2003). Interpretation and utilità of infrasonic records from erupting volcanoes. J. Volcanol. Geotherm. Res., 121, 15-63.

Johnson, J.B., Harris, A.J.L., Sahetapy-Engel, S.T.M., Wolf, R., Rose, W.I. (2004). Explosion dynamics of pyroclastic eruptions at Santiaguito volcano. Geophys. Res. Lett., 31, L06610, doi:10.1029/2003GL019079.

Johnson, J.B. (2005). Source location variability and volcanic vent mapping with a small-aperture infrasound array at Stromboli Volcano, Italy. Bull. Volcan., 67, 1–14.

Johnson, J.B., Aster, R.C. (2005). Relative partitioning of acoustic and seismic energy during Strombolian eruptions. J. Volcanol. Geotherm. Res., 148, 334–354, doi:10.1016/j.jvolgeores.2005.05.002.

Johnson, J.B., Ruiz, M.C., Lees, J.M., Ramón, P. (2005). Poor scaling between elastic energy release and eruption intensity at Tungurahua volcano, Ecuador. Geophys. Res. Lett., 32, L15304, doi:10.1029/2005GL022847.

Johnson, J.B. (2007). On the relation between, infrasound, seismicity, and small pyroclastic explosions at Karymsky volcano. J. Geophys. Res., 112, B08203, doi:10.1029/2006JB004654.

Johnson, J.B., Ripepe, M. (2011). Volcano infrasound: A review. J. Volcanol. Geotherm. Res., 206, 61-69, doi:10.1016/j.jvolgeores.2011.06.006.

Johnson, J.B., Anderson, J., Anthony, R., Sciotto, M.. Detecting geyser activity with infrasound. In preparation.

Jones, K.R., Johnson, J.B. (2010). Mapping complex vent eruptive activity at Santiaguito, Guatemala using network infrasound semblance. J. Volcanol. Geotherm. Res., doi:10.1016/j.jvolgeores.2010.08.006.

Jones, J.P., Carniel, R., Malone, S.D. (2011). Decomposition, location, and persistence of seismic signals recovered from continuous tremor at Erta 'Ale, Ethiopia. J. Volcanol. Geotherm. Res., doi:10.1016/j.jvolgeores.2011.07.007.

Jong, A.T.d., Bijl, H. (2010). Investigation of higher spanwise Helmholtz resonance modes in slender covered cavities. J. Acoust. Soc. Am., 128 (4), 1668-1678.

Kao, H., Shan, S.J. (2004). The source-scanning algorithm: mapping the distribution of seismic sources in time and space. Geophys. J. Int., 157, 589–594.

Kawakatsu, H., Yamamoto, M. (2007). Volcano Seismology, In Treatise on Geophysics (Schubert, G. Ed.), 4, 389-420, Oxford: Elsevier.

Kinsler, L.E., Frey, A.R., Coppens, A.B., Sanders, J.V. (1982). Fundamentals of Acoustics. Third Edition ed., John Wiley and Sons, 480pp.

Kobayashi, T., Ida, Y., Ohminato, T. (2005). Small inflation sources producing seismic and infrasonic pulses during the 2000 eruptions of Miyake-jima, Japan. Earth Planet. Sci. Lett., 240, 291–301.

Kobayashi, T., Namiki, A., Sumita, I. (2010). Excitation of airwaves caused by bubble bursting in a cylindrical conduit: Experiments and a model. J. Geophys. Res., 115, B10201, doi:10.1029/2009JB006828.

Konstantinou, K. I., Schlindwein, V. (2003). Nature, wavefield properties and source mechanism of volcanic tremor: A review. J. Volcanol. Geotherm. Res., 119(1–4), 161-187, doi:10.1016/S0377-0273(02)00311-6.

Kubotera, A., (1974). Volcanic tremors at Aso volcano, In "Physical Volcanology" (Civetta, Gasparini, Luongo and Rapolla Eds.), Elsevier, Amsterdam, 29-47.

Kumagai, H., Chouet, B. (1999). The complex frequencies of long-period seismic events as probes of fluid composition beneath volcanoes. Geophys. J. Int., 138, F7-F12.

Kumagai, H., Chouet, B.A. (2000). Acoustic properties of a crack containing magmatic or hydrotermal fluids. J. Geophys. Res., 105, 25493-25512.

Kumagai, H., Chouet, B.A. (2001). The dependence of acoustic properties of a crack on the resonance mode and geometry. Geophys. Res. Lett., 28, 3325-3328, doi:10.1029/2001GL013025.

Kumagai, H., Nakano, M., Maeda, T., Yepes, H., Palacios, P., Ruiz, M., Arrais, S., Vaca, M., Molina, I., Yamashima, T. (2010). Broadband seismic monitoring of active volcanoes using deterministic and stochastic approaches. J. Geophys. Res., 115, B08303, doi:10.1029/2009JB006889.

Kumazawa, M., Imanishi, Y., Fukao, Y., Furumoto, M., Yamamoto, A. (1990). A theory of spectral analysis based on the characteristic property of a linear dynamic system. Geophys. J. Int., 101, 613-630, doi:10.1111/j.1365-246X.1990.tb05574.x.

La Spina, A., Burton, M., Salerno, G.G. (2010). Unravelling the processes controlling gas emissions from the Central and Northeast craters of Mt. Etna. J. Volcanol. Geotherm. Res., 198, 368-376, doi:10.1016/j.jvolgeores.2010.09.018.

Lahr, J., Page, R.A., Chouet, B.A., Stephens, C.D., Harlow, D.H. (1994). Seismic evolution of the 1989–90 eruption sequence of Redoubt Volcano, Alaska. J. Volcanol. Geotherm. Res., 62, 69–94.

Langer, H., Falsaperla, S., Messina, A., Spampinato, S., Behncke, B. (2011). Detecting imminent eruptive activity at Mt Etna, Italy, in 2007-2008 through pattern classification of volcanic tremor data. J. Volcanol. Geotherm. Res., 200, 1–17, doi: 10.1016/j.jvolgeores.2010.11.019.

Lees, J.M., Ruiz, M. (2008). Non-linear Explosion Tremor at Sangay, Volcano, Ecuador. J. Volcanol. Geotherm. Res., 176(1): 170-178 doi:10.1016/j.jvolgeores.2007.08.012.

Lees, J.M., Johnson, J.B., Ruiz, M., Troncoso, L., Welsh, M. (2008). Reventador Volcano 2005: Eruptive activity inferred from seismo-acoustic observation. J. Volcanol. Geotherm. Res., 176, 179-190, doi:10.1016/j.jvolgeores.2007.10.006.

Lentini, F., Carbone, S., Guarnieri, P. (2006). Collisional and postcollisional tectonics of the Apenninic-Maghrebian orogen (southern Italy), in Dilek, Y., and Pavlides, S., eds., Postcollisional tectonics and magmatism in the Mediterranean region and Asia, Geological Society of America Special Paper 409, 57–81, doi:10.1130/2006.2409(04).

Lesage, P., Mora, M.M., Alvarado, G.E., Pacheco, J., Métaxian, J-P. (2006). Complex behaviour and source model of the tremor at Arenal volcano, Costa Rica. J. Volcanol. Geotherm. Res., 157, 49-59, doi:10.1016/j.jvolgeores.2006.03.047.

Lesage, P. (2008). Automatic estimation of optimal autoregressive filters for the analysis of volcanic seismic activity. Nat. Hazards Earth Syst. Sci., 8, 369-376, doi:10.5194/nhess-8-369-2008.

Lin, G., Shearer, P.M., Hauksson, E. (2007). Applying a three-dimensional velocity model, waveform cross correlation, and cluster analysis to locate southern California seismicity from 1981 to 2005. J. Geophys. Res., 112, B12309, doi:10.1029/2007JB004986.

Lo Giudice, E., Patanè, G., Rasà R., Romano, R. (1982). The structural framework of Mount Etna. Mem. Soc. Geol. Ital., 23, 125– 158.

Lo Giudice, E., Rasà, A. (1992). Very shallow earthquakes and brittle deformation in active volcanic areas: the Etnean region a san example. Tectonophysics, 257-268.

Lokmer, I., Bean, C. J., Saccorotti, G., Patanè, D. (2007a). Moment-tensor inversion of LP events recorded on Etna in 2004 using constraints obtained from wave simulation tests. Geophys. Res. Lett., 34, L22316, doi:10.1029/2007GL031902.

Lokmer, I., Saccorotti, G., Lieto, B. D., Bean, C. J. (2007b). Temporal evolution of long-period seismicity at Etna Volcano, Italy, and its relationship with the 2004– 2005 eruption. Earth Planet. Sci. Lett., 34, 205-220.

Maceira, M., Rowe, C.A., Beroza, G., Anderson, D. (2010). Identification of low-frequency earthquakes in non-volcanic tremor using the subspace detector method. Geophys. Res. Lett., 37, L06303, doi:10.1029/2009GL041876.

Marchetti, E., Ripepe, M., Uliveri, G., Burton, M., Caltabiano, T., Salerno, G. (2008). Gas flux rate migration of the magma column, in The Stromboli Volcano, An integrated study of the 2002-2003 eruption, edited by Calvari S., S. Inguaggiato, G. Puglisi, M. Ripepe, M. Rosi, American Geophysical Union, Geophysical Monography Series, 182, 339.

Marchetti, E., Ripepe, M., Harris, A.J.L., Delle Donne, D. (2009a). Tracing the differences between Vulcanian and Strombolian explosions using infrasonic and thermal radiation energy. Earth Planet. Sci. Lett., 279, 273–281, doi:10.1016/j.epsl.2009.01.004.

Marchetti, E., Ripepe, M., Uliveri, G., Caffo, S., Privitera, E. (2009b). Infrasonic evidences for branched conduit dynamics at Mt. Etna volcano, Italy. Geophys. Res. Lett., 36, L19308, doi:10.1029/2009GL040070.

Martini, M., Giudicepietro, F., D'auria, L., Esposito, A. M., Caputo, T., Curciotti, R., De Cesare, W., Orazi, M., Scarpato, G., Caputo, A., Peluso, R., Ricciolino, P., Linde, A., Sacks, S. (2007). Seismological monitoring of the February 2007 effusive eruption of the Stromboli volcano. In: Annals of Geophysics, 50 (6), 775-788.

Matoza, R.S., Hedlin, M.A.H., Garces, M.A. (2007). An infrasound array study of Mount St. Helens. J. Volcanol. Geotherm. Res., 160, 249-262, doi:10.1016/j.jvolgeores.2006.10.006.

Matoza, R.S., Garcés, M.A., Chouet, B.A., D'Auria, L., Hedlin, H., De Grooth-Hedlin, C., Waite, G. P. (2009a). The source of infrasound associated with long-period events at Mount St. Helens. J. Geophys. Res., 114, B04305, doi:10.1029/2008JB006128.

Matoza, R.S., Fee, D., Garcés, M.A., Seiner, J.M., Ramon, P.A., Hedlin, M.A.H. (2009b). Infrasonic jet noise from volcanic eruptions. Geophys. Res. Lett., 36, L08303, doi:10.1029/2008GL036486.

Matoza, R.S., Fee, D., Garcés, M.A. (2010). Infrasonic tremor wavefield of the Pu'u'Ō'ō crater complex and lava tube system, Hawaii, in April 2007. J. Geophys. Res., 115, B12312, doi:10.1029/2009JB007192.

McGonigle, A.J.S., Aiuppa, A., Giudice, G., Tamburello, G., Hodson, A.J., Gurrieri, S. (2008). Unmanned aerial vehicle measurements of volcanic carbon dioxide fluxes. Geophys. Res. Lett., 35, doi:10.1029/2007GL032508.

McGreger, A.D., Lees, J.M. (2004). Vent discrimination at Stromboli Volcano, Italy. J. Volcanol. Geotherm. Res., 137, 169-185, doi:10.1016/j.jvolgeores.2004.05.007.

McLeod, P., Tait, S. (1999). The growth of dykes from magma chambers. J. Volcanol. Geotherm. Res., 92, 231–246.

McNutt, S.R., Rymer, H., Stix, J. (2000) Synthesis of volcano monitoring, in Encyclopedia of Volcanoes, edited by H. Sigurdsson et al., 1167–1185, Academic, San Diego, Calif.

McNutt, S.R. (2005). A Review of Volcanic Seismology. Annual Reviews of Earth and Planetary Sciences, 33, 461-491 doi: 10.1146/annurev.earth.33.092203.122459.

Miklós, A., Hess, P., Bozóki, Z. (2001). Application of acoustic resonators in photoacoustic trace gas analysis and metrology. Rev. Sci. Instrum., 72, 1937-1955.

Milluzzo V., Cannata A., Alparone S., Gambino S., Helleweg M., Montalto P., Cammarata L., Diliberto I.S., Gresta S., Liotta M., Paonita A. (2010). Tornillos at Vulcano: clues to the dynamics of the hydrothermal system. J. Volcanol. Geotherm. Res., doi:10.1016/j.jvolgeores.2010.09.022.

Monaco, C., Tapponnier, P., Tortorici, L., Gillot, P.Y. (1997). Late Quaternary slip rates on the Acireale–Piedimonte normal faults and tectonic origin of Mt. Etna (Sicily). Earth Planet. Sci. Lett., 147, 125– 139.

Montalto, P., Cannata, A., Privitera, E., Gresta, S., Nunnari, G., Patanè, D. (2010). Towards an automatic monitoring system for infrasonic events at Mt. Etna: strategies for source location and modelling. Pure Appl. Geophys., doi:10.1007/s00024-010-0051-y.

Moran, S.C. (2003). Multiple seismogenic processes for high-frequency earthquakes at Katmai National Park, Alaska: Evidence from stress tensor inversions of fault-plane solutions. Bull. Seism. Soc. Am., 93, 94–108.

Moran, S.C., Malone, S.D., Qamar, A.I., Thelen, W.A., Wright, A.K., Caplan-Auerbach, J. (2008a). Seismicity associated with the renewed dome-building eruption of Mount St. Helens 2004-2005, in A Volcano Rekindled: The Renewed Eruption of Mount St. Helens, 2004-2006, edited by D. R. Sherrod, W. E. Scott, and P. H. Stauffer, U.S. Geol. Surv. Prof. Pap., 1750, 27–54.

Moran, S.C., Matoza, R.S., Garcés, M.A., Hedlin, H., Bowers, D., Scott, W.E., Sherrod, D.R. Vallance, J.W. (2008b). Seismic and acoustic recordings of an unusually large rockfall at Mount St. Helens, Washington. Geophys. Res. Lett., 35, L19302, doi:10.1029/2008GL035176.

Morrissey, M.M., Chouet, B.A. (2001). Trends in long-period seismicity related to magmatic fluid compositions. J. Volcanol. Geotherm. Res., 108, 265-281, doi:10.1016/S0377-0273(00)00290-0.

Morrissey, M.M., Garcés, M.A., Ishihara, K., Iguchi, M. (2008). Analysis of infrasonic and seismic events related to the 1998 Vulcanian eruption at Sakurajima. J. Volcanol. Geotherm. Res., 175, 315–324, doi:10.1016/j.jvolgeores.2008.03.008.

Morse, P. M., Ingard, K.U. (1986). Theoretical Acoustics. Princeton University Press, Princeton, NJ.

Murase, T., McBirney, A.R. (1973). Properties of some common igneous rocks and their melts at high temperatures. Geol. Soc. Am. Bull., 84, 3563–3592, doi:10.1130/0016-7606(1973)84<3563:POSCIR>2.0.CO;2.

Napoli, R., Currenti, G., Del Negro, C., Greco, F., Scandura, D. (2008). Volcanomagnetic evidence of the magmatic intrusion on 13th May 2008 Etna eruption. Geophys. Res. Lett., 35, L22301, doi:10.1029/2008GL035350.

Neidel, N., Tarner, M.T. (1971). Semblance and other coherency measures for multichannel data. Geophys., 36, 482-497.

Neri, M., Acocella, V., Behncke, B. (2004). The role of the Pernicana Fault System in the spreading of Mt. Etna (Italy) during the 2002–2003 eruption. Bull. Volcanol., 66, 417-430.

Neuberg, J., Luckett, R., Ripepe, M., Braun, T. (1994). Highlights from a seismic broadband array on Stromboli volcano. Geophys. Res. Lett., 21, 749-752.

Neuberg, J. (2000). External modulation of volcanic activity. Geophys. J. Int., 142, 232–240.

Norini, G., E. De Beni, D. Andronico, M. Polacci, M. Burton, and F. Zucca (2009), The 16 November 2006 flank collapse of the south-east crater at Mount Etna, Italy: Study of the deposit and hazard assessment. J. Geophys. Res., 114, B02204, doi:10.1029/2008JB005779.

Ohminato, T., B. Chouet, P. Dawson, Kedar, S. (1998). Waveform inversion of very long period impulsive signals associated with magmatic injection beneath Kilauea Volcano, Hawaii. J. Geophys. Res., 103, 23839-23862.

Oshima, H., Maekawa, T. (2001) Excitation process of infrasonic waves associated with Merapi-type pyroclastic flow as revealed by a new recording system. Geophys. Res. Lett., 28, 1099–1102, doi:10.1029/1999GL010954.

Palano, M., Puglisi, G., Gresta, S. (2008). Ground deformation patterns at Mt. Etna from 1993 to 2000 from joint use of InSAR and GPS techniques. J. Volcanol. Geotherm. Res., 169, 99-120.

Patanè, D., Barberi, G., Cocina, O., De Gori, P., Chiarabba, C. (2006). Time-Resolved Seismic Tomography Detects Magma Intrusions at Mount Etna. Science, 313, 821-823.

Patanè, D., Di Grazia, G., Cannata, A., Montalto, P., Boschi, E. (2008). The shallow magma pathway geometry at Mt. Etna volcano. Geochem. Geophys. Geosyst., 9, Q12021, doi:10.1029/2008GC002131.

Peltier, A., Bachèlery, P., Staudacher, T. (2009). Magma transport and storage at Piton de La Fournaise (La Réunion) between 1972 and 2007: A review of geophysical and geochemical data. J. Volcanol. Geotherm. Res., 184, 93–108, doi:10.1016/j.jvolgeores.2008.12.008.

Patanè, D., Aliotta, M., Cannata, A., Cassisi, C., Coltelli, M., Di Grazia, G., Montalto, P., Zuccarello, L. (2011). Interplay between Tectonics and Mount Etna's Volcanism: Insights into the Geometry of the Plumbing System. In: Schattner, U. (Ed.), New Frontiers in Tectonic Research - At the Midst of Plate Convergence. Intech open access publisher.

Petersen, T., McNutt, S.R. (2007). Seismo-acoustic signals associated with degassing explosions recorded at Shishaldin Volcano, Alaska, 2003-2004. Bull. Volcanol., 69, 527-536, doi: 10.1007/s00445-006-0088-z.

Pierce, A.D. (1981). Acoustics - An introduction to Its Physical Principles and Applications. McGraw-Hill, New York.

Pinkerton, H., Wilson, L., Macdonald, R. (2002). The transport and eruption of magma from volcanoes: a review. Contemp. Phys., 43, 197–210.

Privitera, E., Sgroi, T., Gresta, S. (2003). Statistical analysis of intermittent volcanic tremor associated with the September 1989 summit explosive eruptions at Mount Etna, Sicily. J. Volcanol. Geotherm. Res., 120, 235–247, doi:10.1016/S0377-0273(02)00400-6.

Raichel, D.R. (2006). The science and applications of acoustics. New York, Springer.

Rauscher, C., Janssen V., Minihold, R. (2001). Fundamentals of Spectrum Analysis, First edition, Rohde & Schwarz GmbH & Co. KG, Mühldorfstrasse 15, 81671 München, Germany.

Rienstra, S.W., Hirschberg, A. (2012). An introduction to acoustics. Eindhoven University of Technology. 10 July.

Rioul, O., Vetterli, M. (1991). Wavelets and signal processing, Signal Processing Magazine, IEEE 8(4): 14-38.

Ripepe, M., Braun, T. (1994). Air-wave phases in strombolian explosion quake seismograms: a possible indicator for the magma level? Acta Vulcanologica, 5, 201-206.

Ripepe, M., Poggi, P., Braun, T., Gordeev, E. (1996). Infrasonic waves and volcanic tremor at Stromboli. Geophys. Res. Lett., 23, 181–184, doi:10.1029/95GL03662.

Ripepe, M., Ciliberto, S., Schiava, M. D. (2001a). Time constraints for modeling source dynamics of volcanic explosions at Stromboli. J. Geophys. Res., 106, 8713–8727, doi:10.1029/2000JB900374.

Ripepe, M., Coltelli, M., Privitera, E., Gresta, S., Moretti, M., Piccinini, D. (2001b). Seismic and infrasonic evidences for an impulsive source of the shallow volcanic tremor at Mt. Etna, Italy. Geophys. Res. Lett., 28(6), 1071–1074, doi:10.1029/2000GL011391.

Ripepe, M., Marchetti, E. (2002). Array tracking of infrasonic sources at Stromboli volcano. Geophys. Res. Lett., 29 (22), 33-1-33-4. doi:10.1029/2002GL015452.

Ripepe, M., Harris, A.J.L., Carniel, R. (2002). Thermal, seismic and infrasonic evidences of variable degassing rates at Stromboli volcano. J. Volcanol. Geotherm. Res., 118, 285-297, doi:10.1016/S0377-0273(02)00298-6.

Ripepe, M., Marchetti, E., Ulivieri, G., Harris, A.J.L., Dehn, J., Burton, M., Caltabiano, T., Salerno, G. (2005). Effusive to explosive transition during the 2003 eruption of Stromboli volcano. Geology, 33, 341-344, doi:10.1130/G21173.1.

Ripepe, M., Delle Donne, D., Lacanna, G., Marchetti, E., Ulivieri, G. (2009). The onset of the 2007 Stromboli effusive eruption recorded by an integrated geophysical network. J. Volcanol. Geotherm. Res., 182, 131-136, doi:10.1016/j.jvolgeores.2009.02011.

Ripepe, M., Marchetti, E., Bonadonna, C., Harris, A.J.L., Pioli, L., Ulivieri, G. (2010). Monochromatic infrasonic tremor driven by persistent degassing and convection at Villarrica Volcano, Chile. Geophys. Res. Lett., 37, L15303, doi:10.1029/2010GL043516.

Rittmann, A. (1973). Structure and evolution of Mount Etna. Philos. Trans. R. Soc. Lond., 274A, 5-16.

Rowe, C.A., Aster, R.C., Kyle, P.R., Dibble, R.R., Schlue, J.W. (2000). Seismic and acoustic observations at Mount Erebus Volcano, Ross Island, Antarctica, 1994-1998. J. Volcanol. Geotherm. Res., 101, 105-128, doi:10.1016/S0377-0273(00)00170-0.

Ruiz, M.C., Lees, J.M., Johnson, J.B. (2006). Source constraints of Tungurahua volcano explosion events. Bull. Volcanol., 68, 480–490, doi:10.1007/s00445-005-0023-8.

Rust, D., & Neri, M. (1996). The boundaries of large-scale collapse on the flanks of Mount Etna, Sicily. In: Volcano instability on the Earth and other planets. McGuire, W.J., Jones, A.P., Neuberg, J., 193–208, Geol. Soc. Lond. Spec. Pub. 110.

Rust, D., Behncke, B., Neri, M., Ciocanel, A. (2005). Nested zones of instability in the Mount Etna volcanic edifice, Sicily. J. Volcanol. Geotherm. Res., 144, 137–153. http://dx.doi.org/10.1016/j.jvolgeores.2004.11.021.

Saab, R., McKeown, M.J., Myers, L.J., Abu-Gharbieh, R. (2005). A Wavelet Based Approach for the Detection of Coupling in EEG Signals, paper presented at 2th International, Neural Engineering, IEEE EMBS Conference on Neural Engineering, Arlington.

Saccorotti, G., Zuccarello, L., Del Pezzo, E., Ibanez, J., Gresta, S. (2004). Quantitative analysis of the tremor wavefield at Etna Volcano. J. Volcanol. Geotherm. Res., 136, 223–245, doi:10.1016/j.jvolgeores.2004.04.003.

Saccorotti, G., Lokmer, I., Bean, C.J., Di Grazia, G., Patanè, D. (2007). Analysis of sustained long-period activity at Etna Volcano, Italy. J. Volcanol. Geotherm. Res., 160, 340-354.

Sahetapy-Engel, S.T., Harris, A.J.L., Marchetti, E. (2008). Thermal, seismic and infrasound observations of persistent explosive activity and conduit dynamics at Santiaguito lava dome, Guatemala. J. Volcanol. Geotherm. Res., 173, 1–14, doi:10.1016/j.jvolgeores.2007.11.026.

Schick, R., Riuscetti, M. (1973). An analysis of volcanic tremors at South ltalian volcanoes. Z. Geophysik, 39, 247–262.

Schweitzer, J., Fyen, J., Mykkeltveit, S., Gibbons, S.J., Pirli, M., Kühn, D., Kværna, T. (2011). Seismic Arrays, in P. Bormann (Ed.), New Manual of Seismological Observatory Practice (NMSOP) (1-70). Potsdam: Deutsches GeoForschungsZentrum GFZ, doi:10.2312/GFZ.NMSOP-2_ch9.

Serway, R.A., Jewett, J.W. (2006). Principles of physics: a calculus-based text. Brooks/Cole, Belmont, CA, USA.

Sharma, B.K., Kumar, A., Murthy, V.M. (2010). Evaluation of seismic event detection algorithms. J. Geol. Soc. India, 75, 533-538.

Sparks, R.S.J. (2003). Forecasting volcanic eruptions. Earth Planet. Sci. Lett., 210, 1-15.

Sparks, R.S.J., Biggs, J., Neuberg, J.W. (2012). Monitoring Volcanoes. Science, 335, 1310-1311.

Spina, L., Cannata, A., Privitera, E., Vergniolle, S., Ferlito, C., Gresta, S., Montalto, P., Sciotto, M. Insights into the Mt. Etna shallow plumbing system from the analysis of infrasound signals (August 2007-December 2009). Submitted to Pageoph.

Steinberg, G.S., Steinberg, A.S. (1975). On possible causes of volcanic tremor. J. Geophys. Res., 80, 1600–1604.

Stephens, C.D., Chouet, B.A. (2001). Evolution of the December 14, 1989 precursory long period event swarm at Redoubt Volcano, Alaska. J. Volcanol. Geotherm. Res., 109, 133–148, doi:10.1016/S0377-0273(00)00308-5.

Sturton, S., Neuberg, J. (2006). The effects of conduit length and acoustic velocity on conduit resonance: Implications for low-frequency events. J. Volcanol. Geotherm. Res., 151, 319–339, doi:10.1016/j.jvolgeores.2005.09.009.

Taddeucci, J., Pompilio, M., Scarlato, P. (2002). Monitoring the explosive activity of the July–August 2001 eruption of Mt. Etna (Italy) by ash characterization. Geophys. Res. Lett., 29 (8), 1029–1032, 1230, doi:10.1029/2001GL014372.

Tait, S., Jaupart, C., Vergniolle, S. (1989). Pressure, gas content and eruption periodicity of a shallow, crystallising magma chamber. Earth Planet. Sci. Lett., 92, 107-123.

Tanguy, J.C., Condomines, M., Kieffer, G. (1997). Evolution of Mount Etna magma: constraints on the present feeding system and eruptive mechanism. J. Volcanol. Geotherm. Res., 75, 221– 250.

Tilling, R.I. (2008). The critical role of volcano monitoring in risk reduction. Adv. Geosci., 14, 3–11, doi:10.5194/adgeo-14-3-2008.

Torrence, C., Compo, G.P. (1998). A practical guide to wavelet analysis. Bull. Am. Met. Soc., 79(1), 61-78.

Trnkoczy, A. (2012). Understanding and parameter setting of STA/LTA trigger algorithm. In New Manual of Seismological Observatory Practice (NMSOP-2), Bormann, P. (Ed.), IASPEI, GFZ German Research Centre for Geosciences, Potsdam.

Uhira, H., Takeo, M. (1994). The source of explosive eruptions of Sakurajima volcano, Japan. J. Geophys. Res., 99, 17775-17789.

Van Trees, H.L. (1968). Detection, Estimation and Modulation Theory, John Wiley and Sons, New York.

Varley, N., Arámbula-Mendoza, R., Reyes-Dávila, G., Stevenson, J., Harwood, J. (2010). Long-period seismicity during magma movement at Volcán de Colima. Bull. Volcanol., 72, 1093–1107, doi:10.1007/s00445-010-0390-7.

Vergniolle, S., Brandeis, G. (1996). Strombolian explosions: a large bubble breaking at the surface of a lava column as a source of sound. J. Geophys. Res., 101 (B9), 20433–20448.

Vergniolle, S., Caplan-Auerbach, J. (2004). Acoustic measurements of the 1999 basaltic eruption of Shishaldin volcano, Alaska: 2) Precursor to the Subplinian activity. J. Volcanol. Geotherm. Res., 137, 135–151, doi:10.1016/j.jvolgeores.2004.05.004.

Vergniolle, S., Boichu, M., Caplan-Auerbach, J. (2004). Acoustic measurements of the 1999 basaltic eruption of Shishaldin volcano, Alaska: 1) Origin of Strombolian activity. J. Volcanol. Geotherm. Res., 137, 109-134, doi:10.1016/j.jvolgeores.2004.05.003.

Vergniolle, S., Ripepe, M. (2008). From Strombolian explosions to fire fountains at Etna Volcano (Italy): what do we learn from acoustic measurements? Geol. Soc. London, Special Publications, 307, 103–124.

Vidal, V., Gèminard, J.C., Divoux, T., Melo, F. (2006). Acoustic signal associated with the bursting of a soap film which initially closes on overpressurized cavity. Eur. Phys. J. B, 54, 321-339, doi:10.1140/epjb/e2006-00450-0.

Vidal, V., Ripepe, M., Divoux, T., Legrand, D., Géminard, J.C., Melo, F. (2010). Dynamics of soap bubble bursting and its implications to volcano acoustics. Geophys. Res. Lett., 37, L07302, doi:10.1029/2009GL042360.

Weill, A., Brandeis, G., Vergniolle, S., Baudin, F., Bilbille, J., Fevre, J., Piron, B., Hill, X. (1992). Acoustic sounder measurements of the vertical velocity of volcanic jets at Stromboli volcano. Geophys. Res. Lett., 19, 2357–2360.

Witham, F., Llewellin, E.W. (2006). Stability of lava lakes. J. Volc. Geotherm. Res., 158, 321–332.

Withers, M., Aster, R., Young, C., Beiriger, J., Harris, M., Moore, S., Trujillo, J. (1998). A comparison of Select Trigger Algorithms for Automated Global Seismic Phase and Event Detection. Bull. Seism. Soc. Am., 88, 95-106.

Yokoo, A., Tameguri, T., Iguchi, M. (2009). Swelling of a lava plug associated with a Vulcanian eruption at Sakurajima Volcano, Japan, as revealed by infrasound record: case

study of the eruption on January 2, 2007. Bull. Volcanol., 71 (6), 619-630, doi:10.1007/s00445-008-0247-5.

Zobin, V. (2012). Introduction to volcanic seismology. Elsevier, Amsterdam.

APPENDIX

Optimization of sensor deployment

In this section we will describe a synthetic test about the sensor deployment strategy. The need to face this topic raised from a volcano geophysical field methods course held in Yellowstone National Park in 2011, when an infrasound monitoring experiment was carried out. The experiment consisted in deploying two 4-element microphone arrays (hereafter referred to as WA and EA) in the area of Lower Geyser Basin (LGB) and placed as shown in Figure 6.1. The survey proved how such an acoustic monitoring can concretely support the study of geyser eruption statistics, duration and style of eruption (Johnson et al., in preparation). Indeed, during the experiment, about 5 major fountain-type geysers of LGB, several kilometres far from the arrays, were located and characterized (Johnson et al., in preparation). Nevertheless, such a distribution and location of arrays did not allow to detect clear signals from Upper Geyser Basin (UGB), placed more than 8.5 km far from arrays (**Fig. A.1**). Starting from this limitation, a test for the optimization of sensor deployment was carried out. The goal of the test is to identify the best position for the deployment of a third array, which, coupled with the two arrays WA and EA, is capable of locating geothermal features even in the UGB.

Methodology and results

The synthetic test was performed maintaining fixed the position of WA and EA arrays and systematically changing the position of the third array within a 2D grid. Such a grid has dimension 5x12 km^2 with a 1 km spacing (78 array positions in total; **Fig. A.1**). Microphones in each array were placed at the vertices and at the center of a equilateral triangle (with 30 m side length).

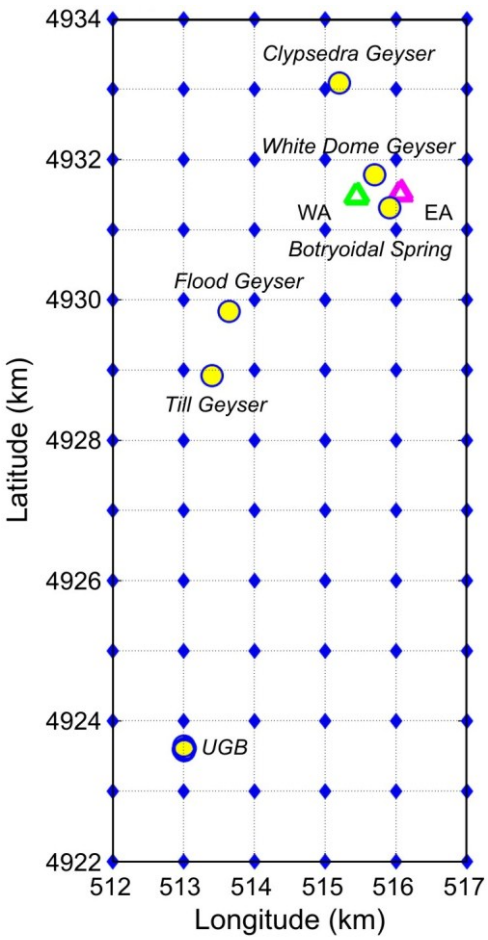

Fig. A.1 *Configuration of the 2D search grid nodes (blue diamonds) representing the third array positions during the synthetic test, WA and EA locations (green and pink triangles, respectively), and source positions (geysers of the Lower Geyser Basin and Middle Geyser Basin, named MGB) where synthetic acoustic signals were generated (yellow circles).*

The approach used to perform the test consists of: i) synthetic pressure signal generation at given sources; ii) source location; iii) estimation of the distance between the real source position and the source location by the three arrays (considered as the error location). This method produces a distribution map of the parameters chosen to describe the accuracy of the location, thus allowing to identify the best position for the third array deployment.

To simulate infrasonic transient at sources (geothermal features), a rapid change of flux (gas release) at a simple acoustic point source was considered. The arbitrary mass flux was (J) estimated following Johnson (2003):

$$J = \frac{j}{t^2 + 0.01} \qquad t < 0 \qquad (6.1)$$

$$J = \frac{j}{t^2 + 0.1} \qquad t > 0 \tag{6.2}$$

where t is the time and j is the arbitrary gas mass. The excess pressure signal was then calculated by means of the time derivative of the mass flux (Johnson, 2003 and reference therein). The acoustic signal at the source was perturbed by adding red noise evaluated as the univariate lag-one autoregressive process (Torrence and Compo, 1998):

$$x_n = \alpha x_{n-1} + z_n \tag{6.3}$$

where α is the lag-one autocorrelation and z_n is the Gaussian white noise. Furthermore, atmospheric effects and wind gradients on propagation path were simulated by randomly varying acoustic wave velocity in the range 340 m/s ± 4%. In particular, at each source acoustic signals with 20 different velocity values were generated. For the test, 9 source positions were chosen (yellow circles in **Fig. A.1**): 3 geysers in the LGB (Clypsedra Geyser, White Dome Geyser and Botryoidal Spring), 2 in MGB (Flood Geyser and Till Geyser) and 4 in UGB (Sawmill, Tardy, Spasmodic and Old Tardy Geyser), which we are mostly interested in. In order to locate synthetic signals, first arrays were independently used to identify incident coherent plane wave energy and then the intersection region of the backazimuth beams was found (for details about location method see Johnson et al., in preparation). The synthetic signals were located by using all the three arrays, and the distance between the real source position and the location was calculated. Since for each position of the third array we performed 20 x 9 locations of synthetic signals, the median and the mean of the distances were obtained for every grid node. Finally, by performing about 14000 source locations the space distributions of these two parameters were drawn in **Figure A.2a, b**.

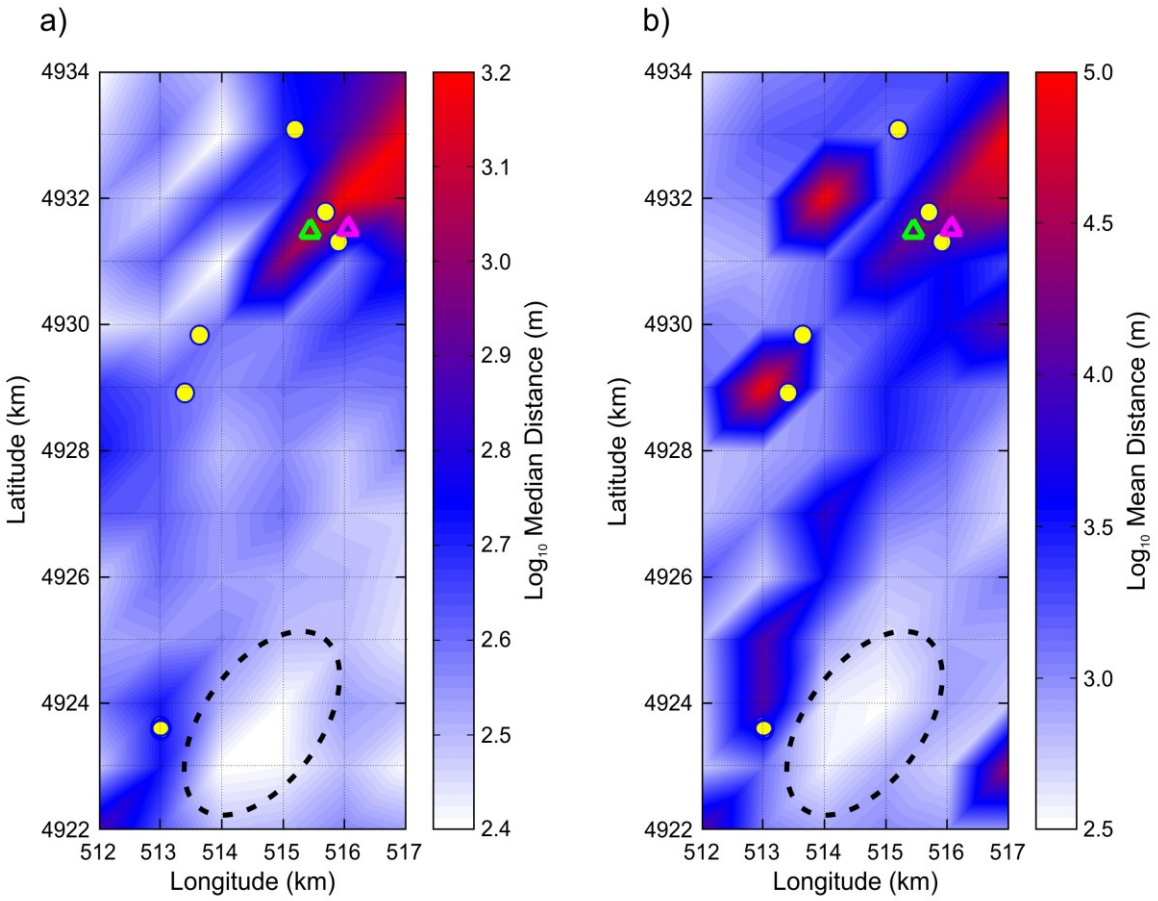

Fig. A.2 ***(a)*** *Distribution map of the logarithm of the median values of the distances between real source positions and source locations.* ***(b)*** *Distribution map of the logarithm of the mean values of the distances between real source positions and source locations. Black dashed lines in* ***(a)*** *and* ***(b)*** *frame areas with the minimum location error. See the text for details.*

In this way the area characterized by minimum location error in the map can be identified in the southern sector of the grid and represents the position in which the third array, coupled with WA and EA, should be deployed in order to well locate geysers in LGB, MGB and UGB (area encircled by black dashed lines in **Fig. A.2**).

In such a setting, where numerous geysers with different features are active, a better strategic deployment of arrays could favor a comprehensive monitoring (Johnson et al., in preparation). This test intends to be an easy tool to project and plan deployments of arrays.